به نام خدا

مرکز دانلود رایگان
مهندسی متالورژی و مواد

www.lran-mavad.com
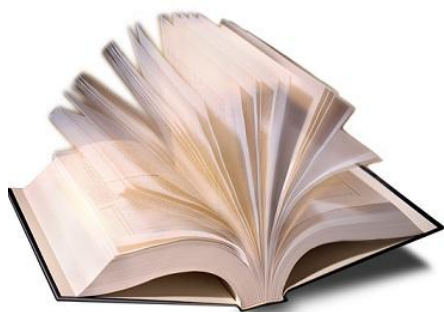
Failure mechanisms of advanced welding processes

Edited by Xin Sun

Failure mechanisms of advanced welding processes

Related titles:

Friction stir welding
(ISBN 978-1-84569-450-0)
Friction stir welding (FSW) is a solid-state welding process that is gaining wide acceptance in industry, especially the shipbuilding, aerospace, mass transportation and automotive industries. FSW is particularly suited to those industries that use aluminium and its alloys. This authoritative book provides a comprehensive review of the subject of friction stir welding and covers topics such as process basics, equipment, modelling, inspection and quality control and applications.

Weld cracking in ferrous alloys
(ISBN 978-1-84569-300-8)
Weld cracks are unacceptable defects that can compromise the integrity of welded structures. Most cracks are the result of solidification, cooling and stresses that develop due to weld shrinkage. Weld cracking can lead to structural failures which at best will require remedial action and at worst can lead to loss of life. All industries that utilise welding can be affected, including nuclear, aerospace, automotive, shipbuilding and civil engineering. This book covers the processes of weld cracking in different ferrous alloys and for different welding technologies. It also covers methods of testing for weld cracks, avoidance and repair.

Real-time weld process monitoring
(ISBN 978-1-84569-268-1)
Welding processes are being increasingly automated and are operating at higher speeds. Monitoring the quality of welds produced by such processes is becoming ever more important as humans are becoming more and more remote from the actual welding operation. Many new systems are being developed which can monitor automated (and non-automated) welding processes in real time. The systems can also detect hidden defects that even a trained quality assurance professional would find difficult to spot. The monitoring systems are non-destructive and improve the quality of the weld and components produced, as well as reducing the scrap rate. The systems are fast, reliable and cost-effective.

Details of these and other Woodhead Publishing materials books can be obtained by:

* visiting our web site at www.woodheadpublishing.com
* contacting Customer Services (e-mail: sales@woodheadpublishing.com; fax: +44 (0) 1223 893694; tel.: +44 (0) 1223 891358 ext.130; address: Woodhead Publishing Limited, Abington Hall, Granta Park, Great Abington, Cambridge CB21 6AH, UK)

If you would like to receive information on forthcoming titles, please send your address details to: Francis Dodds (address, tel. and fax as above; e-mail: francis.dodds@woodheadpublishing.com). Please confirm which subject areas you are interested in.

Failure mechanisms of advanced welding processes

Edited by
Xin Sun

CRC Press
Boca Raton Boston New York Washington, DC

WOODHEAD PUBLISHING LIMITED
Oxford   Cambridge   New Delhi

Contents

v

www.iran–mavad.com

مرجع دانشجویان و مهندسین مواد

Contributor contact details

(* = main contact)

Editor, Chapter 2 and 11

X. Sun*
Pacific Northwest National
  Laboratory
902 Battelle Blvd.
Richland, WA 99352
USA
E-mail: xin.sun@pnl.gov

Chapter 1

J. Pan* and K. Sripichai
Mechanical Engineering
University of Michigan
Ann Arbor, MI 48109
USA
E-mail: jwo@umich.edu
kulthida@umich.edu

P-C. Lin
Mechanical Engineering
National Chung Cheng University
Chia-Yi 621
Taiwan
E-mail: imepcl@ccu.edu.tw

D-A. Wang
Institute of Precision Engineering
National Chung Hsing University
Taichung
Taiwan

S-H. Lin
Wheel Group
SuperAlloy Industrial Co. Ltd.
Yun-Lin 640
Taiwan

Chapter 3

M. Tumuluru
United States Steel Corporation
Research and Technology Center
800 East Waterfront Drive
Munhall, PA 15120
USA
E-mail: mtumuluru@uss.com

Chapter 4

S. K. Khanna*
La Pierre Associate Professor
Assistant Director, Missouri
    Industrial Assessment Center
Mechanical and Aerospace
    Engineering
University of Missouri
Columbia, MO 65211
USA
E-mail: khannas@missouri.edu

X. Long
Senior Research Engineer
Center for Reliable Energy
    Systems
5960 Venture Drive
Dublin, OH 43017
USA
E-mail: xinlong99@gmail.com

Chapter 5

B. Ghaffari*
Materials and Processes
    Department
Research and Advanced
    Engineering
Ford Motor Company
MD 3182/RIC, P.O. Box 2053
Dearborn, MI 48121-2053, USA
E-mail: bghaffar@ford.com

G. Mozurkewich
Ford Motor Company (retired)
1872 Snowberry Ridge Road
Ann Arbor, MI 48103
USA

Chapter 6

K. J. Colligan
Concurrent Technologies
    Corporation
15091, Alabama Highway 20,
    Suite A
Madison, AL 35756
USA
E-mail: colligan@ctc.com

Chapter 7

M. N. James*
School of Marine Science and
    Engineering
University of Plymouth
Drake Circus
Plymouth PL4 8AA
UK
E-mail: mjames@plymouth.ac.uk

D. G. Hattingh, H. Lombard, I.
    Wedderburn, D. L. H. Bulbring
    and A. Els-Botes
Mechanical Engineering
Nelson Mandela Metropolitan
    University
Gardham Avenue
Box 77000
Port Elizabeth, 6031
South Africa
E-mail: danie.hattingh@nmmu.ac.za

A. Steuwer
ESS Scandinavia
Stora Algatan 4
22350 Lund
Sweden
E-mail: axel.steuwer@esss.se

Chapter 8

L. Liu
School of Materials Science and
  Engineering
Dalian University Of Technology
2 Linggong Road
Dalian City 116024
Liaoning Province
China
E-mail: liulm@dlut.edu.cn

Chapter 9

V. Caccese
Mechanical Engineering
University of Maine
Orono, ME 04469
USA
E-mail: vince.caccese@umit.maine.
  edu

Chapter 10

A. A. Zadpoor*
Materials Innovation Institute
  (M2i)
Mekelweg 2
Delft 2628CD
The Netherlands
E-mail: a.a.zadpoor@tudelft.nl

J. Sinke
Faculty of Aerospace Engineering
Delft University of Technology
  (TU Delft)
Kluyverweg 1
Delft 2629HS
The Netherlands
E-mail: j.sinke@tudelft.nl

<div align="right">

1

</div>

Mechanics modeling of spot welds under general loading conditions and applications to fatigue life predictions

J. P A N and K. S R I P I C H A I, University of Michigan, USA, P-C. L I N, National Chung Cheng University, Taiwan, D-A. W A N G, National Chung Hsing University, Taiwan, S-H. L I N, Wheel Group, SuperAlloy Industrial Co. Ltd., Taiwan

Abstract: A mechanics model of a spot weld in a finite plate under general loading conditions is presented first. Available closed-form stress, moment and transverse shear force solutions are then discussed for a plate with a rigid inclusion subjected to various types of loading conditions. Based on a strip model, closed-form analytical stress intensity factor solutions for spot welds are presented under various types of loading conditions. A kinked crack growth model is then presented and adopted to predict the fatigue lives of resistance spot welds in lap-shear specimens of dual phase, low carbon and high strength steels. Comparisons of predicted fatigue lives based on the kinked crack growth model with the experimental data indicate that the fatigue life predictions are in agreement with or lower than the experimental data.

Key words: fatigue, fatigue crack propagation, *J* integral, kinked crack, spot weld, stress intensity factor, structural stress.

1.1 Introduction

Resistance spot welding is widely used to join sheet metals in the automotive industry. These spot welds are subjected to complex multiaxial service loads. In order to be able to predict the fatigue lives of spot welds in vehicles, the fatigue lives of spot welds in various types of specimens have been investigated by many researchers. Many researchers have conducted experiments and correlated their experimental results with empirical relationships. However, these empirical relations are only applicable to the spot welds under particular welding and testing conditions. Since a spot weld provides a natural crack or notch along the nugget circumference, fracture mechanics appears to be a logical choice to characterize or correlate the fatigue data of these welds. Fracture mechanics has been adopted to investigate the fatigue lives of spot welds in various types of specimens or configurations (Pook, 1975, 1979; Radaj, 1989; Radaj and Zhang, 1991a, 1991b, 1992; Sheppard, 1993; Swellam *et al.*, 1994; Zhang, 1997, 1999, 2001;

<div align="right">

1

</div>

Wang *et al.*, 2005a, 2005b; Lin *et al.*, 2007). Zhang (1999) showed that fracture mechanics solutions can be used to correlate the fatigue data of spot welds in different types of specimens. However, the stress intensity factor and structural stress solutions proposed by Radaj (1989), Radaj and Zhang (1991a, 1991b, 1992) and Zhang (1997, 1999, 2001) have not been adopted widely for characterizing the fatigue behavior of spot welds in specimens and automotive structural components.

Pook (1975, 1979) made significant contributions using the energy release rate concept to obtain the stress intensity factor solutions for various configurations of beam and plates with connections. Pook (1979) indicated that, for a class of transversely loaded configurations consisting of two thin plates or beams joined over part of their common plane under symmetric loading conditions, the energy release rate or the stress intensity factor at a crack tip depends on the bending moment acting on the beam or plate in the vicinity of the crack tip. Wang *et al.* (2005a) conducted a three-dimensional finite element analysis of circular plates with connection under opening loading conditions. Wang *et al.* (2005b) also conducted a three-dimensional finite element analysis of a nearly square large lap-shear specimen. The results of the three-dimensional finite element analyses of Wang *et al.* (2005a, 2005b) suggest that using the bending moments and the membrane forces or the corresponding structural stresses to obtain the stress intensity factor solutions for spot welds, assumed to be rigid inclusions in thin plates, can be quite accurate.

The closed-form solutions for thin plates with rigid inclusions under shear, central bending, counter bending and opening loading conditions were obtained by Muskhelishvili (1953), Reißner (1929), Goland (1943), Timoshenko and Woinowsky-Krieger (1959) and Lin *et al.* (2007), respectively. These solutions, except those of Goland (1943) and Lin *et al.* (2007), were used by Zhang (1997, 1999, 2001) to obtain the structural stresses at several critical locations of spot welds in various types of specimens and automotive structures, where the spot welds were treated as a rigid inclusion in the analytical or numerical solution procedures. Rupp *et al.* (1990, 1995) used a beam element model, whereas Salvini *et al.* (1997, 2000) and Vivio *et al.* (2002) used a spot weld assembly finite element model to represent a spot weld in order to obtain the resultant forces and moments through the spot weld for fatigue life estimations.

In this chapter, the theoretical frameworks for spot welds under various types of loading conditions are presented, based on elasticity theories and fracture mechanics. Available closed-form stress, moment and transverse shear force solutions are reviewed for a plate with a rigid inclusion subjected to various types of resultant loads on the inclusion and various types of resultant loads on the plate lateral surface. Based on the *J* integral for a strip model, closed-form analytical stress intensity factor solutions for spot

welds are derived in terms of the structural stresses around a rigid inclusion in a plate under various types of loading conditions. As an example to demonstrate the applicability of the stress intensity factor solutions for spot welds, a fatigue crack growth model is presented that correlates the fatigue lives of resistance spot welds in lap-shear specimens of dual phase, low carbon and high strength steels under cyclic loading conditions based on the experimental observations of spot welds that failed in a kinked crack propagation mode. The fatigue crack growth model is based on the global stress intensity factor solutions for main cracks, the local stress intensity factor solutions for kinked cracks as functions of the kink length, the experimentally determined kink angles and the Paris law for kinked crack propagation. The predicted fatigue lives based on the fatigue crack growth model are then compared with the experimental data.

1.2   Spot weld in a finite plate under general loading conditions

Figure 1.1 shows schematically two metal sheets joined by a spot weld and also shows the surface tractions $\mathbf{T}_U$ and $\mathbf{T}_L$ which are applied to the lateral
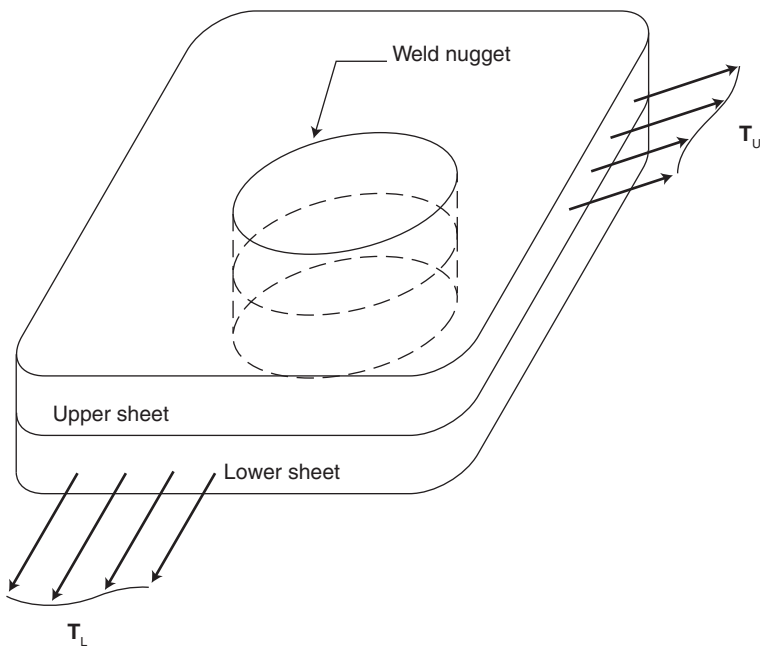
1.1 Two metal sheets are joined by a spot weld. The metal sheets are under surface traction $\mathbf{T}_U$ and $\mathbf{T}_L$.
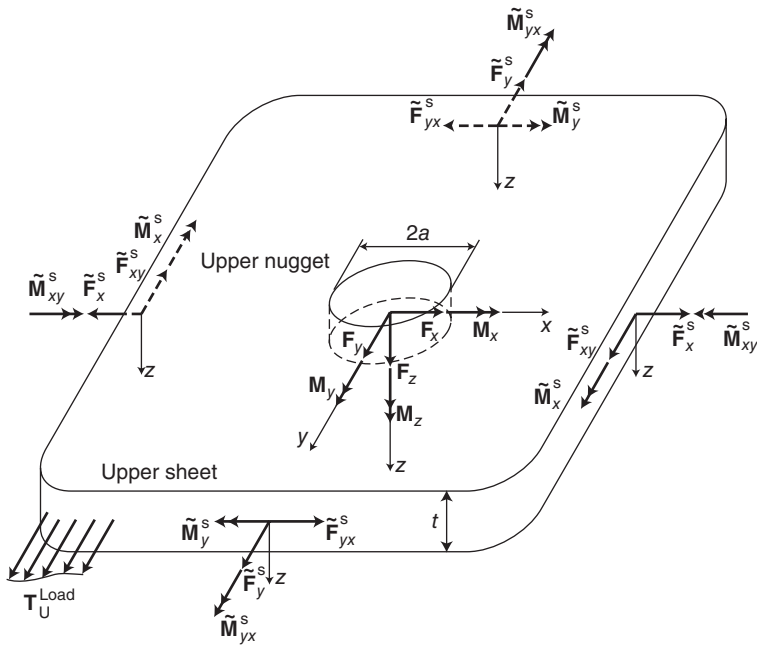
1.2 Upper sheet with the upper half nugget is shown with the surface traction $\mathbf{T}_U^{\text{Load}}$, the resultant loads **F** and **M** and the self-balanced resultant loads $\mathbf{F}^s$ and $\mathbf{M}^s$. The upper sheet has the thickness t and the nugget has the diameter $2a$.

surfaces of the upper and lower sheets, respectively. The weld nugget is idealized as a circular cylinder. Next, we consider the upper half of the weld nugget in the upper sheet as shown in Fig. 1.2. The upper sheet has the thickness t and the nugget has the diameter $2a$. Figure 1.2 shows the upper sheet with the upper half nugget with a surface traction $\mathbf{T}_U^{\text{Load}}$, the resultant loads **F** and **M** acting on the lower surface of the upper half nugget, and the self-balanced resultant loads $\mathbf{F}^s$ and $\mathbf{M}^s$. Note that the load-balanced part $\mathbf{T}_U^{\text{Load}}$ is statically in equilibrium with the resultant loads **F** and **M**.

Most researchers approximate the general loading condition of spot welds by using the resultant loads applied to the interfacial circular cross-section of the weld nugget, for example, Swellam *et al.* (1994), Rupp *et al.* (1995) and Salvini *et al.* (2000). However, Zhang (1997, 2001), Wang *et al.* (2005b) and Lin *et al.* (2007) indicated that the closed-form stress solutions for a rigid inclusion under the self-balanced surface tractions of the plate are important in obtaining the analytic solutions of the stress intensity factors for spot welds. As shown in Fig. 1.2, the resultant force **F** and the

resultant moment $\mathbf{M}$ are now decomposed into three resultant forces $\mathbf{F}_x$, $\mathbf{F}_y$ and $\mathbf{F}_z$ and three resultant moments $\mathbf{M}_x$, $\mathbf{M}_y$ and $\mathbf{M}_z$, respectively. The self-balanced resultant force $\mathbf{F}^s$ and the self-balanced resultant moment $\mathbf{M}^s$ due to the self-balance traction $\mathbf{T}_U^{Self}$ on the plate lateral surface can now be decomposed into two uniform tensile forces $\tilde{\mathbf{F}}_x^s$ and $\tilde{\mathbf{F}}_y^s$, two uniform shear forces $\tilde{\mathbf{F}}_{xy}^s$ and $\tilde{\mathbf{F}}_{yx}^s$, two uniform bending moments $\tilde{\mathbf{M}}_x^s$ and $\tilde{\mathbf{M}}_y^s$, and two uniform twisting moments $\tilde{\mathbf{M}}_{xy}^s$ and $\tilde{\mathbf{M}}_{yx}^s$.

Note that the forces $\tilde{\mathbf{F}}_x^s$, $\tilde{\mathbf{F}}_y^s$, $\tilde{\mathbf{F}}_{xy}^s$, and $\tilde{\mathbf{F}}_{yx}^s$ and the moments $\tilde{\mathbf{M}}_x^s$, $\tilde{\mathbf{M}}_y^s$, $\tilde{\mathbf{M}}_{xy}^s$ and $\tilde{\mathbf{M}}_{yx}^s$ represent the uniformly distributed forces and moments applied to the lateral surface of the sheet. The units of the forces and moments with tilde signs are force per unit length and moment per unit length, respectively. In the following, we investigate the stresses, moments and transverse shear forces near a spot weld in a sheet under various types of loading conditions based on elasticity theories. Note that, in the following sections, the spot weld is assumed to be a rigid inclusion.

1.3 Closed-form solutions for a plate with an inclusion

Closed-form solutions for a plate with an inclusion under different resultant forces and moments were presented by Lin and Pan (2008a). The different loading and boundary conditions considered by Lin and Pan (2008a) are shown schematically in Fig. 1.3 where a plate with a rigid inclusions is subjected to (a) a shear force $\mathbf{F}_x$, (b) an opening force $\mathbf{F}_z$ and a clamped edge, (c) an opening force $\mathbf{F}_z$ and a simply supported edge, (d) a central bending moment $\mathbf{M}_x$ and a clamped edge, (e) a central bending moment $\mathbf{M}_x$ and a simply supported edge, and (f) a twisting moment $\mathbf{M}_z$. Closed-form solutions for plates with inclusions under different self-balanced resultant forces and moments were presented by Lin and Pan (2008a). The different loading and boundary conditions considered by Lin and Pan (2008a) are shown schematically in Fig. 1.4 where a plate with a rigid inclusion is subjected to (a) a remote uniform tensile force $\tilde{\mathbf{F}}_x^s$, (b) a remote uniform counter bending moment $\tilde{\mathbf{M}}_x^s$, (c) a uniform counter bending moment $\tilde{\mathbf{M}}_x^s$ along two edges of a square plate, (d) a remote uniform shear force $\tilde{\mathbf{F}}_{xy}^s$, and (e) a remote uniform twisting moment $\tilde{\mathbf{M}}_{xy}^s$. The closed form solutions are quite complex and can be found in Lin and Pan (2008a).

1.4 Stress intensity factor solutions for a strip under various types of loading conditions

Once the moments, transverse shear forces and structural stresses along the rigid inclusion circumference are determined from a plate with a rigid
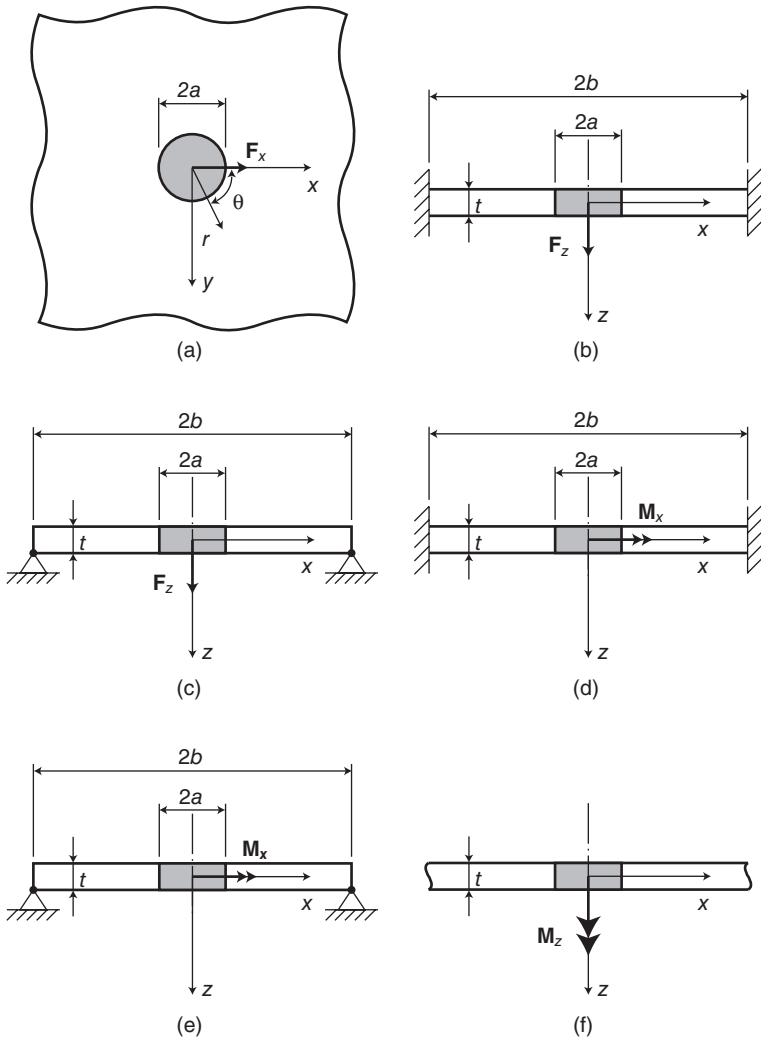
1.3 Plate with a rigid inclusion subjected to various types of resultant loads and subjected to different types of boundary conditions, (a) a shear force $\mathbf{F}_x$, (b) an opening force $\mathbf{F}_z$ and a clamped edge, (c) an opening force $\mathbf{F}_z$ and a simply supported edge, (d) a central bending moment $\mathbf{M}_x$ and a clamped edge, (e) a central bending moment $\mathbf{M}_x$ and a simply supported edge, and (f) a twisting moment $\mathbf{M}_z$.

inclusion under various types of the loading conditions (Lin and Pan, 2008a), the strip model of Radaj and Zhang (1991a) can then be adopted to derive approximate stress intensity factor solutions for spot welds under various types of loading conditions. Figure 1.5 shows a two-dimensional
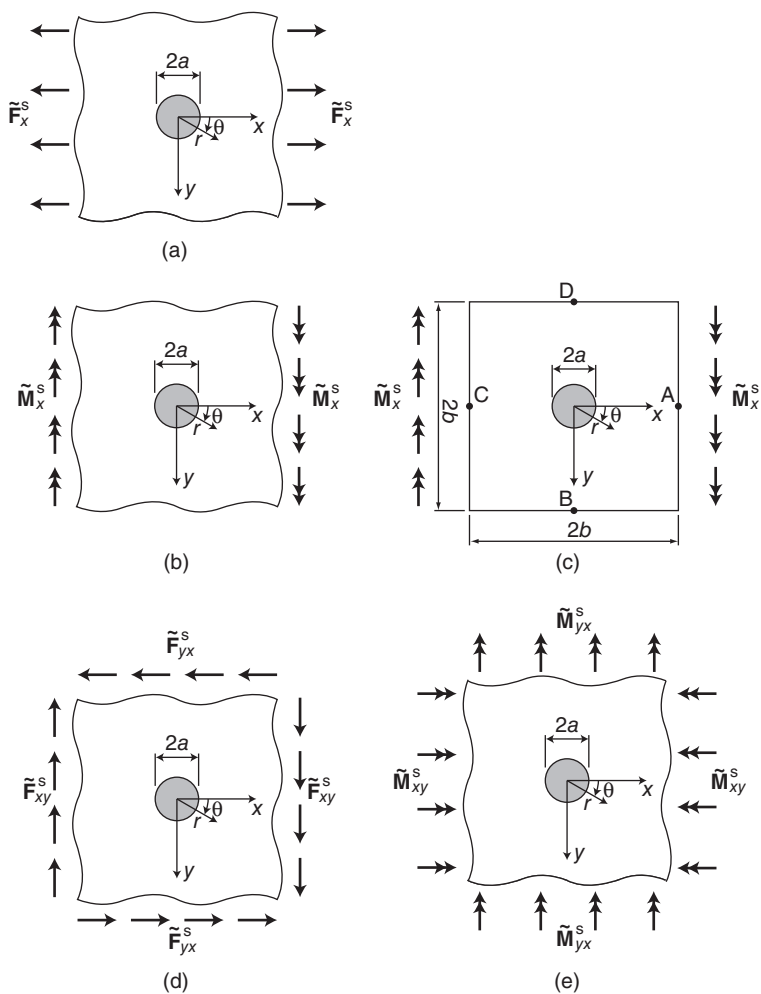
1.4 Plate with a rigid inclusion subjected to various types of self-balanced resultant loads on the plate lateral surface, (a) a remote uniform tensile force $\tilde{\mathbf{F}}_x^s$, (b) a remote uniform counter bending moment $\tilde{\mathbf{M}}_x^s$, (c) a uniform counter bending moment $\tilde{\mathbf{M}}_x^s$ along two edges of a square plate, (d) a remote uniform shear force $\tilde{\mathbf{F}}_{xy}^s$, and (e) a remote uniform twisting moment $\tilde{\mathbf{M}}_{xy}^s$.

model of two infinite strips with connection under plane strain conditions. For simplicity, we consider two strips with the same thickness *t*. As shown schematically in Fig. 1.5, the radial stress σ_{rr} and the shear stress $\sigma_{r\theta}$ along the rigid inclusion circumference obtained from a plate with a rigid inclusion under various types of loading conditions are used to represent the structural stresses σ_x and τ_{xz} for the strip model, respectively, with respect
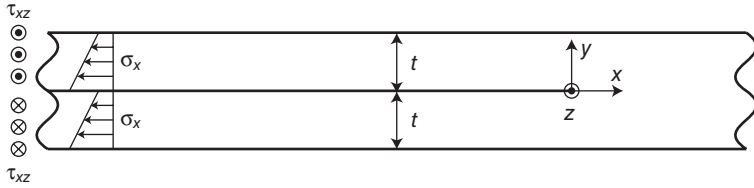
1.5 Two-dimensional model of two infinite strips with connection under plane strain conditions.

to the Cartesian coordinate system as shown in Fig. 1.5. The stress intensity factor solutions can then be determined from the structural stress distributions and the J integral (Rice, 1968) based on the strip model shown in Fig. 1.5.

Based on the works of Radaj (1989) and Radaj and Zhang (1991a), general structural stress distributions for a strip model can be decomposed into several symmetric and anti-symmetric distributions. Figure 1.6 shows schematically the decomposition of the general structural stress distributions of a strip model. Schematics of various types of structural stress distributions are shown from model A to G in Fig. 1.6. The general structural stress distributions are shown as model A. Here, the normal stresses σ_{ui}, σ_{uo}, σ_{li} and σ_{lo} represent the normal stresses σ_x at the inner (i) and outer (o) surfaces of the upper (u) and lower (l) strips, respectively. The shear stresses τ_u and τ_l represent the shear stress τ_{xz} of the upper (u) and lower (l) strips, respectively. The structural stress distributions of model A are then decomposed into several symmetric or anti-symmetric types of structural stress distributions: symmetric counter bending (model B), anti-symmetric central bending (model C), symmetric tension/compression (model D), anti-symmetric in-plane shear (model E), symmetric out-of-plane shear (model F) and anti-symmetric out-of-plane shear (model G).

The stress intensity factor K_I, K_{II} and K_{III} solutions for spot welds in various types of specimen show strong dependence on the structural stresses near the spot weld (Radaj, 1989; Radaj and Zhang, 1991a, 1991b, 1992; Zhang, 1997, 2001). For example, the K_I solution is a function of the

1.6 Decomposition of the general structural stress distributions of a strip model. Model A represents a strip model under general distributions of the normal stresses σ_x and the shear stresses τ_{xz}. The general stress distributions of model A can be decomposed into several symmetric or anti-symmetric structural stress distributions: symmetric counter bending (model B), anti-symmetric central bending (model C), symmetric tension/compression (model D), anti-symmetric in-plane shear (model E), symmetric out-of-plane shear (model F) and anti-symmetric out-of-plane shear (model G).

A (General loading)

B (Counter bending)

C (Central bending)

D (Tension/compression)

E (In-plane shear)

F (Symmetric out-of-plane shear)

G (Anti-symmetric out-of-plane shear)
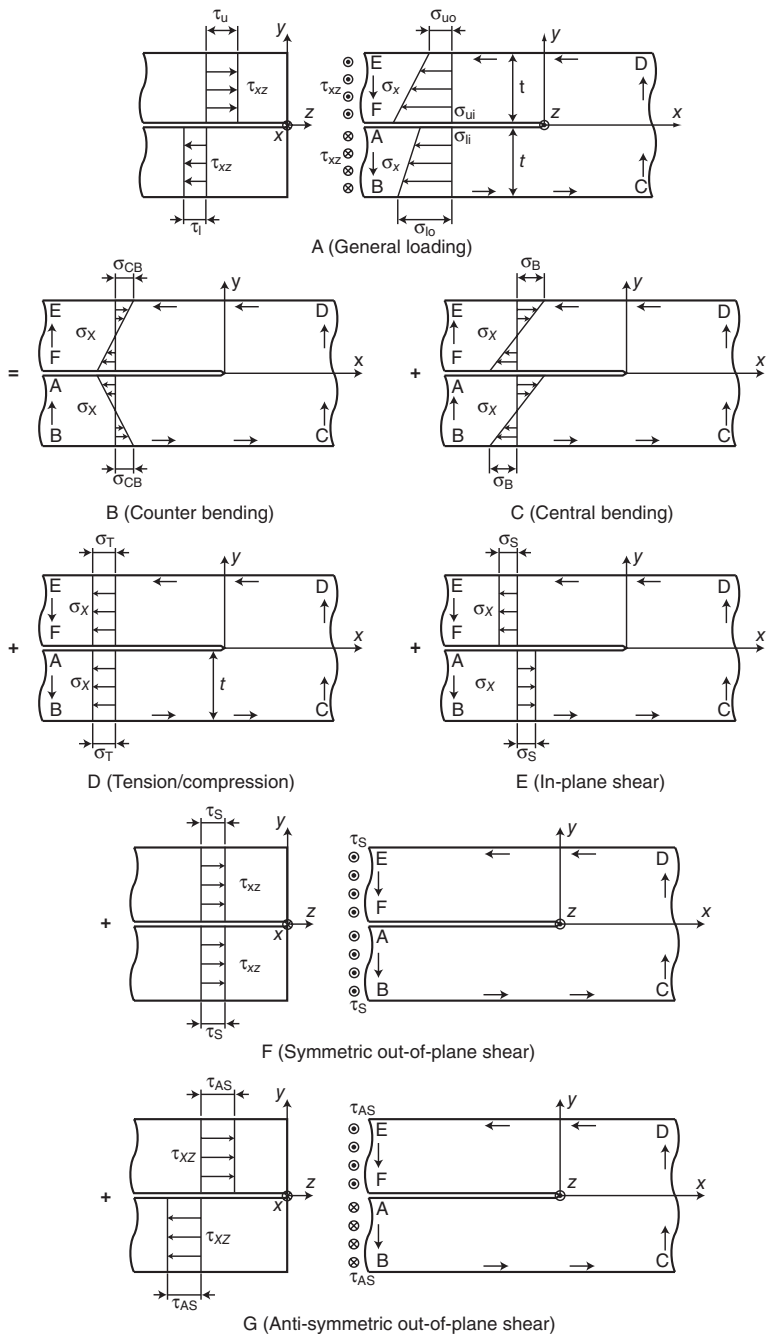
structural stresses near the spot weld under symmetric counter bending conditions (model B shown in Fig. 1.6). The K_{II} solution is a function of the structural stresses near the spot weld under anti-symmetric central bending and anti-symmetric in-plane shear conditions (models C and E shown in Fig. 1.6). The K_{III} solution is a function of the structural stresses near the spot weld under anti-symmetric out-of-plane shear conditions (model G shown in Fig. 1.6). Note that the structural stresses under symmetric tension/compression and symmetric out-of-plane shear conditions (models D and F shown in Fig. 1.6) make no contribution to any stress intensity factor.

The maximum values of the normal stress σ_x, marked as σ_{CB} for counter bending (model B), σ_B for central bending (model C), σ_T for tension/compression (model E) and σ_S for in-plane shear (model D), in terms of the normal stresses σ_{ui}, σ_{uo}, σ_{li}, and σ_{lo} as shown for general loading (model A) in Fig. 1.6 are defined as:

$$\sigma_{CB} = \frac{1}{4}(\sigma_{ui} - \sigma_{uo} + \sigma_{li} - \sigma_{lo}) \qquad [1.1a]$$

$$\sigma_B = \frac{1}{4}(\sigma_{ui} - \sigma_{uo} - \sigma_{li} + \sigma_{lo}) \qquad [1.1b]$$

$$\sigma_T = \frac{1}{4}(\sigma_{ui} + \sigma_{uo} + \sigma_{li} + \sigma_{lo}) \qquad [1.1c]$$

$$\sigma_S = \frac{1}{4}(\sigma_{ui} + \sigma_{uo} - \sigma_{li} - \sigma_{lo}) \qquad [1.1d]$$

The values of the shear stress τ_{xz}, marked as τ_S for symmetric out-of-plane shear (model F) and τ_{AS} for anti-symmetric out-of-plane shear (model G), in terms of the shear stresses τ_u and τ_l as shown for general loading (model A) in Fig. 1.6 are defined as:

$$\tau_S = \frac{1}{2}(\tau_u + \tau_l) \qquad [1.2a]$$

$$\tau_{AS} = \frac{1}{2}(\tau_u - \tau_l) \qquad [1.2b]$$

1.4.1   Solution for a strip model under counter bending (model B)

As shown in Fig. 1.6, model B represents a strip model under counter bending conditions. The K_I solution for model B is:

$$K_I = \frac{\sigma_{CB}\sqrt{t}}{\sqrt{3}} \qquad [1.3]$$

1.4.2 Solution for a strip model under central bending (model C)

Model C represents a strip model under central bending conditions. The K_{II} solution for model C is:

$$K_{II} = \frac{\sigma_B \sqrt{t}}{2} \qquad [1.4]$$

1.4.3 Solution for a strip model under in-plane shear (model E)

Model E represents a strip model under in-plane shear conditions. The K_{II} solution for model E is:

$$K_{II} = \frac{\sigma_S \sqrt{t}}{2} \qquad [1.5]$$

1.4.4 Solution for a strip model under anti-symmetric out-of-plane shear (model G)

Model G represents a strip model under anti-symmetric out-of-plane shear conditions. The K_{III} solution for model G is:

$$K_{III} = \tau_{AS} \sqrt{2t} \qquad [1.6]$$

Note that the structural stresses for strip models under symmetric tension/compression (model D) and under symmetric out-of-plane shear (model F) make no contribution to any stress intensity factor and the *J* integral for them is zero.

1.5   Kinked fatigue crack model for spot welds

Automobile manufacturers prefer spot welds in vehicles not to fail in service. However, if spot welds were to fail, they should fail in the nugget pull-out or circumferential failure mode. Therefore, kinked cracks emanating from the spot weld natural crack front should be considered to be the main mechanism for the fatigue failure of spot welds in the vehicle design and development stage. The fatigue cracking mechanisms of spot welds in different types of specimen are different owing to different geometries and loading conditions (Lin and Pan, 2004; Lin *et al.*, 2007). Figure 1.7(a) shows a schematic plot of the symmetry cross-section of a lap-shear specimen with the sheet thickness *t* under the applied force *P*. Figure 1.7(b) shows a micrograph of the symmetry cross-section near a failed spot weld in a lap-shear
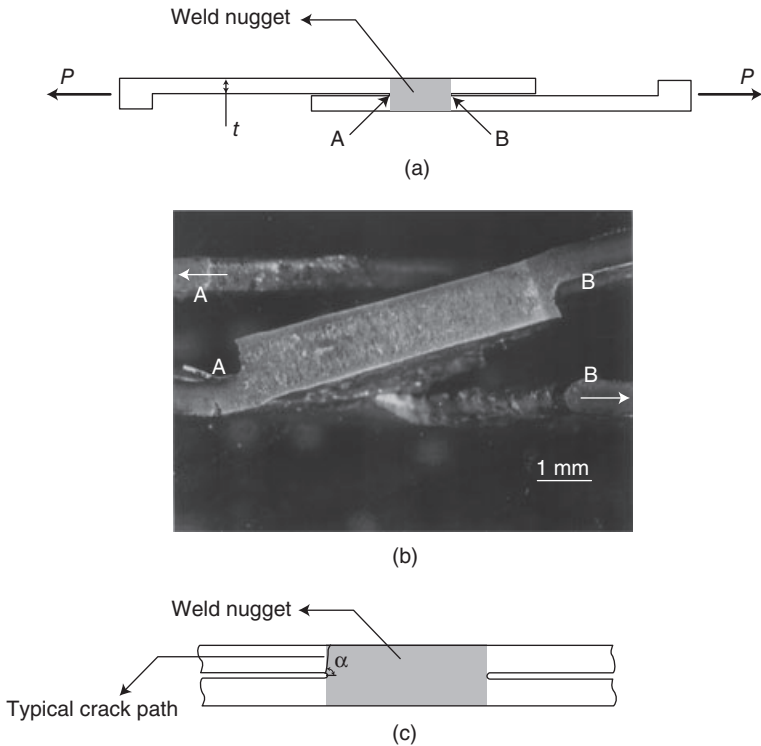
1.7 (a) Schematic plot of the symmetry cross-section of a lap-shear specimen and the applied force *P* shown as the bold arrows.
(b) Micrograph of the symmetry cross-section of a failed spot weld in a lap-shear specimen of dual phase steel sheet under cyclic loading conditions. (c) Schematic plot of the symmetry cross-section near a spot weld.

specimen of a dual phase steel sheet 0.65 mm thick (Lin *et al.*, 2007). The kinked crack appears to grow from the main notch or crack tip to the surface of the sheet. Figure 1.7(c) shows a schematic plot of the symmetry cross-section near a spot weld. The fatigue crack is schematically shown as a thin solid line growing from the main notch or crack tip with a kink angle α as shown in Fig. 1.7(c). The kink angle α appears to be near 90° for lap-shear specimens under cyclic loading conditions. Note that, as shown in a parametric study in Lin and Pan (2004), when the selection of the kink angle is close to 90°, the fatigue life prediction is not critically dependent upon the selection of the kink angle.

Figure 1.7(c) also schematically shows a kinked crack emanating from the critical location (point A). Note that, due to symmetry, kinked cracks
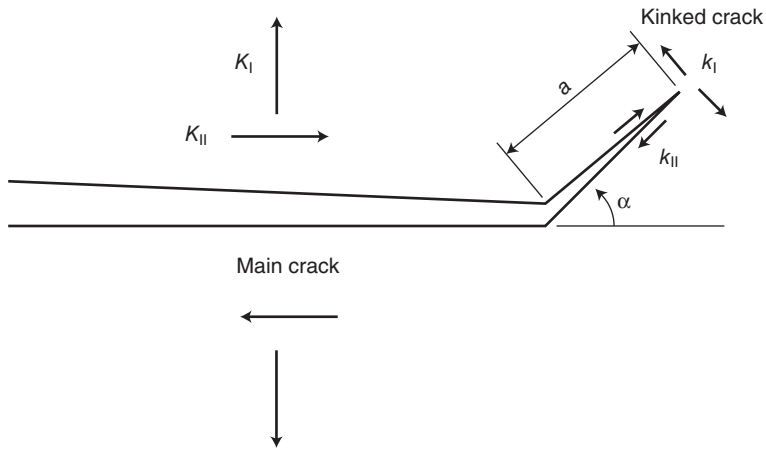
1.8 Schematic diagram of a main crack and a kinked crack with kink length *a* and kink angle α.

can emanate from either of the two critical locations (point A and point B) when the upper and lower sheets have the same thickness. However, only one of them will become the dominant kinked crack and lead to the initial through-thickness failure of the spot weld in lap-shear specimens (Swellam *et al.*, 1992). Microscopically, the main crack tips observed from the sectional views of spot welds usually have finite root radii. The effects of the notch geometry on the local stress intensity factor solutions for kinked cracks have been studied by Wang *et al.* (2005a). However, when the main crack is treated as a sharp crack, global stress intensity factor solutions can be used to correlate the fatigue lives of spot welds, see Zhang (1999).

In order to develop an engineering fatigue model, we idealize the three-dimensional spot friction weld problem in lap-shear specimens as a two-dimensional crack problem as in Newman and Dowling (1998) and Lin *et al.* (2007). Figure 1.8 shows a schematic diagram of a main crack and a kinked crack with the kink length *a* and the kink angle α. Note that, in the discussion of the kinked fatigue crack model and life prediction in Sections 1.5 and 1.6, the kinked length is denoted *a* following the conventional use of *a* for the crack length. However, for discussion of the spot weld model in Section 1.2, *a* is denoted as the radius of the spot weld. Here, K_I and K_{II} represent the global stress intensity factors for the main crack, and k_I and k_{II} represent the local stress intensity factors for the kinked crack. Note that the arrows in the figure represent the positive values of the global and local stress intensity factors K_I, K_{II}, k_I and k_{II}.

For kinked cracks, when the kink length approaches 0, the local stress intensity factors k_I and k_{II} can be expressed as functions of the kink angle

α and the global K_I and K_{II} for the main crack. The local $(k_I)_0$ and $(k_{II})_0$ solutions are given as (Bilby *et al.*, 1977; Cotterell and Rice, 1980):

$$(k_I)_0 = \frac{1}{4}\left(3\cos\frac{\alpha}{2} + \cos\frac{3\alpha}{2}\right)K_I - \frac{3}{4}\left(\sin\frac{\alpha}{2} + \sin\frac{3\alpha}{2}\right)K_{II} \qquad [1.7]$$

$$(k_{II})_0 = \frac{1}{4}\left(\sin\frac{\alpha}{2} + \sin\frac{3\alpha}{2}\right)K_I + \frac{1}{4}\left(\cos\frac{\alpha}{2} + 3\cos\frac{3\alpha}{2}\right)K_{II} \qquad [1.8]$$

where $(k_I)_0$ and $(k_{II})_0$ represent the local k_I and k_{II} solutions for kink length a approaching 0.

However, the local k_I and k_{II} solutions for kinked cracks from resistance spot welds are functions of the normalized kink length a/t'. Note that we assume the total crack growth distance t' is equal to $t/\sin\alpha$ due to the kink angle α as shown in Fig. 1.8. Therefore, we can express the local k_I and k_{II} solutions as:

$$k_I(a) = f_I \cdot (k_I)_0 \qquad [1.9]$$

$$k_{II}(a) = f_{II} \cdot (k_{II})_0 \qquad [1.10]$$

where f_I and f_{II} are geometric functions which depend on the geometric parameters of lap-shear specimens, such as the nugget diameter d, the sheet thickness t, the specimen width $2W$, the overlap length V, the aspect ratio of the crack, and the location of the crack front of interest (Wang and Pan, 2005).

Wang and Pan (2005) investigated the local stress intensity factor solutions for kinked cracks near spot welds in lap-shear specimens by three-dimensional finite element analyses. Semi-elliptical cracks with various kink depths are assumed in the three-dimensional finite element analyses. Figure 1.9(a) shows a schematic plot of a half lap-shear specimen. The specimen has the same dimensions as those of the lap-shear specimens used in Lin *et al.* (2007) as discussed earlier. Both the upper and lower sheets have the same thickness. The kinked crack front with the maximum kink depth a is shown as dashed lines in the figure. Figure 1.9(a) also shows the loading and boundary conditions applied to the lap-shear specimen.

The mesh for the left half of the finite element model with $a/t = 0.5$ is shown in Fig. 1.9(b). A close-up view of the mesh near the kinked crack is shown in Fig. 1.9(c). The aspect ratio of the maximum kink depth a to the half length c along the nugget circumference for the semi-elliptical kinked crack is taken as 0.4. As shown in Fig. 1.9(c), the mesh of the weld nugget is removed to display the mesh for the kinked crack clearly. The main crack and the kinked crack fronts are shown as dashed lines in the figure. The main crack surfaces are shown as solid lines in the figure. The geometric functions f_I and f_{II} for the two-dimensional kinked crack model are obtained
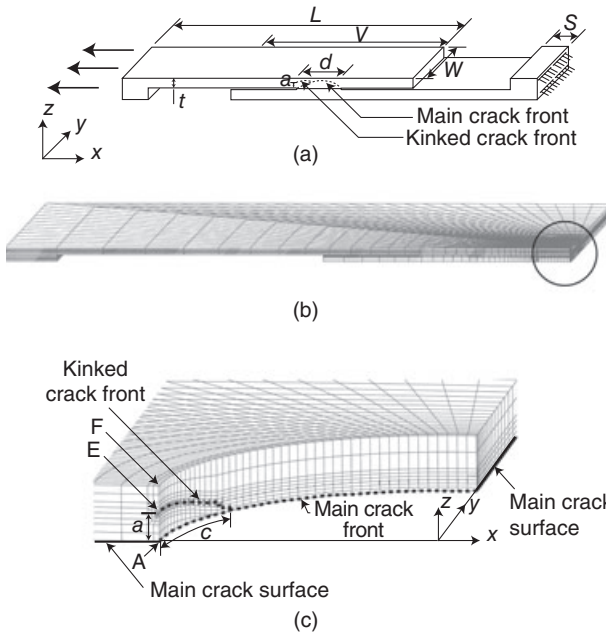
1.9 (a) Schematic plot of a half lap-shear specimen with a uniform displacement applied to the left edge surface of the specimen, shown as bold arrows, and the clamped boundary conditions of the right edge surface of the specimen. (b) Mesh for a left half, three-dimensional finite element model. (c) Close-up view of the mesh near the kinked crack.

from the three-dimensional finite element analyses. Details of the computations were presented by Wang and Pan (2005).

Since the kink crack growth should be dominated by the local combined mode I and mode II loading conditions, a local equivalent stress intensity factor can be defined as:

$$k_{eq} = \sqrt{k_I^2 + \gamma k_{II}^2} \qquad [1.11]$$

where γ is an empirical constant to account for the sensitivity of the fatigue crack growth to the local mode II loading conditions. Without further information, γ is taken as 1. Now we adopt the Paris law to describe the fatigue crack propagation as:

$$\frac{da}{dN} = C \left(\Delta k_{eq} \right)^m \qquad [1.12]$$

where a is the kink length, N is the life or number of cycles, C and m are material constants and Δk_{eq} is the range of the local equivalent stress intensity factor. As discussed earlier, the local stress intensity factor solutions are dependent on the kink length a. The load ratio R of the experiments on dual phase steel by Lin et $al.$ (2007) was set at 0.2. The experimental data in Swellam et $al.$ (1992) were obtained with a load ratio $R = 0$ and those in Zhang et $al.$ (2001) were obtained with a load ratio $R = 0.1$. Therefore, the load ratio effect as discussed in Swellam et $al.$ (1994) and Newman and Dowling (1998) may not become important and only the stress intensity factor range without the load ratio effect is used in Equation [1.12].

When the local stress intensity factor solutions are dependent on the kink length a, the fatigue life for lap-shear specimens can be expressed as:

$$N = \frac{1}{C}\left[\int_{0}^{0.05t'}\left[\Delta k_{eq}(a)\right]^{-m}\mathrm{d}a + \int_{0.05t'}^{0.2t'}\left[\Delta k_{eq}(a)\right]^{-m}\mathrm{d}a + \cdots + \int_{0.7t'}^{t'}\left[\Delta k_{eq}(a)\right]^{-m}\mathrm{d}a\right]$$

[1.13]

where $0, 0.05, 0.2, \ldots,$ and 0.7 represent the values of the normalized kink length a/t where the computational stress intensity factor solutions are available from Wang and Pan (2005).

When we assume that the local stress intensity factor solutions are independent of the kink length a, the fatigue life of spot welds can be obtained by integrating Equation [1.12] as:

$$N = \frac{t}{C\left(\Delta k_{eq}\right)^{m}\sin\alpha}$$

[1.14]

Here we assume the total crack growth distance is equal to $t/\sin\alpha$ owing to the kink angle α. Now we can rearrange Equation [1.14] as:

$$\Delta k_{eq} = \left(\frac{t}{C\sin\alpha}\right)^{\frac{1}{m}}N^{-\frac{1}{m}}$$

[1.15]

Based on the various stress intensity factor solutions for various specimens discussed in Lin and Pan (2008b), we can write a general solution for various specimens according to linear elasticity as:

$$\Delta k_{eq} = F(\alpha, a, t, \text{geometric parameters})\Delta P$$

[1.16]

where F represents a function of α, a, t and the necessary geometric parameters such as the specimen width and the eccentricity distance e for coach-peel specimens. Here, Δk_{eq} is linearly proportional to ΔP, which represents the range of applied load.

Combining Equations [1.15] and [1.16], we can write a general solution consistent with the conventional stress–life equation as:

$$\Delta P = H(\alpha, a, t, C, \text{geometric parameters})N^{-\frac{1}{m}} \qquad [1.17]$$

where H represents a function of α, a, t, the material constant C, and the necessary geometric parameters of specimens. According to Equation [1.17], when ΔP is plotted as a function of N on a log-log scale, the slope is determined by the material constant m. Equation [1.17] shows that the fatigue crack growth model based on a fracture mechanics approach can lead to a solution essentially following the form of the traditional stress–life approach. When the local stress intensity factor solutions are dependent on the kink length a, Equation [1.17] is still approximately valid.

1.6 Life predictions for spot welds in lap-shear specimens

The lap-shear specimens of Lin *et al.* (2007) were made from galvanized and bare DP500 dual phase steels. The lap-shear specimens have the sheet thickness t of 0.65 mm, the nugget diameter d of 6.4 mm and a width $2W$ of 38 mm. Based on the experimental results of Lin *et al.* (2007), the kink angle α is taken as 100°. The material constants C and m used in the Paris law are chosen for martensitic steels as $C = 1.36 \times 10^{-7}$ MPa$\sqrt{\text{m}}$ and $m = 2.23$ as in Lin *et al.* (2007).

Figure 1.10 shows the experimental results of Lin *et al.* (2007) for spot welds in lap-shear specimens made from DP500 dual phase steel and the fatigue life predictions based on the fatigue crack growth models based on Equations [1.13] and [1.14]. The fatigue life predictions based on the fatigue crack growth model in Equations [1.13] and [1.14] appear to agree very well with the experimental results. Note that the fatigue life predictions based on the fatigue crack growth model in Equation [1.13] are lower than the fatigue life predictions based on the fatigue crack growth model in Equation [1.14] since the local equivalent stress intensity factor ranges are larger than those based on the vanishing kink length for most of a/t'.

The lap-shear specimens of Zhang *et al.* (2001) were made from IF260GA high strength steels. The specimens have a sheet thickness t of 1.5 mm, a nugget diameter d of 7.35 mm and a width $2W$ of 50 mm. Based on the experimental observations of Gao *et al.* (2001), the kink angle α is taken as 80°. The material constants C and m used in the Paris law are chosen for martensitic steels as $C = 1.36 \times 10^{-7}$ MPa$\sqrt{\text{m}}$ and $m = 2.23$ as in Lin *et al.* (2007).

Figure 1.11 shows the experimental results of Zhang *et al.* (2001) for spot welds in lap-shear specimens made from high strength steels and fatigue life predictions based on the fatigue crack growth models in Equations [1.13] and [1.14]. The fatigue life predictions based on the fatigue crack
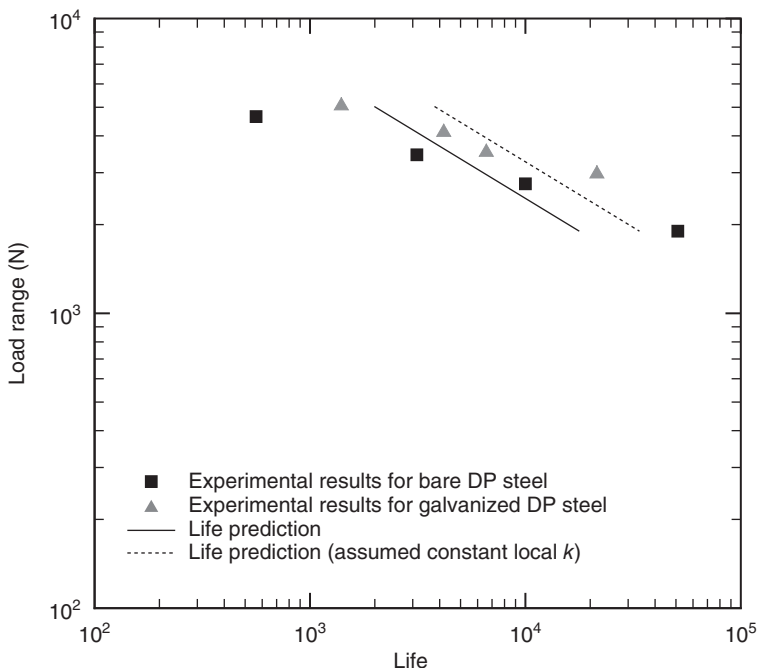
1.10 Predicted fatigue lives based on local stress intensity factor solutions as functions of the kink length, predicted fatigue lives based on the constant local stress intensity factor solutions and experimental results for spot welds in lap-shear specimens of dual phase steels.

growth model in Equations [1.13] and [1.14] appear to agree well with the experimental results. Note that fatigue life predictions based on the fatigue crack growth model in Equation [1.13] are lower than the fatigue life predictions based on the fatigue crack growth model in Equation [1.14] since the local equivalent stress intensity factor ranges are larger than those based on the vanishing kink length for most of a/t'.

The lap-shear specimens of Swellam *et al.* (1994) were made from low carbon steels. The specimens have a sheet thickness t of 1.4 mm, a nugget diameter d of 4.8 mm, and a width $2W$ of 38 mm. Based on the experimental observations of Swellam *et al.* (1992), the kinked angle α is taken as 80°. Since the fatigue crack growth paths of the failed spot welds are relatively close to the base metal, the material constants C and m used in the Paris law are chosen for ferrite-pearlite steels as $C = 6.89 \times 10^{-9}$ MPa$\sqrt{\text{m}}$ and $m = 3$ as in Lin *et al.* (2007).

Figure 1.12 shows the experimental results of Swellam *et al.* (1992) for spot welds in lap-shear specimens made from low carbon steels and fatigue
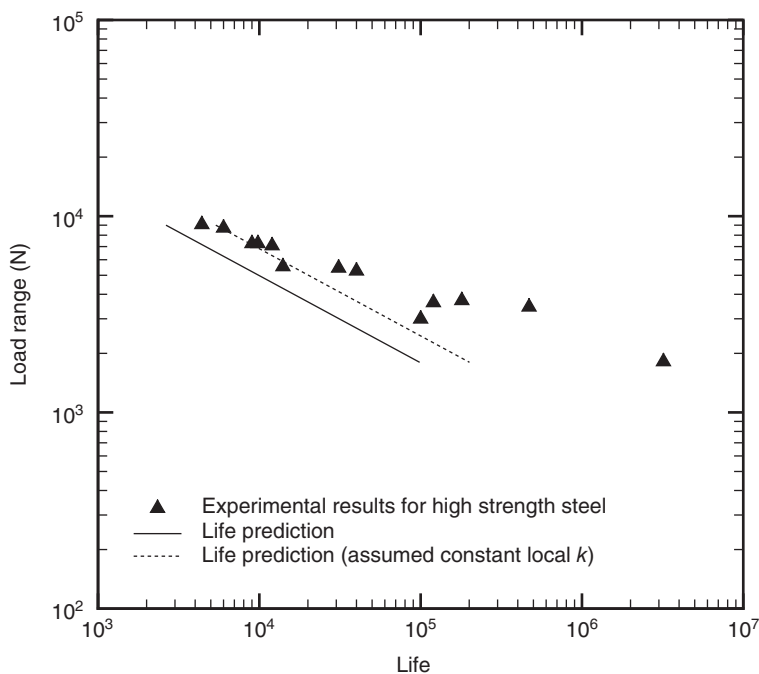
1.11 Predicted fatigue lives based on the local stress intensity factor solution as functions of the kink length, predicted fatigue lives based on the constant local stress intensity factor solutions and experimental results of spot welds in lap-shear specimens of high strength steels.

life predictions based on the fatigue crack growth models in Equations [1.13] and [1.14]. The fatigue life predictions based on the fatigue crack growth model in Equations [1.13] and [1.14] appear to be lower than the experimental results. Note that the fatigue life predictions based on the fatigue crack growth model in Equation [1.13] are lower than the fatigue life predictions based on the fatigue crack growth model in Equation [1.14] since the local equivalent stress intensity factor ranges are larger than those based on the vanishing kink length for most of a/t'.

1.7   Conclusions

This chapter has presented a mechanics model of a spot weld in a finite plate under general loading conditions in order to establish a theoretical framework to model a spot weld. The spot weld is assumed to be a rigid inclusion in order to develop closed-form analytical solutions. Based on the stress function approach and the Kirchhoff plate theory for linear elastic materials, the available closed-form stress, moment and transverse shear
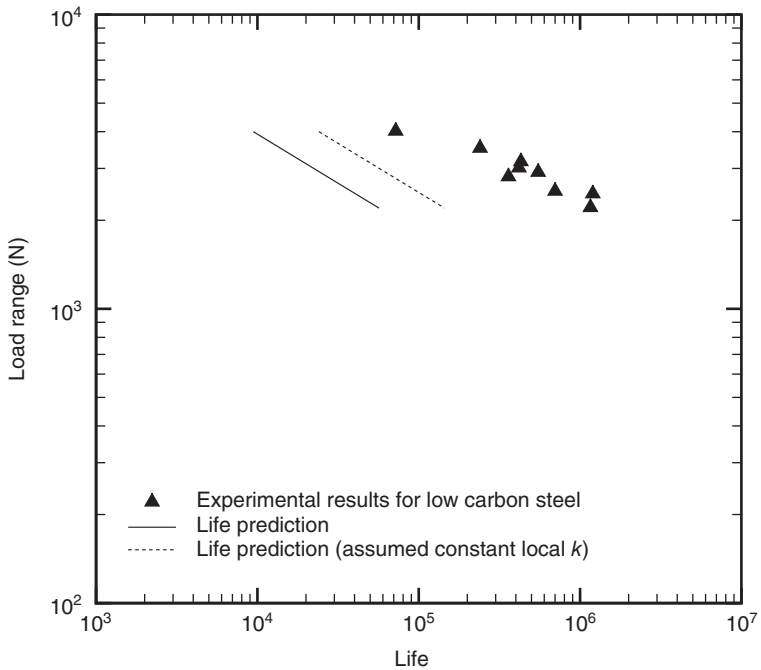
1.12 Predicted fatigue lives based on the local stress intensity factor solution as functions of the kink length, predicted fatigue lives based on the constant local stress intensity factor solutions and experimental results of spot welds in lap-shear specimens of low carbon steels.

force solutions are discussed for a plate with a rigid inclusion subjected to various types of resultant loads on the inclusion and various types of resultant loads on the plate lateral surface. Based on the *J* integral for a strip model, closed-form analytical stress intensity factor solutions for spot welds are presented in terms of the structural stresses around a rigid inclusion in a plate under various types of loading conditions. The closed-form solutions are used as the basis for developing analytical stress intensity factor solutions for spot welds in various types of specimen or structural components.

As an example, to demonstrate the applicability of the stress intensity factor solutions for spot welds, a fatigue crack growth model is presented next to correlate the fatigue lives of resistance spot welds in lap-shear specimens of dual phase, low carbon and high strength steels under cyclic loading conditions based on the experimental observations of spot welds that failed in a kinked crack propagation mode. The fatigue crack growth model is based on global stress intensity factor solutions for main cracks,

local stress intensity factor solutions for kinked cracks as functions of the kink length, experimentally determined kink angles and the Paris law for kinked crack propagation. Predicted fatigue lives based on the fatigue crack growth model are then compared with the experimental data. The results indicate that the fatigue life predictions based on the fatigue crack growth model are in agreement with or lower than the experimental results.

1.8   Acknowledgements

1.9   References

BILBY B A, CARDEW G E and HOWARD I C (1978), 'Stress intensity factors at the tips of kinked and forked cracks', *Fourth International Conference on Fracture*, University of Waterloo, Ontario, June 19–24, 1977, Pergamon Press, New York, 3A, 197–200.

COTTERELL B and RICE J R (1980), 'Slightly curved or kinked cracks', *International Journal of Fracture*, **16**, 155–69.

GAO Y, CHUCAS D, LEWIS C and MCGREGOR I J (2001), 'Review of CAE fatigue analysis techniques for spot-welded high strength steel automotive structures', *SAE Technical Paper No. 2001-01-0835*, Society of Automotive Engineers, Warrendale, PA.

GOLAND M (1943), 'The influence of the shape and rigidity of an elastic inclusion on the transverse flexure of thin plates', *Journal of Applied Mechanics*, **10**, A-69-A-75.

LIN S-H and PAN J (2004), 'Fatigue life predictions for spot welds in coach-peel and lap-shear specimens with consideration of kinked crack behavior', *International Journal of Materials and Product Technology*, **20**, 31–50.

LIN P-C and PAN J (2008a), 'Closed-form structural stress and stress intensity factor solutions for spot welds under various types of loading conditions', *International Journal of Solids and Structures*, **45**, 3996–4020.

LIN P-C and PAN J (2008b), 'Closed-form structural stress and stress intensity factor solutions for spot welds in commonly used specimens', *Engineering Fracture Mechanics*, **75**, 5187–206.

LIN P-C, WANG D-A and PAN J (2007), 'Mode I stress intensity factor solutions for spot welds in lap-shear specimens', *International Journal of Solids and Structures*, **44**, 1013–37.

MUSKHELISHVILI N I (1953), *Some Basic Problems of the Mathematical Theory of Elasticity*, Noordhoff, Groningen.

NEWMAN J A and DOWLING N E (1998), 'A crack growth approach to life prediction of spot-welded lap joints', *Fatigue & Fracture of Engineering Materials & Structures*, **21**, 1123–32.

POOK L P (1975), 'Fracture mechanics analysis of the fatigue behavior of spot welds', *International Journal of Fracture*, **11**, 173–6.

POOK L P (1979), 'Approximate stress intensity factors obtained from simple plane bending theory', *Engineering Fracture Mechanics*, **12**, 505–22.

RADAJ D (1989), 'Stress singularity, notch stress and structural stress at spot-welded joints', *Engineering Fracture Mechanics*, **34**, 495–506.

RADAJ D and ZHANG S (1991a), 'Stress intensity factors for spot welds between plates of unequal thickness', *Engineering Fracture Mechanics*, **39**, 391–413.

RADAJ D and ZHANG S (1991b), 'Simplified formulae for stress intensity factors of spot welds', *Engineering Fracture Mechanics*, **40**, 233–6.

RADAJ D and ZHANG S (1992), 'Stress intensity factors for spot welds between plates of dissimilar materials', *Engineering Fracture Mechanics*, **42**, 407–26.

REIßNER H (1929), 'Über die unsymmetrische biegung dünner kreisringplatten', *Ingenieur-Archiv*, **1**, 72–83.

RICE J R (1968), 'A path independent integral and the approximate analysis of strain concentration by notches and cracks', *Journal of Applied Mechanics*, **35**, 379–86.

RUPP A, GRUBISIC V and RADAJ D (1990), 'Betriebsfestigkeit von punktschweissverbindunghen', *Sonderdruck aus Materialprüfung*, **32**, 1–6.

RUPP A, STORZEL K and GRUBISIC V (1995), 'Computer aided dimensioning of spot welded automotive structures', *SAE Technical Paper No. 950711*, Society of Automotive Engineers, Warrendale, PA.

SALVINI P, SCARDECCHIA E and VIVIO F (1997), 'Fatigue life prediction on complex spot weld joints', SAE Transaction, *Journal of Materials and Manufacturing*, **106**, 967–75.

SALVINI P, VIVIO F and VULLO V (2000), 'A spot weld finite element for structural modeling', *International Journal of Fatigue*, **22**, 645–56.

SHEPPARD S D (1993), 'Estimation of fatigue propagation life in resistance spot welds', *Advances in Fatigue Lifetime Predictive Techniques*, Mitchell M R and Landgraf R W (eds), Vol. 2, ASTM STP 1211, American Society for Testing and Materials, Philadelphia, pp. 169–85.

SWELLAM M H, KURATH P and LAWRENCE F V (1992), 'Electric-potential-drop studies of fatigue crack development in tensile-shear spot welds', *Advances in Fatigue Lifetime Predictive Techniques*, Mitchell M R and Landgraf R W (eds), ASTM STP 1122, American Society for Testing and Materials, Philadelphia, pp. 383–401.

SWELLAM M H, BANAS G, LAWRENCE F V (1994), 'A fatigue design parameter for spot welds', *Fatigue and Fracture of Engineering Materials and Structures*, **17**, 1197–204.

TIMOSHENKO S, WOINOWSKY-KRIEGER S (1959), *Theory of Plates and Shells*, 2nd edition, McGraw-Hill, New York.

VIVIO F, FERRARI G, SALVINI P and VULLO V (2002), 'Enforcing of an analytical solution of spot welds into finite element analysis for fatigue-life estimation', *International Journal of Computer Applications in Technology*, **15**, 218–29.

WANG D-A and PAN J (2005), 'A computational study of local stress intensity factor solutions for kinked cracks near spot welds in lap-shear specimen', *International Journal of Solids and Structures*, **42**, 6277–98.

WANG D-A, LIN S-H and PAN J (2005a), 'Stress intensity factors for spot welds and associated kinked cracks in cup specimens', *International Journal of Fatigue*, **27**, 581–98.

WANG D-A, LIN P-C and PAN J (2005b), 'Geometric functions of stress intensity factor solutions for spot welds in lap-shear specimens', *International Journal of Solids and Structures*, **42**, 6299–318.

ZHANG S (1997), 'Stress intensities at spot welds', *International Journal of Fracture*, **88**, 167–85.

ZHANG S (1999), 'Approximate stress intensity factors and notch stress for common spot-welded specimens', *Welding Research Supplement*, **78**, 173s–179s.

ZHANG S (2001), 'Fracture mechanics solutions to spot welds', *International Journal of Fracture*, **112**, 247–74.

ZHANG J, DONG P and GAO Y (2001), 'Evaluation of stress intensity factor-based predictive technique for fatigue life of resistance spot welds', *SAE Technical Paper No. 2001-01-0830*, Society of Automotive Engineers, Warrendale, PA.

2

Resistance spot weld failure mode and weld performance for aluminum alloys

X. S U N, Pacific Northwest National Laboratory, USA

Abstract: This chapter discusses the relationship between fusion zone size and weld performance for aluminum resistance spot welds. Weld performance in terms of failure modes, static strength and energy absorption is examined using a combined experimental, statistical and analytical approach. The main failure modes for aluminum spot welds are nugget pullout and interfacial fracture. It is found that fusion zone size, sheet thickness and the level and location of weld porosity/defects are the main factors influencing the cross-tension failure mode of an aluminum spot weld. Two additional spot weld populations with different fusion zone sizes are used to validate the analytical failure mode model.

Key words: aluminum resistance spot welds, energy absorption, failure modes, fusion zone size, interfacial fracture, nugget pullout, static strength, weld porosity.

2.1   Introduction

Resistance spot welding (RSW) is easy to operate, automate, control and perform and thus is an ideal joining technology for mass production. RSW has been used for decades and it is the primary joining technology for sheet metal assemblies in the automotive and other industries. Over the years, RSW technology has been perfected for various steel grades and sheet metal thicknesses, delivering high-quality, durable structural joints.[1–3] Recently, because of their light weight and relatively high strength, more and more aluminum alloys have been used in the construction of automobile body and panel parts to reduce weight and therefore enhance fuel efficiency. As one of the primary joining methods in the automotive industry, the RSW process for aluminum alloys has been studied intensively over the past two decades.[4–8]

Spot welding of aluminum alloys shares the same overall Joule heating principle as spot welding of steel. However, because of the relatively low density and high thermal and electrical conductivity of aluminum alloys, aluminum spot welding also presents some unique challenges for the automotive industry. Higher welding currents, typically two to three times those of steel and only one-third of the welding duration time are used. The issues associated with production welding of aluminum alloys include weld

24

porosity, weld expulsion, electrode wear and inconsistency in failure mode during coupon-level joint quality evaluation.[9,10]

As a means of quality control, the automotive industry historically has adopted an approach and criterion for aluminum spot welds similar to those used in spot welding mild steel, that is, a peel-test to determine whether a satisfactory weld has been produced. The common criterion is borrowed from the conventional spot-weld criterion for mild steel, in which the minimum weld button diameter (D) should be equal to or larger than $4\sqrt{t}$ (t defined as material thickness in mm).[11] Undersized welds have an average weld button diameter larger than $2\sqrt{t}$ but less than $4\sqrt{t}$. Defective welds have average weld button diameters less than or equal to $2\sqrt{t}$. Any weld that fails in the interfacial fracture mode would be considered a 'bad' weld and would be rejected by the quality control inspector.

This criterion works relatively well for mild steel spot welds because the weld nugget has a significantly higher hardness level (therefore yield strength) than the base material; hence the nugget pullout mode would produce the highest joint strength. On the other hand, the effectiveness of this criterion for evaluation of the quality of an aluminum spot weld and an advanced high strength steel spot weld has not been adequately studied by the automotive welding community; it was adopted from use in mild steel spot welds without much in-depth study. Because of the more frequent occurrence of interfacial fracture, many automotive companies do not have confidence in aluminum spot welds and are now pursuing alternative, yet more expensive, joining techniques such as riveting and/or clinching.

The purpose of this chapter is to examine the effects of fusion zone size and failure modes on the peak load and energy absorption levels of aluminum spot welds. First, two sample weld populations were considered:

- weld population ID14: RSW of 2 mm 5182-O to 2 mm 5182-O
- weld population ID15: RSW of 2 mm 5182-O to 2 mm 6111-T4.

For each weld population, three coupon configurations were included in the static tests: lap shear, cross tension and coach peel; see Figs 2.1 to 2.3 for specimen design, dimensions and fixture design. For each static test, a load versus displacement curve was recorded, as were the failure mode and nugget size/fusion zone size of the joint sample. The total energy absorption, which is represented by the area under the load versus the displacement curve, was then calculated through numerical integration. Thirty identical static strength tests were performed for each joint configuration and statistical analysis was performed to study the effects of different failure modes on the peak load and energy absorption of the weld joints.

Next, a simple, limit-load based analytical model was derived to rationalize the experimental observed failure modes for aluminum spot welds with the aid of micro-hardness measurements of the weld samples. Two
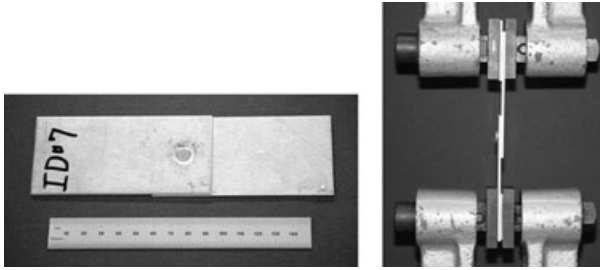
2.1 Lap-shear coupon design and test fixture.
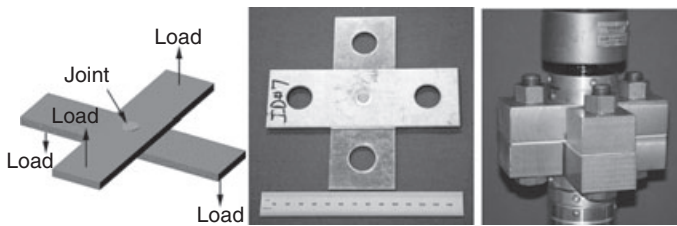
2.2 Cross tension coupon design and test fixture.
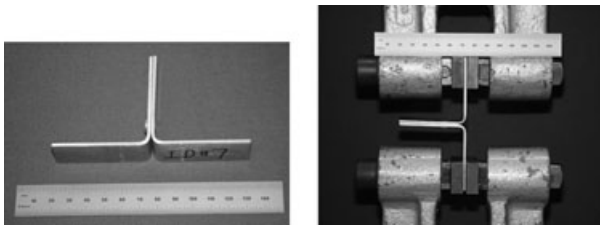
2.3 Coach peel coupon design and fixture.

additional weld populations with different fusion zone sizes were then fabricated and tested to validate the analytical model. The goal of this study is to provide welding engineers with some insight into the anticipated joint failure modes for a given weld population with certain weld attributes and to discuss the effects of weld size and weld porosity (irregularity) level on the anticipated levels of weld strength and failure mode.

2.2   Experimental study of aluminum spot welds

The initial experimental work in this investigation consisted of quasi-static tests of lap shear, coach peel and cross tension of ID14 and ID15. The specimen and test fixture designs are shown in Figs 2.1 to 2.3. The following welding parameters were used in the coupon fabrication process:

- Electrodes: 0.370″ (9.4 mm) face diameter truncated electrode
- Current: ~34.0 kA, 80% current, AC welder
- Force: 1050 lbf (4671 N)
- Weld time: 8 cycles
- Water flow rate: 2.6 gal min^{-1} (197 ml s^{-1}).

Special efforts were made to ensure the location of the welds was in the width center of the specimens. Electrode tips were dressed every 15 welds to ensure weld consistency. Peel tests and metallographic cross-sections were used to maintain a nugget diameter of ~8 mm for all specimens. Figure 2.4 shows the typical weld metallurgical cross-sections for ID14 and ID15, respectively.

Quasi-static tests at a rate of 10 mm min^{-1} were performed on these specimens to determine their load versus displacement curves. Figure 2.5 shows the typical experimental results for ID14 under the three loading configurations. Thirty static tests were performed for each joint population and each loading configuration.
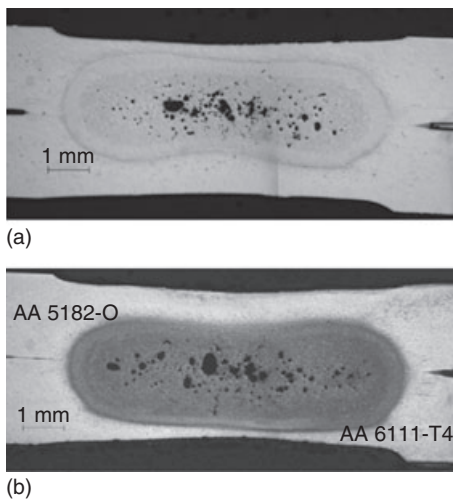
2.4 Typical metallurgical cross-sections for (a) ID14 and (b) ID15.
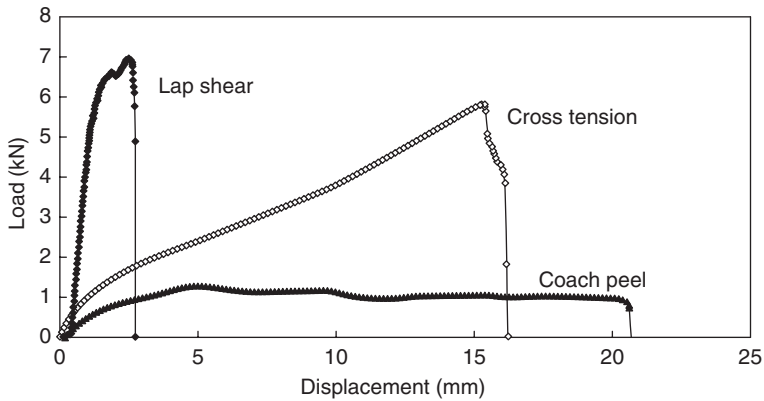
2.5 Sample load versus displacement curves for ID14.

2.2.1 Lap shear tests

For lap-shear samples of both populations ID14 and ID15, interfacial fracture was the only failure mode observed. The average peak failure load for ID14 is 7.16 kN and the average peak failure load for ID15 is 7.17 kN, with no significant sheet bending deformation observed for either population.

2.2.2 Cross tension tests

Both nugget pullout and interfacial fracture modes were observed for the cross tension samples of ID14 and ID15 and the majority of the samples failed in pullout mode. The average peak loads are 6.05 kN and 5.95 kN for ID14 and ID15, respectively. A detailed statistical analysis will be presented in the next section to study whether different failure modes have a significant influence on the peak failure loads for these two populations.

2.2.3 Coach peel tests

Similar to the cross tension samples, the failure modes for coach peel samples were also a combination of nugget pullout and interfacial fracture. However, in coach peel samples, interfacial fracture and partial interfacial fracture (a combination of interfacial fracture and later stage nugget pullout) were more often observed. In some samples, sheet-tearing failure was also observed after nugget pullout, which increases the energy absorption levels of those samples significantly. Again, a statistical analysis will be conducted for the coach peel samples and discussion in the next section will reveal whether different failure modes have a significant impact on the peak load and energy absorption levels of these two populations.

2.3   Statistical data analysis for aluminum spot welds

2.3.1   Weibull plots

The statistical characteristics of a data set can be analyzed using some mathematical tools such as a probability paper.[12,13] Following specific mathematical procedures, if all the data points in a data set plot approximately on a straight line on a certain probability paper, the distribution corresponding to that paper may be an appropriate distribution model for the data population under examination. Moreover, the characteristics of the linear line fitting the data on the probability paper will quantify the mean value and standard deviation of the data population according to the specific distribution type.

In studying the statistical nature of spot welds strength under different loading conditions, the static strength and energy absorption for different failure modes are analyzed using the two-parameter Weibull distribution:

$$F = 1 - \exp\left[-\left(\frac{\sigma}{\sigma_0}\right)^m\right]$$ [2.1]

in which F denotes median estimator of the cumulative failure probability and is given by $F = \dfrac{i - 0.3}{N + 0.4}$, where i is the ranking of each specimen with values $1, 2, \ldots N$, and N is the total number of specimens, σ is the peak load (or energy absorption) and σ_0 and m are Weibull parameters. Physically, as maybe verified from Equation [2.1], σ_0 is the peak load (or energy) value corresponding to a failure probability of 63.2% and m is the slope of $\ln\ln\left(\dfrac{1}{1-F}\right)$ versus $\ln\sigma$ plot, otherwise known as the Weibull modulus or shape parameter.[13] For a unimodal distribution, m is analogous to the inverse of the standard deviation expressed as a fraction of mean strength. Therefore, the more vertical the data line is on a $\ln\ln\left(\dfrac{1}{1-F}\right)$ versus $\ln\sigma$ plot (or Weibull plot), the higher the value m and the less scatter the data has in a statistical sense.

To study the effect of different failure modes on the peak load and energy absorption for the weld samples in ID14 and ID15, we took the static test results obtained in the previous section and categorized them into two sub-populations based on individual sample failure modes, namely, nugget pullout failure and interfacial fracture failure. The data points within each sub-population were then sorted in ascending order in terms of peak load or energy absorption in order to be plotted on Weibull probability paper.[12] Figures 2.6 and 2.8 show the Weibull plots of peak load for ID14 and ID15,
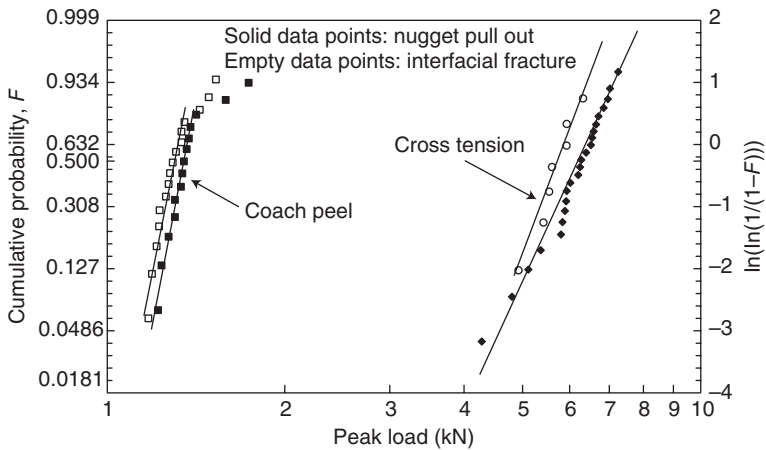
2.6 Weibull distribution comparing ID14 peak load distribution for interfacial fracture and pullout modes.
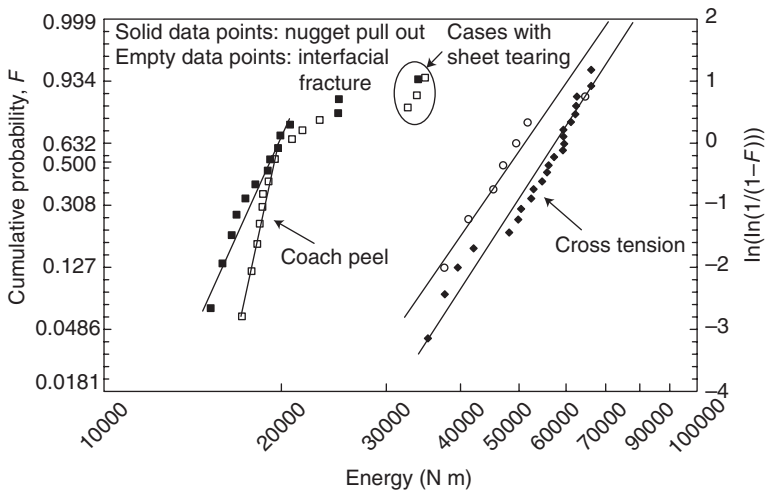
2.7 Weibull distribution comparing ID14 energy absorption for interfacial fracture and pullout modes.

respectively and Figs 2.7 and 2.9 show the Weibull plots of energy absorption levels for ID14 and ID15, respectively. It should be noted that the cases with partial interfacial fracture were grouped as interfacial fracture based on their primary failure modes.

Assuming the available data points in each sub-population of different failure modes are sufficient for statistical significance, the characteristics of
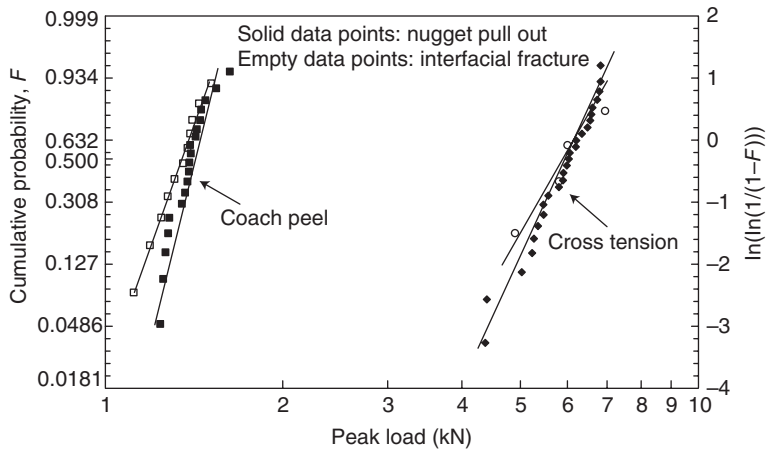
2.8 Weibull distribution comparing ID15 peak load distribution for interfacial fracture and pullout modes.
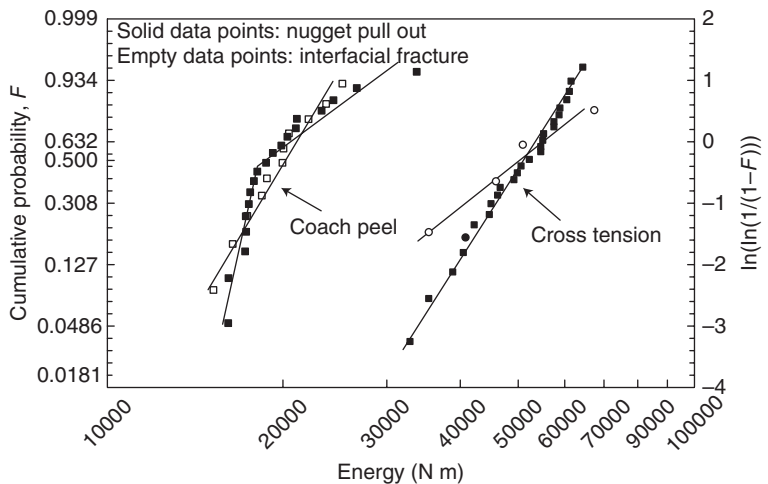
2.9 Weibull distribution comparing ID15 energy absorption for interfacial fracture and pullout modes.

the Weibull plots for interfacial fracture and nugget pullout modes can provide the median value as well as the degree of scatter for each failure mode. It should be noted that, since interfacial fracture was the only failure mode observed for all the lap shear samples of ID14 and ID15, no statistical study was performed on those data.

2.3.2 Cross tension

The linearity of curve fittings for pullout and interfacial fracture failure modes in Figs 2.6, 2.7, 2.8, and 2.9 suggests that the peak load and energy distribution under cross tension for ID14 and ID15 can be modeled approximately using Weibull distributions with different shape parameters.

For ID14 under cross tension, the Weibull plots in Fig. 2.6 show that the median peak load for interfacial fracture is about 10% lower than the median peak load for pullout failure. Consistently, the median energy absorption for interfacial fracture is about 10% lower than that of pullout mode for this population. Since the fitted straight lines in Fig. 2.6 are almost parallel, it is concluded that the interfacial fracture and pullout failure modes have the same shape parameters for the Weibull distribution and therefore the degree of peak load and energy scatter is about the same for these two failure modes for ID14.

For ID15 under cross tension, the Weibull plots in Fig. 2.8 show that the median peak load levels for the two failure modes are almost identical. However, the interfacial fracture mode shows a higher level of scatter on peak load than the pullout mode. Similar observations can be made for the energy absorption levels for the two failure modes for ID15 under cross tension, see Fig. 2.9.

2.3.3 Coach peel

Under coach peel loading configuration, the lack of linearity of the data points for ID14 and ID15 indicates that a uni-modal Weibull distribution cannot be used to model the entire data population correctly, see Figs 2.6, 2.7, 2.8 and 2.9. However, the few cases in the peak load distributions that do not fit the straight lines are mostly the cases with combined failure modes of nugget pullout and sheet tearing. If we were to consider the majority of cases represented by the straight lines, consistent conclusions about peak load distributions under the coach peel condition can again be reached for the two weld populations like those under cross tension: the median peak load for interfacial fracture mode is lower than that for the nugget pullout mode. But the median value difference for the two failure modes is less than 10%.

The distributions for energy absorption under coach peel loading conditions for ID14 and ID15 have a bilinear nature. Therefore, bimodal Weibull distributions may be more suitable for these energy distributions. In Fig. 2.7, the cases with sheet tearing have distinguishable higher energy levels owing to the additional energy absorbed by the base metal tearing deformation.

In conclusion, the above statistical analyses indicate that the median peak load for the cases failed in interfacial fracture mode is about 10% lower

than that for the cases failing in pullout mode for ID14 and that the median peak load is about the same for ID15 with different shape parameters. Similar conclusions can also be reached for the energy absorption levels. These results indicate that, for weld populations ID14 and ID15, the differences in failure modes under cross tension and coach peel conditions do not produce a significant difference in the specimens' peak load and energy absorption levels. Nugget pullout mode only produces slightly higher peak load and energy absorption.

2.4   Analytical failure mode prediction for aluminum spot welds under cross tension loading condition

In this section, we attempt to derive a simple, limit-load based analytical strength model to predict joint strength and the associated failure mode for an aluminum spot weld under static cross tension loading. As shown in Fig. 2.4, a typical cross-section of an aluminum spot-weld consists of base metal, weld nugget and the region between the base metal and the nugget, the heat-affected zone (HAZ). Let us denote the weld fusion zone diameter as D, the sheet thickness on the thinner side as t and assume that the weld has a porosity factor f, which is defined as:

$$f = \frac{A_{total} - A_{porosity}}{A_{total}}, \quad 0 < f \leq 1.0 \tag{2.2}$$

In Equation [2.2], A_{total} is the total area of the fusion zone on the faying interface and $A_{porosity}$ is the projected area of porosity in the fusion zone on the faying interface of the weld. The factor f is defined in such a way that a porosity-free weld has an f value equal to 1.0 and a weld that has some degree of porosity on the faying interface has an f value less than 1.0 but greater than 0. We assume that porosity does not concentrate at the weld periphery, such that the existence of porosities does not affect the local stress distribution around the weld tip and therefore would not influence the local crack growth path for the weld under static cross tension loading.

Assuming axisymmetric deformation under cross tension loading condition, the peak load for a weld to fail in interfacial fracture mode can be approximated as:

$$F_{IF} = f \cdot A_{total} \cdot \sigma_{y-weld} = f \cdot \pi \cdot \frac{D^2}{4} \cdot \sigma_{y-weld} \tag{2.3}$$

where σ_{y-weld} represents the tensile yield strength of the weld metal. We use tensile yield strength of the weld metal instead of ultimate strength because this is a limit load analysis in which no local material hardening or necking is considered.[14]

On the other hand, if the spot welds fail in nugget pullout mode, experiments have shown that failure normally occurs by through-thickness shear in the heat affected zone.[14] Therefore the peak load for a weld to fail in nugget pullout mode under cross tension can be approximated as:

$$F_{PO} = \pi \cdot D \cdot t \cdot \sigma_{y-HAZ-shear} \qquad [2.4]$$

In Equation [2.4], $\sigma_{y-HAZ-shear}$ represents the shear yield strength of the heat-affected zone. Again, this is a limit load estimation in which yield strength is used instead of ultimate strength because no necking or material hardening in the heat affected zone is considered. It should be mentioned that Equation [2.4] also assumes no significant weld indentation. If noticeable weld indentation occurs from the welding process, a reduced level of t should be used based on the actual residual sheet thickness around the weld periphery.

The failure mode of a specific weld under cross tension loading condition can then be determined by selecting the failure mode associated with the lower peak load level according to Equations [2.3] and [2.4] given the values of σ_{y-weld} and $\sigma_{y-HAZ-shear}$. In principle, this methodology should apply for both steel and aluminum spot welds. Here we use an aluminum spot weld as an example.

In order to ensure pullout failure for an aluminum spot weld, the following inequality needs to be satisfied:

$$F_{PO} < F_{IF} \qquad [2.5]$$

Figure 2.10 shows the line plot of hardness measurement of a typical weld in ID15. The hardness data shown in Fig. 2.10 indicate that the difference in the hardness of the base metal and the weld metal is not significant. Consequently, we can deduce that the tensile yield strength of the weld nugget for an aluminum weld should be close to that of the base metal. The average hardness level of the HAZ is about 15% higher than the average hardness of the base metal. These micro-hardness observations for aluminum RSW are in contrast to those for mild steel RSW in which the weld nugget and the HAZ have much higher hardness values than the base metal.[15]

Since the tensile yield strength of a material can be considered linearly related to its hardness level,[15] the tensile yield strength of the weld metal, σ_{y-weld} and the tensile yield strength of the base metal, $\sigma_{y-base\ metal}$, can be considered to be roughly the same. The tensile yield strength of the HAZ, σ_{y-HAZ} is considered to be roughly 15% higher than $\sigma_{y-base\ metal}$. Since it is very difficult to obtain accurate shear data on materials that exhibit some ductility, very little data exist on the shear yield strength for the HAZ, $\sigma_{y-HAZ-shear}$. It is generally agreed that the shear yield strength of ductile cast iron is about 0.6 to 0.7 times its tensile yield strength.[16] Taking a similar
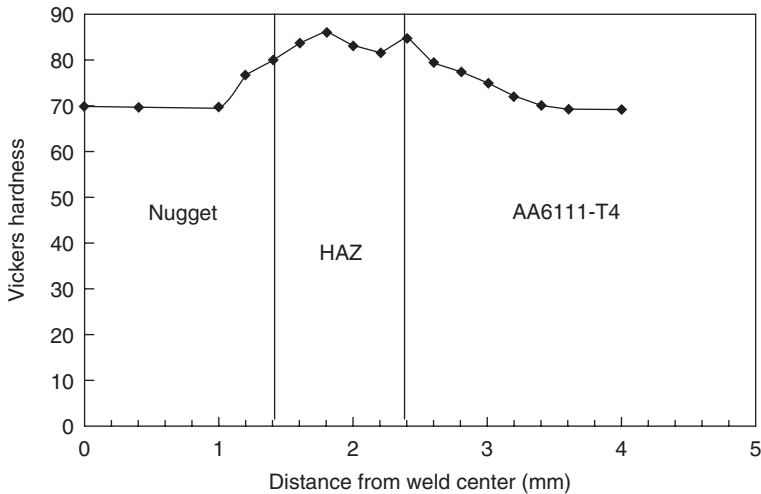
2.10 ID15 Vickers hardness measurement. The test force applied was 100 gf.

approach, we assume here that the shear yield strength of the HAZ is about 70% of its tensile yield strength. Summarizing the above yield strength analyses, we have:

$$\sigma_{y-\text{weld}} = \sigma_{y-\text{base metal}} \tag{2.6}$$

$$\sigma_{y-\text{HAZ-shear}} = 0.7 \times \sigma_{y-\text{HAZ}} = 0.7 \times 1.15 \times \sigma_{y-\text{base metal}} \approx 0.8\, \sigma_{y-\text{base metal}} \tag{2.7}$$

Substituting Equations [2.6], [2.7], [2.3] and [2.4] into inequality [2.5] produces the condition under which pullout failure mode can be ensured:

$$D_{\text{critical}} > \frac{3.2t}{f} \tag{2.8}$$

Therefore, for a certain sheet thickness t and weld porosity factor f, the larger the weld diameter D, the better the chance of ensuring a pullout mode of failure. Also, for a certain sheet thickness, t, the lower the value f, that is, the higher the porosity level, the larger the nugget diameter D is needed to ensure pullout failure.

The failure mode prediction methodology described above can also be illustrated schematically as shown in Fig. 2.11, in which the heavier lines indicate the predicted failure mode. Given a certain material thickness t and porosity factor f, when D is smaller than D_{critical}, $F_{\text{IF}} < F_{\text{PO}}$. Therefore interfacial fracture would be the dominant failure mode under cross tension. On the other hand, when D is greater than D_{critical}, $F_{\text{PO}} < F_{\text{IF}}$. Therefore nugget pullout would be the dominant failure mode under cross tension loading.
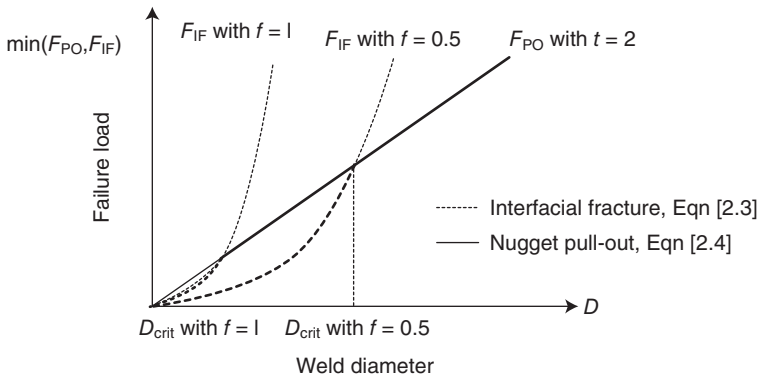
2.11 Schematic illustration of cross tension failure load and failure mode versus weld diameter at different porosity levels.

If one assumes $f = 1.0$, that is, perfect quality aluminum spot welds with no porosity and irregularity, the predicted nugget size of $3.2t$ for pullout mode can be compared with the conventional recommended minimal nugget size of $4\sqrt{t}$. If the thickness of the aluminum sheet being welded is less than 1.5625 mm, the conventional minimal nugget size recommendation of $4\sqrt{t}$ is sufficient to ensure nugget pullout. On the other hand, if the aluminum sheet thickness is greater than 1.5625 mm, the recommended minimal nugget size of $4\sqrt{t}$ is smaller than $3.2t$. Therefore the recommended minimal weld size of $4\sqrt{t}$ is not sufficient to ensure nugget pullout failure under the cross tension loading condition. If one were to take into consideration weld porosity and irregularity of the actual production welds, the nugget size needs to be further increased to ensure nugget pullout.

From another perspective, Fig. 2.11 also indicates that the cross tension strength of the weld depends primarily on the weld diameter D at a certain level of porosity. For weld diameters smaller than $D_{critical}$, interfacial fracture failure mode would be dominant and the peak failure load would increase in a parabolic fashion with respect to the weld diameter. For weld diameters greater than $D_{critical}$, nugget pullout would be the dominant failure mode and peak failure load increases linearly with the weld diameter. This conclusion validates the observations obtained in the previous section on the effect of weld size.

2.5   Model validation and discussion of aluminum spot welds

In order to validate the above analytical failure mode model, two additional populations of aluminum spot welds with 2 mm AA5182-O were fabricated

(a)

(b)
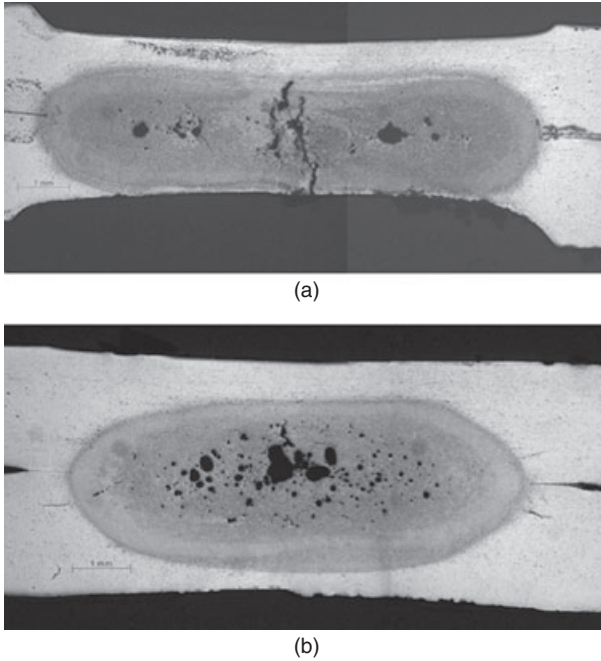
2.12 Typical metallurgical cross-sections for (a) ID14 large weld and (b) ID14 small-weld.

for cross tension loading condition. Our intention was to make one sample population with a weld size smaller than the original ID14 and another sample population with a weld size larger than ID14. We labeled these populations as ID14-small-weld and ID14-large-weld. The intended fusion zone diameter for ID14 small-weld population was 5.5 mm to 6.1 mm and the intended fusion zone size for ID14 large-weld population was 9 mm to 10.6 mm. Typical weld cross-sections for ID14 small-weld and ID14 large-weld are shown in Fig. 2.12. Note that the small weld population has the desired weld size of $4\sqrt{t}$.[11] Again, 30 replicates of quasi-static cross tension tests were conducted for each population and the resulting peak load and joint failure modes were recorded.

According to Figs 2.4 and 2.12, the area percentage of porosity on the faying interface can be estimated as ~15–20% for a typical weld in ID14, ID14 small-weld and ID14 large-weld. Assuming the same level of $f = 0.85$ for all three populations, we derive $D_{critical} = 7.5$ mm according to Equation [2.8] for 2 mm AA5182-O sheet. Since the weld sizes for the samples in ID14 were controlled to be around 8 mm, this may explain why the majority of the cross tension samples in ID14 failed in nugget pullout mode. The
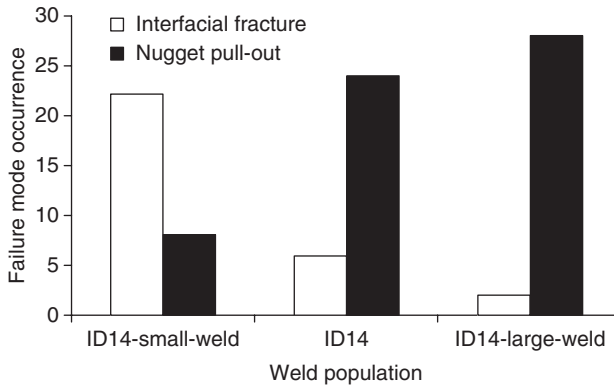
2.13 Comparison of failure modes versus weld fusion zone size.

recorded nugget sizes for ID14 also confirm that all the welds in ID14 that failed in nugget pullout mode have weld diameters greater than 7.5 mm.

Furthermore, when we increased the weld size to 9–10 mm as in population ID14 large-weld, 28 of the 30 welds tested failed in nugget pullout mode. The two welds that failed in interfacial fracture mode have irregular fusion zone shape and their minimum fusion zone diameters are measured to be 4.95 mm and 7.1 mm, respectively.

For ID14 small-weld population, 22 of the 30 welds tested failed in interfacial fracture mode and eight welds failed in nugget pullout mode. The actual fusion zone size for ID14 small-weld is larger than its intended value, with an average fusion zone size of around 7.1 mm. Since their average diameter is lower than the predicted critical value, the majority of the welds failed in interfacial fracture mode.

Figure 2.13 summarizes the experimentally observed failure modes for the original ID14, ID14 small-weld and ID14 large-weld populations. The dominant failure modes for the three populations change from interfacial fracture to nugget pullout with increasing fusion zone size. Considering the statistical nature of weld size, porosity level and distribution, the analytical model works reasonably well in predicting the critical weld size for nugget pullout.

Thus far, we have validated Equation [2.8] for the effect of fusion zone size D for fresh welds with consistent porosity levels. The validations do not include the effects of weld porosity factor f. Since the level of weld porosity and its distributions are closely related to electrode wear,[10] further validations on the effect of porosity factor f should be investigated in conjunction with studies of electrode wear.

It is worth noting that, given the material properties and the nugget size, one can also use Equations [2.3], [2.4], [2.6] and [2.7] to estimate quickly
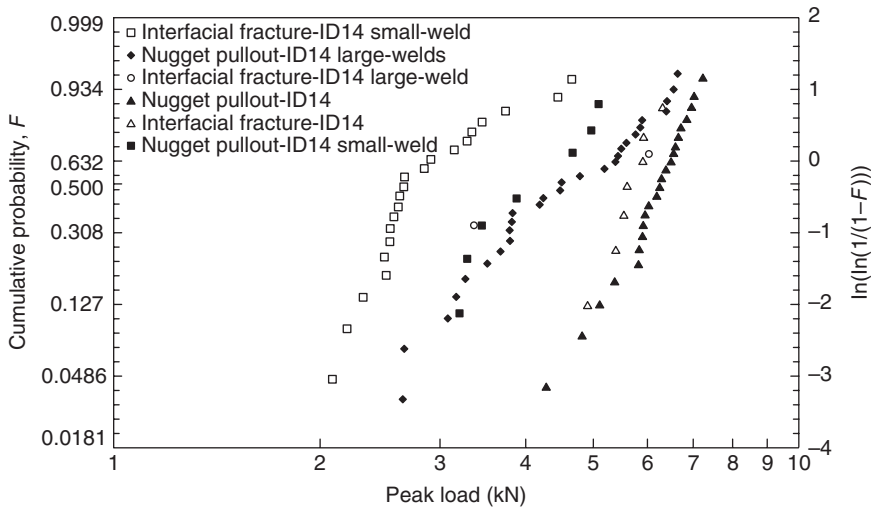
2.14 Comparison of cross tension peak load distributions for ID14, ID14 large-weld and ID14 small-weld.

the anticipated cross tension strength of a spot weld population. For example, the shear strength of AA5182-O used in ID14 and ID15 is about 140 MPa according to the *Metal's Handbook*[16] and *ASM Specialty Handbook*.[17] Given the sheet thickness of 2 mm and the average nugget size of 8.5 mm, Equation [2.4] estimates the weld pullout strength to be:

$$F_{PO} = \pi \cdot D \cdot t \cdot \sigma_{y-HAZ-shear} \approx \pi \cdot 8.5 \cdot 2 \cdot 0.8 \cdot 140 = 5.98 \text{ kN} \qquad [2.9]$$

The estimated cross tension strength in Equation [2.9] is very close to the strength data obtained experimentally.

As noted in Equation [2.4], the actual weld pullout strength under the cross tension loading condition also depends on the degree of weld indentation. Therefore the fact that a weld has a larger fusion zone diameter and that it fails in nugget pullout mode cannot guarantee that it is stronger than a weld with a smaller fusion zone for the same material combination. An example of this is shown in Fig. 2.14 where the peak loads of ID14, ID14 small-weld and ID14 large-weld are compared. Even though ID14 large-weld has larger fusion zone size than ID14, its average static strength is lower than that of ID14 because of its severe weld indentation and therefore reduced effective sheet thickness *t*.

Another important observation from Fig. 2.14 is that, for joint ID14 small-weld, the mean strength of the samples that failed in interfacial fracture mode is considerably lower than that of the samples that failed in nugget pullout mode. With increasing fusion zone sizes for ID14 and ID14

large-weld, the strength differences between the two failure modes decrease. Therefore the observations we made earlier on the effects of failure modes on peak load and energy absorption for ID14 and ID15 cannot be generalized to welds with a fusion zone size smaller than $D_{critical}$. In addition, for a population ID14 large-weld, the samples that failed in interfacial fracture mode have a similar level of median strength but a larger level of scatter than those that failed in nugget pullout mode.

It should also be noted that, even though the analytical part of the study focuses on aluminum spot welds, a similar analysis procedure may also be used for spot welds of advanced high strength steel (AHSS) because of the similar characteristics of the hardness traverse plots. For both of these materials, the weld nugget does not have a significantly higher yield strength than the base metal and the heat-affected zone. Moreover, based on a similar micro-hardness argument, it can be shown that the traditional criterion for rejecting interfacial fracture welds works well in evaluating the quality of mild steel spot welds. Detailed discussions on RSW failure modes for AHSS will be covered in the following chapters.

2.6   Conclusions

Through experimental investigation, statistical study and analytical study, the following conclusions can be derived:

- Theoretically, weld size, sheet thickness and level of weld porosity are the main factors determining the cross tension failure mode for the aluminum spot welds studied in this chapter. For a given sheet thickness and porosity level, the larger the weld size in comparison with $D_{critical}$, the more likely it is that the weld will fail in nugget pullout mode under cross tension. It should be noted that this conclusion is quantitatively valid for situations where the weld metal and HAZ hardness/strength are similar to those of the base metal. If substantial strength disparities exist (e.g. when welding precipitation hardening alloys in the T6 condition), the critical weld diameter for pullout failures could be significantly shifted according to Equations [2.3] and [2.4].

- For the two populations of aluminum spot welds in ID14 and ID15, different failure modes under cross tension and coach peel loading conditions do not significantly influence the static peak load and energy absorption levels of the samples. In a statistical sense, the pullout mode generates a less than 10% higher peak load and total energy absorption compared with the interfacial fracture mode. However, this conclusion can not be generalized to weld populations with fusion zone sizes smaller than $D_{critical}$.

- For the cross tension samples that failed in nugget pullout mode in ID14 and ID15, a larger weld diameter generates higher peak load and higher energy absorption.
- Severe weld indentation reduces the static strength of cross tension samples. In general, if we consider two samples from two different weld populations, the sample with the larger weld size does not guarantee higher cross tension strength even when both samples fail in nugget pullout mode. The degree of weld indentation should also be considered.
- The cross tension strength of aluminum welds can be reasonably estimated given the material's yield strength, sheet thickness, weld size and the level of weld porosity.

The conclusions of this study seem to suggest that one would want to increase the weld size indefinitely to achieve a higher level of peak load and energy absorption. Practically, a larger weld size is also associated with a higher energy requirement for the welding equipment, faster electrode wear and possible weld indentation. Therefore, the optimized value of weld size should be selected based on practicality and fitness-for-service criteria.

2.7   References

1. CHUKO, W.L. and GOULD, J.E. 'Development of appropriate resistance spot welding practice for transformation-hardened steels'. *Welding Journal*, 2002, **81**(1), 1-s–7-s.
2. PERTERSON, W. 'Dilution of weld metal to eliminate interfacial fractures of spot welds in high and ultra high strength steels'. *International Conference on Advances in Welding*, Columbus, OH, 1997.
3. RIESNER, M., SUN, X., WU, S., HWANG, H.Y. and LOW, E. 'Modeling and optimization of structural joints in automotive applications'. *Proceedings of the International Crashworthiness Conference*, London, Sept. 4–7, 2000. Paper No. 2096.
4. BROWNE, D.J., CHANDLER, H.W., EVANS, J.T. and WEN, J. 'Computer simulation of resistance spot welding in aluminum: Part I'. *Welding Journal*, 1995, **74**(10), 339-s–344-s.
5. BROWNE, D.J., CHANDLER, H.W., EVANS, J.T., JAMES, P.S., WEN, J. and NEWTON, C.J. 'Computer simulation of resistance spot welding in aluminum: Part II'. *Welding Journal*, 1995, **74**(12), 417-s–422-s.
6. SPINELLA, D.J., OTTEREN, R.V., BORENIK, B. and PATRICK, E.P. 'Single-sided projection welding of aluminum automotive sheet using the HY-PAK® welding process'. *SAE paper No. 2000-01-2678*, 2000.
7. SUN, X. and DONG, P. 'Analysis of aluminum resistance spot welding processes using coupled finite element procedures'. *Welding Journal*, 2000, **79**(8), 215-s–221-s.
8. SUN, X., DONG, P. and KIMCHI, M. 'The coupled electrical–thermal–mechanical process associated with aluminum RSW'. *Proceedings of the Seventh*

International Conference on Computer Technology in Welding, T. Siewert (ed.), 447–57, 1997.

9. FUKUMOTO, S., LUM, I., BIRO, E., BOOMER, D.R. and ZHOU, Y. 'Effects of electrode degradation on electrode life in resistance spot welding of aluminum alloy 5182'. *Welding Journal*, 2003, **82**(11), 307-s–312-s.

10. CHUKO, W. and GOULD, J. 'Metallurgical interpretation of electrode life behavior in resistance spot welding of aluminum sheet', *Proceedings Joining of Advanced and Specialty Materials*, 9–11 Oct. 2000, St. Louis, MO, ASM International, 114–21.

11. *Weld Quality Test Method Manual*, Standardized Welding Test Method Task Force, Auto/Steel Partnership, October 1997.

12. ANG, A.H-S. and TANG, W.H. *Probability Concepts in Engineering Planning and Design, Volume 1, Basic Principles*, John Wiley & Sons, New York, 1975.

13. KHALEEL, M.A. and SAUNDERS, S.C. 'On the fatigue-life distributions of engineering materials'. *International Journal of Reliability, Quality and Safety Engineering*, 1997, **4**(1), 93–115.

14. LIN, S.-H., PAN, J., WU, S.-R., TYAN, T. and WUNG, P. 'Failure loads of spot welds under combined opening and shear static loading conditions'. *International Journal of Solids and Structures*, 2002, **39**, 19–39.

15. ZHOU, M., HU, S.J. and ZHANG, H. 'Critical specimen sizes for tensile-shear testing of steel sheets'. *Welding Journal*, 1999, **78**(9), 305-s–313-s.

16. *Metal's Handbook Ninth Edition*, *Volume 1 Properties and Selection: Irons and Steels*, American Society for Metals, Metals Park, OH, 1978.

17. *ASM Specialty Handbook: Aluminum and Aluminum Alloys*, ASM International, Metals Park, OH, 1993.

3

Resistance spot weld performance and weld failure modes for dual phase and TRIP steels

M. TUMULURU, United States Steel Corporation, USA

Abstract: This chapter discusses the advantages, physical metallurgy and methods of production of coated (galvanized and galvannealed) dual phase and transformation-induced plasticity (TRIP) steels. Details of the resistance spot welding behavior of these two steels are presented. The details include the welding current ranges and the weld shear and cross-tension strengths. The commonly observed weld failure modes in weld tensile tests are presented. Competition between and the conditions that promote the two fracture modes are discussed. Finally, several recommendations for achieving welds of acceptable quality are presented.

Key words: dual phase and TRIP steels, electrode force, full button pullout fracture, interfacial fracture, resistance spot welding, welding guidelines.

3.1   Introduction

Automotive companies are under pressure to improve the fuel efficiency of their vehicles and to build vehicles from materials that offer improved occupant safety over present-day vehicles. For automotive use, materials selected must be easily formable, weldable, coatable (for corrosion protection) and repairable. Two such materials that show promise for fulfilling all these needs are the dual phase and transformation-induced plasticity (TRIP) steels. Therefore, it is no surprise that the use of these two steels in passenger vehicles is expected to rise from 191 lbs (85 kg) per light vehicle in 2009 to 540 lbs (245 kg) per light vehicle by the year 2020 (Schulz and Abraham, 2009). Dual phase and TRIP steels are considered

43

to be advanced high strength steels (AHSS) to distinguish them from the conventional high strength steels (HSS). HSS types include high-strength low-alloy steels and carbon-manganese steels with tensile strength up to 440 MPa.

3.1.1   Advantages of dual phase and transformation-induced plasticity steels

Some of the frequently cited advantages of dual phase and TRIP steels over the conventional low strength carbon steels (ultimate tensile strength less than 300 MPa) include the following (Engl, 1997; Tumuluru, 2006a):

- excellent formability owing to high ductility
- higher crash energy absorption, thereby allowing better occupant protection
- possibility of using thinner gauges, thereby achieving weight reduction in vehicles, leading to better fuel economy
- good weldability, thereby allowing easy fabrication.

The combination of high strength and high elongation that dual phase and TRIP steels possess in comparison to other automotive steels can be seen in Fig. 3.1.
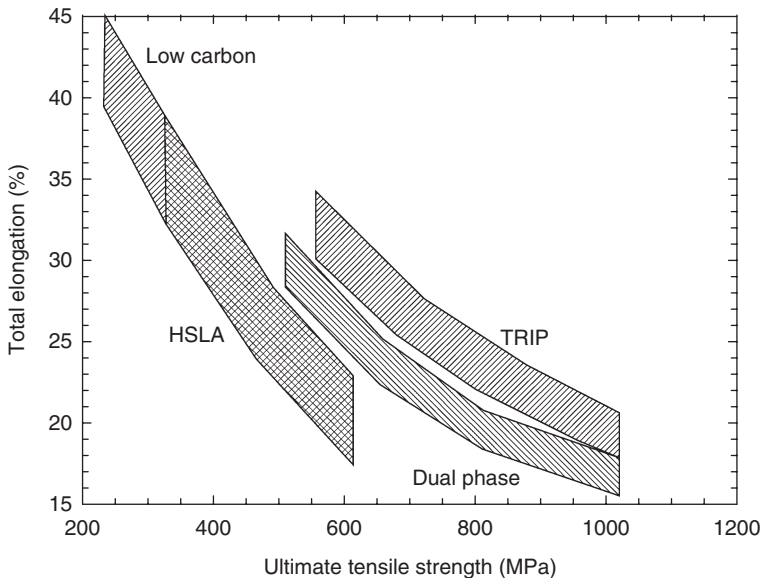
3.1 Plot of nominal ultimate tensile strength and total elongation for various types of steels used in automotive applications.

3.1.2 Coating of steels for automotive applications

Two types of coatings are generally applied to steel sheets used in the automotive industry, namely galvanized and galvanneal coatings. Galvanized coatings essentially contain pure zinc with about 0.3–0.6 wt% aluminum. The term 'galvanize' comes from the galvanic protection that zinc provides to steel substrate when exposed to a corroding medium. A galvanneal coating is obtained by additional heating of the zinc-coated steel between 450 and 550°C immediately after the steel exits the molten zinc bath. This additional heating allows iron from the substrate to diffuse into the coating. One of the methods by which the coatings are applied to the steel sheet surface is through a process called hot dipping. In this process, continuous coils of steel sheet are pulled at a controlled speed through a bath containing molten zinc. The zinc reacts with the steel and forms a bond.

3.2   Method of production and microstructure of steels

The methods of production of coated dual phase and TRIP steels were provided by Tumuluru (2006a) and are shown schematically in Fig. 3.2. TRIP steel is produced by heating the steel into the intercritical temperature range for annealing so that dissolution of cementite occurs and formation of austenite starts. The aim here is to produce a microstructure consisting of a mixture of austenite and a matrix of ferrite. Holding time and temperature determine the proportion of each phase. The annealing temperature may range from 770 to 850°C. Then, the steel is cooled to 400°C where the cooling is interrupted. This leads to isothermal transformation to low carbon bainite and carbon-enriched austenite. The final microstructure consists of low carbon bainite and a carbon-enriched austenite in a ductile ferrite matrix with some martensite.

   The retained austenite transforms to martensite when stress is applied during forming. This transformation is diffusionless and gives improved ductility. Silicon, aluminum and phosphorus are added to the steel to retard cementite formation and help enrich austenite in carbon (De Meyer *et al.*, 1999). The production of dual phase steel is similar to that of TRIP steel except that the steel is alloyed and cooled from the intercritical temperature range in such a way as to avoid the formation of bainite. The final microstructure consists of ferrite and martensite. The room temperature microstructures of both the steels are shown in Fig. 3.3.

3.3   Resistance spot welding behavior

The resistance spot welding behavior of steels is generally described by the welding current ranges they exhibit and the weld shear and cross-tension

(a)
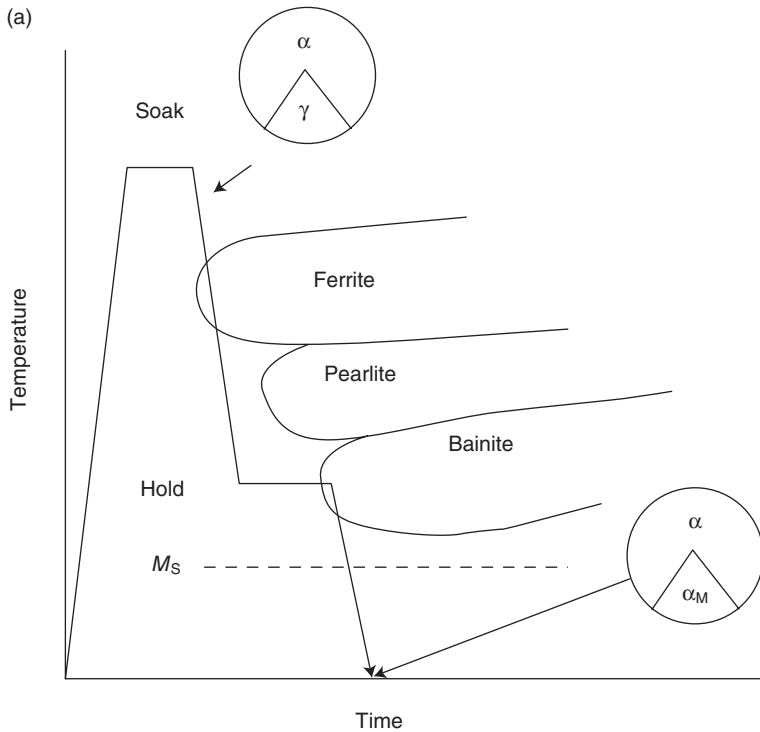
3.2 Schematic illustration of the methods of production for (a) dual phase and (b) TRIP steels (Tumuluru, 2006).

strengths. Therefore, to characterize the resistance spot welding behavior of these steels, useful current ranges and static weld tensile tests are performed. The useful current range is the difference between the welding current required to produce a minimum button size (I_{min}) and the current that causes expulsion of weld metal (I_{max}). The minimum button diameter $4\sqrt{t}$, where t is the nominal sheet thickness, is generally used in the automotive and steel industries.

The procedure for determining current range is described in detail in American Welding Society Specification AWS D8.9M (2002). Peel test coupons measuring 140 mm by 50 mm are used in the current range determination. The coupons overlap by 25 mm and a shunt or anchor weld is made on one side of each coupon pair. Test welds are made on the other side, 35 mm from the edge. The test welds are peeled open and the button sizes are determined using calipers. The current range is useful because it provides a range of welding currents over which welds with buttons of acceptable size can be produced. Prior to determining the current range,

(b)
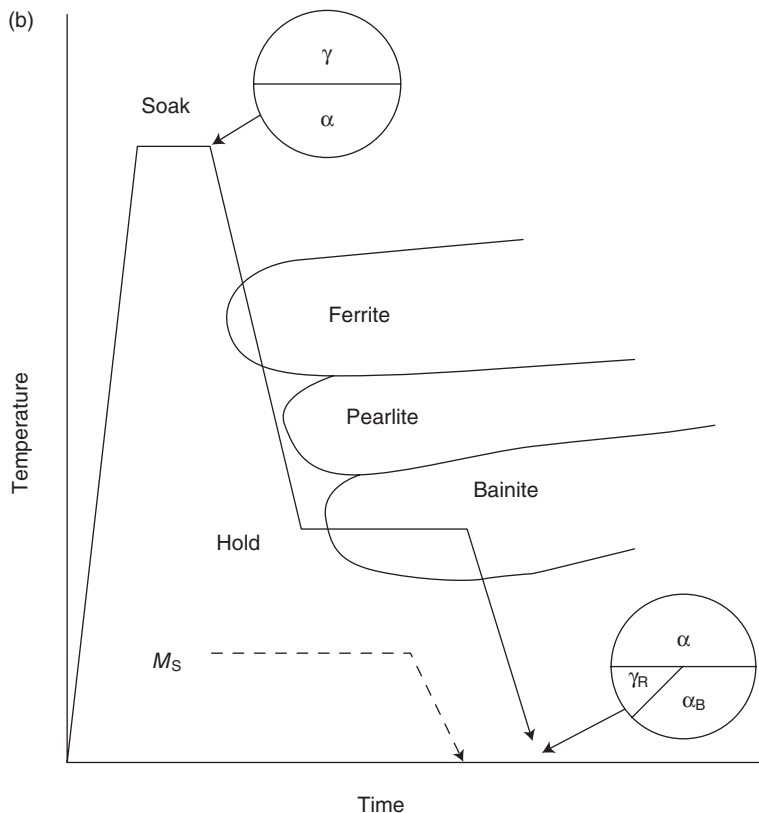
3.2 continued

the electrode tips are conditioned by making 250 welds. Current ranges are then found by first determining the lowest welding current that produces the minimum acceptable button size. Then, the current is gradually increased until weld metal expulsion results.

3.3.1 Effect of electrode force

In resistance welding, heating of the materials to be joined is realized through I^2Rt, where I is the current used for welding, R is the resistance offered to the passage of current and t is the time of passing the current. Therefore, the resistance offered by the steel is an important factor that controls the weld nugget development. The term R here is a sum of all resistances, including the resistance of the two steel sheets being welded, the interfacial resistance at the sheet-to-sheet contact, as well as the two interfacial resistances at the sheet-to-electrode interfaces. The steel

1000×757-ID-T ———— 0.010 mm
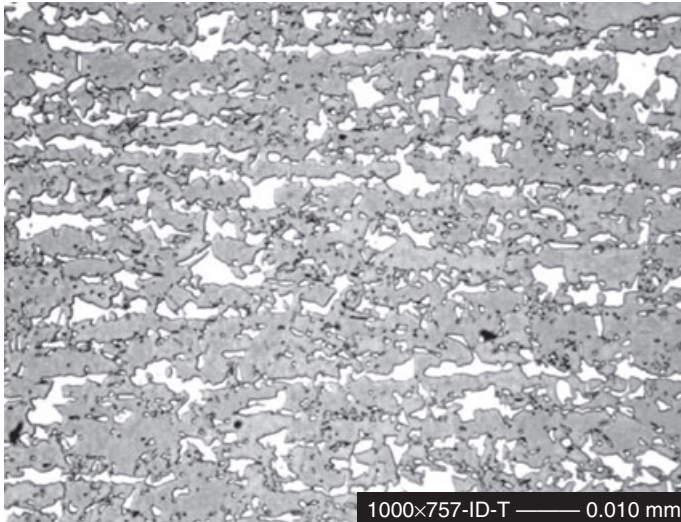
(a)
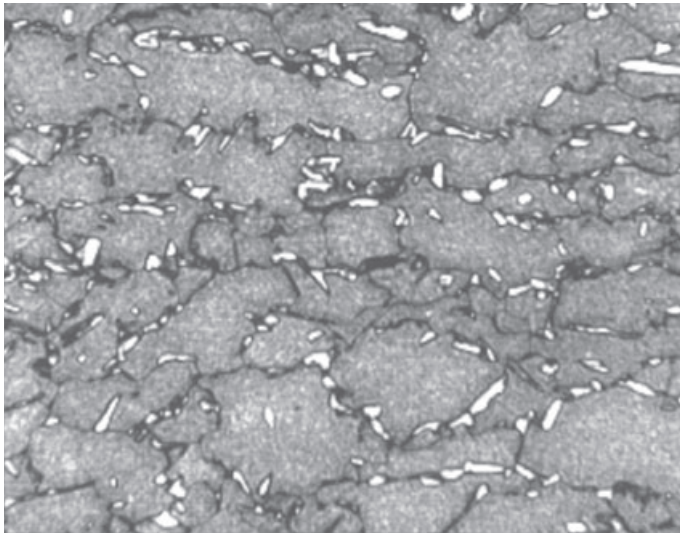
(b)

3.3 Microstructures of (a) dual phase and (b) TRIP steels (Tumuluru, 2006).

resistivity must be controlled so that excessive heat generation can be prevented. Excessive or uncontrolled heat generation can lead to weld metal expulsion.

One way of controling the effect of the higher resistivity of the dual phase steels is to use higher electrode force compared to that used for welding of
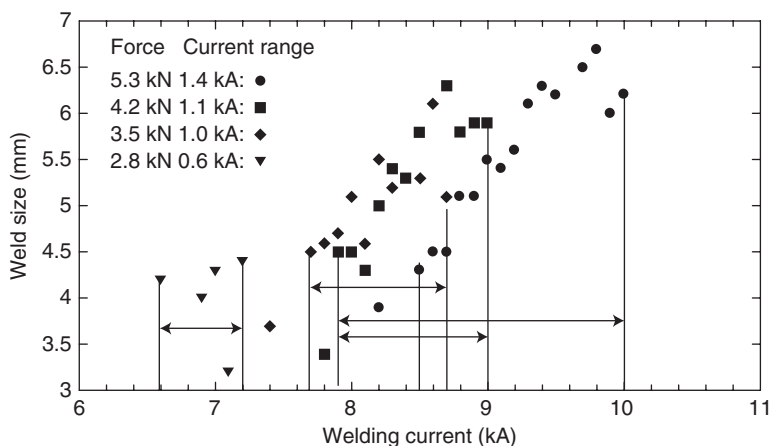
3.4 Effect of welding force on the welding current range in 780 MPa dual phase steel.

low strength (tensile strength less than 300 MPa), interstitial-free (IF) steels. The beneficial effect of the use of higher electrode force can be seen in Fig. 3.4 (Tumuluru, 2006b). As the electrode force was increased from 2.8 kN to 5.3 kN, the welding current range increased from 0.6 kA to 1.4 kA. A current range of 1.0 kA is generally regarded as acceptable by automotive companies for production use.

It is clear from Fig. 3.4 that a welding force of 3.5 kN is required to obtain the 1 kA current range. It is cautioned that, with the use of high force, the electrode indentation into the base material should be monitored, because higher electrode force causes deeper indentation. Generally, indentation at a given force will be greater in low strength steel than in high strength steel. As a guideline, the electrode indentation should be less than 25% of the base material thickness to avoid the possibility of creating a stress raiser.

3.3.2 Weld shear-tension and cross-tension strength determination

The weld tensile strength is determined in order to assess weld load-bearing ability. For shear-tension strength determination, 140 mm by 60 mm samples are sheared and a single spot weld is made at the center of an overlapping section 45 mm long between two samples. For cross-tension strength determination, the test coupons used are 150 mm long and 50 mm wide. Two coupons are placed at 90° to each other and a spot weld is made at the center of the overlapping area. A sketch showing coupon dimensions and layout of shear-tension and cross-tension samples is shown in Fig. 3.5.
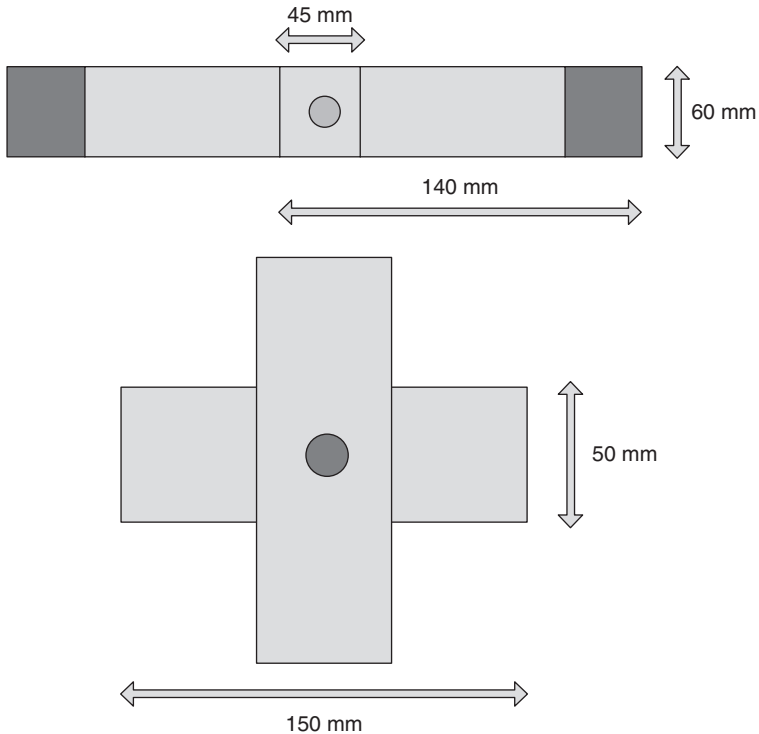
3.5 Sketches showing shear-tension (top) and cross-tension test (bottom) coupons.

Prior to making the weld test samples, the electrode tips are typically stabilized using a procedure described in American Welding Society Specification AWS D8.9M (2002) by making 250 welds on flat panels. Electrode stabilization prepares the electrode faces to stabilize the weld size and promotes reproducibility of test results. The stabilization procedure consists of adjusting the welding current as needed to maintain a specified or fixed weld size. All shear- and cross-tension test samples are prepared with a specified weld size, which is slightly higher than 90% of the electrode face diameter used. Weld sizes are generally verified prior to the tensile tests. The tensile testing procedure is also outlined in detail in American Welding Society Specification AWS D8.9M (2002). Additional details of the testing methodology can be found in this specification.

3.3.3 Factors controlling weld strength

Three factors control the weld strength in dual phase and TRIP steels (Oikawa *et al.*, 2007). Two of these factors, namely weld size (or nugget
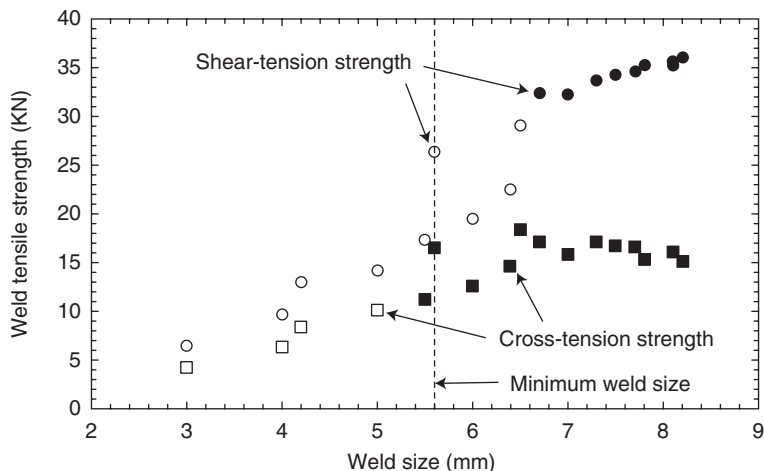
3.6 Plot of weld strength as a function of weld size for hot-dipped galvannealed (HDGA) 780 dual phase steel. Open symbols represent interfacial fractures and closed ones represent full button pullout fractures. Notice that both shear-tension and cross-tension strength increase as the weld size (nugget diameter) increases.

diameter) and the sheet thickness, increase weld tensile strength. The first of these factors that control the weld strength is the weld size. Figure 3.6 shows that the weld shear-tension strength increases as the weld size increases. The weld size is increased by increasing the welding current. However, after a certain maximum weld size is achieved, further increase in the welding current results in expulsion of molten weld metal. This occurs because the high welding current creates so much melting at the sheet interfaces that the amount of molten metal becomes too great to be supported at the faying surfaces. Weld expulsion is detrimental to the weld strength for two reasons. The first reason is that expulsion results in the weld size becoming small owing to molten metal being ejected out. The second reason is that it can cause gross pores to form at the sheet interfaces (faying surfaces) and thereby reduce the load-bearing area of the weld. This, in turn, leads to a lower weld strength.

The second factor that controls weld strength is the sheet thickness. As the sheet thickness increases, the weld strength increases. As the sheet thickness increases, a higher welding current is required to establish a nugget. This necessitates the use of a larger diameter electrode. The use of a higher welding current coupled with the use of a larger diameter electrode creates a bigger weld. Large diameter welds have higher load-bearing ability.

The third factor that controls weld tensile strength is the base material strength. The base material strength has an interesting effect on the weld

tensile strength. As the base material strength goes up, the weld shear-tension strength goes up. However, the weld cross-tension strength decreases from 590 MPa steel to 780 MPa and 980 MPa steels. Although the reason for the decrease in cross-tension strength is not clearly understood, it is believed that this may have to do with hardening in the heat affected zone which occurs as the base material strength goes up. It should be noted that, in order to achieve higher base material strength, more alloying elements are used in the base material. The alloying elements cause hardening in the heat affected zone from the rapid cooling that occurs in resistance spot welds.

3.4   **Weld failure modes**

The fracture appearance of welds is determined on weld tensile test samples after the tensile test. For simplicity, weld tensile test fractures are classified here as full button pullout, interfacial fracture or partial interfacial fracture. However, several combinations of the three modes can also occur in welds. In full button pullout fracture mode, the entire weld nugget pulls out from the sheets, with fracture occurring outside the weld area. In interfacial fracture, the entire weld fails through the plane of the weld. In partial interfacial fracture, part of the weld nugget fails through the plane of the weld and a portion of the weld pulls out as a partial button. Both the full button pullout and interfacial fracture modes are shown in Fig. 3.7.

To understand the origin and the nature of failure modes, it is helpful to understand the events that occur during weld tensile testing. Chao (2003)
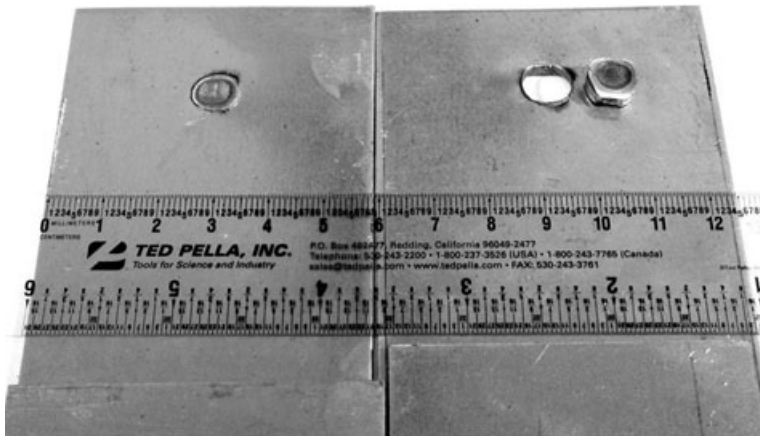
3.7 Photograph showing interfacial fracture mode (left) and full button pullout fracture mode (right) in shear-tension test samples.

provided a summary of the events that occur during shear-tension and cross-tension testing in resistance spot welds. It was observed in shear-tension testing that, as the specimen is pulled by a tensile load, the weld nugget experiences a rotation, which causes the weld to align with the loading axis. This rotation results in the material surrounding the weld being subjected to a predominantly tensile load. Evidence of ductile dimpled rupture fracture was found in samples subjected to shear-tension testing supporting the observation of tensile loading of the material surrounding the weld nugget. In cross-tension testing, as the tensile load is applied normal to the weld, the weld is subjected to a bending stress. This bending stress results in the weld nugget being pulled out from one of the samples and remains with the other. Thus, the failure can be characterized by through-thickness shear around the weld nugget. Evidence of tearing was found to support the characterization of a shear mechanism causing the weld failure. Thus, the shear strength of the base material controls the weld strength.

In the evaluation of the shear-tension test results in spot welds, it is generally believed in the automotive industry that an interfacial shear failure is indicative of poor weld integrity. This has generally been true for low strength steels (tensile strength equal to or less than 300 MPa) in which interfacial failure is normally associated with insufficient fusion or some sort of a weld imperfection, such as gross porosity. However, it is unclear if interfacial fractures in shear-tension tests indicate poor weld integrity in AHSS grades. With the increased use of these steels in automotive bodies, it is important to understand their fracture behavior in shear-tension tests so that welds, which are otherwise sound, are not rejected solely based on fracture appearance. Furthermore, an understanding of the fracture behavior may allow the automotive companies to use these steels and enable them to take advantage of the benefits that these steel grades offer. Radakovic and Tumuluru (2008) performed finite element modeling and fracture mechanics calculations to predict the resistance spot weld failure mode and loads in shear-tension tests of advanced high strength steels (AHSS). They then compared the results to those obtained for an interstitial-free (IF) steel.

3.4.1 Predicting failure modes in shear-tension testing of dual phase and TRIP steels

As mentioned before, in shear-tension testing of resistance spot welds in dual phase or TRIP steels, either the full button pullout or the interfacial fracture mode of failure can occur. In order to predict which of these two modes is more likely to occur in a given grade of steel, it would help to develop predictive mathematical equations. For the pullout failure, the

results of the finite element simulations showed that there were a strong correlations between failure load and the material strength, sheet thickness and weld diameter. The load causing interfacial failure was found to be more strongly dependent on the weld diameter and less on the sheet thickness. The predicted failure loads were found to adhere to the following correlations:

$$F_{PO} = k_{PO} \cdot \sigma_{UT} \cdot d \cdot t \qquad\qquad [3.1]$$

$$F_{IF} = k_{IF} \cdot \sigma_{UT} \cdot d^2 \qquad\qquad [3.2]$$

where F_{PO} is the failure load for a (button or weld) pullout failure, F_{IF} is the failure load for an interfacial fracture, σ_{UT} is the tensile strength of the material, d is the weld diameter and t is the sheet thickness. The above equations were derived, based on the fact that the force required to cause failure is equal to the product of the strength of the material and the area of the failed cross-section. In this analysis, the material was assumed to be homogeneous. Therefore, the strength of the weld and the base metal are both assumed equal to σ_{UT}. In the above equations k_{PO} and k_{IF} are constants determined from the modeling. Experimental data showed that, as predicted in Equations [3.1] and [3.2] above, the failure loads causing pullout were found to be proportional to the weld diameter and the sheet thickness, while those for interfacial failure were proportional to the square of the weld diameters.

Equations [3.1] and [3.2] are plotted graphically in Fig. 3.8(a) for dual phase 590 steel and show the predicted interfacial and pullout failure loads as a function of weld diameter. In this plot, the sheet thickness was assumed to be 1.5 mm and the sheet tensile strength equal to 590 MPa. A sheet thickness of 1.5 mm was chosen because it represented the mid-thickness of the normal range of steels (1 to 2 mm) used in automotive bodies. The minimum allowable tensile strength of the steel (590 MPa) was used in this case. According to the analysis, the lower of the two predicted failure loads, either for the button pullout or interfacial fracture, will determine the mode of failure that occurs. Thus, the point where the two curves intersect indicates where the failure mode changes. The figure shows that, for this sheet thickness and strength, interfacial failures were predicted to occur for weld diameters below 6 mm and pullout failures for diameters greater than 6 mm.

Figure 3.8(b) shows a similar plot with the exception that the weld diameter was assumed to be constant at 7 mm and the failure loads are plotted as a function of sheet thickness. These results indicate that pullout failures are more likely to occur on thinner sheet samples and the mode can change to interfacial when the sheet thickness reaches a critical value (for this example ~ 1.7 mm). By setting Equations [3.1] and [3.2] equal to each other,
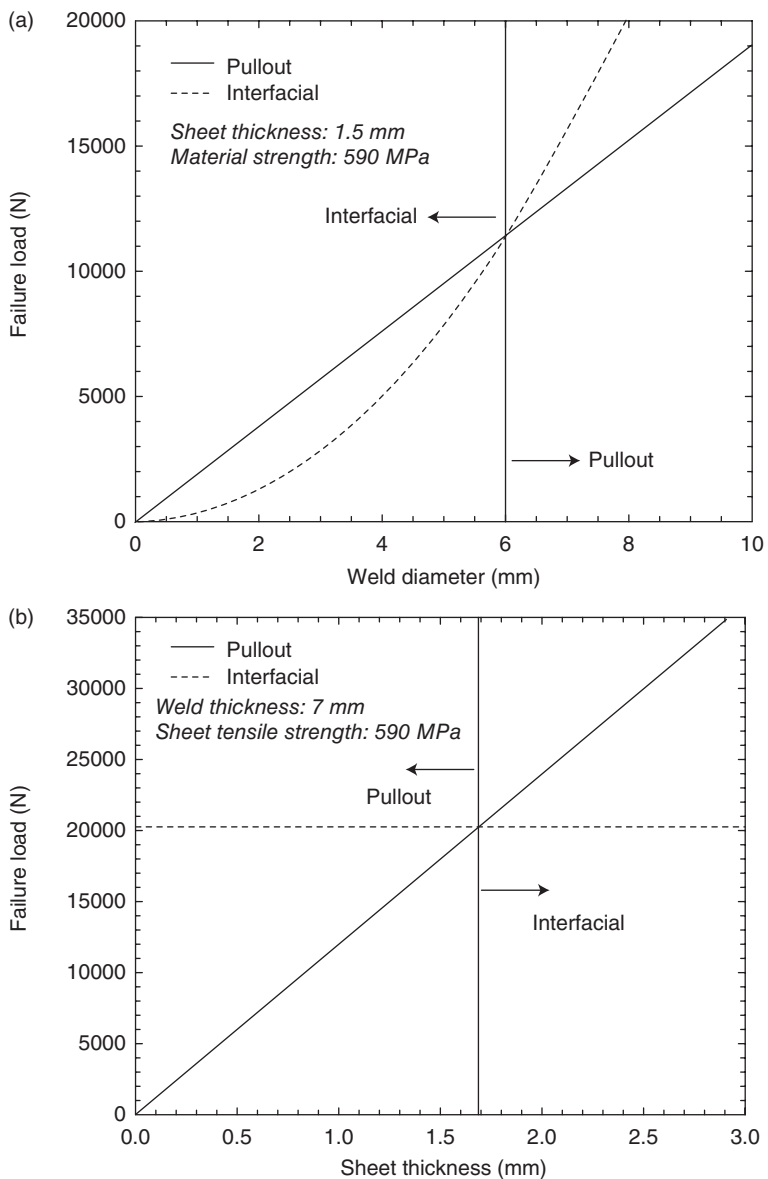
3.8 Predicted failure load for 590 MPa dual phase steel in the analysis of the shear-tension test sample as a function of weld diameter (a) and sheet thickness (b) (Radakovic and Tumuluru, 2008).
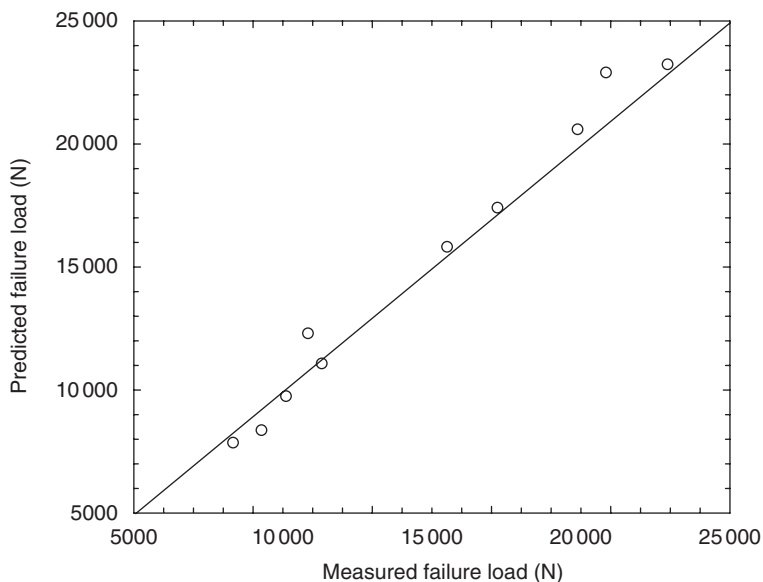
3.9 Comparison of actual failure loads to model-predicted failure loads in the shear-tension test for samples that failed via full button pullout (Radakovic and Tumuluru, 2008).

the ratio of the weld diameter to the sheet thickness is determined to be roughly equal to 4. This suggests, for a homogeneous test sample, that pullout failures will occur if the weld diameter is greater than four times the sheet thickness. Similarly, for a given weld diameter, the sheet thickness has to be less than 25% of the weld diameter for pullout to occur.

3.4.2   Comparison of predicted results and actual test data

The model predictions agreed well with the test data for cases where pullout failures occurred. This is because the pullout failures were most often initiated in the base metal outside the notch at the perimeter of the weld. A comparison of the actual failure loads and model-predicted failure loads for samples that failed via pullout is shown in Fig. 3.9.

   A comparison of the model results and actual data is shown in Table 3.1. The table lists the steel grades, weld diameter, sheet thickness, actual failure load and mode, as well as the predicted failure load had pullout failures occurred in each case. The first two samples listed failed via button pullout and the model-predicted failure loads were in good agreement with the actual loads. The next three samples in the table failed via interfacial fracture. For these cases, the model-predicted loads for pullout failure are

Table 3.1 Comparison of actual shear-tension test results and model predictions

Material	Sheet thickness (mm)	Weld diameter (mm)	Actual test data		Model predictions		Comparison
			Failure mode[a]	Failure load (N)	FEM failure mode	FEM failure load (N)	Actual as a percentage of predicted pullout load[b] (%)
780 DP	1.2	7.5	PO	15 500	PO	15 820	98
780 DP	1.6	8.3	PO	22 900	PO	23 250	98
590 DP	1.0	7.0	IF	9 900	PO	10 340	96
780 DP	1.2	7.5	IF	14 680	PO	15 820	93
780 TRIP	1.6	8.5	IF	22 060	PO	24 330	91

[a] IF = interfacial fracture, PO = full button pullout fracture. FEM = finite element method.
[b] Ratio of the actual failure load to the model-predicted pullout failure loads.

listed. The interesting result shown here is that, although interfacial fracture occurred in the samples, the load carrying capacity of the weld was greater than 90% of the predicted failure load if pullout had occurred. This indicates that the load-bearing capacity of these welds was not significantly affected by the fracture mode. Therefore, the mode of failure should not be the only criteria used to judge the quality of spot welds. The load-bearing capacity of the weld should be the primary focus in the evaluation of the shear-tension test results in dual phase and TRIP steels.

When comparing the model results to actual test data (Table 3.1), the predicted failure loads for the interfacial fractures were less accurate than those when the fracture occurred by full button pullout mode. It was theorized that there were two main reasons for the differences. First, the model assumed that the sample was homogeneous. In reality, the mechanical properties of the weld, base metal and different parts of the heat affected zone are significantly different. Further, the models did not account for the stress intensity at the perimeter of the weld. The model considered that the weld would fail when the strength of the weld metal is exceeded at the interface of the two sheets. This would more closely represent a shear overload of the weld metal rather than a fracture of the weld nugget initiating at the notch around the perimeter of the nugget.

A fracture mechanics study by Radaj and Zhang (1991) provided an estimate of the stress intensity at the perimeter of the spot weld specifically for the shear-tension test. Fracture mechanics theory provides a means to

Table 3.2 Actual test results and predicted stress intensity at failure

Material	Nominal sheet thickness (mm)	Weld diameter (mm)	Failure mode IF or PO[a]	Failure load (N)	Stress intensity (N mm$^{-3/2}$)
780 DP	1.2	7.0	IF	14 230	1294
590 DP	1.0	6.0	IF	9 790	1126
780 TRIP	1.6	8.5	IF	21 800	1385
780 DP	1.2	7.0	PO	15 520	1411
780 DP	1.6	8.0	PO	22 900	1581

[a] IF = interfacial fracture, PO = full button pullout fracture.

evaluate the load-bearing ability of materials that have cracks or flaws. In fracture theory, the fitness for service of a structural member that contains a crack is determined by comparing the predicted stress intensity at the crack tip to the fracture toughness of the material. Like material properties such as tensile strength and elongation, fracture toughness is a material property that is determined from testing. Fracture analysis of a cracked member (in which stress intensity is compared to fracture toughness) is analogous to the analysis of notch-free structural members in which predicted stresses are compared to the strength of the material. Zhang's analysis yielded the following relationship for the stress intensity at the perimeter of the weld in the shear-tension test:

$$K_{eq}^{ts} = 0.694 \cdot \frac{F}{d\sqrt{t}}$$ [3.3]

In this equation, K_{eq}^{ts} is the equivalent stress intensity factor at the spot weld, F is the applied load, d is the weld diameter and t is the sheet thickness. Some actual test results are shown in Table 3.2. The table lists the steel grades, weld dimensions, failure mode, failure load and the calculated stress intensity at failure. The stress intensities were calculated using Equation [3.3]. The first three samples listed in the table failed via interfacial fracture. This suggests that the listed stress intensity at the time of failure is comparable to the fracture toughness of the weld. The stress intensities for the samples that failed via button pullout are also shown. For these two cases, the fracture toughness of the weld was apparently high enough to avoid interfacial fracture (i.e. the fracture toughness was greater than the values listed for the stress intensity when the pullout failure occurred). The stress

intensities for the samples that failed via button pullout are also shown. For these two cases, the fracture toughness of the weld was apparently high enough to avoid interfacial fracture (i.e. the fracture toughness was greater than the values listed for the stress intensity when the pullout failure occurred).

In order to obtain an estimate of the load required for interfacial fracture in the shear-tension test, the stress intensity in Equation [3.3] was set equal to the fracture toughness of the material and the load was solved for. This is shown in Equation [3.4], where F_{IF} is the load causing interfacial fracture of the weld and K_C is the fracture toughness of the material:

$$F_{IF} = 1.44 \cdot K_C \cdot d \cdot \sqrt{t} \qquad\qquad [3.4]$$

The fracture toughness describes the ability of a material to carry load in the presence of a flaw and is determined by testing. Generally, ductile materials tend to have high fracture toughness, while the opposite is true for brittle materials. Based on the work of Radaj and Zhang (1991), Equation [3.4] (rather than Equation [3.2]) was thought to represent the parameters governing the interfacial fracture mode better. The previously determined load causing pullout failure (Equation [3.1]) was, however, considered to be appropriate. The predicted relationship for pullout load is likely to agree well with the measured data because this failure initiates in the form of necking in the base metal near the weld heat-affected zone as opposed to at the notch radius around the perimeter of the weld nugget.

Equations [3.1] and [3.4] are plotted graphically in Fig. 3.10. In this plot, the weld diameter was assumed to be constant at 8 mm, the tensile strength assumed was the minimum allowable for this grade (780 MPa) and the failure load is plotted as a function of sheet thickness. The interfacial fracture load is plotted assuming a fracture toughness of 1560 N mm$^{-3/2}$ (on the high end of the range observed for 780 MPa steels) and the pullout failure load is plotted for a low strength steel (300 MPa) and a higher strength steel (780 MPa). For the curve representing the low strength steel, the predicted pullout failure load is less than the interfacial fracture load over this entire range of sheet thickness. This indicates that pullout failure will occur in every case. For the higher strength sample, the curves for pullout failure and interfacial fracture intersect at a sheet thickness of 1.6 mm. This indicates that, for the high strength sheet sample, interfacial fracture will be the expected failure mode for sheet thicknesses greater than 1.6 mm.

3.4.3 Key findings from the finite element model

In the finite element model of Radakovic and Tumuluru (2008), the heat affected zone and weld properties were assumed to be equal to the base material properties. The model predictions agreed well with the test data
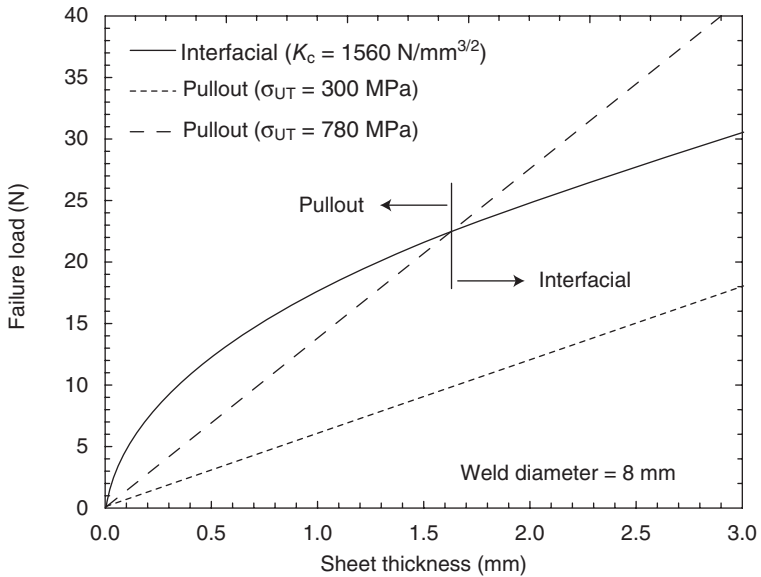
3.10 Plot showing the predicted competition between failure by full button pullout and interfacial fracture modes in the shear-tension test. K_c is the fracture toughness and σ_{UT} is the ultimate tensile strength of the steel (Radakovic and Tumuluru, 2008).

for cases where pullout failures occurred. This is because the pullout failures most often initiated in the base metal outside of the notch at the perimeter of the weld. However, when comparing the model results to actual test data, the predicted failure loads for the interfacial fractures were less accurate than those that failed by pullout mode. For the case of the interfacial failure mode, a relationship was found in the literature for estimating the stress intensity at the weld notch tip. This relationship was used, along with the equation developed for the pullout failure, to define variables that affect the failure mode and load for the shear-tension test. The key findings of the analyses of shear-tension testing of dual phase and TRIP steels can be summarized as follows:

- For low strength steels (tensile strength less than or equal to 300 MPa), a full button pullout occurs even when welds have a poor load-carrying capacity because the load required to cause yielding in the base material is much lower than that required for yielding to occur in the weld. For high strength steels, however, this was not found to be the case. For example, for an 8 mm diameter weld, interfacial fracture was predicted to occur in the shear-tension test, especially for cases where the sheet

thickness was greater than 1.6 mm and weld had superior fracture toughness and a high load-carrying capacity.

- There is a critical sheet thickness above which the failure mode is expected to move from pullout to interfacial fracture. As the strength of the sheet increases, the fracture toughness of the weld required to avoid interfacial fractures must also increase. In the higher-strength, less-ductile steels, this is not likely to occur and interfacial fracture will become the expected failure mode.

- The load-carrying capacity of the samples that failed via interfacial fracture was found to be more than 90% of the maximum load associated with the calculated full button pullout fractures. This indicates that the load-bearing capacity of these welds is not significantly affected by the fracture mode. Thus, the mode of failure should not be the only criterium used to judge the results of the shear-tension test. The load-carrying capacity of the weld should be considered the most important parameter when evaluating the shear-tension test results in dual phase and TRIP steels.

3.4.4   Failure modes in cross-tension testing

As mentioned in Section 3.3.2, the specimen orientation and loading direction for the cross-tension specimen are different from those for the shear-tension specimen. A study of the effect of fusion zone size on the peak load prior to failure, energy absorbed during loading and fracture modes was conducted by Sun *et al.* (2007). Welds that exceeded a certain critical size failed in a full button pullout mode. Below the critical size, welds most often failed in the interfacial fracture mode. This can be seen in Fig. 3.6. Below 5.4 mm weld (or fusion zone) size the cross-tension samples failed in the interfacial fracture mode. However, at weld sizes greater than 5.4 mm, the fractures occurred by full button pullout mode. The energy absorbed and the peak load prior to failure showed a higher degree of scatter for the interfacial fracture failures compared to those of the full button pullout mode failures. At the critical weld size, both interfacial fracture and full button pullout failure were observed. Even though both the interfacial and full button pullout failure modes offer similar distributions in terms of peak load prior to failure, the full button pullout fracture mode offered higher energy absorption in tensile tests (Sun *et al.*, 2007).

3.5   Future trends

Future trends can be classified into two areas, namely material trends and joining trends. In the case of materials, steels with higher strength and

improved ductility are being developed (Kruptizer, 2007). The dual phase and TRIP steels discussed in this chapter are considered to be first generation AHSS. The second generation AHSS include twinning-induced plasticity (TWIP) steels and austenitic stainless steels. Dual phase steels are commercially available up to 980 MPa strength level. Work is also being conducted to develop and produce commercially dual phase steels with strength levels up to 1180 MPa and higher. However, there are several challenges in material development and these are to keep the steels affordable, workable (from a stamping point of view) and weldable.

In the area of joining technologies there have been several advancements in joining dual phase and TRIP steels. Most notable of these is the use of hybrid laser joining techniques. A hybrid laser welding technique is a combination of a laser welding process (carbon dioxide or Nd: YAG) and an arc welding process (gas tungsten arc, gas metal arc, or plasma arc welding method) in a hybrid welding head (Bagger and Olsen, 2005). Both the laser welding and the arc welding process act simultaneously on the same base materials producing a fusion zone. The advantages of hybrid joining techniques include the possibility of high welding speed, deep penetration, low distortion and narrow weld seams. Perhaps the greatest advantage includes the ability to tolerate large gaps between the sheets to be welded. This advantage is particularly attractive in automotive assembly because of the large gaps typically seen in automotive body panels. Because the laser hybrid weld is a linear weld as opposed to being a spot weld (as in resistance spot weld), a hybrid weld provides a stiffer joint than a spot weld. Use of the hybrid welding method is expected grow in the coming years.

3.6   **Summary**

Several considerations are necessary for successful welding of dual phase and TRIP steels (WorldAuto Steel, 2009). For example, when welding dual phase and TRIP steels it is important to control the high resistance at the sheet interface. High resistance at the interface leads to rapid heating during welding and, if not controlled effectively, can quickly lead to weld expulsion. Because expulsion removes weld metal, the presence of expulsion generally lowers the weld size and reduces the strength of the weld. Therefore, weld expulsion should be avoided. One way to accomplish this is to use a higher electrode force. The selection of welding force depends upon the thickness of the sheets being welded. As a general rule of thumb, a 20% higher electrode force than that used for low strength steel (tensile strength less than 300 MPa) of similar thickness should be used for dual phase and TRIP steels if the nominal tensile strength of the steels exceeds 780 MPa.

Owing to the use of higher electrode force and higher welding currents to weld dual phase and TRIP steels, it is essential to maintain proper elec-

trode cooling. Electrode cooling water flow rate through both the tips should be 4 l min^{-1} or higher. Another helpful suggestion to weld dual phase and TRIP steels successfully is to use larger diameter electrode tips than that those used for welding low strength steels. Larger diameter tips have a higher current carrying capacity and provide for lower current density. These two factors help achieve larger weld sizes.

Several studies have shown the importance of achieving a larger weld size in dual phase and TRIP steels (Radakovic and Tumuluru, 2008; Sun *et al.*, 2007). Larger welds have higher load-bearing ability and tend to pull out during tensile loading. Full button pullout fracture mode provides higher energy absorption compared to the interfacial fracture mode.

Resistance welding depends on the interfacial resistance between two sheets. Good and consistent fit-up is important in all resistance welding. Fit-up is even more critical in the welding of AHSS owing to increased yield strength and greater spring back. The larger electrode tip size will have a larger current range, which might compensate for the poor part fit-up. Also, progressively higher electrode force with thicker gauges of steel and gradual increase in welding current (referred to as 'current upslope') can be used to solve poor part fit-up.

3.7   References

AMERICAN WELDING SOCIETY (2002). *Specification D8.9M-2002*, American Welding Society, Miami, FL.

BAGGER, C. and OLSEN, F. O. (2005). 'Review of laser-hybrid welding'. *Journal of Laser Applications*, **17**(1), 19–24.

CHAO, Y. J. (2003). 'Ultimate strength and failure mechanism of resistance spot weld subjected to tensile, shear or combined tensile/shear loads'. *Journal of Engineering Materials and Technology*, **125**, 125–32.

DE MEYER, M., VANDERSCHUREN, D. and DE COOMAN, B. C. (1999). 'Phase transformation and mechanical properties of Si-free CMnAl transformation-induced plasticity-aided steel'. *41st MWSP Conference Proceedings*, Iron and Steel Society (ISS), **XXXVII**, 227–34.

ENGL, B. (1997). 'From 450 MPa dual-phase to 1100 MPa complex-phase steels: Development of a new generation of automotive sheet steels'. Automotive Body Materials, *IBEC Conference*. Papers are available from IBEC.

KRUPTIZER, R. (2007). 'Transitions in automotive high-strength steels since ULSAB-AVC' Invited speech, American Iron and Steel Institute, *AIST Conference on Microalloyed Steels*, Pittsburgh, PA, July 19, 2007, 2–14. Slides available from the author at AIST, Southfield, MI, WA.

OIKAWA, H., SAKIYAMA, T., ISHIKAWA, T., MURAYAMA, G. and TAKAHASHI, Y. (2007). 'Resistance spot weldability of high strength steel (HSS) sheets for automobiles'. *Nippon Steel Technical Report No. 95*, January.

RADAJ, D. and ZHANG, S. (1991). 'Simplified formulae for stress intensity factors of spot welds'. *Engineering Fracture Mechanics*, **40**(1), 233–6.

RADAKOVIC, D. J. and TUMULURU, M. (2008). 'Predicting resistance spot weld failure modes in shear tension tests of advanced high strength automotive steels'. *Welding Journal*, **87**(4), 96S–105S.

SCHULTZ, R. and ABRAHAM, A. (2009). 'North American light vehicle metallic material trends'. Paper presented at *Great Designs in Steel*, Auto/Steel Partnership, American Iron and Steel Institute, Southfield, MI. See AISI website.

SUN, X., STEPHEN, E. V. and KHALEEL, M. (2007). 'Effect of fusion zone size and failure mode on peak load and energy absorption of advanced high-strength steel spot welds'. *Welding Journal*, **86**(1), 18S–25S.

TUMULURU, M. (2006a). 'A comparative examination of the resistance spot welding behavior of two advanced high strength steels'. Paper presented at the *SAE Conference*, Detroit. Society of Automotive Engineers, Warrendale, PA.

TUMULURU, M. (2006b). 'Some considerations in the resistance spot welding of dual phase and TRIP steels'. Paper presented at the *International Conference in Advances in Resistance Welding*, Toronto, Conference organized by SWANTEC Software and Engineering, Denmark, September 24–26.

WORLDAUTO STEEL (2009). *Joining Guidelines for Advanced High Strength Steels*, www.worldautosteel.org.

4

Fatigue behavior of spot welded joints in steel sheets

S. K. K H A N N A, University of Missouri, USA, and
X. L O N G, Center for Reliable Energy Systems, USA

Abstract: Fatigue loading of spot welded joints is one of the most important factors affecting the durability of the structure containing such joints. This chapter summarizes recent and classical studies on fatigue behavior of spot welded joints primarily in steel sheets. The studies presented pertain to fatigue testing, fatigue life modeling and prediction, and fatigue-related fracture. Fatigue testing and life and failure mechanisms of spot welded joints are reported for most modern steels such as mild steel, high strength low alloy steels, dual phase steels, transformation-induced plasticity steels, recovery annealed steels and martensitic steels. The effect of fatigue test coupon types and loading conditions are also discussed. Various numerical models for fatigue life prediction, such as nominal stress approach, structural (hot spot) stress approach, equivalent structural stress approach, fracture mechanics (crack propagation) approach and local notch stress/strain approach are reviewed. The effect of residual stress and random loading is discussed. The need for future development of spot welded joints/structures analysis and testing is addressed.

Key words: fatigue assessment, fatigue fracture, fatigue life prediction, fatigue testing, random fatigue, steel spot welds.

4.1 Introduction

Spot welding is a popular joining method in thin-sheet metal manufacturing, especially in the automotive industry. Although some other fusion welding methods, such as laser beam welding and gas metal arc welding, as well as non-thermal joining approaches, such as riveting, bolting and adhesive bonding, are being used in automotive manufacturing nowadays, spot welding still remains the most important joining method owing to its low cost and high robustness. Typically, a car body contains a few thousand spot welds. Therefore, the mechanical strength and long-term performance of these spot welds significantly affect the safety and reliability of an automobile structure.

A schematic spot welding setup is shown in Fig. 4.1. Application of the appropriate squeezing force results in the formation of a contact interface between the two work pieces or sheets (pre-squeezing cycle). Then a high

65
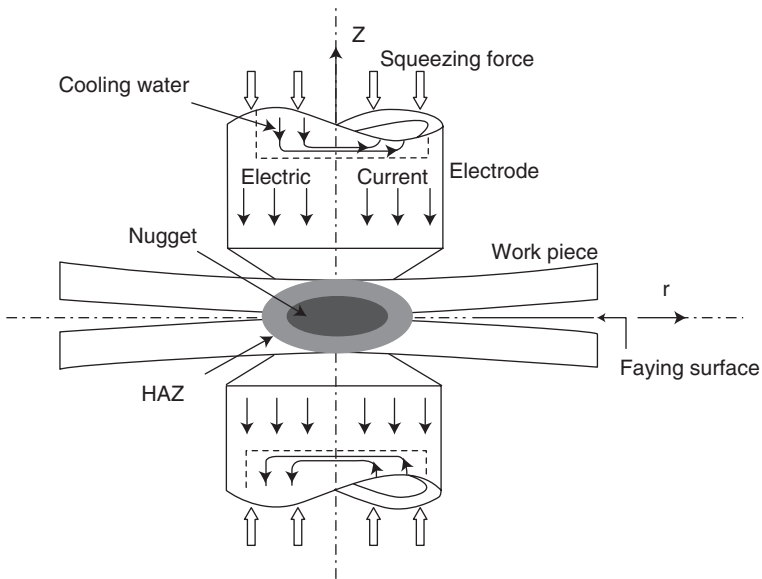
4.1 Schematic of spot welding (HAZ is the heat affected zone).

electric current is passed, which generates localized melting of the metal sheets between the electrodes (welding cycle). When the electric current is turned off, molten metal cools down and solidifies under the pressure of the electrodes, along with water cooling, leading to the formation of a spot weld nugget (holding and cooling cycle). The electrodes are then retracted and the welded joint is allowed to cool down naturally. This method of spot weld fabrication is generally known as the automated method. The spot weld created has an indented surface caused by the pressure applied through the electrodes. A circumferential notch is also created when a spot weld forms between the two metal sheets.[1]

Further, when the welded region cools down, residual stresses are generated owing to the rapid-cooling induced local heterogeneous thermal gradient, heterogeneous thermoplastic deformation (straining) and some phase transformation induced by plastic deformation (i.e. phase transformation-induced deformation). The complex welded joint shape in conjunction with the residual stress state produces a multiaxial stress state in the weld even if subjected to a uniaxial in-plane loading. Thus, the spot welding process involves a complex coupling between thermal, electrical, physical and chemical processes, which makes it difficult to model accurately.

Generally, all the mechanical components in the structure, such as an automobile or a railroad car, experience cyclic or fatigue loading. It has
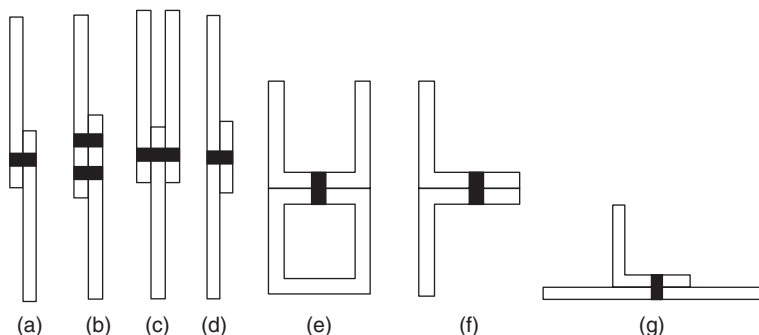
4.2 Spot welded specimens: (a) single face tensile shear specimen, (b) two spot tensile shear specimen, (c) double face tensile shear specimen, (d) through tension specimen, (e) cross tension specimen in cross shape, (f) peel specimen as double angle specimen or coach peel specimen and (g) peel tension specimen as angle to plate variant.

been observed that the unique state of stress in and around a spot weld typically causes about 80% of the failures in an automobile to occur around the spot welds and only about 5% failures occur in the sheet metal away from the welds.[2,3] This reality makes the understanding of fatigue failure, its prevention and reliable analytical modeling, experimental assessment and validation of numerical models, the primary requirement for reliable design of spot-welded structures. Study of fatigue failures in spot welds is an active area of investigation as is borne out by many publications listed in this chapter.

Fatigue failure of a spot weld is typically assessed experimentally through the use of several different types of specimens, as shown in Fig. 4.2. Among these specimens the single face tensile shear specimen and the coach peel specimen are the most commonly used. In addition there are other specimens, such as the modified tensile shear, H-Peel, H-shear and double flange shear specimens.[4,5]

The typical dimensions of the more commonly used single face tensile shear and coach peel specimen are shown in Fig. 4.3.

The types of fatigue failure observed in spot welded sheets are shown in Fig. 4.4.

4.2   Experimental study of fatigue behavior of spot welds

The quality of spot welds depends on a host of factors, such as parent sheet material composition and its temperature-dependent physical and

(a)

35 mm

39 mm

Tab

45 mm

217 mm

(b)

39 mm

155 mm

29 mm
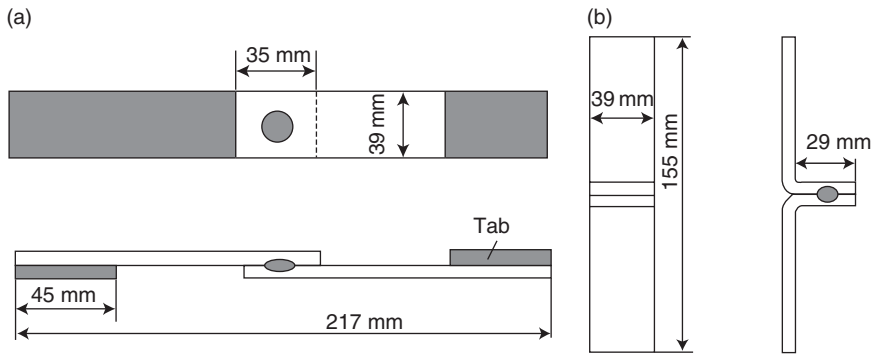
4.3 Dimensions of (a) tensile shear and (b) coach peel spot-welded specimens.

RB
(Round button)

OB
(Oval button)

HB
(Hollow button)

Unfused area

CB
(Crescent button)

OB
(Regular button)

DB
(Double button)

PIF
(Partial interfacial fracture)

Interfacial fracture

Weld button

Weld nugget

FIF
(Full interfacial fracture)

Interfacial fracture

Weld nugget

NF
(No fusion)
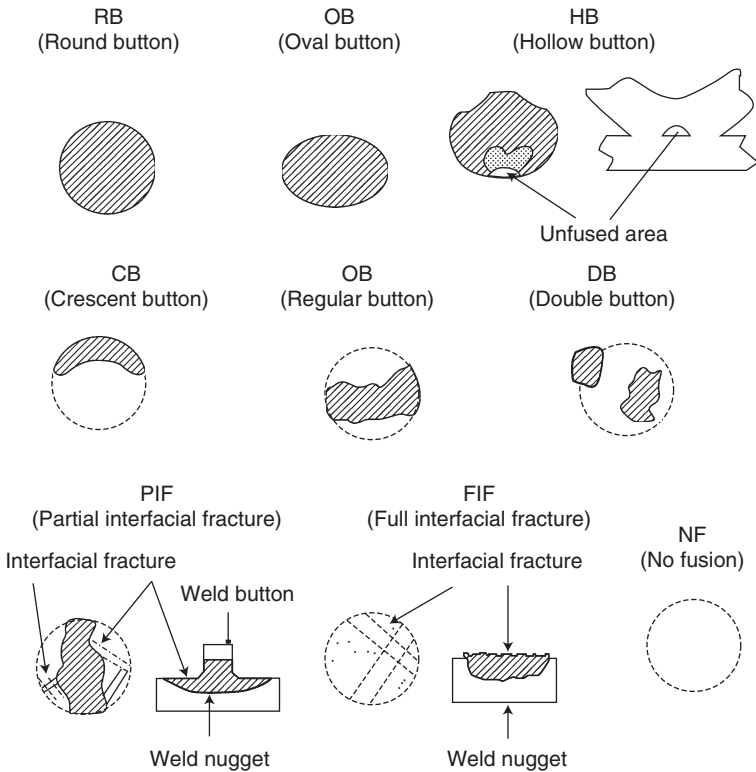
4.4 Fracture or pull-out mode in spot-welded sheets.

mechanical properties, welding parameters including welding current, electrode force, electrode movement as a function of time, squeezing, welding and holding cycle times, contact resistance, electrical and mechanical characteristics of the welding machine, and so on. Owing to the large number of factors affecting the quality of a spot weld in terms of its nugget size, weld penetration, weld indentation, microstructure and hardness in the heat affected zone and fusion zone (nugget), as well as the internal weld stress state, it is often difficult to model accurately the stress state in the weld under different loading conditions and the subsequent fatigue failure modes and durability of the weld.[6–9] Hence it is imperative to perform sufficient experimental tests in conjunction with numerical modeling to generate static and fatigue data for reliable design of spot welded structures. Static mechanical properties of spot welded joints[10–23] and numerical models predicting the stress state and deformation behavior under static loading of spot welds have been extensively studied. Details can be found in the references provided and will not be further elaborated in this chapter.

Several experimental investigations[24–32] have been conducted to develop fatigue design data for spot welded sheet steel structures. One of the most comprehensive reports on these efforts is given by Bonnen *et al.*,[3] the result of a combination of several independent investigations at the University of Missouri at Columbia, Westmoreland Mechanical Testing & Research Lab, Mittal Steel, the University of Michigan at Dearborn, Ford Motor Company, Daimler-Chrysler Corporation and General Motors Corporation. Currently, the most used steels in automotive structures are mild steel (IF, CQSK, DQSK), high strength low alloy steels (HSLA), dual phase steels (DP), transformation-induced plasticity steels (TRIP), recovery annealed (RA) steels and martensitic steels (MS). Boron steels are ultra high strength steels and are also being actively researched and beginning to be used in automobile body frames. Variations in the carbon and manganese content, along with the mechanical properties of yield strength and ultimate strength, of all the above-mentioned steels are provided in Table 4.1.

The fatigue test results under constant amplitude sinusoidal loading are shown in Fig. 4.5.[3] All samples used nominally 1.60 mm steel sheets accept for HSLA340 and Boron with 1.78 mm thickness, CQSK with 1.74 mm and RA830 with 1.39 mm thickness.

The above displayed results indicate that the base metal strength has no influence on the fatigue behavior of the spot weld as all the tensile shear data fall within a narrow band with little scatter.[33] The coach peel data show greater scatter, which is normally expected from such specimens as the moment arm becomes smaller with increasing load. The thickness of the sheets does affect the fatigue performance, which increases with increasing thickness. It may be noted that HSLA340 spot welds exhibit the highest fatigue performance in both the tensile shear and coach peel bands of the

Table 4.1 Material composition and tensile strength of sheet steels

	IF-GI	CQSK	DQSK-GI	HSLA340-GI	DP600-GI	DP800-GA	DP980-Bare	TRIP600-Bare	TRIP600-EG	RA830-GI	MS1300-Bare	Boron-Bare
C (wt%)	0.005	0.047	0.0037	0.0594	0.080	0.118	0.201	0.101	0.091	0.055	0.1839	0.233
Mn (wt%)	0.187	0.202	0.109	0.378	1.740	1.913	0.468	1.470	1.450	1.206	0.445	1.194
YS (MPa)	178	156	170	370	432	414	702	421	510	901	1156	1237
UTS (MPa)	306	350	308	448	671	782	1057	672	839	895	1156	1382

Gl: galvanized, GA: galvanneal, EG: electro-galvanized.

○	DQSK-R0.1
●	DQSK-R0.3
○	CQSK-R0.1
●	CQSK-R0.3
○	IF-R0.1
●	IF-R0.3
□	HSLA340-R0.1
■	HSLA340-R0.3
△	DP600-R0.1
▲	DP600-R0.3
△	DP800-R0.1
▲	DP800-R0.3
△	DP980-R0.1
▲	DP980-R0.3
×	TRIP600-R0.1
×	TRIP600-R0.3
○	TRIP800-R0.1
●	TRIP800-R0.3
+	RA830-R0.1
+	RA830-R0.3
✳	MS1300-R0.1
✳	MS1300-R0.3
◇	Boron-R0.1
◆	Boron-R0.3
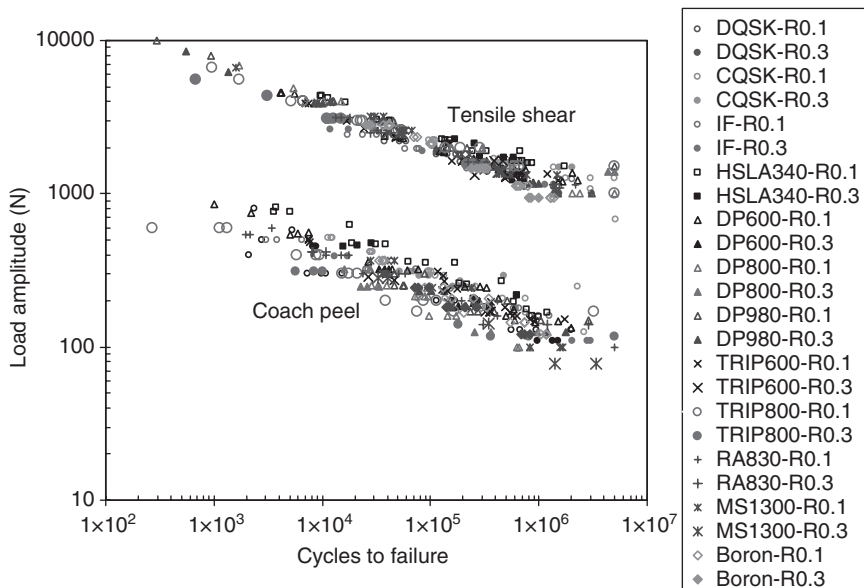
4.5 Fatigue life of various spot welded steel sheets. Average nugget diameter is 7 mm. Labels ending in 0.1 and 0.3 indicate *R* = 0.1 and *R* = 0.3, respectively.

fatigue data. Lastly, there is a minimal effect of the mean stress (through the R-ratio) on fatigue life. The effect of the width of the specimens made from high strength steels was investigated by Long and Khanna.[24] Fatigue tests were conducted with wide tensile shear samples of 125 mm width compared to the conventional width of 39 mm for DP600 and HSLA340 materials and no difference was found in the fatigue performance.

4.3   Micro-hardness measurements in spot welds

Hardness is the property of a metal which gives it the ability to resist being permanently deformed when a load is applied. For materials with inhomogeneity, fine microstructure and multiple phases, macro-hardness measurements will typically result in high variability and will not be able to identify individual phase features. This is where micro-hardness measurements are most appropriate. Micro-hardness is generally determined by forcing an indenter such as a Vickers or Knoop indenter into the surface of the material under low loads of 15 to 1000 gf (0.147 to 9.806 N).[34] The micro-indentations are so small that they must be measured with a microscope. These tests are capable of determining the hardness of different micro-constituents within a structure or of measuring steep hardness gradients such as those encountered in welds.

Micro-hardness tests were conducted along the centerline on a plane at half thickness of a spot-weld for each of the materials using a Vickers pyramidal indenter at a load of 300 g. Figure 4.6 shows the micro-hardness variation for the materials examined, with a distance from 0 to 3.5 mm representing the weld nugget, 3.5 mm to about 4.2 mm the heat affected zone (HAZ) and beyond 4.5 mm the base metal. It can be seen from Fig. 4.6 that the DP600 GI spot weld has the highest hardness of about 420 HV in the weld nugget and 250 HV in the base metal, followed by TRIP600 with about 400 HV in the weld nugget and 220 HV in the base metal and HSLA340Y GI has a hardness of 320 HV in the weld nugget and 160 HV in the base metal. It has been observed that DP600 GI shows some softening during high load and low cycle fatigue tests, while HSLA340Y GI samples showed more significant softening in the spot nugget and in the HAZ region. This behavior is similar to that reported in a previous study.[35,36] The low load and high cycle tests for all three materials did not show any significant softening or hardening effect.

Figure 4.7 shows the micro-hardness changes in a CQSK steel spot weld when subjected to fatigue loading. High cycle fatigue produces strain softening, but the results from low and medium cycle fatigue loading do not show any definite trend in softening or hardening behavior based on the limited tests conducted thus far.

Figure 4.8 shows the micro-hardness changes in a boron steel spot weld when subjected to fatigue loading. In general, fatigue loading tends to produce a small strain softening effect in boron steel spot welds.

4.4   Fracture modes and microstructure in spot welds

Spot welding of a pair of steel sheets results in a nugget formation that has a microstructure consisting of the weld nugget and a heat affected zone (HAZ), as shown in Fig. 4.9.

Two primary modes of failure in spot welds are weld button pull-out and interfacial fracture. The factors influencing weld failure modes are: type of loading condition, that is shear or tensile, stiffness of the weldment area and the loading rate. The loading mode and stiffness of the weldment affect the magnitudes of shear and tensile loading components on the weld. Interfacial fracture can occur if the shear loading component is high or if the weld's shear strength is low, or both. Tensile-shear and twisting loads tend to produce interfacial fracture compared to peel or cross-tension loading. The alloy content of the steel and the resulting microstructure of the weld nugget and HAZ and weld defects such as shrinkage voids can also make a major contribution to interfacial fracture. Geometric considerations such as sheet thickness and displacement constraint can also influence interfacial fracture. For example, tensile shear loading of a thick sheet specimen or
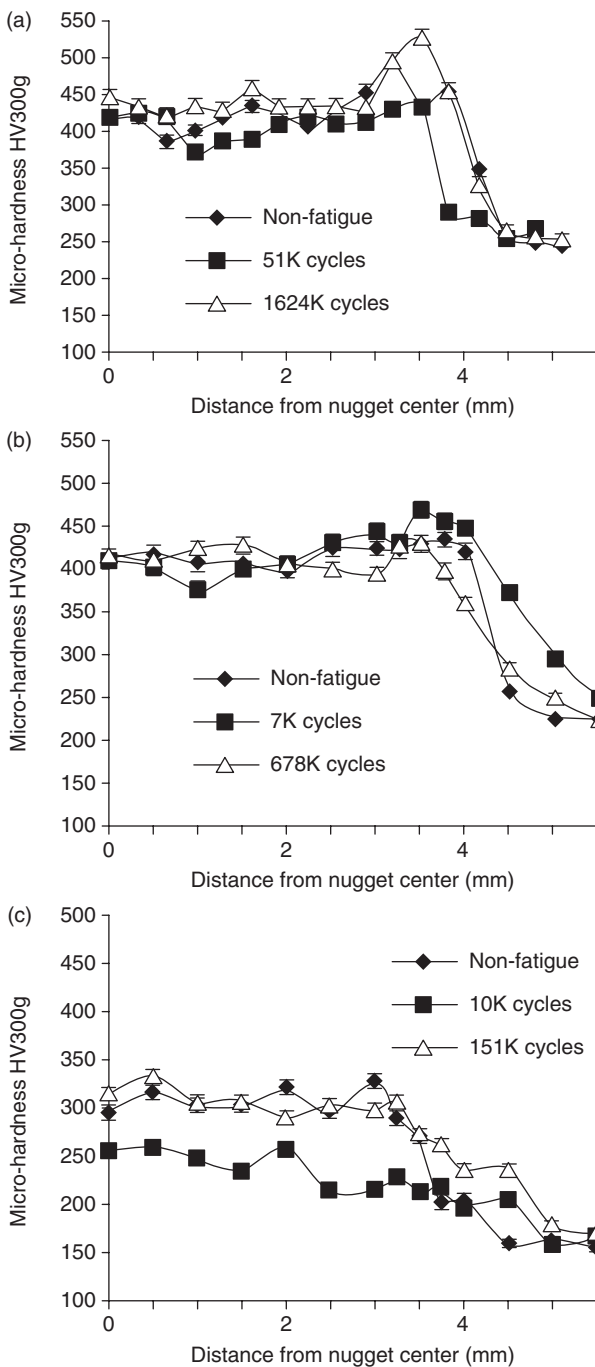
4.6 Micro-hardness variation in the half-thickness plane of (a) DP600 GI, (b) TRIP600 and (c) HSLA340Y GI spot-welded samples as a function of number of cycles to fatigue failure.
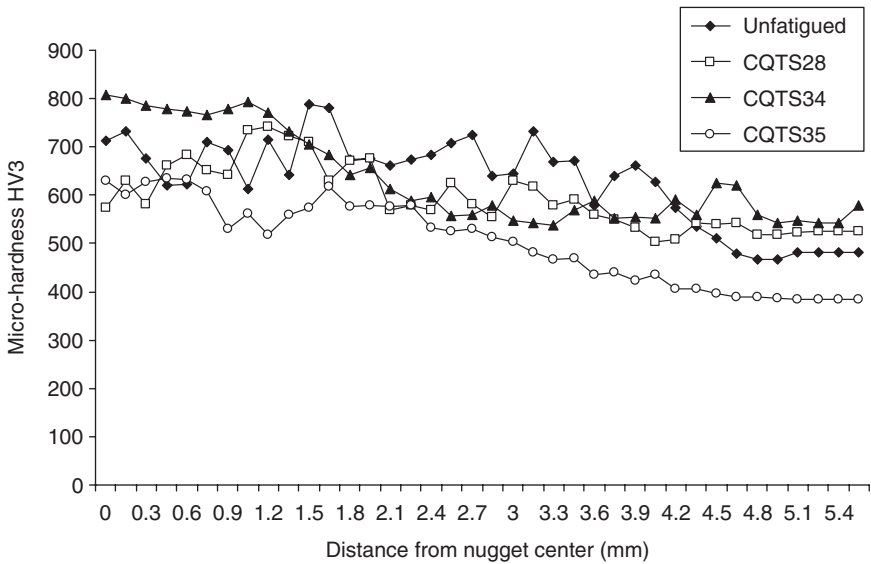
4.7 Micro-hardness variation in the half-thickness plane of the nugget, where sample 28 has 258 524 cycles to failure, sample 34 has 12 508 cycles to failure and sample 35 has 2 597 754 cycles to failure.
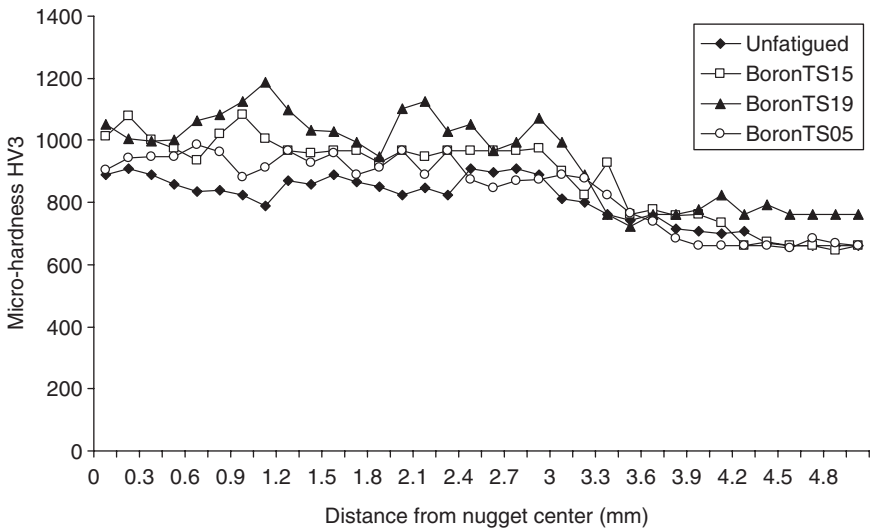
4.8 Micro-hardness variation in the half-thickness plane of the nugget, where sample 15 has 616 000 cycles to failure, sample 19 has 1 375 000 cycles to failure and sample 05 has 36 900 cycles to failure.

600 µm
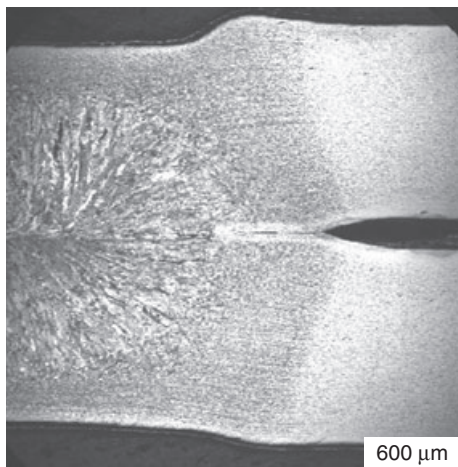
4.9 Cross-sectional view of the microstructure in a typical spot-weld, only half of the weld-nugget is shown for clarity.

(a)   (b)
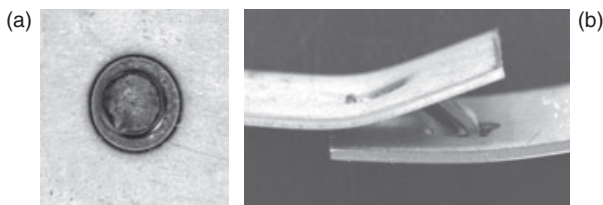
4.10 (a) An interfacial fracture and (b) button pull-out failure mode in a spot weld.

thinner very high strength steel specimen would result in a high stiffness specimen, which when loaded in tensile shear will cause a large shear component in the weld and thus interfacial fracture may result. Conversely, in a weldment with low stiffness, a relatively larger rotation will result in a weld button pull-out if the weld's tensile strength is low. A high rate of loading may produce interfacial fracture in a spot weld that might otherwise fail in the button pull-out mode under quasi-static or low frequency fatigue loading. A typical interfacial fracture and button pull-out mode in a spot weld specimen is shown in Fig. 4.10.

In advanced high strength steels (AHSS), the force required to produce a complete weld button pull-out failure has been found to be proportional to the tensile strength and thickness of the base metal sheet, and the diameter of the weld. The force producing an interfacial weld fracture was related to the fracture toughness of the weld, sheet thickness and weld
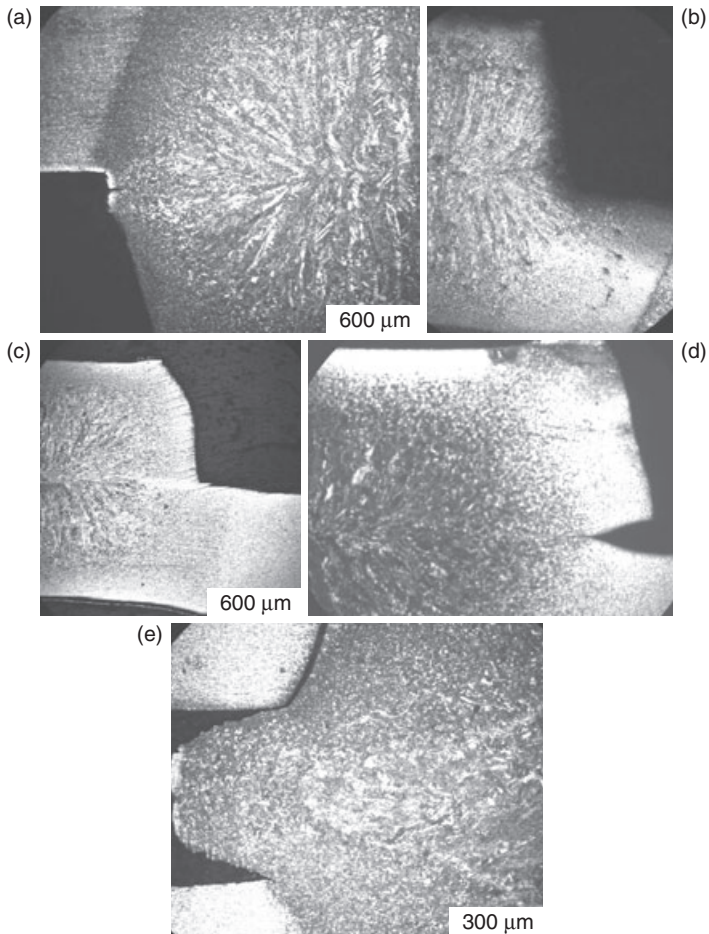
4.11 Fatigue cracking behavior with respect to the microstructure of spot welds in various steels: (a) DP600, (b) Boron, (c) HSLA, (d) CQSK, (e) TRIP.

diameter.[37] In high strength steels, there is a critical sheet thickness above which the expected failure mode could make the transition from pullout to interfacial fracture. In addition, as the strength of the steel increases, the fracture toughness of the weld required to avoid interfacial fracture must also increase.

Microstructures and fatigue crack surface morphologies for several steel spot welds are shown in Fig. 4.11. It has been found that, at high load, a fatigue crack in tensile shear specimens tends to propagate along the faying surface (work pieces interface), into the weld nugget for a short distance and then propagates perpendicular to the interface to the sheet outer

surface leading to a complete fracture, as shown in Fig. 4.11(a) and (b) for DP600 and Boron, respectively. While under low load, the fatigue crack propagates directly perpendicular to the faying interface from the heat affected zone (HAZ) until complete fracture, as shown in Fig. 4.11(c) and (d) for HSLA and CQSK, respectively. However, in the case of TRIP tensile shear specimens, it was found that a 'tongue' formed at the faying surface around the spot nugget as shown in Fig. 4.11(e). This tongue forms owing to the use of high current intensity and high squeeze force during welding of TRIP steels and is usually the location for initiation of a fatigue crack.[26]

4.5   Random loading fatigue test in spot welds

Even though in real life automobiles are subjected to variable amplitude or random fatigue loading, most of the testing is conducted under constant amplitude. Variable amplitude fatigue of spot welds has been studied by a few researchers.[38–42] Results from a variable amplitude fatigue testing regimen of tensile shear and coach peel samples made from various steel sheets was conducted by the authors. The base history selected for random load fatigue testing was the bending channel of the SAE grapple-skidder history (available at http://fde.uwaterloo.ca/Fde/Loads/Skidder/skidder. html). The history was mean shifted to bring the lowest load to 0 N and the maximum peak was scaled to 1000 N. The unedited history contains 198 886 reversals (a reversal is a single load peak or valley), as shown in Fig. 4.12, and to facilitate completion of testing in a reasonable time, all load excursions less than one-quarter of the fatigue limit were removed, resulting in a history containing 7744 reversals for tensile shear and 10 958 reversals for coach peel. Figure 4.13 shows the shorter of the two histories for tensile shear samples; the longer history for coach peel samples has the same appearance.
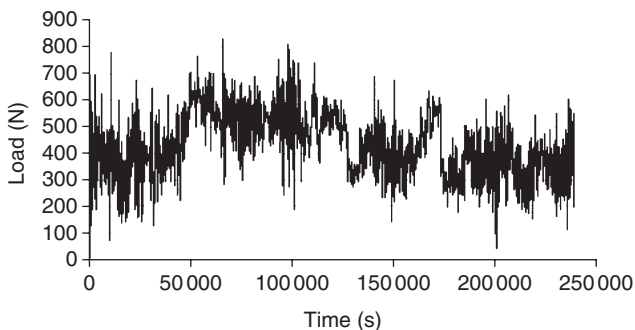
4.12 Part of the random loading history.
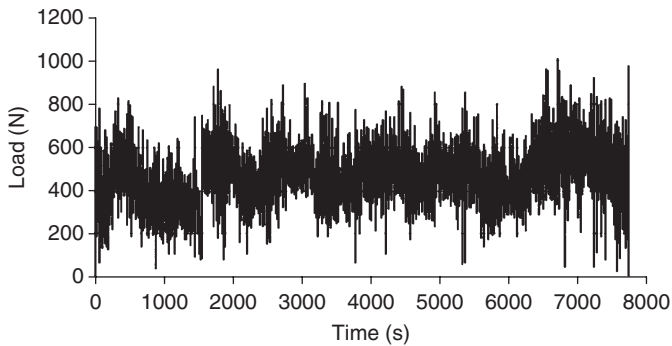
4.13 Condensed fatigue history for tensile shear samples.

Table 4.2 Spectrum loading fatigue tests for DP600 GI and HSLA340Y GI samples

Specimen type	Scale	Cycles to failure				
		DP600 GI	HSLA340Y GI	Boron Bare	CQSK	IF-GI
Tensile shear	X11	187 158	296 909	472 972	210 524	
		195 489	328 110	462 839	234 197	
	X12					26 343
						12 421
	X6	1 591 074	3 443 103	2 248 819	2 278 317	1 001 077
		2 035 769	3 500 000 (run out)	2 276 131	1 535 704	875 704
Coach peel	X1.8	184 087	397 935	142 864	298 567	unavailable
		295 268	464 585	65 154	259 494	
	X1.0	1 883 017	1 930 433	3 253 845	827 249	2 881 954
		2 636 914	2 285 532	2 229 526	1 001 339	2 772 374

Random loading fatigue test results are shown in Table 4.2. It can be seen that DP600 GI has a much lower fatigue strength compared to HSLA340Y GI and Boron steel for tensile-shear specimens and a comparable life for coach peel specimens. However, for coach peel samples, HSLA alloy shows the best fatigue performance. The fatigue response of spot welds under random loading is different from the results obtained with constant amplitude load fatigue tests, in which DP600 GI and HSLA340Y GI have very similar fatigue strengths. Thus spot welded steel joints have a different response to the load interaction and sequence effects during random loading, which cannot be described by the Miner linear damage rule.[24,43] This indicates that the fatigue failure mechanism under random loading is

different from that under constant amplitude loading for spot welded joints. McMahon *et al.*[44] found that spot welded low carbon and high strength steel joints have shorter crack initiation cycles under variable amplitude (random) fatigue loading than under constant amplitude loading.

4.6   Effect of residual stress on fatigue behavior of spot welded joints

Residual stresses are defined as self-equilibrating stresses existing in materials under uniform temperature conditions without external loading. Being self-equilibrating, residual stresses produce zero resultant force and resultant moment. Residual stresses can be generated during manufacturing processes, such as machining, forming, heat-treating, surface coating and welding. Welding-induced residual stresses are generated by non-uniform cooling, inhomogeneity and non-simultaneous phase transformations and elastoplastic deformation gradients.

It is important to characterize the residual stress state in a spot weld as it can affect the operating performance both favorably and adversely. For example, it is well known that, in general, compressive residual stress has a beneficial effect on the fatigue life, crack propagation and stress corrosion of materials, whereas tensile residual stress reduces their performance. In the context of spot welds, it is not unambiguously clear how the residual stress affects the durability of spot welded joints under constant amplitude and random fatigue loading, especially when more and more new steels (such as high strength and advanced high strength steels) with thinner thickness are being used in the automotive industries and other industries; spot welding is a low cost and rapidly automated manufacturing process, which makes it cost-prohibitive to implement additional processes to modify the residual stress states in the spot welds.

Several studies have investigated the effect of residual stress on the fatigue life of spot welded joints, as has been reviewed by Khanna and Long.[45] Lawrence *et al.*[46] performed a series of fatigue tests on spot welded low-carbon and HSLA steel joints. They tried to improve the fatigue properties of spot welded joints by controlling the residual stress, weld geometry, increasing base metal strength and steel sheet surface condition. They observed that tensile shear spot welded specimens show significant fatigue strength improvement by treatments which either reduce the tensile residual stress or induce compressed residual stress. The improvement through modification of weld geometry was smaller than that obtained by residual stress control.

The state of surface condition (bare or galvanized) was found to have little influence on the fatigue strength. The methods used to control residual stress included control of welding conditions (such as using non-circular

cross-section electrodes to generate elliptical weld nugget, adding temper welding cycle or changing current slope, introducing forging force after welding, etc.), using post-weld treatment (such as pre-load specimens up to 75% of their tensile strength before fatigue testing) and using different coining (squeezing) treatments, hydrostatic coining and hydrodynamic coining, in which a large compressive force was applied to the electrode impression of the spot weld.

The residual stress was measured using an X-ray method in as-welded and post-weld treated welds. It was found that the pre-loading treatment can remarkably improve fatigue strength of spot welded joint by producing very large compressive residual stress at the site of crack initiation (outside of nugget area); the improvement is more pronounced for the higher strength steels and under low amplitude fatigue loading. The effect of coining treatment were even more significant than that of pre-loading method. It was determined that a higher coining force produces more improvement in the fatigue life of specimens and that a flat punch tip is not as effective as curved punch tips. They also found that the elliptical nugget spot welds did not show a longer fatigue life than the circular nugget spot welds that have the same cross-sectional area. Changing the weld current slope and adding a temper cycle did not cause a noticeable improvement in fatigue life. The addition of a forging force immediately after the welding cycle increased the fatigue life of HSLA welds by about 40%, while applying a forge force after the nugget cools down only showed a small effect. A fatigue life prediction model of a spot welded joint based on experimental observation was also created in their study, which considered the effect of residual stress.

Anastassiou *et al.*[47] found that residual stress in the spot welded joint increases with the thermal cycle intensity, but expulsion and post-heating reduces residual stress. They also found that residual stress affects the fatigue strength of the joint in a high cycle fatigue regime of around 10^7 cycles (or at low fatigue load). The fatigue strength of a spot weld made above the expulsion limit exhibited a higher fatigue strength compared to those without expulsion. However, Anastassiou *et al.* found that the post-heating cycle does not improve fatigue strength because, even though the post-heating cycle decreases the residual stress level, it decreases the ultimate strength of the material at the same time. In addition, they found that the weld geometry (spot nugget edge notch radius) has a more significant effect on fatigue strength than residual stress under high fatigue life (10^7 cycles), which is believed to be due to the high stress concentration in the circumferential notch in the joint produced by different welding conditions.

Spitsen *et al.*[48] performed post-weld cold working (similar to coining) on a low carbon steel spot welded joint using a special shaped indenter after

welding to produce beneficial residual stresses. They found that cold working increases the fatigue strength of low carbon steel spot welded joint by about 67% under high cycle (4×10^6) fatigue, with no effect on the static tensile shear strength of the joint. Chang et al.[49] also investigated the effect of forging applied immediately after the welding cycle on the residual stress distribution in spot welded aluminum alloy sheets. Finite element analysis was used to determine the residual stress distribution with and without forging treatment. They suggested that forging significantly reduces the residual stress in the HAZ area but no noticeable reduction could be found in the spot nugget edge area. Fatigue tests were carried out and showed that fatigue strength of spot welded aluminum alloys improved and the crack always initiated in the nugget edge area, compared to initiation at both the nugget edge and HAZ area for the unforged welded specimens.

Bae et al.[50] used a three-dimensional non-linear finite element model to simulate residual stress distribution in spot welded cold-rolled steel sheets. The simulated results were compared with stresses measured using X-rays and good agreement was found. This three-dimensional (3D) specimen model was then used to conduct stress analysis of a tensile shear spot welded joint under fatigue loading. Once the stress distribution in the joint was determined, a fatigue strength assessment approach that considered the residual stress was also proposed. In this approach, Goodman's equation was modified by adding residual stress as shown in Equation [4.1]:

$$\sigma_{\alpha-res} = S_e \left\{ 1 - \frac{\sigma_{mean} + \sigma_{res}}{S_{ut}} \right\} \qquad [4.1]$$

where σ_{a-res} is the stress amplitude that considers residual stress and σ_{res} is welding residual stress at the edge of the weld nugget, S_e is the fully reversed fatigue strength, σ_{mean} is the mean stress, and S_{ut} is the material's ultimate strength. Then a σ_{a-res} versus N_f curve, where N_f is the total fatigue life, was used to substitute the conventional σ_a versus N_f curve for spot welded sample fatigue assessment, which showed good agreement with the experimental results. This model showed that the fatigue strength of spot welds with consideration of residual stress is about 25% lower than those without consideration of residual stress.

Yang et al.[51] used a three-dimensional thermal elastic–plastic finite element model (not a fully coupled electrical–thermal–metallurgical–mechanical model) to determine residual stress in a spot weld and to obtain the multiaxial stress state in the weld under applied fatigue load. Corresponding to this mutiaxial stress state, an equivalent uniaxial stress S_N was obtained using Sine's method as shown in Equation [4.2]:

$$\left[(\sigma_1 - \sigma_2)^2 + (\sigma_2 - \sigma_3)^2 + (\sigma_3 - \sigma_1)^2 \right]^{1/2} + m(\sigma_{m1} + \sigma_{m2} + \sigma_{m3}) = \sqrt{2}\, \frac{S_N}{K} \quad [4.2]$$

where σ_1, σ_2, σ_3 are alternating stresses, σ_{m1}, σ_{m2}, σ_{m3} are mean stresses, m is the coefficient of mean stress influence, K is the fatigue notch factor and S_N is the uniaxial fully reversed fatigue stress that is expected to give the same life as the multiaxial stress state for smooth specimens. Alternating stress and mean stress can be obtained by finite element analysis. Then the fatigue life can be estimated through the fatigue S–N curve under uniaxial loading for smooth mild steel specimens:[52]

$$S = 10^C N^b \text{ for } 10^3 < N < 10^6 \qquad [4.3]$$

where S is the alternative stress, N is the number of cycles to failure and the material constants C and b can be determined by empirical equations.[51] A good agreement between experimentally obtained fatigue life and estimated fatigue life of a spot-welded joint with consideration of residual stress was reached. This model also shows a significant fatigue life improvement if the residual stress is not present in the spot-welded joint. The authors also suggested that the fatigue failure location is the heat affected zone (HAZ) because the highest tensile residual stress occurs in this region. But the authors did not specify the failure location difference between high cycle fatigue and low cycle fatigue.

Khanna *et al.*[53] have determined the residual stress variation in steel spot welds using the moiré interferometric method and hole drilling by developing the optical equivalent of a three-element strain gauge rosette. The displacement field near the edge of the blind hole was measured in the x-, y- and 45°-directions using the corresponding moiré fringe patterns and the biaxial residual stress field was calculated. They measured residual stress state in several different spot weld configurations such as single face tensile shear, double face tensile shear and through tension specimens. The residual stress distributions measured using the optical method agree with other experimental and modeling studies. In general, the residual stress is tensile in the spot nugget and a maximum at the center and rapidly decreases towards the edge of the nugget. The residual stress outside the nugget was not measured in this study. They also found that, under low cycle fatigue loading with the fatigue tests being stopped after 10 000 cycles, the residual stress redistributed by significantly decreasing at the nugget center and increasing at the nugget edge area, as shown in Table 4.3.

It should be noted that residual stress is not the only factor that affects the fatigue strength of a spot-welded joint; other factors, such as weld geometry and materials properties are also important. For example, it is interesting to note that increasing the base metal strength does not improve the fatigue strength.[46,47] For instance, spot-welded high strength low alloy (HSLA) steels and advanced high strength steels (AHSS) do not exhibit higher fatigue strengths than those of normal mild steel. One reason is that the increase in strength is offset by the higher tensile residual stress in the

Table 4.3 Residual stress in spot welds and the effect of fatigue loading

Specimen type	Loading conditions	Principal residual stress at weld center		Principal residual stress at weld edge	
		σ_1 (MPa)	σ_2 (MPa)	σ_1 (MPa)	σ_2 (MPa)
SFTS	None (as welded)	237 (215–255)	165 (130–200)	75 (61–82)	45 (40–51)
SFTS	10 000 cycles 1 200/155 N	163 (157–169)	85 (61–109)		
Through tension	10 000 cycles 2 070/245 N	143 (111–173)	40 (33–46)	183 (166–201)	102 (98–106)
DFTS	None (as welded)	242 (236–247)	122 (78–165)	69 (69–88)	23 (9–36)
DFTS	1 000 cycles 4 450/465 N	170 (154–200)	84 (48–108)	141 (105–178)	51 (30–72)

SFTS: single face tensile shear spot weld specimen.
DFTS: double face tensile shear spot weld specimen.
Numbers in parentheses represent the range of residual stress valves for different specimens.

joint. In addition, none of the above-mentioned studies relate the microscopic deformation mechanisms in the spot weld to various fatigue loading conditions which could affect the residual stress state.

The exact mechanism for redistribution of the residual stress state in a spot weld under fatigue loading is not yet well understood. It can be speculated that a combination of the external loading (magnitude and number of fatigue cycles), stress concentration at the notch around the weld nugget, plastic flow and the movement of dislocations from the center of the weld to the edge of the welded zone will contribute to the observed residual stress state and the fracture behavior. A preliminary study by Long and Khanna[25,26] has found that, after being subjected to high fatigue loads, the dislocation density in the spot nugget edge is much higher than that in nugget center area, which indicates that significant plastic deformation occurred at the edge of spot nugget during fatigue testing as shown in Figs 4.14 and 4.15. Under low fatigue load, dislocation density is quite low in both the edge and center area of a spot nugget.

Some studies[3,4] suggest that residual stress does not affect the fatigue life, based on the assumption that the presence of residual stress is equivalent to a mean stress effect. This conclusion is based on the experimental observations that varying the *R*-ratio from low ($R = 0.1$) to higher values ($R = 0.3$) does not produce any changes in the fatigue life and the *R*-ratio is a measure of the mean stress. Thus, the issue of how to model the effect of

(a)   (b)

200 nm   0.2 μm
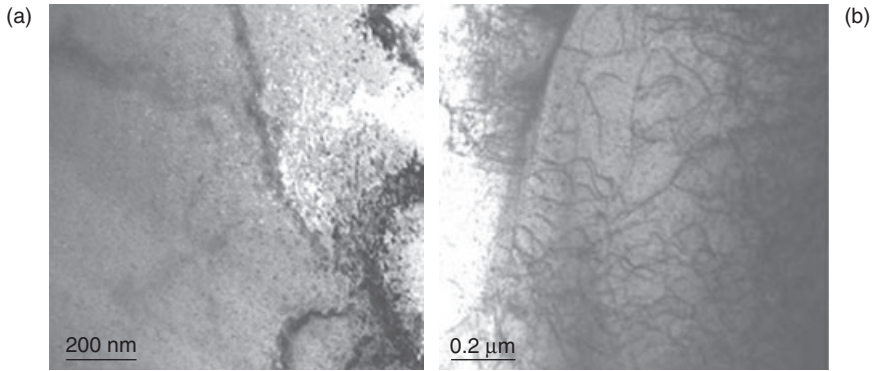
4.14 Microstructure and dislocation structure at the edge of (a) an as-welded spot weld specimen and (b) a spot weld specimen after 1000 cycles of fatigue loading with a maximum load of 3.3 kN and a load ratio *R* = 0.1.

(a)   (b)

100 nm   0.2 μm
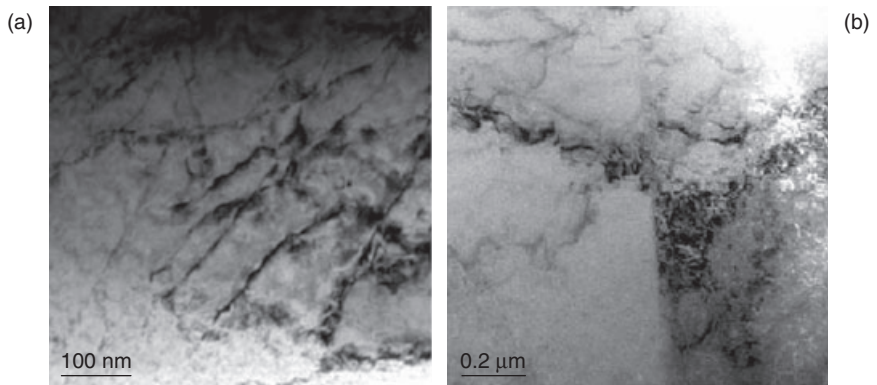
4.15 Microstructure and dislocation structure at the center of (a) an as-welded spot weld specimen and (b) a spot weld specimen after 1000 cycles of fatigue loading with a maximum load of 3.3 kN and a load ratio *R* = 0.1.

residual stress state on spot weld fatigue life still needs further investigation and clarification.

4.7 Models for fatigue life prediction of spot welded joints

Various analytical and numerical fatigue life prediction models have been proposed in the literature. The analytical methods are the stress–life method,

strain–life method or the fracture mechanics method. The stress-based approaches are based on the assumption that the elastic stress state controls the fatigue behavior and it is generally an accurate representation of high cycle fatigue, while it is not accurate for low cycle fatigue applications. These typically involve phenomenological relations between stress amplitude, mean stress, mechanical properties such as ultimate strength and yield strength, and fully reversed fatigue strength. Several existing models are the modified Goodman, Gerber, Soderberg, Morrow and ASME-elliptic.[54–56] If the structure is subjected to loading conditions resulting in multiaxial stress states, equivalent uniaxial alternating and mean stresses can be used in fatigue calculations for proportional loading cases. For non-proportional loading cases, more sophisticated numerical methods should be used, such as the critical plane method.

The strain–life approach considers the plastic deformation that may occur during fatigue loading. This method accounts for localized yielding, which is often the case in metal components displaying low cycle fatigue (that is a relatively short fatigue life). The stress–life approach utilizes average or nominal stresses, while the strain–life approach uses local stresses and strains. Some of the common strain-based approaches are the Coffin–Mason relationship, Morrow's mean stress approach and the Smith, Watson and Topper Parameter.[55–57] Neither of these two approaches includes analysis of crack growth, while the fracture mechanics approach does through formulations such as the Paris law, Walker equation and Forman equation.

The above-mentioned stress–life and strain–life approaches have been applied to spot weld fatigue.[4] Ertas *et al.*[4] found better correlation with experimental data using the strain–life approach compared to the stress–life approach, which was overly conservative. It is believed that the stress–life approach is not a good representation since it does not account for localized plastic deformation in the circumferential notch region. Among the strain–life approaches, the Coffin–Mason model captured the fatigue life trend better than the Morrow mean stress model. This difference could contribute to the fact that the Coffin–Mason approach does not take into account the mean stress, while the Morrow approach does account for the mean stress. Hence Ertas *et al.*[4] concluded that the mean stress effects in spot weld fatigue, for example caused by residual stress or external loading, are not important.

Bonnen *et al.*[3] evaluated the performance of five fatigue damage parameters in the context of large fatigue data sets consisting of hundreds of tests. One parameter by Swellam[57] is based on a fracture mechanics approach, while the other four by Rupp *et al.*,[58] Sheppard,[59] Dong[60] and Kang[61] are based on a structural stress approach. One of the evaluation methods used by Bonnen *et al.*[3] is to estimate the specimen life using the parameter and

compare the estimate against the actual fatigue life observed in laboratory tests. Figure 4.16 shows a plot for each parameter of the observed specimen life versus that predicted by the parameter. All parameters resulted in a reasonable fit to the experimental data for these specimen geometries, with the Swellam's parameter showing the most scatter among them.

4.8   Fatigue life assessment approaches for spot welds

Traditionally, the fatigue life of a spot welded joint is estimated by using specimen nominal stress along with the experimentally obtained *S–N* curve.[62] This approach does not require much calculation, but it is not accurate and therefore is difficult to use for complex structures. With increasing processing speed of computer hardware and capabilities of finite element analysis (FEA) software, numerical simulation of fatigue behavior and prediction of fatigue life of spot-welded joints has improved significantly in the last few years.

There are several approaches that can be used to predict the fatigue life of a spot-welded joint. These approaches are summarized below with some brief explanations. More detailed analysis and discussion can be found in the related references.

4.8.1   Nominal stress approach

The nominal stress approach is the most traditional method for predicting the fatigue life of a structural component. However, this method is sometimes very difficult to apply in real spot-welded structures because it is hard to determine the nominal stress in complicated structures. In addition, the local stress concentration due to the spot weld geometry and a circumferential notch is not considered in this approach. The nominal stress approach lends itself to simple calculations but also has the least accuracy.

4.8.2   Structural (hot spot) stress approach

Structural (hot spot[1]) stress is a type of geometrical stress, which describes the macrostructural behavior of welded structure but without considering the local notch effect, that is no local stress/strain concentration is considered. A hot spot is a potential location of fatigue initiation. The structure stress is used to compare with hot spot stress (or structural stress) *S–N* curve in order to assess the fatigue life of the structure. Because the stress
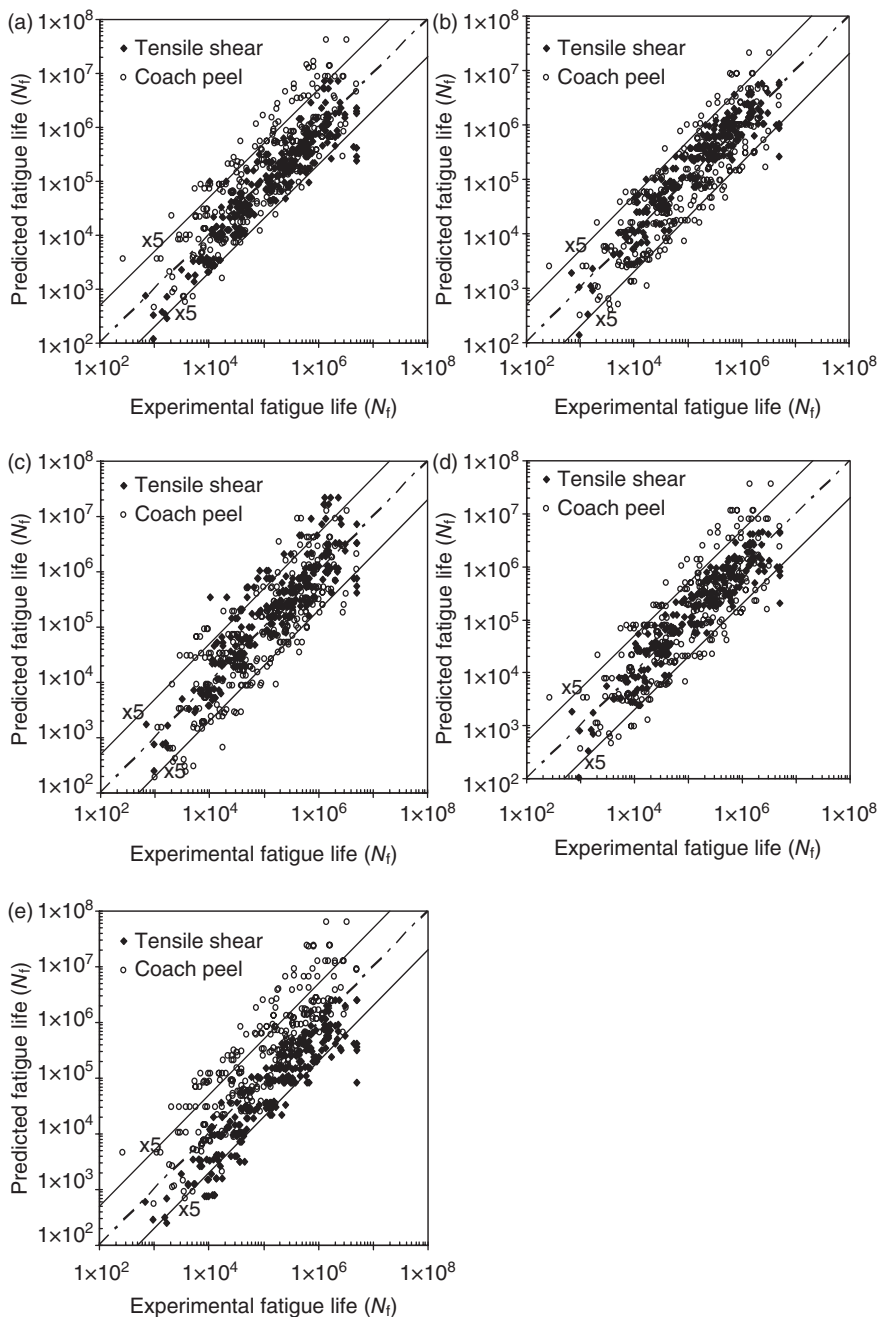
4.16 Predicted vs. experimental fatigue lives for (a) Rupp *et al.*,[58] (b) Sheppard,[54] (c) Dong,[60] (d) Kang,[61] and (e) Swellam[57] spot-weld fatigue parameters.[3]

concentration caused by a change in structural geometry is considered, it is more accurate than the nominal stress approach. Structural stress can be obtained either by numerical analyses, such as the finite element analysis (FEA) or experimental measurement.[58,62–65] In the FEA method, the structural stresses of spot-welded joints are calculated based on the cross-sectional forces and moments of the simplified spot weld model using beam, shell and plate theory. The detailed calculations and the assumptions of the geometry model, force and moments may be slightly different in different structural stress approaches, which has been discussed and compared with real experimental results by Bonner *et al.*[3] However, owing to the accuracy of hot spot stress (structural stress) measurement in experiment, as well as the effects of mesh size on the accuracy of the hot stress finite element calculation, improvement in the hot spot structural stress approach is limited compared to the traditional nominal stress approach.

4.8.3   Equivalent structural stress approach

Based on elementary structure stress analysis, Dong and his coworkers[60,66,67] proposed a modified structural stress approach, the equivalent structures stress method. There are also some other forms of equivalent structure stress approaches, which will be discussed in the next section. The equivalent structural stress approach is a mesh insensitive method, which eliminates the effects of different mesh size on the stress concentration calculation in finite element analysis in the hot spot stress approach or the local notch stress approach (discussed in the next section). The equivalent structural stress consists of a bending stress component and a membrane stress component at the location of interest (as shown in Equation [4.4]), usually at the stress concentration area such as the the toe of the weld:

$$\sigma_s = \sigma_b + \sigma_m \qquad\qquad [4.4]$$

where σ_s is structural stress, σ_b is bending stress component and σ_m is membrane stress component. The local stress diagram together with the definition of structure stress in a spot-welded structure are shown in Fig. 4.17 and
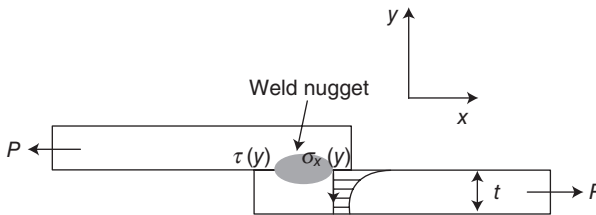
4.17 Local shear and normal stress in the thickness direction at the edge of a spot nugget.[68,69]
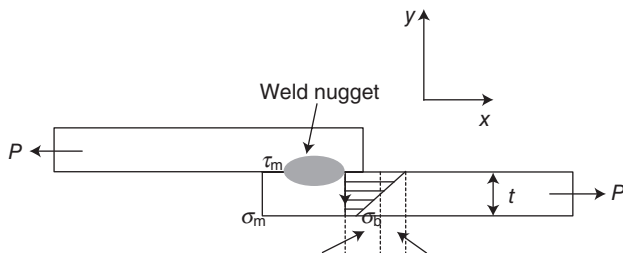
4.18 Structure stress definition at the edge of a spot nugget.[68,69]

Fig. 4.18, respectively.[68,69] Stress components σ_b and σ_m can be obtained by imposing equilibrium condition equations between the location of interest and a reference location a certain distance away. The stress state at the reference location is normally more uniform owing to its distance from the stress concentration area and it can be obtained consistently by regular finite element analysis. Since the equivalent structural stress at the local stress concentration area is obtained by elementary structure mechanics theory during post-processing of the regular finite element output, it is not affected by the mesh size and therefore eliminates the mesh size effects in the traditional structure stress (hot spot stress) approach. After recalculating the existing large amount of well-documented *S–N* fatigue data, Dong and his coworkers found that *S–N* curves for different types of welded joint can be reduced to one equivalent structure stress *S–N* curve, the so-called master curve. The application of the equivalent structural stress approach to fatigue life prediction a of spot-welded joint will be discussed in the following section.

4.8.4   Fracture mechanics (crack propagation) approach

It is very common to treat the imperfections in the weld, such as defects and inclusions, as cracks, which is a relatively conservative way of dealing with them. The fatigue initiation stage, therefore, can be neglected and the fatigue propagation stage can be studied by fracture mechanics and the Paris law. For a spot-welded joint, the circumferential edge of the spot nugget is naturally a sharp notch, which can be treated as a crack. In order to estimate the remaining fatigue life using the fracture mechanics approach, the crack initiation length, final length and crack stress intensity factor are needed. The stress intensity factor can be obtained from finite element analysis or a weight functions approach.[63,70–80] It should be noted that the fracture mechanics approach deals with the fatigue crack propagation stage, which is believed to be the majority of the fatigue life in welded joints, especially in joints with defects. However, some researchers suggested that

there is still a crack initiation stage for welded joints with defects or notches.[63,81] Therefore, sometimes, the fracture mechanics approach is combined with other approaches which can estimate the crack initiation stage, such as the following local notch strain approach, to predict more accurately the fatigue life of welded structures.

### 4.8.5   Local notch stress/strain approach

The local notch stress approach mainly focuses on the stress concentration in the notch area in order to obtain the effective stress in the notch area. The stress concentration factor is normally calculated by elastic analysis. However, if the notch is too sharp, the effect of materials microstructure (such as plastic deformation in the plastic zone) has to be considered and the effective stress concentration factor should be used.[63] The notch stress approach also needs to be used with S–N curves and it is most effective for high cycle fatigue assessment because the load amplitude is low and stress is the dominant control factor in the fatigue process, while for strain controlled low cycle fatigue, the local notch strain approach should be used. The notch strain approach can assess the fatigue strength of the material or structure up to the technical crack initiation stage. In this approach, strain is the fatigue assessing criterion.

4.9   Current status of fatigue life prediction of welded materials or structures

Almost all of above fatigue assessment approaches can be used for spot-welded joint fatigue life prediction. However, for a complex welded structure, such as a typical automotive body structure with 3000–5000 spot welds, it is very difficult to conduct fatigue life assessment using a complicated assessing procedure or using complicated 3D finite element models. Generally, there are some important issues that should be considered for fatigue life prediction of multi-spot-welded structures. First, a simple finite element model has to be chosen but it should capture the load redistribution and stiffness change in the welded structure owing to different degrees of fatigue damage in the multiple spots. Second, an appropriate fatigue life prediction method has to be determined to incorporate with finite element analysis. Many efforts have been made in these two areas to create accurate fatigue life prediction methodologies, which are briefly summarized below.

4.9.1   Development and application of equivalent structure stress approach

Rahman and coworkers[68–69] used simple shell/plate, beam and rigid elements to model the spot-welded structure, as shown in Fig. 4.19. This model
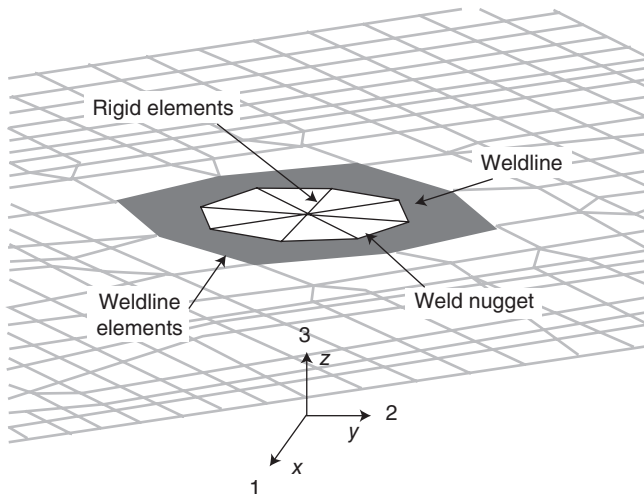
4.19 Finite element mesh of a spot-welded structure.[75,83]

can be used for large-scale structures, such as an automobile, containing a large number of spot welds. They utilized Dong's equivalent structure stress approach[60,66,67] to predict the fatigue life of the spot-welded tensile shear and coach peel specimens. However, no experimental data were provided to support their results.

Salvini and coworkers[84–86] conducted a series of spot-welded structure fatigue analyses. The structure they modeled is an H shape coach peel multi-spot-welded structure. Two finite element models, namely pure shell-beam model and shell-beam with a three-dimensional submodel, were compared in their analyses. They pointed out that there are two major drawbacks of the pure shell-beam model: (i) the stress field near the nugget edge is three-dimensional and cannot be modeled by shell elements and (ii) the global stiffness of the spot weld connections in a multi-spot-welded structure cannot be modeled by beam elements and the stiffness change caused by fatigue will affect the structure loading. On the other hand, it is not realistic to use all three-dimensional elements to model spot-welded structures. Therefore, they used coarse shell-beam elements to model the entire structure and used three-dimensional brick elements to model the spot nugget area. The fatigue life prediction approach they used is called the extrapolated radial stress (ERS) approach, which is a modification of regular structure stress approach developed by Radaj and Soegiharto.[87,88] and Rupp *et al.*[58] for spot-welded joint fatigue life prediction using the maximum radial stress around the sport core as the parameter governing damage.

ERS represents the maximum radial stress on the spot edge not considering stress concentration due to the notch effect, but it can be affected by a

change in local stiffness. Details of the ERS procedure can be found in Salvini and coworkers.[84–86] They tried to establish an ERS-*N* fatigue curve to assess the fatigue life of spot-welded structures. The method worked well with the tensile shear and coach-peel specimens according to experimental verification, but its extension to complex structures has yet to be verified. It should also be noted that another criterion for spot-welded joint fatigue life was proposed,[84] which uses the measurement of welded structure stiffness change, not the crack propagating through the work-piece nor the specimen's total failure. For complex spot-welded structures, this may be a good alternative for fatigue life measurement owing to the difficulties and uncertainties in measuring crack propagation during fatigue.

Kang[89] proposed another equivalent structural stress approach which was calculated at the edges of the spot weld nugget using forces and moments based on a von Mises equivalent stress equation:

$$\sigma_S^i = \frac{1}{\sqrt{2}} \left[\left(\sigma_x^i - \sigma_y^i \right)^2 + \left(\sigma_y^i - \sigma_z^i \right)^2 + \left(\sigma_z^i - \sigma_x^i \right)^2 + 6 \left(\left(\tau_{xy}^i \right)^2 + \left(\tau_{yz}^i \right)^2 + \left(\tau_{zx}^i \right)^2 \right) \right]^{1/2}$$

[4.5]

where σ_S^i is the equivalent structural stress at the edge of a spot weld in each sheet. Here, *i* is an index representing the top sheet ($i = 1$) or bottom sheet ($i = 2$) and *S* is an index representing equivalent stress. σ_x^i, σ_y^i and σ_z^i represent normal stresses in the *x*-, *y*- and *z*-directions on the top or bottom sheet, respectively. τ_x^i, τ_x^i and τ_x^i represent shear stresses in the *xy*, *yz* and *zx* planes on the top or bottom sheet, respectively.

Normal stresses and shears stresses can be calculated using the membrane load, bending load and axial load obtained from statics analysis, such as linear elastic finite element analysis using beam and shell elements in Kang's study. Then the maximum equivalent structure stress amplitude versus fatigue life curve (σ_S–*N*) was obtained to predict the fatigue life of a spot weld subjected to any loading conditions and geometry variations. The predicted results were in good agreement with experimental results from combined tension and shear loading specimens and simple shear loading specimens. This approach is very similar to Dong's equivalent approach, mentioned before. Again, this approach has not been verified against the large amount of existing fatigue testing data as indicated by Kang.[89]

4.9.2   Development and application of fracture mechanics approach

Pan and his coworkers have been focusing on the fracture mechanics approach in recent years.[74–82] They developed local stress intensity factor

solutions for spot welds under different loading conditions and specimen geometries by finite element analysis and analytical closed-form solutions. Some details have been discussed in Chapter 1. The new analytical stress intensity factor solutions provide detailed stress intensity factor solutions around the entire nugget circumference in various types of specimens. The new analytical solutions provide the size dependence of mode I stress intensity factor solutions for spot welds in various types of specimens allowing future consolidations of the fatigue test data to be obtained from specimens of different designs in the literature. The local stress intensity factors were used for crack growth predictions, which had very good agreement with experimental results.

Lee and Choi[90] proposed a *J* integral-based fatigue life prediction of spot-welded structure using a fracture mechanics approach. Three-dimensional solid elements were used in their model. Material properties in the heat affected zone (HAZ) were considered in the model. An effective *J* integral, J_e, expressed by the stress intensity factor (K) was correlated to fatigue life based on linear elastic fracture mechanics finite element analysis. The experimental test results from multi-spot-welded seat belt anchor specimens were in a good agreement with the finite element predictions.

4.9.3 Development and application of local notch stress/strain approach

Dincer *et al.*[91] compared five popular spot weld models, namely rigid beam–spot weld model, elastic beam–spot welded model, umbrella–spot-welded model, nine point contact–spot-welded model and the weld element CWELD in NASTRAN commercial finite element software. The fatigue life estimation for each spot model is completed using the software FLAP developed by the Ford Motor Company. The FLAP software utilizes the Smith–Watson–Topper fatigue life prediction, which is like a local notch strain approach. After comparison with experimental results, it was found that the nine point contact model gives the most accurate results.

Gowhari-Anaraki *et al.*[92] studied three different finite element models describing a single spot-welded joint of sheet metals under pure-tension low cycle fatigue loading. In their models, three-dimensional solid elements were used to model the plate, while the spot weld nugget was modeled by three types of elements: 3D solid elements, beam elements with a rigid link and one rigid link element. The fatigue prediction theory was based on the local notch stress approach.

Elastic and elastic–plastic finite element analyses were conducted. In elastic analysis, the stress concentration factor (SCF) was studied for correlation to geometry factors, such as nugget diameter, work-piece thickness, work-piece width and length. In the elastic–plastic analysis for low cycle

fatigue testing, notch–stress–strain conversion rules, such as by Neuber,[93] Hardrath and Ohman,[94] linear and intermediate rules,[95] were used to estimate the local strains.

Deng and coworkers studied the detail of a 3D finite element model of spot weld[96] and four different simplified spot-welded joint finite element models under different loading conditions.[97] They found that most of the simplified spot weld joint models can lead to good accuracy in terms of structural stiffness when a joint is subjected to tension, out-of-plane torsion and out-of-plane bending. But under in-plane torsion and in-plane shear conditions, large errors can be introduced even with fine meshes. Unfortunately, no direct fatigue analysis was carried out in their study.

4.10   Conclusions

This chapter has discussed the fatigue behavior of spot-welded joints for different steels under different loading conditions. Both experimentally reported spot weld fatigue life and various methods for fatigue life predictions are summarized. Fatigue loading and consequent deformation and failure are very common among most structures, especially mobile structures such as automobiles. Automobiles are fabricated primarily by a spot welding processes, although other forms of welding such as friction stir spot welding, metal inert gas welding (MIG) and laser welding are also being investigated. Although most of the fatigue tests are conducted under constant amplitude loading, variable amplitude loading or random loading is predominant during actual use. Variable amplitude fatigue test data is more difficult to obtain and hence is not as popularly reported compared to constant amplitude fatigue data. The development of a standard variable amplitude fatigue test is possibly in order. Materials property data of the weld nugget and the heat-affected zone must be determined by using miniature samples for mechanical testing, or micro-mechanical testing or non-destructive means and these actual data should be used to model the mechanical behavior of the spot welded specimens. The effect of residual stress in the spot weld is an important parameter that can affect the fatigue performance of the spot weld. However, there are still different schools of thoughts in this regard and thus more experimental testing and modeling effort are needed to bring clarity to the effect of residual stress in spot weld fatigue behavior.

With regard to analytical and numerical modeling of a spot-welded structure under load, the equivalent structural stress approach, which was developed from the traditional structural stress approach, has attracted the most attention and applications in recent years owing to its simplicity and relative robustness as a single fatigue assessment parameter. It has the most potential to be used in large and complex multi-spot-welded structures, like an

automobile. However, the accuracy and ease of use of the equivalent structural stress approach still needs improvement. Other methods, such as the fracture mechanics approach and the local notch stress/strain approach are still of interest. As mentioned earlier, the fracture mechanics approach may need to be combined with the local notch strain approach in order to model both fatigue crack initiation and propagation. The local notch stress approach has a significant dependence on structure geometry, which may not be easy or accurate for use in large and complex welded structures.

4.11   Acknowledgements

4.12   References

1 ZHANG, H. and SENKARA, J. (2006), *Resistance Welding: Fundamentals and Applications*, CRC Press Francis and Taylor, Boca Raton, Florida, USA.

2 DI FANT-JAECKELS, H. and GALTIER, A. (2001), 'Fatigue lifetime prediction models for spot welded structures', *Rev. Metall/Cah. Inf. Tech.*, **1**, 83–95.

3 BONNEN, J. J. F., AGRAWAL, H., AMAYA, M. A., IYENGAR, R. M., KANG, H. T., KHOSROVANEH, A. K., LINK, T. M., SHIH, H., WALP, M. and YAN, B. (2006), '*Fatigue of advanced high strength steel spot-welds*', *2006 SAE World Congress*, Detroit, Michigan, SAE Technical paper Series, 2006-01-0978.

4 ERTAS, A. H., VARDAR, O., SONMEZ, F. O. and SOLIM, Z. (2009), 'Measurement and assessment of fatigue life of spot weld joints', *J. Eng. Mater. Technol.*, **131**, 011011-1-11.

5 SONSINO, C. M., RADAJ, D. and FRICKE, W. (2007), 'Overview on local concepts for the fatigue of welded structures', *Welding in the World*, **51**, 23–44.

6 KANG, H., BONNEN, J. J. F. and IYENGAR, R. M. (2007), 'Sources of variability in the fatigue strength of spot welded specimens', *Materials Science and Technology Conference, MS and T'07 – Exploring Structure, Processing, and Applications Across Multiple Materials Systems*, Detroit, Michigan, 16–20 September, **1**, 201–19.

7 YANG, H.-G., ZHANG, Y.-S., LAI, X.-M. and CHEN, G.-L. (2008), 'Relationship between quality and attributes of elliptical spot welds of high strength steel', *J. Shanghai Jiaotong University*, **13**(6), 734–8.

8 ZHOU, M., ZHANG, H. and HU, S. J. (2003), 'Relationships between quality and attributes of spot welds', *Welding Rese.*, 72s–77s.

9 YANG, L., SAMALA, P. R., LIU, S., LONG, K. W. and LEE, Y. L. (2005), Measurement of nugget size of spot weld by digital shearography, *Proceedings of SPIE–The International Society for Optical Engineering and Optical Diagnostics*, San Diego, California, 3–4 August, **5880**, 1–8.

10 SUN, X., STEPHENS, E. V. and KHALEEL, M. D. (2008), 'Effects of fusion zone size and failure mode on peak load and energy absorption of advanced high strength steel spot welds under lap shear loading conditions', *Eng. Failure Anal.*, **15**, 356–67.

11 RADAJ, D. (1996), 'Theory of forces and stresses in spot-welded overlap joints', *Arch. Appl. Mech.*, **67**(1–2), 22–34.

12 RADAJ, D. and ZHENG, M. (1990), 'Local stress parameters at the weld spot of various specimens', *Eng. Fracture Mech.*, **37**(5), 933–51.

13 RADAJ, D. and ZHANG, S. (1995), 'Geometrically nonlinear behavior of spot welded joints in tensile and compressive shear loading', *Eng. Fracture Mech.*, **51**(2), 281–94.

14 SATONAKA, S., KALEDA, K. and OKAMOTO, S. (2004), 'Prediction of tensile shear strength of spot welds based on fracture modes', *Welding in the World*, **48**(5–6), 39–45.

15 DARWISH, S. M. and AL-SAMHAN, A. M. (2004), 'Peel and shear strength of spot-welded and weld-bonded dissimilar thickness joints', *J. Mater Process. Techno.*, **147**(1), 51–9.

16 LIN, S. H., PAN, J., TYAN, T. and PRASAD, P. (2003), 'A general failure criterion for spot welds under combined loading conditions', *Int. J. Solids and Structures*, **40**(21), 5539–64.

17 ZHANG, S. (2001), 'Approximate stress formulas for a multiaxial spot weld specimen', *Welding J.*, **80**(8), 201s-203s.

18 SATONAKA, S., HATTA, K. I., KIYOTA, H., TSUKAMOTO, K. and SHIRAKAWA, H. (2003), 'Tensile shear strength of spot welded structures: prediction of strength and effect of weld position', *Welding Res. Board*, **49**(2), 36–41.

19 CHAO, Y. J. (2003), 'Ultimate strength and failure mechanism of resistance spot weld subjected to tensile, shear, or combined tensile/shear loads', *J. Eng. Mater. Technol.*, **125**, 125–32.

20 WUNG, P., WALSH, T., OURCHANE, A., STEWART, W. and JIE, M. (2001), 'Failure of spot welds under in-plane static loading', *Experimental Mech.*, **41**(1), 100–06.

21 RADAJ, D. and ZHANG, S. (1998), 'Weld spot force evaluation with dented sheet material', *Eng. Fracture Mech.*, **61**(5–6), 673–8.

22 LEE, Y.-L., WEHNER, T. J., LU, M.-W., MORRISETT, T. W. and PAKALNINS, E. (1998), 'Ultimate strength of resistance spot welds subjected to combined tension and shear', *J. Testing and Evaluation*, **26**(3), 213–19.

23 ZUNIGA, S. and SHEPPARD, S. D. (1997), *Resistance Spot Weld Failure Loads and Modes in Overload Conditions*, ASTM Special Publication, V1296, ASTM, Conshohocken, PA, USA, 469–89.

24 LONG, X. and KHANNA, S. K. (2008), 'Fatigue performance of spot welded and weld bonded high strength steel sheets', Special Issue on Spot Welding, *J. Sci. Technol. Welding and Joining*, **13**(3), 241–7.

25 LONG, X., KHANNA, S. K. and ALLARD, L. (2007), 'Effect of fatigue loading and residual stress on microscopic deformation mechanisms in a spot welded joint', *Mater. Sci. Eng. A*, **454–455**, 398–406.

26 LONG, X. and KHANNA, S. K. (2007), 'Fatigue properties and failure characterization of spot welded high strength steel sheet', *Int. J. Fatigue*, **29**(5), 879–86.

27 XU, J., ZHANG, Y. S., XINMIN, L. and CHEN, G. L. (2008), 'Experimental investigation of fatigue performance of spot-welded dual phase steel sheets', *Sci. Technol. Welding and Joining*, **13**(8), 726–31.

28 LANCIOTTI, A. and POLESE, C. (2008), 'Fatigue crack propagation in tensile shear stainless steel spot welded specimens', *Fatigue Fracture Eng. Mater. Structures*, **31**(1), 76–84.

29 CHOI, B.-H., JOO, D.-H. and SONG, S.-H. (2007), 'Observation and prediction of fatigue behavior of spot welded joints with triple thin steel plates under tensile shear loading', *Int. J. Fatigue*, **29**(4), 620–27

30 RATHBUN, R. W., MATLOCK, D. K. and SPEER, J. G. (2003), 'Fatigue behavior of spot welded high strength sheet steels', *Welding J.*, **28**(8), 207s–218s.

31 BARKEY, M. E., KANG, H. and LEE, Y. L. (2001), 'Failure modes of single resistance spot welded joints subjected to combined fatigue loading', *Int. J. Mater. Product Technol.*, **16**(6–7), 510–527.

32 MA, C., CHEN, D. L., BHOLE, S. D., BOURDEAU, G., LEE, A. and BIRO, E. (2008), 'Microstructure and fracture characteristics of spot welded DP600 steel', *Mater. Sci. Eng. A*, **485**, 333–46.

33 YAN, B., LALAM, S. H. and ZHU, H. (2005), *Performance Evaluation of GMAW Welds for Four Advanced High Strength Steels*, SAE International Paper No. 2005-01-0904.

34 ASTM STANDARD E384-99E1 (1999), *Standard Test Method for Microhardness of Materials*, ASTM International, West Conshohocken, PA, USA.

35 FREDRIKSSON, K., MELANDER, A. and HEDMAN, M. (1988), 'Influence of prestraining and ageing on fatigue properties of high-strength sheet steel', *Int. J. Fatigue*, **10**(3), 139–51.

36 ASTM STANDARD E-1049. (1998), 'Cycle counting for fatigue analysis', *Annual Book of ASTM Standards*, V03.01, ASTM, West Conshohocken, PA, 693.

37 RADAKOVIC, D. J. and TUMULURU, M. (2008), 'Predicting resistance spot weld failure modes in shear tension tests of advanced high-strength automotive steels', *Welding J.*, **87**(4), 96s–105s.

38 OVERBEEKE, J. L. (1979), 'Random fatigue of spot welded lap joints', *Metal Construction*, **11**, 81–8.

39 BARSOM, J. M., DAVIDSON, J. A. and IMHOLF, E. J., JR. (1985), *Fatigue Behavior of Spot Welds Under Variable Amplitude Load History*, SAE Technical paper 850369.

40 E-SAYED, M. E. M., STAWIARSKI, T. and FRUTIGER, R. (1996), 'Fatigue analysis of spot-welded joints under variable amplitude load history', *Eng. Fracture Mech.*, **55**, 363–9.

41 PAN, N., SHEPPARD, S. D. and WIDMANN, J. M. (1999), *Fatigue and Fracture Mechanics: 29th Volume*, ASTM STP 1332, T. L. Panontin and S. D. Sheppard (eds), ASTM, West Conshohocken, PA, USA, 802–14.

42 HENRYSSON, H. F. (2002), 'Variable amplitude fatigue of spot welds', *Fatigue Fracture Eng. Mater. Structures*, **25**(12), 1187–97.

43 SAKUMA, Y., KIMURA, N., ITAMI, A. *et al.* (1995), *Next-Generation High-Strength Sheet Steel Utilizing Transformation-Induced Plasticity (TRIP) Effect*, Nippon Steel Technical Report, No.64, 20–5.

44 MCMAHON, J. C., SMITH, G. A. and LAWRENCE, F. V. (1990), *Fatigue and Fracture Testing of Weldments*, H. I. McHenry and J. M. Potter (eds), ASTM STP 1058, ASTM, West Conshohocken, PA, USA, 47–77.

45 KHANNA, S. K. and LONG, X. (2008), 'Review: residual stresses in resistance spot welded steel joints', *Sci. Technol. Welding and Joining*, **13**(3), 278–88.

46 LAWRENCE, F. V., CORTEN, H. T. and MCMAHON, J. C. (1993), 'Study I–the effect of temper cycle, mechanical treatment, weld geometry and welding conditions on sheet spot weld fatigue resistance', *Welding Research Council Bulletin*, **384**, 1–49.

47 ANASTASSIOU, M. and BABBIT, M. L. (1990), 'Residual stresses and microstructure distribution in spot-welded steel sheets: relation with fatigue behavior', *Mater. Sci. Eng. A: Structural Materials: Properties, Microstructure and Processing*, **A125**(2), 141–56.

48 SPITSEN, R., KIM, D., FLINN, B., RAMULU, M. and EASTERBROOK, E. T. (2005), 'The effects of post-weld cold working processes on the fatigue strength of low carbon steel resistance spot welds', *Trans. ASME, J. Manufacturing Sci. Eng.*, **127**, 718–723.

49 CHANG, B. H., DU, D., SUI, B., ZHOU, Y., WANG, Z. and HEIDARZADEH, F. (2007), 'Effect of forging force on fatigue behavior of spot welded joints in aluminum alloy 5182', *J. Manufacturing Sci. Technol.*, **129**(1), 95–100.

50 BAE, D. H., SOHN, I. S. and HONG, J. K. (2003), 'Assessing the effects of residual stresses on the fatigue strength of spot welds', *Welding J.*, **82**(1), 18/S–23/S.

51 YANG, Y. S., SON, K. J., CHO, S. K., HONG, S. G., KIM, S. K. and MO, K. H. (2001), 'Effect of residual stress on fatigue strength of resistance spot weldment', *Sci. Technol. Welding and Joining*, **6**, 397–401.

52 BANNANTINE, J. A., COMER, J. J. and HANDROCK, J. L. (1990), *Fundamentals of Metal Fatigue Analysis*, Prentice-Hall, London, 1–6.

53 KHANNA, S. K., HE, C. and AGRAWAL, H. N. (2001), 'Residual stress measurement in spot welds and the effect of fatigue loading on redistribution of stresses using high sensitivity moiré interferometry', *ASME J. Eng. Mater. Technol.*, **123**, 132–8.

54 BUDYNAS, R. G. and NISBETT, J. K. (2008), *Shigley's Mechanical Engineering Design*, 8th edition, McGraw Hill, Boston, MA, USA.

55 COLLINS, J. A. (1993), *Failure of Materials in Mechanical Design*, 2nd edition, Wiley Interscience, New York, USA.

56 DOWLING, N. E. (2006), *Mechanical Behavior of Materials: Engineering Methods for Deformation, Fracture and Fatigue*, 3rd edition, Prentice Hall, Upper Saddle River, New Jersey.

57 SWELLAM, M. H. (1991), *A Fatigue Design Parameter for Spot Welds*, PhD Thesis, The University of Illinois at Urbana-Champaign.

58 RUPP, A., STORZEL, K. and GRUBISIC, V. (1995), *Computer Aided Dimensioning of Spot-Welded Automotive Structures*, SAE Technical Report No. 950711, Detroit, Michigan.

59 SHEPPARD, S. D. (1996), 'Further refinement of a methodology for fatigue life estimation in resistance spot weld connections', *Advances in Fatigue Lifetime Prediction Techniques*, Volume 3, ASTM STP 1292, American Society for Testing and Materials, Philadelphia, 265–82.

60 DONG, P. (2001), 'A structural stress definition and numerical implementation for fatigue analysis of welded joints', *Int. J. Fatigue*, **23**, 865–76.

61 KANG, H. T. (2005), 'A fatigue damage parameter of spot welded joints under proportional loading', *Int. J. Automotive Technol.*, **6**(3), 285–91.

62 HOBBACHER, A. (1996), *Fatigue Design of Welded Joints and Components*, IIW doc. XIII-1539-96.

63 RADAJ, D. and SONSINO, C. M. (2006), *Fatigue Assessment of Welded Joints by Local Approaches*, 2nd edition, Woodhead Publishing, Cambridge, UK.

64 RADAJ, D. (1987), 'Hot spot stress concept for spot-welded joints', *Structural Design and Crack Worthiness of Automobiles*, Springer-Verlag, Berlin, pp.149–70.

65 SHEPPARD, S. D. (1996), 'Further refinement of a methodology for fatigue life estimation in resistance spot weld connections', *Advances in Fatigue Lifetime Prediction Techniques*, Volume 3, ASTM STP 1292, American Society for Testing and Materials, Philadelphia, 265–82.

66 DONG, P. and HONG, J. K. (2002), *CAE Weld Durability Prediction: a Robust Single Damage Parameter Approach*, SAE Technical Paper No. 2002–01–0151.

67 DONG, P. (2001), *A Robust Structural Stress Procedure for Characterizing Fatigue Behaviour of Welded Joints*, SAE Technical Paper. 2001-01-0086.

68 RAHMAN, M. M., BAKAR, R. A., NOOR, M. M., REJAB, M. R. M. and SANI, M. S. M. (2008), 'Fatigue life prediction of spot-welded structures: a finite element analysis approach', *European J. Sci. Res.*, **22**(3), 444–56.

69 RAHMAN, M. M., ROSLI, A. B., NOOR, M. M., SANI, M. S. M. and JULIE, J. M. (2009), 'Effect of spot diameter and sheets thickness of fatigue life of spot welded structure based on FEA approach', *Am. J. Appl. Sci.*, **6**, 137–42.

70 RADAJ, D. and ZHANG, S. (1991), 'Stress intensity factors for spot welds between plates of unequal thickness', *Eng. Fracture Mech.*, **39**, 391–413.

71 RADAJ, D. and ZHANG, S. (1991), 'Simplified formulae for stress intensity factors of spot welds', *Eng. Fracture Mech.*, **40**, 233–6.

72 RADAJ, D. and ZHANG, S. (1992), 'Stress intensity factors for spot welds between plates of dissimilar materials', *Eng. Fracture Mech.*, **42**, 407–26.

73 ZHANG, S. (2001), 'Fracture mechanics solutions to spot welds', *Int. J. Fatigue*, **112**, 247–71.

74 SHEPPARD, S. D. and STRANGE, M. (1992), 'Fatigue life estimation in resistance spot welds: initiation and early growth phase', *Fatigue Fracture Eng. Mater. Structures*, **15**, 531–9.

75 SHEPPARD, S. D. and PAN, N. (2003), 'Stress intensity factors in spot welds', *Eng. Fracture Mech.*, **70**, 671–84.

76 LIN, S. H., PAN, J., WUNG, P. and CHIANG, J. (2006), 'A fatigue crack growth model for spot welds under cyclic loading conditions', *Int. J. Fatigue*, **28**, 792–803.

77 WANG, D. A. and PAN, J. (2005), 'A computational study of local stress intensity factor solutions for kinked cracks near spot welds in lap-shear specimens', *Int. J. Solids and Structures*, **42**, 6277–98.

78 WANG, D. A., LIN, P. C. and PAN, J. (2005), 'Geometric functions of stress intensity factor solutions for spot welds in lap-shear specimens', *Int. J. Solids and Structures*, **42**, 6299–318.

79 LIN, P. C. and PAN, J. (2008), 'Closed-form structural stress and stress intensity factor solutions for spot welds in commonly used specimens', *Eng. Fracture Mech.*, **75**, 5187–206.

80 LIN, S. H., PAN, J., WUNG, P. and CHIANG, J. (2008), 'A fatigue crack growth model for spot welds under cyclic loading conditions', *Int. J. Solids and Structures*, **45**, 3996–4020.

81 LIN, P. C. and PAN, J. (2008), 'Closed-form structural stress and stress intensity factor solutions for spot welds under various types of loading conditions', *Int. J. Solids and Structures*, **45**, 3996–4020.

82 LIN, P. C., WANG, D. A. and PAN, J. (2007), 'Mode I stress intensity factor solutions for spot welds in lap-shear specimens', *Int. J. Solids and Structures*, **44**, 1013–1037.

83 DARCIS, P., LASSENT, T. and RECHO, N. (2006), 'Fatigue behavior of welded joints Part 2: Physical modeling of the fatigue process', **85**, 19s–26s.

84 SALVINI, P., SCARDECCHIA, E. and DEMOFONTI, G. (1997), 'A procedure for fatigue life prediction of spot welded joints', *Fatigue Fracture Eng. Mater. Structures*, **20**, 1117–1128.

85 VIVIO, F., FERRARI, G., SALVINI, P. and VULLO, V. (2002), 'Enforcing of an analytical solution of spot welds into finite element analysis for fatigue-life estimation', *Int. J. Computer Applications Technol.*, **15**, 218–229.

86 SALVINI, P., VIVIO, F. and VULLO, V. (2009), 'Fatigue life evaluation for multi-spot welded structures', *Int. J. Fatigue*, **31**, 122–129.

87 RADAJ, D. (1990), 'Structural stress, notch stress and stress intensity factor approach for assessment of fatigue strength of spot welded joints', *Welding in the World*, **28**(1–2), 29–39.

88 RADAJ, D. and SOEGIHARTO, S. (1990), 'Structural stress concentration at spot-welded joints: improved model, comparision of results, stress singularity', *Welding in the World*, **28**, 183–9.

89 KANG, H. T. (2007), 'Fatigue prediction of spot welded joints using equivalent structural stress', *Mater. Design*, **28**, 837–43.

90 LEE, H. and CHOI, J. (2004), 'Overload analysis and J_e-based fatigue life prediction of spot-welded auto seat belt anchors', *Fatigue Fracture Eng. Mater. Structures*, **27**, 245–51.

91 DINCER, S., CINAR, A., KEPENEK, D., ASURECILER, B., DURAN, E. T. and MUGAN, A. (2006), *A Comparative Study on the Finite Element Models for Spot Welds and Their Verification*, SAE Technical Paper Series, 2006-01-0590.

92 GOWHARI-ANARAKI, A., PIPELZADEH, M. K. and HARDY, S. J. (2002), 'Experimental and numerical analysis of low cycle fatigue of spot-welded joints under peel-tension loading', *Mecánica Computacional*, **XXI**, 786–804.

93 NEUBER, H. (1961), 'Theory of stress concentration for shear strained prismatical bodies with arbitary nonlinear stress–strain law', *J. Appl. Mech.*, **28**, 544–50.

94 HARDRATH, H. F. and OHMAN, L. (1953), *A Study of Elastic and Plastic Stress Concentration Factors due to Notches and Fillets in Flat Plates*, National Advisory Committee for Aeronautics, NACA report 1117, 213–22.

95 FUCHS, H. O. and STEPENS, R. I. (1980), *Metal Fatigue in Engineering*, J. Wiley and Sons, New York.

96 DENG, X., CHEN, W. and SHI, G. (2000), 'Three-dimensional fnite element analysis of the mechanical behavior of spot welds', *Finite Elements in Analysis and Design*, **35**, 17–39.

97 XU, S. and DENG, X. (2004), 'An evaluation of simplified finite element models for spot-welded joints', *Finite Elements in Analysis and Design*, **40**, 1175–94.

5

Non-destructive evaluation of spot-weld quality

B. GHAFFARI, Ford Motor Company, USA,
and G. MOZURKEWICH, Ford Motor Company
(retired), USA

Abstract: This chapter discusses non-destructive evaluation of spot welds, with emphasis on ultrasonic inspection of resistance spot welds in mild steel. Detection of stick welds and of small nuggets surrounded by a zinc corona are the principal challenges faced by resistance spot-weld inspection. The post-process single-element ultrasonic method is the most common inspection technique currently employed in manufacturing environments. Recent interest has centered on imaging techniques, which offer spatially resolved information and increased sensitivity, and on in-process inspection, which allows examination of the events that occur during the course of the welding process. These techniques are described and their strengths and weaknesses are discussed.

Key words: friction spot welding, in-process inspection, mild steel, non-destructive evaluation, non-destructive testing, resistance spot welding, spot welding, stick welds, ultrasonic spot welding, ultrasonic testing.

5.1   Introduction

Resistance spot welding of sheet metal has been a valuable manufacturing process for many decades, notably for producing vehicle bodies and enclosures. The speed, simplicity and low expense associated with this technique have helped enable rapid and cost-efficient assembly of sheet metal components in various manufacturing environments. Reliable operation of resistance spot welders, however, requires careful control of several variables, principally welding current, force and time. Allowing any of these parameters to wander outside optimal ranges results in production of unsatisfactory spot welds, diminishing the structural integrity and lifetime performance of the final products. For example, some of the squeak and rattle problems observed in older vehicles are related to degradation of spot welds under the typical mechanical loads experienced by vehicle bodies. Such problems adversely affect customer satisfaction and warranty costs and are of great concern to manufacturers.

101

Strict quality-control procedures are, therefore, employed in manufacturing plants to ensure production of satisfactory spot welds and to discover degradation rapidly in welding operations. One approach is to utilize a multitude of sensors to measure the factors that affect welding separately. Examples are provided by the various adaptive control methodologies, in which parameters such as welding current, dynamic resistance and electrode displacement are measured. These techniques, however, do not inspect the spot weld itself and are not considered to be non-destructive evaluation; as such we will not discuss them further.

As a quality measure, the most definitive gauge of the welding process is the strength of the spot welds. This assessment involves destructive testing of randomly selected components, in order to confirm by inference the quality of other spot welds that were produced in the same batch. The obvious shortcomings of destructive testing, mentioned in the next section, have led to numerous efforts to devise and implement non-destructive evaluation (NDE) techniques for quality control of resistance spot welds.

Owing to escalating demand for weight reduction and higher quality, the customary use of mild steel in sheet metal products has been partly supplanted by use of other sheet materials, such as aluminum and advanced high-strength steels. Although these materials can be resistance spot welded, the process variability and failure modes are comparatively new to manufacturing plants, necessitating careful adherence to quality practices. Furthermore, these demands have led to the development of novel sheet welding techniques, for example ultrasonic spot welding, friction spot welding and laser spot welding. These techniques possess particular advantages over resistance spot welding and are being considered for implementation in appropriate circumstances. However, introduction of any new manufacturing technique, which could suffer from unfamiliar manufacturing or reliability issues, dictates tandem use of dependable quality control equipment and procedures. Because of the higher cost of these materials, destructive testing is less cost-effective, compounding the need for appropriate NDE techniques.

Non-destructive evaluation cannot reveal the strength of a spot weld directly. Instead, non-destructive techniques rely on measuring other tangible characteristics of the weld that bear a strong correlation to weld strength. As discussed in previous chapters, the principal tangible characteristics that control weld quality are geometry and materials properties. Thus the goal of spot-weld NDE is to provide sufficient information about the geometry and metallurgical properties of the heated region to permit a meaningful inference to be made about weld quality.

Although numerous manufactured goods rely on spot welding, the quality and integrity of spot welds are most crucial to the automotive industry to assure the structural rigidity, durability and crashworthiness of vehicle

bodies. Aerospace applications were one of the drivers for early NDE work, but other sheet joining techniques have largely replaced the use of spot welds in modern aircraft manufacturing. Therefore, development of NDE techniques for spot welds has been dominated by automotive applications, which will be the focus of this chapter.

Numerous NDE techniques have been tested on spot welds. Among these, ultrasonic methods have become most prevalent in industrial settings. Consequently, this chapter is mostly dedicated to description of ultrasonic NDE of spot welds. The dominant spot welding technique used in manufacturing is resistance spot welding, while other advanced techniques remain the subject of current research. Moreover, resistance spot welding has mostly been applied to mild steel sheets. Therefore, the content here is primarily about resistance spot welds in mild steel.

The content in this chapter is divided as follows. In Section 5.2, the process of resistance spot welding and associated quality-control issues are discussed. Section 5.3 provides a brief overview of the various NDE techniques devised for spot welds. Ultrasonic techniques, the most promising and prevalent of these methods, will be treated in detail in the remainder of this chapter. Section 5.4 covers single-element ultrasonics, the most common NDE technique employed in manufacturing facilities. Section 5.5 describes imaging ultrasonics. Section 5.6 outlines issues related to resistance spot welding of other materials and other spot welding techniques. Section 5.7 presents a brief discussion of in-process ultrasonic NDE techniques. Section 5.8 provides a selective history of ultrasonic NDE of resistance spot welding, along with current trends. Finally Section 5.9 presents some concluding remarks.

5.2   Background

The process of resistance spot welding involves passing electrical current through metal sheets within a localized area, leading to fusion of the sheets (RWMA, 2003). The sheets to be welded are clamped between two water-cooled electrodes. After the clamping force has stabilized, current is passed through the clamped location. Joule heat generated by the electrical resistance within and between the sheets causes the sheet material to soften and melt, beginning at an interior location and growing outward as heat is added. A consequence of this softening is that the electrodes press into the outer sheet surfaces, leaving behind indentation marks. After the current is shut off, pressure is maintained until the molten metal has solidified, forming a 'nugget' that joins the sheets.

Current, force and time must be controlled within a suitable range for the production of satisfactory spot welds. The range depends on sheet thicknesses, alloys and coatings, among other factors. If the current is too small
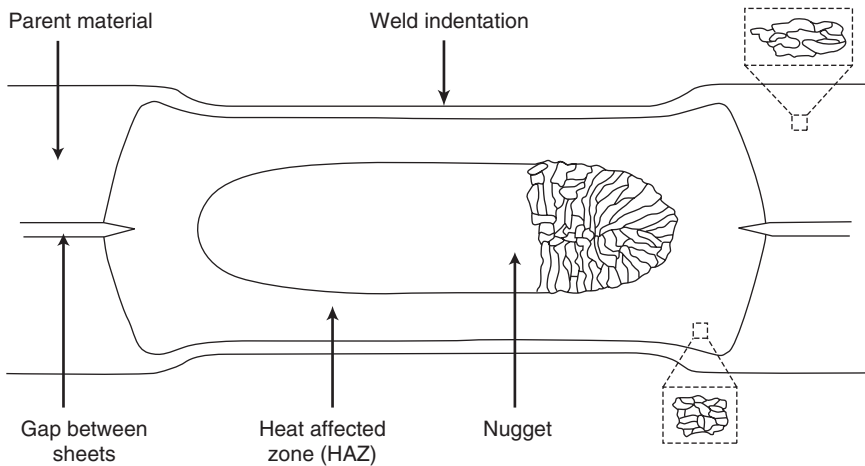
5.1 Sketch of a steel resistance spot weld. Some grains are shown to illustrate typical size variations with location in the weld.

or is applied too briefly, the nugget will be smaller than the desired size ('undersized weld'), or the sheets can be joined by a weak braze or solid-state bond at the weld interface ('stick weld' or 'cold weld'), or they may not be joined at all. If the current is too large or is applied for too long, the molten zone can approach the electrode surfaces too closely, resulting in excessively deep indentations ('burnt' weld). The clamping force must be sufficient to contain the molten zone between the sheets. If the force is too small, molten material can escape along the sheet interface ('faying surface') or from between the sheets and electrode tips, a situation that is called 'expulsion'.

The structure of a typical satisfactory resistance spot weld in mild steel is sketched in Fig. 5.1. The indentations at the top and bottom result from plastic deformation caused by the welding electrodes. The nugget forms more or less centrally and has a roughly ellipsoidal shape. As the nugget rapidly cools, it largely transforms into a martensitic structure, even in steels that have a very low carbon content. The nugget is surrounded by a heat affected zone (HAZ) that has been strongly influenced by heating and cooling even though the material in this region did not melt. The HAZ can contain both grain-refined and grain-coarsened regions, depending on its detailed thermal history, but it is always metallurgically distinct from the unmodified ('parent' or 'base') sheet material (Kou, 2003; Messler, 1999).

Despite the seemingly straightforward character of resistance spot welding, it can suffer from numerous process errors. Even if current, force and time fall within the specified range, the welding electrodes can become

misaligned or misoriented, changing the distribution of current within the sheets. The electrodes can alloy with material from the sheets, changing their resistance, or the electrode tips can change shape ('mushroom'), decreasing current density or introducing non-uniformities into the current distribution. The flow of cooling water can become hindered, allowing temperatures to rise too high. Foreign material or misfit between the parts being joined can prevent proper clamping of the sheets. Moreover, process errors can occur that are unrelated to the welding apparatus. For example, the sheet composition or coating thickness can vary from nominal. As a result of these and other process errors, the weld can be burnt, material can be lost to expulsion, the nugget diameter or thickness can be too small, the metallurgical condition of the weld can be incorrect, and so on, leading to production of unsatisfactory spot welds.

Such variations indicate a need to monitor the spot welding process. Some parameters, like welding current and water flow, can be measured by sensors on the welding apparatus. Others, such as burnt welds and electrode misalignment, can be spotted visually. However, some critical characteristics of the weld, for example the nugget size, are hidden. Therefore, additional means are required to monitor weld quality.

The traditional laboratory tests of weld quality, instrumented strength tests using a tensile testing machine and metallurgical sectioning (AWS, 2002), are ill suited for routine use in a manufacturing plant. Automotive manufacturers have settled instead for a less well-controlled and less informative 'peel test', in which one sheet is peeled away from the other until the sheets separate. 'Teardown' tests, in which all spot welds on a part are peeled, are performed on an audit basis according to a preset schedule. In the case of mild steel, the sheets tend to tear around the nugget because the nugget is harder than the parent material. The entire nugget remains attached to one sheet, appearing as a projection or 'button' on that sheet and leaving a corresponding hole in the other sheet. The diameter of the button is measured by calipers according to specified procedures and is compared to a specified minimum acceptable button size to determine whether the weld was satisfactory (AWS, 2002). Because the button diameter is approximately equal to the nugget diameter in mild steel, the button is a reasonable substitute for the nugget in assessments of weld quality. The situation becomes more complicated for spot welds in other materials, as explained in Section 5.6.

Because the peel test destroys otherwise sellable product and the time delay between producing and testing parts leads to a slow response to welding problems, manufacturing plants developed an alternative quality test. In the 'pry test' or 'chisel test', a chisel is forcibly inserted between the sheets near a weld so as to pry the sheets apart by a predetermined amount (Zhang and Senkara, 2006). If the weld does not fail, it is presumed to be

satisfactory and the plastically distorted sheet in the vicinity of the weld is hammered back into place. This easy-to-perform test, which is often described as 'non-destructive', is less than satisfactory because the results are non-quantitative and because it can damage the weld or the nearby sheets. Moreover, welds can be classified as non-pryable for a variety of reasons. In high-strength steel, it may be difficult to apply sufficient force, or a perfectly good weld may fail interfacially without distortion of the surrounding material. For some metals, and for adhesively bonded sheets, the distortion is irreversible. Some welds are located in places that are inaccessible to the chisel. Therefore, much effort has been spent over many years to develop better, truly non-destructive tests.

5.3   Techniques for non-destructive evaluation of spot welds

Non-destructive evaluation techniques can be broadly classified as in-process or post-process. In-process techniques, in which welding is monitored in real time, can provide a measure of the quality of the completed weld, or be used as a feedback signal to optimize the welding process. Using feedback, welding current could, for example, be terminated immediately after the melted region has reached the optimum size, preventing production of burnt welds. In-process techniques add cost and complexity to the welding equipment and the resulting potential for increased down time for repair and maintenance could reduce production rates. Thus, post-process techniques, in which the weld is examined after welding is fully completed, have been predominant in industrial settings.

Non-destructive techniques can be also divided into two classes depending on whether the signal being monitored is generated by the welding process itself, for example temperature or acoustic emissions, or whether the weld is interrogated using external excitation. In the latter case, the spot weld is exposed to external energy, causing a measurable response, from which inferences can be made. Various energy modes and physical phenomena have been used for NDE of spot welds, among them sound waves, electromagnetic radiation of various frequencies (infrared, optical, X-rays), AC or DC electric current and magnetic flux. In most cases, the energy is intended to interact with the internal structure of the weld, to assess the bond quality between the sheets or the nugget size and materials properties, or to detect flaws. However, some NDE techniques have also attempted to rely on visual indications to evaluate spot welds, as will be mentioned.

Sound waves in the ultrasonic frequency regime have proven especially valuable for examining weld quality because of their acute sensitivity to materials properties. They are readily reflected by abrupt changes in density or sound velocity, for example those at the sheet interface and weld bound-

aries. In addition, metallurgical changes caused by welding can influence attenuation and speed of sound in the material. Based on these physical phenomena, several post-process and in-process ultrasonic techniques have been developed. These will be discussed in detail in later sections.

X-ray techniques rely on differential absorption and scattering of radiation based on integrated density along the X-ray beam path. The technique can provide images of internal pores and flaws. X-ray radiography is, however, not well suited to monitoring spot welds, since it can only detect weld indentation and large pores, but it cannot distinguish the nugget size or properties (Gardner and Redwood, 1955; Kruger and Lehmann, 1993; USAMP, 2003). Even for resistance spot welding of aluminum, for which internal flaws are more common and larger in size, detection is challenging for standard X-ray techniques. More sophisticated techniques, such as X-ray tomography, can obtain three-dimensional images of the weld geometry and internal pores but are expensive and time consuming for typical manufactured goods. More importantly, because they are still incapable of distinguishing the weld nugget, they have limited value for NDE of spot welds.

Infrared techniques have also been investigated, involving either the infrared radiation produced by the welding process, or exposing completed spot welds to external infrared energy. In the former case, since welding electrodes largely obstruct the weld, an alternative technique observes cooling of the welded area immediately after electrodes are removed (Denis *et al.*, 1979). In the latter case, heat is introduced into the welds either by flash lamps illuminating the weld surface, or by passing electric current through spot welds. Since thermal response depends on weld size and the presence of internal pores or cracks, some unacceptable spot welds can be detected via deviation from typical cooling rates or non-uniform flow of heat within and around the welded area. Despite some promising laboratory results (Bekeshko and Popov, 1972; Brown and Bangs, 1986; Shepard *et al.*, 1998, Turler *et al.*, 2003), the relatively large thermal diffusion distances in metals degrade the accuracy with which undersized spot welds can be detected. Moreover, infrared techniques are not capable of distinguishing the weak brazing in stick welds from satisfactory welds.

Another approach is based on the decrease in electrical resistance of spot welds with increasing nugget size (Cohen and West, 1983; Hain, 1988) and can be measured simply using a four-point electrical conductivity probe. However, the zinc corona around undersized welds and the zinc braze of stick welds lead to overestimation of nugget size (Westgate, 1993). Moreover, proximity to sheet edges and adjacent welds can skew the measurement (Westgate, 1993).

Eddy current techniques, which measure the electromagnetic response of spot welds, have also been utilized to assess the size and metallurgical properties of weld nuggets. Surface irregularities, material magnetism and

the depth of the weld nugget can, however, lead to complications that have not been overcome by standard eddy current techniques (Fastritsky *et al.*, 1973; Scott and Dodd, 1982). Recently, more sophisticated electromagnetic NDE techniques have succeeded with aluminum friction stir welds (Grundy *et al.*, 2006) and could be extendable to friction spot welds and even resistance spot welds.

Yet another technique is in-process detection of acoustic emissions produced by thermal and microstructural transformations in the welded material during welding. Despite promising laboratory results (Crostack, 1977; Vahaviolos, 1984) and established standards (ASTM, 1996), this technique has not advanced in manufacturing plants. Other post-process techniques include optical (visible light) methods, in which a single reading or image of the weld outer surface is scrutinized (Weerasinghe and Hameed, 2001; Maetschke, 2002), response to an applied magnetic field (Lavrent'eva *et al.*, 1988; Banerjee *et al.*, 2008) and shearography (Yang *et al.*, 2005).

It is worth noting that additional ultrasonic techniques have also been tested. For example, in-process Lamb waves (Rokhlin and Bendec, 1983; Rokhlin and Adler, 1985) were utilized, but have displayed problems in distinguishing stick welds. Also, difficulty with consistent coupling of ultrasound into resistance spot welds using the traditional piezoelectric transducers have led to investigation of electromagnetic acoustic transducers (EMAT) (MacLauchlan and Latham, 2001) for NDE of spot welds. Although the method for producing the ultrasonic waves is different, the physical phenomena behind the interaction with the weld nugget are similar to other ultrasonic techniques.

As described above and in previous review articles (Jones, 1999; Satonaka and Matsuyama, 2000), numerous schemes have been tested as possible NDE techniques for spot welds. Although these techniques have their proponents and have shown promise in laboratory environments, most have struggled with process and materials variations, and with other noise sources typical of manufacturing environments. Furthermore, introduction of NDE into the automotive manufacturing environment must overcome some industry-specific challenges (Mozurkewich, 2004). The remainder of this chapter is devoted to a closer description and analysis of the most promising of these NDE techniques: pulsed ultrasound. A detailed examination of this technique and its advantages and shortcomings in manufacturing plants will also serve as a case study for the issues faced by all NDE techniques.

5.4   Single-element ultrasonic inspection

5.4.1   Echo timing

Single-element ultrasonic inspection of spot welds is based on the observation of echoes reflected from abrupt changes in the density or speed of

sound, for example from boundaries of the sheets or from voids in the weld. Echo timing provides information about the location of discontinuities. Echo amplitude provides information about the size of discontinuities and about the amount of attenuation occurring in the material.

When ultrasound generated by a transducer is introduced into a single metal sheet normal to its surface, the sound propagates through the sheet, reflects from the opposite face and returns to the first surface, producing an echo. The time when the echo arrives is determined by the distance traveled (twice the sheet thickness) divided by the speed of sound. Some of the energy in the echo is transferred out of the sheet and back into the transducer, allowing the arrival time and amplitude of the echoes to be recorded. The remainder of the ultrasonic energy is reflected again, commencing another round trip through the sheet. It is common to observe a dozen or more echoes. Some energy is lost to attenuation during each round trip, reducing the size of successive echoes. Processes that attenuate sound energy include absorption of sound by the material through which it propagates, scattering of sound by variations in material properties or by rough surfaces, spreading of the ultrasonic beam by diffraction and transmission of the beam through surfaces into neighboring materials. The resulting pattern of echo amplitude versus time is called an A-scan.

Echo timing provides the standard technique for determining whether two sheets are intimately bonded. If the transducer is located over an unbonded sheet, the time separation between the echoes corresponds to the sheet thickness (Fig. 5.2a). On the other hand, if the transducer is located over an area where two sheets are bonded, the echo separation corresponds to the sum of the thicknesses of the two sheets (Fig. 5.2b). Whereas this latter situation corresponds to a properly formed spot weld, the presence of any intermediate echoes indicates an unsatisfactory weld.

The most common cause of additional echoes is reflection from an unbonded faying surface. Ordinarily, the inspector chooses a transducer that has a diameter approximately equal to the desired diameter of the weld nugget. Intermediate echoes caused by reflections from the faying surface appear in the echo pattern if the actual weld diameter is smaller than the selected transducer diameter. In this case, the observed echo pattern consists of two independent echo sequences, one from the fully bonded region, in which the echo spacing corresponds to a round trip in the full thickness, and a second sequence, corresponding to a round trip in the top sheet (Fig. 5.2c). Intermediate echoes also appear if the transducer is displaced from the center of the weld. Thus, when intermediate echoes are observed, the inspector must adjust the transducer location laterally to seek the center of the weld. A diagnosis of undersized weld is rendered if no location can be found at which the intermediate echoes disappear.

(a)

(b)

(c)
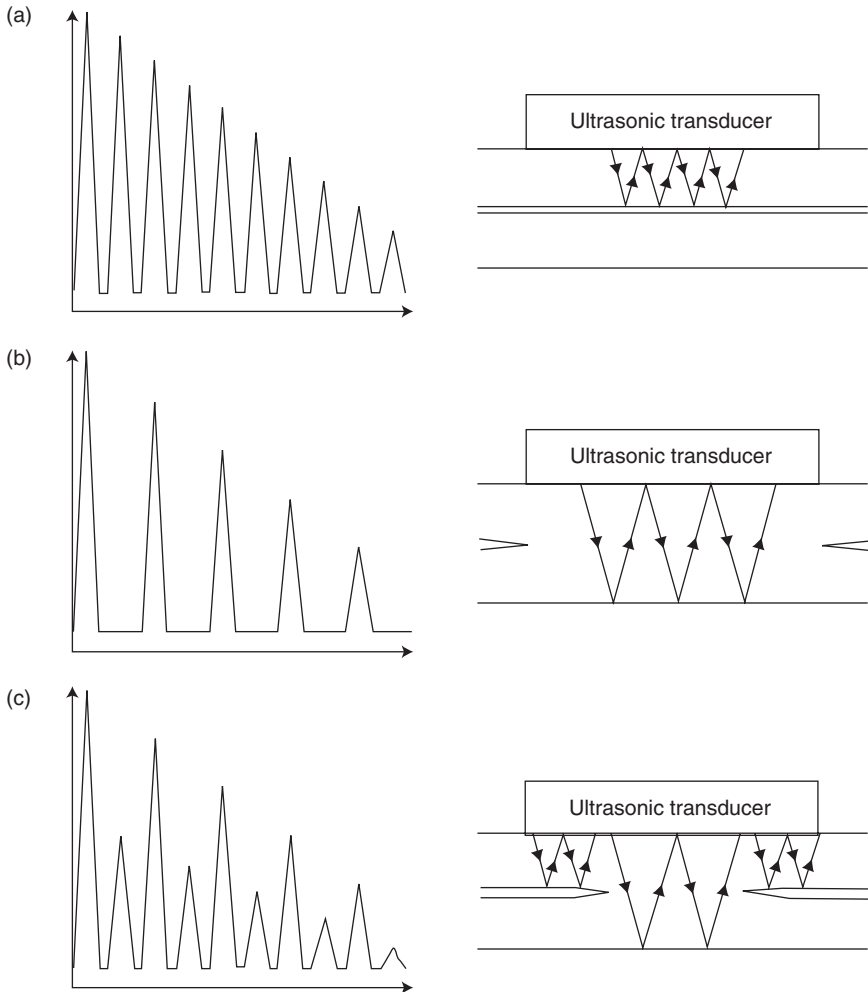
5.2 Schematic representations of rectified A-scans (plots of voltage versus time) corresponding to a transducer located above (a) an unbonded region, (b) a satisfactory spot weld and (c) an undersized weld. The arrows representing the ultrasonic beam path are drawn at an angle solely to allow differentiation of beam paths.

A second cause of additional echoes is the presence of a gross flaw inside the weld nugget. Pores and shrinkage cracks produce reflections between those corresponding to the full sheet thickness. When the depth of such a discontinuity differs from the thickness of the top sheet, the timing of the intermediate echoes can distinguish the discontinuity from faying surface echoes. If the sheets are of equal thickness, however, it is hard to distinguish

center-plane voids from faying surface echoes, although some success has been reported (Sokolowski *et al.*, 2006; Register and Servent, 2009).

A third cause of intermediate echoes is the presence of a weakly reflecting layer at the faying surface, arising from a weak bond between the sheets. Under the influence of heat and pressure, a solid-state bond can form between the sheets by diffusion. Such bonds are rarely perfect because of interface roughness and contamination. Thus they are weaker than fully fused spot welds and can be weak enough to fail interfacially. Weak bonds also can form between galvanized steel sheets if the zinc melts and resolidifies, brazing the sheets together. Because of the low strength of zinc, they also fail interfacially. Both situations are classified as 'stick welds' (or 'cold welds') and should be rejected. Moreover, an undersized nugget can be surrounded by a corona of zinc braze or solid-state bond.

Stick welds entail appreciable mechanical contact between the sheets, substantially reducing the magnitude of ultrasonic reflection at the interface. When the intermediate echoes have moderate amplitude, weak bonds can be recognized by a bell-shaped echo envelope, called 'Napoleon's hat' (Kaminski, 1997). The peak in the pattern of intermediate echoes arises from the interplay between ultrasound transmitted through the faying surface and ultrasound reflected by it. In other cases, faying-surface echoes from a well-formed solid-state bond or very thin zinc-brazed joint can become so small that the resulting intermediate echoes from the stick weld are smaller than the instrument noise. Therefore, while observation of Napoleon's hat provides solid evidence for a weakly bonded faying surface, the absence of Napoleon's hat does not prove that the sheets are fully fused. A stick weld can look ultrasonically like a satisfactory weld and a corona of weak boning can cause an undersized weld to appear larger than it actually is.

5.4.2 Attenuation

The serious challenge of identifying stick welds was addressed through the empirical observation that satisfactory spot welds tend to have higher ultrasonic attenuation than weak ones (Anonymous, 1966; Pittaway, 1967; Mansour, 1988). Thus, by combining information from attenuation (high versus low) and from intermediate echoes (presence versus absence), the weld condition can be inferred according to the prescription given in Table 5.1.

The larger attenuation in a satisfactory spot weld was interpreted in terms of the metallurgical structure of the weld. In contrast to a stick weld, a satisfactory weld contains a nugget of appreciable thickness, the melted region having penetrated through a significant fraction of the sheet thickness. The nugget material has a cast morphology (RWMA, 2003) containing

Table 5.1 Algorithm for inferring weld condition from an A-scan in single-element inspection

Observed A-scan	Inferred condition
Single-thickness echoes	No weld
Full-thickness echoes plus intermediate echoes	Undersized weld or flaw in weld
Full-thickness echoes only, low attenuation	Stick weld
Full-thickness echoes only, high attenuation	Satisfactory weld

large crystalline grains, in contrast to the small grains of the wrought parent material (Fig. 5.1). Because large grains scatter ultrasound more strongly than small grains (Papadakis, 1968; Mansour, 1988), the nugget material could be expected to exhibit increased attenuation. Therefore, the observed increased attenuation was assumed to stem from appreciable thickness of the nugget.

The difficulty of demonstrating a consistent connection between attenuation magnitude and weld quality has, however, been pointed out repeatedly (Hain, 1988; Westgate, 1993; Satonaka and Matsukawa, 2000; Roberts *et al*., 2002). The connection has also been more directly challenged. Measurements on resistance spot welds before and after flattening their surfaces to remove the welding electrode indentations have shown that attenuation in as-made mild-steel welds is caused largely by surface unevenness within the indentations (Roberts *et al*., 2000). Spatially resolved attenuation measurements found that attenuation within the nugget of a mild-steel weld does not differ greatly from that in the parent material and a satisfactory weld can have lower attenuation than a weak one (Mozurkewich *et al*., 2008). The evidence indicates that attenuation in mild-steel spot welds is affected more strongly by surface condition than by thickness of the nugget ('nugget penetration').

To appreciate the role of attenuation in spot-weld inspection, it helps to understand how surface condition can influence attenuation through dephasing of the ultrasonic wave. Because piezoelectric transducers are phase sensitive, the voltage corresponding to a received ultrasonic echo is reduced if the phase of the echo is not uniform over the transducer's active area. When phase variation increases with number of round trips, dephasing reveals itself as an 'apparent attenuation', that is as an attenuation contribution that is not related to absorption or scattering within the weld. Figure 5.3 sketches some situations that lead to dephasing. Uneven weld surfaces cause the ultrasonic path length to vary erratically from place to place. A curved indentation causes a systematic variation with location, as do non-
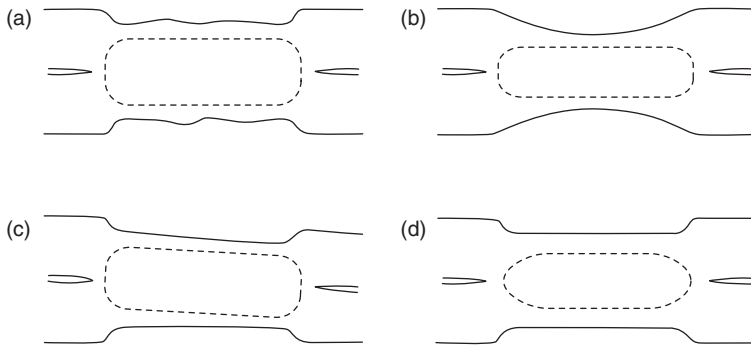
5.3 Causes of dephasing: (a) weld surface unevenness, (b) curved indentations, (c) nonparallel indentations, (d) ellipsoidal nugget.

parallel indentation surfaces. Although unrelated to surface condition, dephasing can also be caused by non-uniform nugget penetration since the ultrasonic speed is different in the nugget. For an ellipsoidal nugget, phase variation occurs over a substantial portion of the weld diameter, while for a more rectangular one, the variation is restricted to its periphery.

Computing the magnitude of the associated amplitude reduction is beyond the scope of this discussion. Yet one can appreciate the significance of these effects by estimating the phase variation across the transducer. If the phase variation is a substantial fraction of a radian, the effect can appreciably influence echo amplitude. Using plausible values for the parameters involved (peak-to-peak surface unevenness of 0.1 mm, and/or electrode-tip radius of 50 mm, speed of sound in the nugget reduced by 3.5% (Mozurkewich *et al.*, 2008)), we find that these effects can cause appreciable dephasing at a typical operating frequency of 15 MHz and thus can contribute to apparent attenuation.

The apparent attenuation produced by dephasing can provide useful information about weld quality if and only if the cause of dephasing correlates with weld quality. For example, because indentation depth increases with welding current and time, it provides indirect information about weld quality. If the electrode tips are curved, apparent attenuation will increase in tandem with indentation depth and would likewise serve as an indirect indicator of weld quality. Similarly, worn electrodes impress their uneven tip shape into the softened weld surfaces, resulting in apparent attenuation that can indirectly indicate weld quality. We believe such effects account for much of the observed relationship between attenuation and weld quality. In contrast, flat-tipped electrodes might produce no discernable increase in apparent attenuation with indentation depth and therefore might provide no useful information about weld quality.

Dephasing effects represent a serious complication in single-element inspection. In some situations, the resulting apparent attenuation can provide useful information relevant to weld quality, while in other situations it cannot. Which situation applies depends on considerations such as electrode tip shape, frequency of tip dressing and nugget shape. Lack of attention to such details could cause the inspector to be misled. We believe this state of affairs explains some of the discouragement that seems to plague implementation of spot-weld ultrasonic testing (Utrata, 1998; Roberts *et al*., 2002).

5.4.3   Classification reliability

To judge the accuracy of an NDE regimen, inferences from non-destructive tests must be compared with objective determinations of weld condition. Laboratory tests of NDE techniques might entail comparison with the weld strength measured using a tensile testing machine or with the nugget diameter obtained through metallographic sectioning. However, the test most commonly practiced in manufacturing plants and sanctioned by various standards (AWS, 2007) involves the size of the button.

After the welds are classified as either OK or not OK (NOK) based on the non-destructive test, they are peeled, the buttons are measured and each weld is classified as satisfactory or unsatisfactory by comparing its button to the minimum acceptable size. The resulting numbers of welds are compiled in a two-by-two contingency table, Table 5.2. For instance, the number of welds that are satisfactory based on button size and also called OK by NDE are designated by b. The rate of false calls, α, is defined by the ratio of the number of satisfactory welds erroneously called NOK to the total number of satisfactory welds:

$$\alpha = \frac{d}{b+d}$$

Similarly, the rate of misses, β, is the ratio of the number of unsatisfactory welds mistakenly called OK to the total number of unsatisfactory welds:

$$\beta = \frac{a}{a+c}.$$

For the non-destructive inspection regimen to be qualified for plant use, manufacturers commonly require empirical evidence that both α and β are sufficiently small. While each manufacturer specifies exactly how small is small enough, representative values are $\alpha < 0.05$ and $\beta < 0.10$. Both α and β must be evaluated. It is not sufficient to determine the ratio of the total number of mistakes $(a + d)$ to the total number of welds because modern

Table 5.2 Contingency table for evaluating non-destructive spot weld tests. The letters *a*, *b*, *c* and *d* designate the number of welds falling into each category

	Button unsatisfactory	Button satisfactory
Called OK by NDE	*a*	*b*
Called NOK by NDE	*c*	*d*

welding lines often produce greater than 98% satisfactory welds. Thus a careless inspector who simply declares every weld to be OK would be wrong less than 2% of the time, if judged solely by the total proportion of mistakes.

Despite the widespread use of this criterion for qualifying an inspection, the α and β error rates are not determined solely by the characteristics of the inspection regimen. Rather, they are a combined property of both the inspection regimen (instrument, inspector training, etc.) and the set of welds used in the test. In particular, the values of α and β depend on the proportion of welds that fall near the minimum acceptable diameter. This fact has been empirically demonstrated (Roberts *et al.*, 2002) and can be appreciated by considering hypothetical cases (Mozurkewich, 2006). For instance, consider adding a large number of unambiguously unsatisfactory welds to the test set. By increasing c in Table 5.2, the rate of misses (β) would be decreased, without modifying any characteristic of the non-destructive test: same inspector, same instrument, different result.

Every measurement process entails error and better measurement processes entail smaller error. This observation motivates a better metric for qualifying an inspection, the prediction uncertainty, σ (Mozurkewich, 2006). If a weld produces a button exactly equal to the minimum acceptable diameter, M, any inspection method is equally likely to classify the weld as OK or NOK; that is, any inspection has a 50% chance of being wrong. If, however, the button size greatly exceeds the minimum acceptable diameter, any competent inspection is almost certain to classify the weld as OK. The misclassification probability decreases monotonically from 50% in the first case to 0% in the second. Prediction uncertainty is defined such that the misclassification probability is 16% for a button diameter equal to $M \pm \sigma$, or, equivalently, 5% for button diameter of $M \pm 1.645\ \sigma$. This metric is independent of the distribution of welds being tested.

No extensive studies of error rates in actual manufacturing environments have, to our knowledge, been published in the open technical literature. To estimate the order of magnitude of σ, we turn to a United States Automotive Materials Partnership (USAMP) study in which one set of 150 coupon welds was classified by several parties, each using different ultrasonic

apparatus (USAMP, 2003). Enough data were available to estimate σ for two commercial instruments, the better of which yielded a value of 0.6 mm (Mozurkewich, 2006). This value indicates that a weld that is 1.645×0.6 mm $= 1.0$ mm larger than the minimum acceptable diameter would be classified correctly 95% of the time. This value should be regarded as approximate because the inspectors were not allowed to peel the welds to refine their technique. In a manufacturing environment, extensive effort would be expended to train inspectors about the particular weld stack-ups they would encounter in practice. Under such circumstances, it is possible that smaller values of σ would be obtained.

5.5   Ultrasonic imaging

5.5.1   Motivation and methods

While reasonable success has been attained using the single-element method, improvement is continually sought. Ultrasonic imaging offers a potential route towards better performance. Because a single-element transducer interrogates the entire spot weld simultaneously, the information it provides has necessarily been averaged over the entire weld, limiting analysis to the average reflection at the interface. Small intermediate echoes in a single-element inspection could indicate that most of the weld interface produces no reflections while a small portion produces large reflections, or it could equally well indicate that the entire interface produces small reflections. These physically distinct situations can be differentiated by imaging. In accord with the adage 'A picture is worth a thousand words', it is reasonable to expect that welds could be categorized more accurately and easily using local information from within the weld.

Moreover, finer spatial resolution implies greater sensitivity. The size of the reflection from a small object increases as the area of the ultrasonic beam decreases because the object subtends a larger portion of a smaller beam. Thus an imaging system that has finer spatial resolution is inherently more sensitive to such an object, which could, for instance, be a void or inclusion in an imperfectly formed solid-state bond. While the size of this enhancement can be quite significant, it remains to be determined empirically whether the sensitivity using a particular frequency and size of focal spot is adequate to detect the small reflections that indicate an imperfectly bonded interface.

A weld can be mapped ultrasonically using a transducer that has a tightly focused beam by translating the transducer across the weld surface in a raster pattern (Fig. 5.4a). This technique, called acoustic microscopy, is usually performed in a water tank to facilitate reproducible coupling of ultrasound into and out of the weld. The A-scan from each point on the
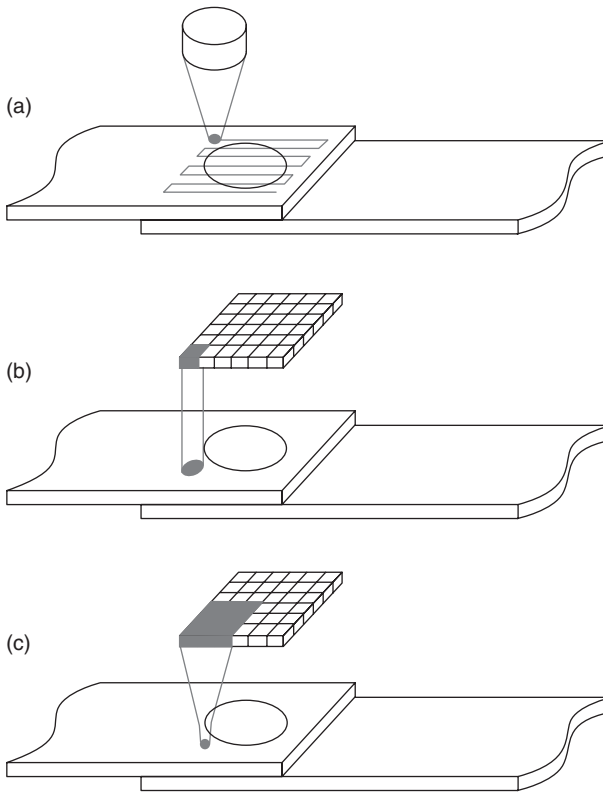
5.4 Schematic representations of (a) mechanical scan of a focused single-element transducer in a raster pattern, (b) two-dimensional (2D) passive array, (c) 2D phased array. The array elements that are excited to produce the displayed beam are shaded.

map is analyzed to obtain a quantitative measure of the weld at that point. A plot of this metric over the raster area is called a C-scan (Krautkramer and Krautkramer, 1990). Typically, C-scans present the magnitude of reflection from the faying surface (Fig. 5.5), although other metrics, like weld indentation topography, can be plotted. Acoustic microscopy is commonly used in laboratory settings, but is not well suited to manufacturing environments because the equipment is expensive and delicate and scans are slow.

A passive ultrasound array provides one practical method for rapidly producing an ultrasonic map outside the laboratory environment (Macovski, 1979). A passive array consists of a large number of small transduction elements arranged on a grid. Each individual element generates ultrasound independently and detects the corresponding echoes in order to inspect the material directly below it, contributing one pixel to the overall map
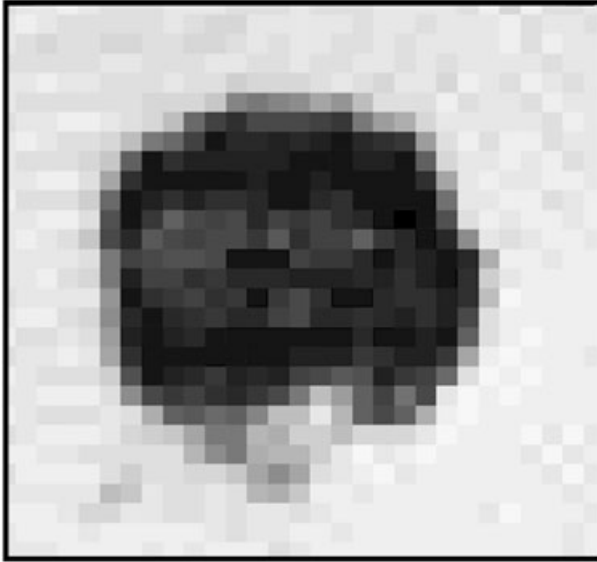
5.5 Example of a C-scan. The image shows the magnitude of the reflection from the faying surface of a spot weld. Darker shades correspond to smaller echo amplitudes. This raw C-scan displays the pixilation inherent in the spatial resolution chosen for the raster pattern. (In many cases, such raw images are smoothed, increasing the apparent spatial resolution of the scans, by interpolating the pixel values.)

(Fig. 5.4b). The element size is constrained by beam spreading, which is proportional to the ultrasonic wavelength divided by width of the element. This places a practical limit on spatial resolution (pixel size). On the other hand, a passive array is electronically simple, requiring only a multiplexing interface to connect each element sequentially to the electronic pulser-receiver unit which generates the excitation pulse and records the echoes.

A second practical method for rapid ultrasonic mapping is provided by a phased, or active, array (Lupien, 2007; Shung, 2005; Macovski, 1979). In this method, the element dimensions are intentionally made smaller than a wavelength so that the ultrasonic beam from each element overlaps the beams from several neighbors, bringing into play the phenomenon of wave interference. By exciting several elements with prescribed small time delays relative to each other, the focal length of the resultant beam can be tailored as required by the application and, by varying the subset of elements that are excited, the beam can be translated electronically across the specimen (Fig. 5.4c). The synthetic aperture focusing technique can also be applied

(Ikeda *et al.*, 2006). While a phased array is harder to build (owing to small element size) and requires more complex electronics to operate, it permits finer spatial resolution than a passive array. It also allows beam steering and active focusing, which will not be discussed here.

Various hybrid systems are possible. To avoid the cost of a two-dimensional array, a one-dimensional array can be mechanically scanned in the perpendicular direction (Reverdy and Hopkins, 2004) or rotated about a central axis (Dasch, 2006) to cover the entire area of interest. Similarly, apparatus have been developed for scanning a focused transducer along a line without recourse to a water tank (Yuasa and Masazumi, 1996; Fleming and Clark, 2005).

Once an image has been generated, it can be analyzed to assess weld quality. Various algorithms attempt to extract directly from the C-scan an average diameter or an area that can be converted to an average diameter. For example, one can estimate the weld area by simply adding the area of all pixels for which the reflection from the faying surface falls below some threshold level (Reverdy and Hopkins, 2004). Of course, an appropriate criterion for choosing the threshold must be developed. Because thresholded images tend to be discontinuous, attempts have been made to obtain more consistent results by imposing physically based expectations of compactness and contiguity onto the raw image. These include image processing algorithms like erosion and dilation (Reverdy and Hopkins, 2005) and algorithms that fit the image to a geometrical form (Denisov *et al.*, 2004). An alternative, less direct approach uses various features extracted from the image as inputs into a multiple regression model for weld size (Davis, 2008; USAMP, 2009).

Ordinarily the analysis is based on echo amplitudes from the faying surface. Alternatively, one can attempt to capture information from the entire A-scan. One approach begins by Fourier transforming the rectified A-scan and then computing the ratio of the heights of the frequency-domain peaks corresponding to single-sheet and full-thickness echo timing. This 'frequency ratio' has been used as a proxy for interface reflectivity (Reverdy and Hopkins, 2004).

The imaging methods described thus far place emphasis on a two-dimensional planar image (C-scan) of the faying surface, the data for which represent a specific subset of the plethora of data contained in the multiple A-scans recorded by the array. An alternative approach presents the A-scans from a line of neighboring pixels with the time axis lying along the vertical coordinate. In such an image, called a B-scan, the horizontal coordinate corresponds to distance along the array, the vertical axis represents the depth into the weld and brightness corresponds to echo amplitude at a particular depth (Krautkramer and Krautkramer, 1990). While any individual B-scan presents only a single cross-section through the weld, the
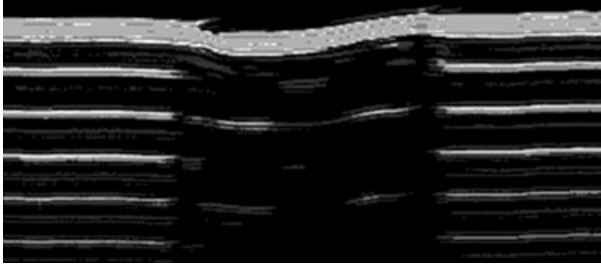
5.6 Example of a B-scan of a resistance spot weld. Brighter lines indicate greater reflection amplitudes (courtesy of H Zhang and M Fleming, University of Toledo).

Table 5.3 Comparison of prediction uncertainty for various ultrasonic imaging techniques and for single-element ultrasonic NDE of resistance spot welds

1.645 σ (mm)	Data source
0.6 to 1.2	USAMP (2009); ignores indentation information
0.4 to 1.1	USAMP (2009), Davis (2008); includes indentation information
0.8	Commercial instrument based on Denisov *et al.* (2004)
1.0	Single-element method

B-scan contains a wealth of information not contained in C-scans, revealing geometric variations in the depth of reflecting features, as well as amplitudes of several successive echoes (Fig. 5.6). The diameter of the bonded portion of the faying surface can be estimated directly from the B-scan, along with information about indentation depth and diameter. Voids can be detected, located and sized. Furthermore, it has been suggested that information from later echoes can be valuable for identifying stick welds (Zhang and Senkara, 2006).

5.5.2 Assessment of performance

An unresolved question is whether imaging lives up to its expectation of providing more accurate weld classification. This question can be addressed using the concept of prediction uncertainty, σ, introduced in Section 5.4.3. Some estimates of σ for mild-steel coupon welds are given in Table 5.3. The first two rows give ranges of '95% upper error margin at the threshold' (roughly equivalent to 1.645 σ) over several combinations of sheet thickness. Data were recorded using a one-dimensional phased array scanned

mechanically in the perpendicular direction and weld size was estimated using multiple regression. In the first row, indentation data were excluded from the regression. These values may be overly optimistic, however, being based on regressions using all the welds; traditional statistical analyses would use a subset of the welds to generate a model that is subsequently tested against the remaining welds. The third row gives 1.645 σ computed by us for an extensive set of coupon welds measured by a commercial passive array and analyzed using a circle-fitting algorithm. For these samples, strain was applied to the welds before inspection, in an attempt to destroy weak bonds. We do not have access to data from other imaging systems, although an examination of Fig. 7a in Lozev *et al.* (2008) suggests that 1.645 σ for their coupons lies in a similar range. The last row repeats the results of the single-element study discussed at the end of Section 5.4.3.

Taken as a whole, Table 5.3 suggests that imaging methods as currently configured classify welds with reliability similar to that for the single-element method. Stated differently, imaging does neither substantially better nor substantially worse. This conclusion is provisional because, on the one hand, the values in the first two rows may be overly optimistic and, on the other hand, as explained in Section 5.4.3, the value in the fourth row may not have captured the ultimate capability of the single-element method. In our opinion, the issue of the comparative reliability of imaging and single-element methods remains unresolved. Much value would be derived from a direct comparison of single-element and imaging approaches on the same set of specimens.

The fact that ultrasonic imaging does not do convincingly better than the single-element method might seem surprising, considering its substantially greater sensitivity to small reflections from an imperfectly bonded faying surface. We should consider why imaging does not do better than it does. Some careful investigations using acoustic microscopy provide empirical evidence that the increase in sensitivity associated with finer spatial resolution, while sizeable, is insufficient to detect reliably a weakly bonded interface.

Scans of as-made spot welds using a typical inspection frequency of 15 MHz (Potter *et al.*, 2006) and using higher frequencies (Chertov and Maev, 2007) failed to distinguish reliably between the central, well-fused nugget and a corona of a weakly bonded interface. Accordingly, ultrasonic imaging tends to overestimate nugget diameter. Scans using a 100-MHz transducer of a spot weld that was polished to prevent distortion of the A-scans by the indentation and surface unevenness (Potter and Ghaffari, 2007) also failed to identify weakly bonded interface reliably. We conclude that the sensitivity of imaging methods for the combinations of ultrasonic frequency and spatial resolution used to date remains inadequate to the task of discriminating weak bonds from the nugget on a pixel-by-pixel basis.

As currently configured, imaging methods tend to classify welds without regard to attenuation. In contrast, attenuation information is critical for successful classification by the single-element method. Yet the two methods yield similar values of prediction uncertainty. In light of the conclusion of the previous paragraph, we should consider why imaging methods do as well as they do. We speculate that pixel-to-pixel variation in a C-scan contains clues about the condition of the faying surface that cannot be obtained by considering the A-scans individually. A low-variation area in the image is likely to correspond to a highly uniform region, such as the nugget, while areas exhibiting higher variation may arise from imperfectly bonded regions of the faying surface containing a complex, spatially varying microscopic structure (Potter *et al.*, 2006; Potter and Ghaffari, 2007). This additional information embedded in images happens to produce a similar level of classification reliability as does the indirect information from dephasing in the single-element method.

Imaging approaches are able to extract information about indentation depth and shape that may provide valuable input for identification of stick welds. The use of indentation depth as a quality indicator is somewhat controversial in the automotive industry because indentation depth can vary for welds of similar strength or button size (RWMA, 2003) and because most manufacturers specify limits to allowable indentation depth. Nonetheless, welds having more than minimal indentation are unlikely to be stick welds. Thus the difficulty of identifying stick welds leads to the pragmatic choice to use indentation depth as an indirect indicator of weld quality in many inspection procedures.

As a practical consideration in comparing inspection regimens, values of σ obtained from production parts tend to be larger than those from coupons because production parts exhibit sources of variation not found with coupons. For example, using data from the passive array referred to in row 3 of Table 5.3, we obtained 1.645 σ = 0.8 mm for coupons and 1.645 σ = 1.7 mm for production welds made in tandem with the coupons. Westgate (1993) has made a similar observation. This consideration is important when assessing the capability of a particular inspection regimen under plant conditions.

Apart from the question of classification reliability, ultrasonic imaging presents several distinct benefits. Foremost is the ability to determine the size of spot welds in various sheet thickness combinations using a single transducer; in contrast, single-element inspection requires matching the transducer to the desired weld size. Imaging provides auxiliary geometric data, including indentation depth and shape and electrode orientation (Hopkins *et al.*, 2009). Indentation information, as mentioned above, can improve classification reliability and electrode orientation could provide useful process feedback. Imaging can detect localized flaws, like cracks and

pores, and can determine whether they are located in critical regions of the weld. An active array could, in principle, steer its beam to compensate for geometric imperfections like tilted electrodes or to optimize sensitivity to cracks. Finally, human inspectors intuitively grasp the information contained in images, easing acceptance into the manufacturing environment.

5.6   Additional materials and welding techniques

5.6.1 Other metals

The technique for resistance spot welding of aluminum, advanced high strength steels (AHSS) and other metals is qualitatively the same as for welding mild steel. The welder applies force, current and time within the range experimentally determined to be appropriate for the material. Though quantitative details differ, the optimal end result of an appropriate welding schedule is an adequately sized nugget joining the sheets. Consequently, the techniques for ultrasonic testing of spot welds in these materials are qualitatively the same as in mild steel (Spinella *et al*., 2005; Sokolowski *et al*., 2006; Shellberg and Sokolowski, 2008). In the single-element method, detection of intermediate echoes and use of attenuation to distinguish stick welds remain the cornerstones of the method. Likewise, imaging techniques for aluminum and AHSS are basically the same as for mild steel (Lozev *et al*., 2008; Zhang and Senkara, 2006).

Aluminum and AHSS do differ in some ways that are relevant to ultrasonic testing. One difference is their increased tendency to form internal voids and cracks when welded (Sokolowski *et al*., 2006; Zhang and Senkara, 2006). Although welding practices exist that substantially reduce formation of voids and cracks, given the propensities of the materials and the cost sensitivity of automotive production, a successful NDE regimen must be prepared to encounter such flaws. When voids are confined to the center of the nugget, they have a minor impact on weld strength (RWMA, 2003; Thornton *et al*., 1996). Single-element detection of voids was discussed in Section 5.4. The lateral position of the flaw cannot, however, be determined using the single-element method. In this respect, ultrasonic imaging presents a distinct advantage (Hopkins *et al*., 2009; Zheng and Senkara 2006; Lozev *et al*., 2008).

As for cracks, their orientation affects their detectability because the apparent size of a crack in ultrasonic inspection is roughly proportional to its projection onto the faying surface. The ability of a phased array to steer its beam into the weld at an angle raises the possibility of detecting cracks oriented in such a way as to be invisible to a normally incident beam.

Advanced high strength steels also differ from mild steel in their tendency to fail interfacially; that is, without pulling a button (Chuko and

Gould, 2002; AWS, 2007). Thus interfacial failure during destructive testing does not necessarily indicate that the weld is unsatisfactory. This can present a problem when correlating non-destructive test results with destructive tests, if the personnel involved are not sensitive to this issue. In short, if a destructive test fails to pull a button from a weld that ultrasonic testing called satisfactory, the ultrasonic test is not necessarily wrong.

5.6.2   Other methods of spot welding

Alternative joining techniques are being developed for materials novel to automobile production. These include ultrasonic spot welding (USW) for aluminum and spot friction welding for various metals.

Ultrasonic spot welding is performed by applying a brief burst of extremely intense transverse vibrations through two welding tools that clamp the sheets together (Hetrick *et al*., 2005). A rubbing action breaks up oxides between the sheets, allowing the clean, plastically deformed faying surface to bond.

Ultrasonic spot welds have been inspected in a laboratory environment using an ultrasonic imaging technique (Ghaffari *et al*., 2005). To prepare suitable surfaces for inspection, the test specimens were flattened by grinding away the jagged indentations left by the welding tools. Lap-shear strength was found to correlate well with 'weighted ultrasonic contact area', a metric derived from C-scans of the faying surface. Imaging has provided useful feedback during subsequent development of the ultrasonic welding process for automotive aluminum sheet (Ward *et al.*, 2006). The technique is not suited to a production environment, however, because of the need to flatten the surfaces before imaging the weld.

The problem of inspecting an ultrasonic spot weld through the coarsely indented surface can be evaded by performing the inspection simultaneously with the welding process, thus taking advantage of the intimate conformance between the sheets and the welding tools. The amplitude of ultrasonic pulses transmitted between the welding tools increases as the welded area grows. The amplitude at the end of welding correlates well with the lap-shear strength of the welds (Ward *et al.*, 2006).

Spot friction welding (SFW) is a variant of friction stir welding in which a rapidly spinning tool is 'plunged' into the sheets. Welding results from mechanical intermixing of the sheet materials aided by severe plastic deformation and friction-generated heat (Pan, 2007). Issues related to SFW quality include ensuring adequate penetration of the mixed zone and detecting kissing bonds. Lap-shear strength of SFW welds varies non-monotonically with plunge time or final depth of the tool. Strength increases initially as mixing becomes more extensive, subsequently decreasing as overwelding introduces weld flaws.

Spot friction welds have also been inspected using an ultrasonic imaging technique (Ghaffari, 2007). A metric related to the size of the bonded area, derived from C-scans of the faying surface, correlates well with the non-monotonic strength variation. Because one surface of the weld remains smooth and relatively flat, inspections of production parts using this technique have obtained promising results. As with USW, imaging has also provided useful feedback during development of this welding process.

5.7   In-process ultrasonic monitoring

A dramatically different approach, described as in-process, in situ or real-time, monitors weld formation throughout the welding process. Section 5.3 mentioned real-time monitoring of process variables, weld temperature, Lamb waves and acoustic emission. In-process ultrasonics will be explained here.

In-process ultrasonics is motivated by a number of potential benefits. The good conformance between electrodes and sheets that occurs naturally during welding ensures good coupling of ultrasound and reproducible alignment. No operator intervention is required to manipulate ultrasonic transducers. Assurance of having made a satisfactory weld is immediate and its real-time nature raises the possibility of actively controlling welding current or time based on information contained in the signals. Perhaps the most important motivation, though, derives from the wealth of information that becomes available by observing the behavior during the welding process, as the metal melts and resolidifies, instead of just examining the final result.

A prerequisite for in-process ultrasonic inspection is making provision for generating and receiving ultrasound through the welding electrodes. Attaching the transducer to the back of the welding electrode (Burbank and Taylor, 1965) provides the best ultrasonic coupling but converts a commodity electrode into an expensive and delicate piece of equipment, replacement of which is more time consuming and complicated. Alternatively, the transducer may be mounted in the cooling water behind the electrode (Matting and Wilkens, 1965), which permits electrodes and transducers to be replaced independently of one another (Deutsch and Wilkens, 1968) but introduces complexity into the propagation path. For transverse or torsional waves, the transducers can be mounted externally on the electrode shank (Müller and Waschkies, 2002; Batzinger et al., 2007; Waschkies, 2008), permitting easy access and replacement. It is not yet clear which approach will prove to be most practical. Transducers can be attached to either one or both electrodes. A single transducer allows reflection experiments, analogous to single-element post-process inspection. Using two

transducers permits reflection measurements from both sides and transmission in one or both directions, offering additional information along with some degree of cross-checking capability.

The most important capability offered by in-process ultrasonic monitoring lies in confirming adequate nugget penetration, to circumvent the stick-weld issue. Differences in density and speed of sound between molten and solid metal cause reflections from solid–liquid boundaries. In transmission configuration, reflections at the boundaries of the molten metal reduce the amplitude of the transmitted signal. To make use of amplitude changes, other factors affecting amplitude must also be understood. The efficiency of transmission of sound through the metal-to-metal contacts between the electrodes and the sheets varies with the degree of conformity between the surfaces, which is influenced by temperature, pressure and plastic deformation (Burbank and Taylor, 1965; Murray, 1967; Deutsch and Wilkens, 1968). Because sound travels slower in the liquid metal, the elliptical molten zone acts as a lens, changing the received amplitude through its focusing effect (Roden, 1968). Also, the amplitude is affected by interference effects and temperature-dependent attenuation.

Because of these complexities, echo timing is a valuable technique for interpreting the state of the weld. In the reflection configuration, the echo from the solid–liquid boundary arrives sooner as penetration increases and the boundary moves closer to the electrode tip (Crecroft and Warner, 1969). Total penetration could be estimated by using reflections from both sides. In transmission configuration, arrival of ultrasonic pulses is delayed by an amount proportional to weld penetration because sound propagates more slowly in the molten metal (Chertov and Maev, 2004).

Because transversely polarized ultrasound does not propagate through liquids, the molten zone blocks transmission of transverse waves. As the molten zone grows in the plane of the sheets, the blockage increases, permitting estimation of the nugget diameter from the reduction in transmitted amplitude (Batzinger *et al.*, 2007). This effect cannot be used to estimate penetration directly, however, because a thin molten zone blocks transverse sound as well as does a thick zone. Penetration can be estimated by noting the time interval during which sound is blocked: greater penetration implies a longer time in the molten state and thus a longer interval during which transmission of transverse sound is reduced. Alternatively, penetration could be measured in the reflection configuration by using reflections from both sides, as mentioned in the previous paragraph.

Besides nugget size, additional information may be gleaned from in-process ultrasonic signals. If melting of the zinc layer or phase transitions in the cooling nugget can be observed from sudden amplitude variations, the timing of these events could provide useful clues about the welding process. Moreover, as in post-process inspection, cracks and voids cause

extra echoes and influence signal amplitude in the completed weld before it is released from the welder.

In-process ultrasonic monitoring systems have recently become commercially available. Two systems use longitudinal waves (Vogt *et al.*, 2006; Stocco *et al.*, 2008) and a third uses transverse waves (Müller and Waschkies, 2002). Plant trials have been performed to investigate issues such as reliability of detecting unsatisfactory welds, robustness of instrumentation under conditions in mass-production facilities and the balance between capital and maintenance costs on the one hand and quality and warranty savings on the other. If ultrasonic signals are used for active process control, there is also the issue of whether the parameters that can be controlled are adequate to the task. In case of surface contamination, more current or a longer weld time may be suitable. In case of poor part fit-up, on the other hand, increased current or weld time may simply cause a badly burnt weld.

5.8   History and future trends

The earliest documentation of spot-weld ultrasonic testing known to us is a patent issued to The Budd Company (Tarbox and Callender, 1948). It disclosed an in-process method involving transmission of low-frequency, continuous-wave ultrasound between the welding electrodes with the goal of detecting defective welds immediately after the weld was made.

After a 15-year gap, a major flurry of activity occurred. Several groups investigated in-process techniques using pulsed ultrasound (Burbank and Taylor, 1965; Matting and Wilkens, 1965; Deutsch and Wilkens, 1968; Murray, 1967; Roden, 1968; Crecroft and Warner, 1969). During the same decade, the first discussions of post-process inspection appeared (Cram and Dodge, 1963; Anonymous, 1966; Pittaway, 1967; Heffan *et al.*, 1967). Also, the first ultrasonic images of spot welds were made (Muenow, 1965). By 1971, sufficient literature had accumulated to warrant publication of a review article (Hall and Crecroft, 1971) covering post-process and in-process ultrasonic methods along with acoustic emission. The plethora of approaches is indicative of the demand for resistance spot-weld NDE.

The technique employed for the inspection of steel spot welds by Fisher and Ludlow Ltd. (Anonymous, 1966) and its successor company, Pressed Steel Fisher Ltd. (Pittaway, 1967) already incorporated the essential features of the post-process technique in most common use today. A transducer, matching the desired weld size and coupled to the weld through a water path, was operated in the reflection configuration; the absence of intermediate echoes was interpreted as indicating adequate weld diameter and the observation of increased attenuation was taken to verify adequate weld penetration. At nearly the same time, spot welds in aluminum sheet were also examined (Heffan *et al.*, 1967).

Prior to these publications, plant trials had been undertaken in 1965/66 at several Ford plants in the USA, UK, Belgium and Germany (Dodge, 2009). The trials incorporated an ultrasonic transducer with a captive water column, designed by Automation Industries. An analogue integrating circuit produced a readout proportional to total energy in the A-scan. This work was neither patented nor published because of concerns about losing competitive advantage. We suspect that the technique spread to other companies through the efforts of Automation Industries to sell its transducers and instruments.

The Ford trials were abandoned after about a year for reasons that may sound eerily familiar to present-day NDE practitioners. Feedback from the ultrasonic test was not considered to be sufficiently rapid. The poor surface condition of many production welds, resulting from over-welding and lax tip dressing, made ultrasonic testing difficult, yet production personnel were not eager to address these issues, especially because the sparks resulting from expulsion were taken as evidence of successful welding. Furthermore, the inspection supervisors were spread too thin to maintain adequate training and support.

In the early days, ultrasonic testing of spot welds seems to have found limited use. Hall and Crecroft (1971) wrote 'This method has been very successful in quality control, particularly in the automotive industry', presumably alluding to efforts at Fisher. Nevertheless, we have found little additional evidence of its use other than in niche applications (Papadakis, 1976).

Single-element, post-process inspection of spot welds reappeared in the literature in the mid 1980s (Allen, 1986; Midora, 1987; Mansour, 1988). While the principles on which the inspection was based remained unchanged, technical improvements had gradually accumulated. Improved high-frequency transducers permitted interrogation of welds in the thinner-gauge sheet used in body construction. Robust, compact instrument packaging was better adapted to severe manufacturing environments. Widespread efforts to introduce routine spot-weld ultrasonic testing were made at this time, in particular at Ford and General Motors. Despite the improvements, these trials suffered similar impediments: the time interval between welding and testing, lack of acceptance by tradition-bound plant personnel and insufficient resource dedication. While ultrasonic testing of spot welds has persisted in European plants on a relatively continuous basis (Kaminski, 1997), the implementation and support of the technique has been inconsistent in North America.

Perhaps the principal impediment to continued utilization of ultrasonic NDE was the difficulty of identifying stick welds (Hain, 1988; Westgate, 1993; Utrata, 1998). While this difficulty already existed with uncoated steel, increasing use of galvanized material in automobile construction exacer-

bated the problem (Kaminski, 1997). Successful identification of stick welds was dependent on the expertise and dedication of the inspectors. Over the last decade or so, the surge in computing power has led to improved algorithms providing valuable assistance to the inspectors, with a corresponding expansion in the use of ultrasonic inspection (Hawkins and Rabinovich, 2005; Sokolowski *et al.*, 2006; Register and Servent, 2009). Nonetheless, the single-element technique has not convincingly shown an ability to detect stick welds reliably under all circumstances.

In response to this state of affairs, a significant research effort has been spent in complementary directions. Imaging techniques, which attracted a low level of interest two decades ago (Adams, 1984; Adams, 1985; Satonaka *et al.*, 1989; Wüstenberg *et al.*, 1990), have recently spawned the major research efforts discussed in Section 5.5. Renewed interest in in-process methods has led to the commercial products mentioned in Section 5.7. Meanwhile, a fully automated single-element, post-process approach involving robotic transducer placement and orientation is undergoing trials (Register and Servent, 2009).

The current status of ultrasonic testing in the automotive industry for resistance spot welds in mild steel is mixed. Ultrasonic testing is used extensively in Europe. The situation in Japan is not known to us. Some North American manufacturers and suppliers use ultrasonic testing; others do not. Of those who do, most use the single-element technique, although ultrasonic imaging is beginning to win a segment of the market. While the trend seems to be upward, pry-bar testing still dominates in many plants because it is quick, and thus inexpensive, and stick welds are readily identified.

At present, the major driver for increased use of spot-weld ultrasonic testing is the proliferation of non-pryable welds. Among these are welds in advanced high-strength steels, in aluminum and in combination with adhesive. We expect this trend to expand, along with continuing research, development and deployment of ultrasonic imaging and in-process monitoring systems. It remains to be seen whether the advantages of the more complex imaging and in-process inspection systems justify their cost.

5.9   Conclusions

The longstanding challenge in post-process spot-weld ultrasonic testing has been detection of stick welds and of small nuggets surrounded by a corona of weak bonding. While observation of ultrasonic interface echoes unambiguously reveals the presence of unbonded or weakly bonded regions within the ultrasonic beam, the converse does not hold, allowing weakly bonded interface to masquerade as nugget. Successful ultrasonic classification of spot welds requires the use of additional data.

In the single-element method, apparent attenuation provides this additional information. The larger attenuation observed in satisfactory welds was originally attributed to increased scattering by the coarse grain structure in the nugget. Recent experiments contradict that interpretation, at least for mild steel. It appears that the increased attenuation commonly observed in satisfactory welds is caused instead by secondary effects, such as dephasing of the ultrasonic wave from weld surface unevenness. While these secondary effects undoubtedly provide useful information about weld quality, the evidence derived from them is largely indirect. Being indirect, the strength of the correlation with weld quality varies with factors like indentation shape and electrode age. These factors need to be fully appreciated and accounted for to attain the utmost capability of ultrasonic spot-weld testing.

Compared to single-element inspection, ultrasonic imaging techniques offer spatial resolution with a consequent sensitivity enhancement. The hope that these capabilities would resolve the difficulty of identifying weak bonds has not been realized, the sensitivity of current systems being insufficient to the task. A substantial improvement in sensitivity would require sizeable increases in frequency and spatial resolution, which might not be practical in the plant environment. Nevertheless, imaging offers classification reliability comparable to single-element inspection, along with the additional advantages mentioned in Section 5.5.

In the long run, it would be desirable to develop an inspection technique (not necessarily ultrasonic) that directly detects the presence of nugget. For steel welds, direct detection of the spatial distribution of martensite is a goal worth pursuing. Modern electromagnetic imaging techniques may provide a route towards this goal. On the other hand, successful implementation of in-process ultrasonic techniques would resolve the stick-weld issue and make post-process detection of nugget superfluous.

For now, post-process ultrasonic testing remains the best non-destructive method available for spot welds. Recognizing that this technique provides insufficient information to determine nugget diameter and penetration with certainty, inspection protocols must be adapted to make the best use of any additional information that can be procured. The most valuable additional information comes from the ultrasonic signatures and corresponding weld quality for similar welds, particularly for welds made previously by the same welding apparatus in the same weld location on a prior part. Idiosyncrasies of particular welding machines or of welds in particular locations on a component introduce unique variations into the ultrasonic signatures. Comparing signatures from the weld in a particular location on successive parts permits such idiosyncrasies to be compensated. In an inspection protocol based on this principle, the goal shifts from spotting unsatisfactory welds to detecting changes in the signals from particular weld locations over time,

which provides early warning of degradation in the welding apparatus or setup. By enabling trend monitoring in this way, NDE emphasis switches from finding and removing unsatisfactory welds to preventing such welds, thus transforming what some might deem an undesirable cost of manufacturing into a value-adding process.

5.10   References

ADAMS T (1984), 'Ultrasonic microscope aids in spotting unsound welds', *Welding J*, **63** (8), 47–8.

ADAMS T (1985), 'Nondestructive evaluation of resistance spot welding variables using ultrasound', *Welding J*, **64** (6), 27–8.

ALLEN L A (1986), 'Ultrasonic inspection of resistance spot welds', in *Sheet Metal Welding Conference II*, AWS Detroit Section, Detroit, MI, paper A02.

ANONYMOUS (1966), 'Testing of spot welds', *Ultrasonics*, **4**, 84–7.

ASTM (1996), 'Standard practice for acoustic emission monitoring during resistance spot welding', *American Society for Testing and Materials*, Standard E 751-96.

AWS (2002), 'Recommended practices for test methods for evaluating the resistance spot welding behavior of automotive sheet steel materials', *American Welding Society*, Standard D8.9M:2002.

AWS (2007), 'Specification for automotive weld quality – Resistance spot welding of steel', *American Welding Society*, Standard D8.1M:2007.

BATZINGER T J, FAIDI W I, RAMASWAMY S, MEETHAL M K K, OBERDOERFER Y, SPLITT G, ROYE W, BUECHLER J and CHANDRASEKHARAN R (2007), *System and Method for Monitoring a Weld Operation*, US Patent Application 2007/0 068 907.

BANERJEE G, PAL T K and MITRA A (2008), 'Magnetic hysteresis of resistance spot welded interstitial free steels', *Materials Evaluation*, **66** (9), 963–5.

BEKESHKO N A and POPOV Y U A (1972), 'Thermography used for the nondestructive inspection of spot welded joints', *Welding Production*, **19** (4), 93–5.

BROWN B and BANGS E (1986), 'The measurement and monitoring of resistance spot welds using infrared thermography', in *Proceedings of International Conference on Thermal Infrared Sensing for Diagnostics and Control* (Thermosense VIII), Kaplan H (ed.), SPIE Proceedings, SPIE, Bellingham, WA, **581**, 57–69.

BURBANK G E and TAYLOR W D (1965), 'Ultrasonic in-process inspection of resistance spot welds', *Welding J Supplement*, **44** (5), 193s–198s.

CHERTOV A M and MAEV R G (2004), 'Inverse problem solution to find real-time temperature distribution inside the spot weld medium using ultrasound time of flight methods', in *Review of Progress in Quantitative Nondestructive Evaluation*, vol 23, Thompson D O and Chimenti D E (eds), American Institute of Physics, Melville, New York, 1492–8.

CHERTOV A M and MAEV R G (2007), 'Acoustic microscopy of internal structures of resistance spot welds', *IEEE Transaction on Ultrasonics, Ferroelectrics, and Frequency Control*, **54** (8), 1521–9.

CHUKO W L and GOULD J E (2002), 'Development of appropriate resistance spot welding practice for transformation-hardened steels', *Welding J Supplement*, **81** (1), 1s–7s.

COHEN R L and WEST K W (1983), 'Nondestructive testing of spot-weld strength by electrical conductivity measurements', *SME Technical Paper*, IQ83-959.

CRAM M E and DODGE D D (1963), *Ultrasonic Inspection Method*, US Patent Office, Pat No 3 115 770, Dec 31, 1963.

CRECROFT D I and WARNER G (1969), 'Ultrasonic evaluation of electrical resistance spot welds', *Nondestructive Testing*, **2** (1), 40–3.

CROSTACK H A (1977), 'Investigations of the strength behavior of spot welds by means of acoustic emission analysis', *Schweisstechnik (Berlin)*, **27** (4), 187.

DASCH C J (2006), *Cylindrically-rotating Ultrasonic Phased Array Inspection Method for Resistance Spot Welds*, US Patent Office, Pat No 7 021 143, Apr 4, 2006.

DAVIS W B (2008), 'Predicting spot weld button area with an ultrasonic phased array', in *Review of Progress in Quantitative Nondestructive Evaluation*, vol 27, Thompson D O and Chimenti D E (eds), American Institute of Physics, Melville, New York, 731–8.

DENIS J F, DZALBA-LYNDIS S I, KUCHELBECKER R L and PETIT J A V (1979), *Process and Apparatus for Monitoring the Quality of Weld Spots Produced by Resistance Spot Welding*, US Patent Office, Pat No 4 168 430, Sep 18, 1979.

DENISOV A A, SHAKARJI C M, LAWFORD B B, MAEV R G and PAILLE J M (2004), 'Spot weld analysis with 2D ultrasonic arrays', *Journal of Research of the National Institute of Standards and Technology*, **109**, 233–44.

DEUTSCH K and WILKENS G (1968), *Method and Apparatus for Resistance Welding and Testing*, US Patent Office, Pat No 3 410 983, Nov 12, 1968.

DODGE D D (2009), personal interview, February 2009.

FASTRITSKY V S, FISHKIN P S, TIMOHOVICH E A and RIBALKIN E P (1973), 'The eddy current test of spot welds by means of surface probes', in *17th International Conference on Nondestructive Testing*, Warsaw, Poland, paper No D-15.

FLEMING M F and CLARK J P (2005), *Methods for Ultrasonic Inspection of Spot and Seam Resistance Welds in Metallic Sheets and Spot Weld Examination Probe System (SWEPS)*, US Patent Office, Pat No 6 948 369, Sept 27, 2005.

GARDNER N K and REDWOOD E A (1955), 'The radiography of spot welds in light alloy sheets', *Welding and Metal Fabrication*, **23** (7), 245–9.

GHAFFARI B (2007), 'Ultrasonic evaluation of aluminum spot friction welds,' *American Society for Nondestructive Testing Conference, Automotive Industry Advancements with NDT*, May 16–17, 2007, Dearborn, Michigan (abstract only).

GHAFFARI B, HETRICK E T, MOZURKEWICH G and REATHERFORD L V (2005), 'Ultrasonic evaluation of weld strength for aluminum ultrasonic spot welds', in *Review of Progress in Quantitative Nondestructive Evaluation*, vol 24, Thompson D O and Chimenti D E (eds), American Institute of Physics, Melville, New York, 1197–203.

GRUNDY D, ZILBERSTEIN V, GOLDFINE N, GREEN J and STOL I (2006), 'MWM®-array inspection for quality control of friction stir welded extrusions', in *Trends in Welding Research: Proceedings of the 7th International Conference*, David S, Debroy T, Lippold J, Smartt H and Vitek J (eds), ASM International, Materials Park, Ohio, 227–32.

HAIN R (1988), 'Resistivity testing of spot welds challenges ultrasonics', *Welding J*, **67** (5), 46–50.

HALL E T and CRECROFT D I (1971), 'Bonded joints and nondestructive testing: NDT of resistance spots, roll-spot, stitch, and seam welds', *Nondestructive Testing*, **4**, 181–91.

HAWKINS R and RABINOVICH S (2005), 'Ultrasonic inspection of resistance spot welding continues to progress', *Inspection Trends*, **8** (2), 30–3.

HEFFAN H J, MAUCH J W, SMITH R C and CUSICK J H (1967), 'Quality evaluation of missile structure spot-weld joints', *Materials Evaluation*, **25** (1), 15–19.

HETRICK E, JAHN R, REATHERFORD L, WARD S, WILKOSZ D, SKOGSMO J, DEVINE J, GRAFF K and GEHRIN R (2005), 'Ultrasonic spot welding: a new tool for aluminum joining', *Welding J*, **84** (2), 26–30.

HOPKINS D L, NEAU G N and DAVIS W B (2009), 'Welding process feedback and inspection optimization using ultrasonic phased arrays', in *Review of Progress in Quantitative Nondestructive Evaluation*, vol 28, Thompson D O and Chimenti D E (eds), American Institute of Physics, Melville, New York, 840–7.

IKEDA T, KARASAWA H, MATSUMOTO S, SATONAKA S and IWAMOTO C (2006), 'Development of new ultrasonic inspection technique for spot welds with matrix arrayed probe and SAFT', *Welding in the World*, **50** (5/6), 3–13.

JONES M (1999), 'NDT of resistance spot welds: trends and spikes', *Materials Evaluation*, **57** (12), 1243–8.

KAMINSKI R (1997), *Ultrasonic Testing of Spot-welded Joints on Coated Steel Sheets and Optimization of Welding Parameters*, Krautkrämer GmbH document SD 296. Accessed at http://www.spotweldtesting.com/schweisspunktpruefung.de/english/sd_296_en.pdf.

KOU S (2003), *Welding Metallurgy*, 2nd edition, Wiley-Interscience, Hoboken, New Jersey.

KRAUTKRAMER J and KRAUTKRAMER H (1990), *Ultrasonic Testing of Materials*, 4th fully revised edition, Springer, Berlin.

KRUGER U and LEHMANN K (1993), 'Microfocus x-ray technique – nondestructive test procedure for resistance welds of aluminum materials', DVS Berichte, No 154, in *Welding in Aerospace Industry, Proceedings of the 3rd International Conference*, Essen, Sept. 21–22, 1993, Kruger U (ed.), Dusseldorf, Germany, DVS-Verlag for Deutscher Verband fur Schweisstechnik, 104–8.

LAVRENT'EVA V M, SHAVROVA A M and VASIL'EV A S (1988), 'Magnetic method of inspecting spot welded joints', *Defektoskopiya*, **10**, 13–21.

LOZEV M, SPENCER R, HUANG T-C, PETERSON W and CRUZ J (2008), '2-D matrix phased-array examination of advanced high-strength steel resistance spot welds', in *Sheet Metal Welding Conference XIII*, AWS Detroit Section, Detroit, MI, paper 6-2.

LUPIEN V (2007), 'Principles of phased array ultrasound for nondestructive testing', *Materials Evaluation*, **65** (1), 24–32.

MACLAUCHLAN D T and LATHAM W M (2001), *EMATs for Spot Weld Examination*, US Patent Office, Pat No 6 250 163, Jun 26, 2001.

MACOVSKI A (1979), 'Ultrasonic imaging using arrays', *Proceedings of the IEEE*, **67** (4), 484–95.

MAETSCHKE S R (2002), *Analysis of Weld Image to Determine Weld Quality*, US Patent Office. Pat No 6 414 261, July 2, 2002.

MANSOUR T M (1988), 'Ultrasonic inspection of spot welds in thin-gage steel', *Materials Evaluation*, **46** (5), 650–8.

MATTING A and WILKENS G (1965), 'Testing of spot welds', *Ultrasonics*, **3** (4), 161–5.

MESSLER R W (1999), *Principles of Welding: Processes, Physics, Chemistry, and Metallurgy*, Wiley-Interscience, New York.

MIDORA T (1987), 'On-the-spot testing of welds', *Mechanical Engineering*, **109** (9), 76–8.

MOZURKEWICH G (2004), 'Nondestructive testing activities, needs, and trends in the automotive industry', in *16th World Conference on Nondestructive Testing*, Montreal. Accessed at http://www.ndt.net/abstract/wcndt2004/303.htm.

MOZURKEWICH G (2006), 'Measuring reliability of spot-weld nondestructive tests', *SAE Technical Paper* 2006-01-0090.

MOZURKEWICH G, GHAFFARI B and POTTER T J (2008), 'Spatially resolved ultrasonic attenuation in resistance spot welds: Implications for nondestructive testing', *Ultrasonics*, **48**, 343–50.

MUENOW R A (1965), 'A preliminary study of resistance welds by improved image conversion techniques,' *Materials Evaluation*, **23** (9), 449–52.

MÜLLER H-U and WASCHKIES E (2002), 'Securing spot-weld quality online in the body shop using ultrasound', in *2002 Annual Meeting of the German Society for Nondestructive Testing*, Weimar, (in German). Accessed at http://www.ndt.net/article/dgzfp02/papers/v48/v48.htm.

MURRAY E E (1967), 'Ultrasonic in-process control of spot welding quality,' *Materials Evaluation*, **25** (10), 226–30.

PAN T-Y (2007), 'Friction stir spot welding (FSSW) – a literature review,' *SAE Technical Paper* 2007-01-1702.

PAPADAKIS E P (1968), 'Ultrasonic attenuation caused by scattering in polycrystalline media,' in *Physical Acoustics: Principles and Methods*, Mason W P (ed.), vol 4B, Academic Press, New York, 269–328.

PAPADAKIS E P (1976), 'Ultrasonic velocity and attenuation: Measurement methods with scientific and industrial applications', in *Physical Acoustics: Principles and Methods*, vol 12, Mason W P and Thurston R N (eds), Academic Press, New York, 277–374.

PITTAWAY R G (1967), 'Ultrasonic testing of resistance spot welds', *Welding and Metal Fabrication*, **35** (11), 443–7.

POTTER T and GHAFFARI B (2007), 'Detailed ultrasonic and metallographic analysis of a cold resistance spot weld', *Ford Research & Advanced Engineering Technical Report*, SRR-2007-0210.

POTTER T J, GHAFFARI B, MOZURKEWICH G, REVERDY F and HOPKINS D (2006), 'Comparison of metallurgical and ultrasonic inspections of galvanized steel resistance spot welds,' in *Review of Progress in Quantitative Nondestructive Evaluation*, vol 25, Thompson D O and Chimenti D E (eds), American Institute of Physics, Melville, New York, 1786–93.

REGISTER J and SERVENT R (2009), 'Robotic ultrasonic test system for the inspection of spot welds', in *Sheet Metal Welding Conference XIII*, AWS Detroit Section, Detroit, MI, paper 6-3.

REVERDY F and HOPKINS D (2004), 'Inspection of spot welds using an ultrasonic phased array', in *Review of Progress in Quantitative Nondestructive Evaluation*, vol 23, Thompson D O and Chimenti D E (eds), American Institute of Physics, Melville, New York, 801–8.

REVERDY F and HOPKINS D (2005), 'Inspection of spot welds using a portable ultrasonic phased-array system', in *Review of Progress in Quantitative Nondestructive Evaluation*, vol 24, Thompson D O and Chimenti D E (eds), American Institute of Physics, Melville, New York, 1212–19.

ROBERTS D, MASON J and LEWIS C (2000), 'Ultrasonic spot weld testing: attenuation study,' *Insight*, **42**, 720–4.

ROBERTS D, MASON J and LEWIS C (2002), 'Ultrasonic spot weld testing with automatic classification', *Science and Technology of Welding and Joining*, **7**, 47–50.

RODEN W A (1968), 'Evaluation of resistance welding in-process monitors', *Welding J Supplement*, **47** (11), 515s–521s.

ROKHLIN S I and ADLER L (1985), 'Ultrasonic evaluation of spot weld quality', *Welding J Supplement*, **64** (7), 191s–200s.

ROKHLIN S I and BENDEC F (1983), 'Coupling of Lamb waves with the aperture between two elastic sheets', *J Acoustic Society America*, **73** (1), 55–60.

RWMA (2003), *Resistance Welding Manual*, Revised 4th Edition, Resistance Welder Manufacturers' Association, Philadelphia.

SATONAKA S and MATSUYAMA K (2000), 'Review on inspection techniques for spot welds', *Welding in the World*, **44** (3), 4–10.

SATONAKA S, TATSUKAWA I and YAMAMOTO M (1989), 'Ultrasonic measurement for nugget geometry of resistance spot welds of thin plates with imaging techniques', *Quarterly Journal of the Japan Welding Society*, **7** (3), 112–16 (in Japanese).

SCOTT G W and DODD C V (1982), 'Volumetric inspection of moderately thick austenitic stainless steels by multifrequency eddy current', *J Nondestructive Evaluation*, **2** (1), 23–33.

SHELLBERG T and SOKOLOWSKI F (2008), 'Benefits of using ultrasound to monitor spot weld quality in specific welding groups categorized as non-pryable in automotive sheet metal assemblies', in *Sheet Metal Welding Conference XIII*, AWS Detroit Section, Detroit, MI, paper 6-1.

SHEPARD S, CHAUDHRY B, PREDMESKY R and ZALUZEC M (1998), 'Pulsed thermographic inspection of spot welds', *Proceedings SPIE*, **3361**, 320–4.

SHUNG K K (2005), *Diagnostic Ultrasound: Imaging and Blood Flow Measurements*, Taylor and Francis, Boca Raton.

SOKOLOWSKI F, BUSCHKE P, LIU X, SU X, SHAYAN A R, ZHANG H, HERNER K and BOILARD R (2006), 'Using ultrasonic techniques to validate resistance weld quality of new automotive metals', in *Sheet Metal Welding Conference XII*, AWS Detroit Section, Detroit, MI, paper 8-4.

SPINELLA D J, BROCKENBROUGH J R and FRIDY J M (2005), 'Trends in aluminum resistance spot welding for the auto industry', *Welding J*, **84** (1), 34–41.

STOCCO D, MAEV R G, CHERTOV A M and BATALHA G F (2008), 'Comparison between in-line ultrasonic monitoring of the spot weld quality and conventional NDT methods applied in a real production environment', in *17th World Conference on Nondestructive Testing*, 25–28 Oct 2008, Shanghai, China, paper #318. Accessed at http://www.ndt.net/article/wcndt2008/papers/247.pdf.

TARBOX J P and CALLENDER E M (1948), *Weld Testing Apparatus*, US Patent Office, Pat No 2 433 963, Jan 6, 1948.

THORNTON P H, KRAUSE A R and DAVIES R G (1996), 'The aluminum spot weld', *Welding J Supplement*, **75** (3) 101s–108s.

TURLER D, HOPKINS D and REVERDY F (2003), 'Nondestructive evaluation of spot welds using acoustic and thermographic imaging techniques', *SAE Technical Paper* 2003-01-0980.

USAMP (2003), *Round-robin Evaluation of NDE Systems for Resistance Spot Welds*, a report prepared by Reverdy F, Hopkins D, Lawrence Berkeley National Laboratory for USCAR NDE of Welded Metals Industry Steering Committee AMD 303, Nov 2003.

USAMP (2009), *NDE Inspection of Resistance Spot Welds in Automotive Structures Using an Ultrasonic Phased Array*, final report for project AMD409 of the Automotive Metals Division of USAMP, 2009.

UTRATA D (1998), 'Quantitative guidelines for ultrasonic inspection of spot welds', *Materials Evaluation*, **56** (10), 1196–8.

VAHAVIOLOS S J (1984), 'Applications of acoustic emission to factory automation and process control', *Materials Evaluation*, **42** (13), 1650–5.

VOGT G, RIEGER D and KÖHLER C (2006), 'State of art in ultrasonic spotweld testing – Offline & inline – New materials and coatings', in *9th European Conference on Nondestructive Testing*, Berlin, Germany, paper Th.3.4.5. Accessed at http://www.ndt.net/article/ecndt2006/doc/Th.3.4.5.pdf.

WARD S, HETRICK E, BAER R, COOPER R, GRIMA A, HOUSTON D, KRAUSE A, MARIAM H, REATHERFORD L, SUBRAMANIAN S, WILKOSZ D, GHAFFARI B, MOZURKEWICH G, POTTER T, SCHOLL D, DONLON W, JAHN R, DEVINE J, MILLER M, WALSH J, BERD Z and EASTMAN J (2006), 'Part III: ultrasonic metal welding – enabling the all aluminum vehicle', *Ford Research & Advanced Engineering Technical Report*, SRR-2006-0127; work pursued under the National Institute of Standards and Technology ATP Award No 70NANB3H3015.

WASCHKIES E (2008), *Method for Evaluating a Weld Joint Formed During a Welding Process*, US Patent Office, Patent No 7 373 822, May 20, 2008.

WEERASINGHE V M and HAMEED S A (2001), *Monitoring of Resistance Welding*, World Intellectual Property Organization, Pat Application No WO 01/73 416 A1, Oct 4, 2001.

WESTGATE S A (1993), 'An evaluation of ultrasonic and electrical resistance methods for the non-destructive testing (NDT) of resistance spot welds in low carbon steel sheet', *TWI J*, **2**, 250–82.

WÜSTENBERG H, ROTTER B, KRAUSE H J and DEUTSCH V (1990), 'Ultrasonic testing of spot welds by means of imaging techniques', *Materialprüfung*, **32** (6), 171–4 (in German).

YANG L, SAMALA P R, LONG K W and LEE Y (2005), 'Non-destructive evaluation of spot weld using digital shearography', *SAE Technical Paper* 2005-01-0491.

YUASA H and MASAZUMI K (1996), 'Inspection device for spot welded nugget', in *Acoustic Imaging*, vol 22, Tortoli P and Masotti L (eds), Plenum Press, New York, 771–8.

ZHANG H and SENKARA J (2006), *Resistance Welding: Fundamentals and Applications*, Taylor and Francis, Boca Raton.

6

Solid state joining: fundamentals of friction stir welding

K. J. C O L L I G A N, Concurrent Technologies Corporation, USA

Abstract: This chapter introduces the basic concepts relevant to the use and study of friction stir welding, including an overview of the process, a comparison to arc welding processes, a discussion of welding tool design and materials, the effect of process parameters, workpiece materials and joint geometries. References are given to point to early contributions in the various areas of study and to the latest progress in the field.

Key words: friction stir welding, joining, solid state joining.

6.1 Overview of process principles

Friction stir welding (FSW) produces welds by using a rotating, non-consumable welding tool to soften a workpiece locally , through heat produced by friction and plastic work, thereby allowing the tool to 'stir' the joint surfaces. The dependence on friction and plastic work for the heat source precludes significant melting in the workpiece, avoiding many of the difficulties arising from a change in state, such as changes in gas solubility and volumetric changes, which often plague fusion welding processes. Further, the reduced welding temperature makes possible dramatically lower distortion and residual stresses, enabling improved fatigue performance, new construction techniques and making possible the welding of very thin and very thick materials. Owing to the typically high forces in the process, FSW is usually practiced as a fully mechanized process, increasing the cost of the equipment compared to arc welding techniques, while reducing the degree of operator skill required. FSW has also been shown to eliminate or dramatically reduce the formation of hazardous fumes and reduces energy consumption during welding, reducing the environmental impact of the joining process. Further, FSW can be used in any orientation without regard to the influence of gravitational effects on the process. These distinctions from conventional arc welding processes make FSW a valuable new manufacturing process with undeniable technical, economic and environmental benefits.

Central to the FSW process is the design of the welding tool, shown schematically in Fig. 6.1. Many variations and new features have been added
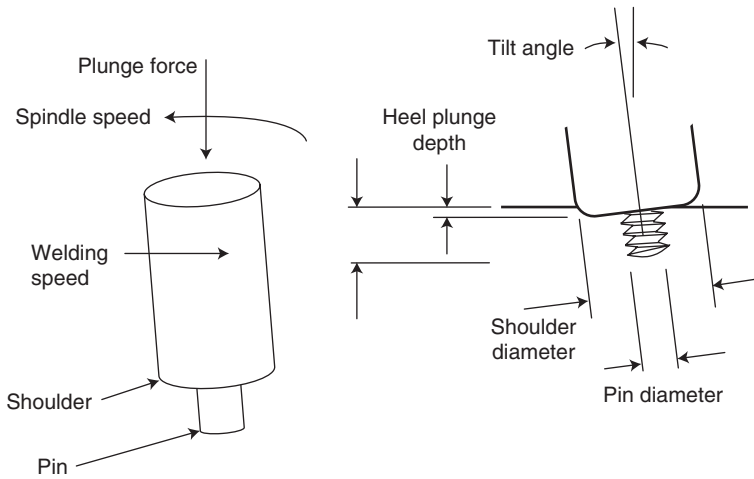
6.1 Conventional FSW tool and key variables.

to this basic tool, as will be discussed further below. Conventional FSW, as the process was originally conceived, is done with a welding tool consisting of a shoulder, which rides on the surface of the workpiece, and a smaller diameter pin, which nearly penetrates the workpiece. The shoulder essentially performs the role of the 'lid on the pot', which prevents the escape of softened workpiece material as the tool is rotated and forced along the joint. The pin commonly employs thread-shaped features which act to push the surrounding workpiece material downward, assisting in the retention of material within the weld zone. The downward force applied to the tool to maintain the correct plunge depth also results in forcible contact between the shoulder and the workpiece surface and relative motion from the tool rotation results in significant heat generation from friction at the shoulder interface.

In conventional FSW, the pin accomplishes the breakup of the original faying surfaces of the joint. For this reason, the pin must penetrate to within 0.5 mm of the back of the workpiece to ensure complete penetration of the weld through the workpiece. Features cut into the pin surface, originally demonstrated as downward-pushing screw threads, prevent the formation of pores or voids in the weld. The pin generates heat both by friction and plastic work, and both seizure and sliding contact have been observed and predicted by modeling results. The design of the pin and shoulder has been an area of intense research since the conception of FSW, which has resulted in improvement in throughput, joint strength and weld quality, and in the
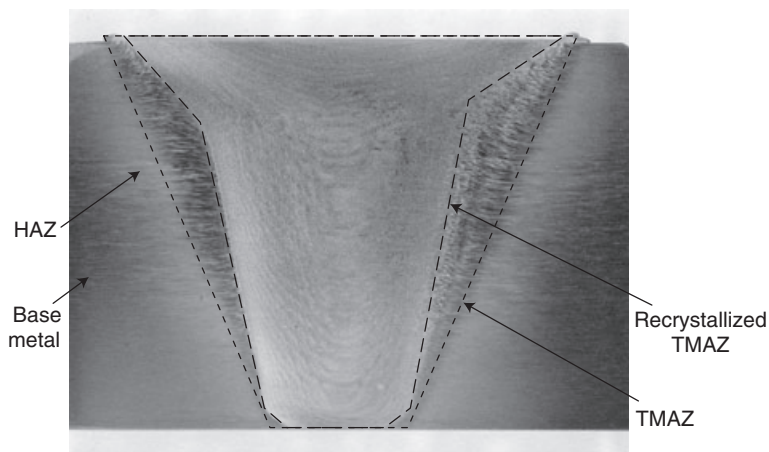
6.2 Typical conventional FSW transverse section in 25.4-mm thick 2195 aluminum–lithium plate.

range of materials, joint geometries, welding parameters and workpiece thickness that can be welded.

A transverse section from a typical, conventional FSW join is shown in Fig. 6.2. The weld is bounded on either side by unaltered base metal (BM). Although BM near the weld zone does experience elevated temperature during welding, this material exhibits essentially the same properties as the workpiece in the as-received condition. Closer to the weld is the heat affected zone (HAZ), which is heated sufficiently during welding to alter its properties without plastic deformation of the base metal's original grain structure. The alteration of properties in the HAZ may include changes in the strength, ductility, corrosion susceptibility and toughness of the workpiece, but typically will not include changes in grain size or chemical makeup. Heating in the HAZ is generally high enough in aluminum alloys to result in recovery of cold work and coarsening of precipitates, which is the root cause of changes in properties in this region.

The thermomechanically affected zone (TMAZ) encompasses all of the plastically deformed material within the joint region. In this region, the workpiece is sufficiently heated and softened and the process forces are sufficiently high to result in plastic deformation of the original grain structure. The TMAZ can be further divided into the unrecrystallized TMAZ and the nugget, or recrystallized TMAZ. In aluminum alloys, the unrecrystallized TMAZ may be an important feature in the weld, since it can be of significant size and can represent a region of low microhardness and
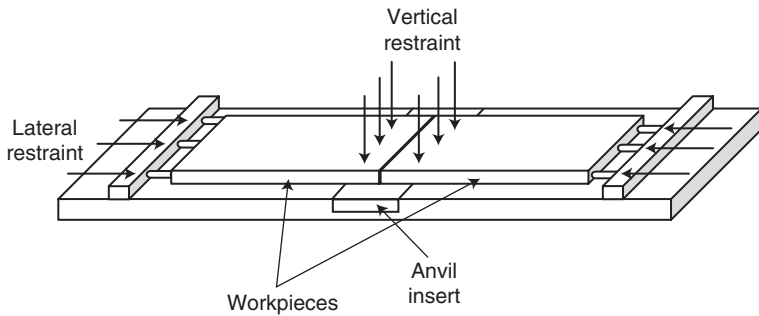
6.3 Conventional FSW fixture requirements.

increased corrosion susceptibility. Further, in aluminum alloys the nugget material is generally composed of fine grain size material and is considered to have experienced severe plastic deformation caused by interaction with the welding tool pin and in some cases may actually mimic the shape of the pin profile. However, in materials that experience thermally induced phase transformation, the TMAZ may consist entirely of recrystallized material, while in other materials the TMAZ may be completely unrecrystallized, without regard to the size or shape of the pin.

Conventional FSW is typically carried out by first rigidly fixing the plates to be joined in a welding fixture, as shown in Fig. 6.3. The plates are typically fixed with no gap at the joint line. The process requires that the workpieces be prevented from spreading or lifting during welding, so welding fixtures are typically equipped with features which restrain the workpiece. It is common for FSW fixtures to be equipped with a removable anvil insert, which can be replaced in the event of inadvertent damage to the anvil from contact with the welding tool pin. Since the anvil insert is very closely coupled to the workpiece at the point of welding in terms of heat transfer, it is important to consider the mass and diffusivity of the anvil insert when designing FSW fixtures.

The FSW process can be thought to consist of three phases: the plunge phase, where the weld is initiated, the main phase, where the weld is made and the termination phase, where the welding tool is withdrawn from the workpiece. The properties of the weld produced are, of course, dependent on the process parameters selected for each phase of the weld, so great care must be taken in establishing these settings.

The plunge phase consists of inserting or 'plunging' the rotating welding tool into the joint. This is typically accomplished by commanding the welding system to drive the tool pin axially into the workpiece at a specific rate or with a specific force. Frictional heating and pressure at the end of

the pin induce workpiece material to displace, forming a ring of expelled, plastically deformed material around the pin as the pin enters the workpieces. As the tool is plunged into the joint, the heat generated is conducted into the surrounding material and the anvil. The plunge phase may be facilitated by drilling a hole at the plunge location, reducing the heat and forces produced. Alternatively, the welding tool may be plunged into the side of the workpiece, although this approach is less commonly applied. Once the welding tool is plunged into the workpiece, the tool is typically driven laterally along the join without delay, although in some materials, it may be necessary to dwell at the plunge location for some time in order to allow the welding tool and workpiece to reach a higher temperature.

Once the welding tool begins to travel along the joint, friction and plastic work produce heat to maintain sufficient softening in the workpiece to permit material flow around the pin. Features cut into the pin surface, such as screw threads, flats and spiral grooves, facilitate this material flow by increasing drag between the pin and the surrounding material in such a way as to prevent the formation of internal voids or fractures. Heat from the welding process is conducted within the workpiece, serving to precondition the material in front of the tool, producing softening from recovery of work hardening and overaging in materials such as aluminum. This metallurgical alteration may be slight, such as when welds are made at very high travel speed, or it may dramatically soften the workpiece. As this preconditioned workpiece material interacts with the features cut into the welding tool, the material is rapidly deformed and heated by quasi-adiabatic friction and plastic work, raising the temperature to near the solidus temperature, but macroscopically not above it. Simultaneously, this material is pulled around the welding tool and deposited behind it in a way that prevents the formation of voids.

It should be noted that the main phase of the weld can be thought of as consisting of an initial period, where the temperature distribution within the welding tool and workpiece is being established, a steady-state period, where the temperature distribution is stabilized and a terminal period, where the temperature distribution is altered by the approaching workpiece boundary. Depending on the welding conditions, the initial and terminal periods may be of different durations and may or may not practically influence the joint produced.

As the welding tool arrives at the end of the joint, forward motion of the tool is typically stopped and the tool is withdrawn from the workpiece, leaving a keyhole at the end of the weld. Alternatively, the tool can be run out the end of the workpiece, producing a tear-out. In either case, the end of the weld is generally not usable and must be trimmed away by sawing or machining. For this reason, it is common to use run-on and run-off tabs at the ends of the joint to facilitate trimming the unusable material.

6.2   Comparison to other welding processes

Comparison of FSW to other welding processes is typically done within the context of justifying the use of the process over other, more conventional techniques. Successful application of FSW depends upon a clear understanding of the characteristics of the process, so that favorable technical and economic justification can be developed. The details of each welding application will dictate the basis for the justification, so in this section the many considerations for technical and economic justification of FSW implementation will be described.

6.2.1   Technical justification of friction stir welding

The unique, favorable characteristics of FSW compared to traditional arc welding methods provide several sources of technical justification for use of the process. One key for successful implementation of the process is a clear understanding of the technical improvements offered by FSW, balanced against the requirements of the process.

The main points for technical justification of FSW compared to arc welding processes are:

- improved weldability
- reduced distortion
- reduced residual stress, improved fatigue, corrosion and stress corrosion cracking performance
- improved cosmetic appearance
- elimination of undermatched filler metal
- improved static strength and ductility
- mechanized process
- high robustness, few process variables.

Each of these technical justifications must be balanced against the unique technical requirements of the process, such as:

- mechanized process
- special fixture requirements
- joint design limitations
- keyhole at end of weld.

Each of these technical points will be discussed briefly, followed by a discussion of the economic justification issues in the following section.

Improved weldability

Since FSW is a solid state process, weldability in certain materials can be improved. This is especially the case in certain aluminum alloys. Some alu-

minum alloys or material forms, such as castings, are difficult or impossible to weld by traditional arc welding processes owing to problems with the formation of brittle phases and cracking. For these alloys, weldability alone may be sufficient to form a justification for the use of FSW over conventional arc welding or other joining techniques, such as mechanical fasteners. Further, FSW makes possible the joining of some dissimilar alloys, which can be of significant benefit in certain applications.

Reduced distortion

The reduced peak temperature reached in FSW compared to arc welding processes also generally leads to reduced longitudinal and transverse distortion, although FSW weldments are certainly not free of residual stress. The balance of residual stress in FSW can result in essentially flat weldments in materials of virtually any practically weldable thickness, although this is affected by welding tool design, joint design, welding parameters and fixture design. This characteristic of FSW makes possible new methods of construction and can significantly affect the total cost of manufacturing an assembly through reduced fit-up problems and secondary machining operations.

The earliest production applications for FSW were based on its use for making products from extruded aluminum shapes, as shown in Table 6.1. The business model for these applications was based on the use of FSW to produce very flat, integrally stiffened assemblies from relatively narrow

Table 6.1 Chronology of production applications for FSW, until 2004

Year	Application	Company
1995	*Hollow heat exchangers	Marine Aluminum, Norway
1996	*Commercial shipbuilding	Marine Aluminum, Norway
1998	Delta II rockets	Boeing, USA
1999	*Commercial shipbuilding	Sapa, Sweden
2000	*Automotive components	Sapa, Sweden
2000	Laser system housings	General Tool, USA
2001	*Motor housings	Hydro Aluminum (formerly Marine Aluminum), Norway
2001	*Automotive components	Showa, Japan
2001	*Train bodies	Hitachi, Japan
2002	*Automotive components	Tower Automotive, USA
2003	Aircraft structure	Eclipse, USA
2003	*Commercial shipbuilding	Advanced Joining Technologies, USA
2004	Space shuttle external tanks	Lockheed Martin, USA
2004	Food trays	RIFTEC, Germany

*Denotes welding of extrusions.

aluminum extrusions. In this case, FSW was justified, based on the fact that had arc welding processes been used, the weldments would have been so distorted as to render them unserviceable.

Improved fatigue, corrosion and stress corrosion cracking performance

The reduced maximum temperature and residual stress also can lead to improved performance under cyclic loading conditions.[1–3] Typically, joints produced by FSW have fatigue strength that is higher than arc welded fatigue strength, but below base metal strength. FSW joints that are machined after welding have been shown to approach base metal fatigue strength. FSW has been justified on the basis of fatigue performance, in concert with economic factors, over the use of mechanical fasteners, such as in its use on the Eclipse aircraft[4] and in other aerospace applications.[1,3,5,6] The reduced residual stress and peak temperature can also improve general corrosion and stress corrosion cracking problems in aluminum alloys. Although this is not generally sufficient as a driver to justify the use of the process, it could in some long service life applications prove to be an enabling technology.

Improved cosmetic appearance

The root side of conventional friction stir welds has been shown to be extremely smooth and flat in a variety of materials and thicknesses. After painting, the root side of the joint can be virtually invisible. This has played a role in justifying the use of the process over other joining processes in commercial shipbuilding, in aircraft manufacture and in the production of food trays.

Elimination of under matched filler metal

In some materials there are no available filler metals for arc welding that match or exceed the strength of the surrounding base metal. However, FSW is an autogenous welding process, obviating the need for filler metals. In these materials it has been demonstrated that improved joint strength and/ or ductility can be achieved with FSW over arc welding processes. The elimination of filler metal in FSW also leads to cost avoidance by eliminating the need for a wire feeding system and improved joint consistency by eliminating problems with wire feeding that can occur in arc welding processes.

Improved static strength and ductility

Even in cases where adequate filler metals are available, the higher temperature reached and limited material deposition rates in arc welding can

degrade the HAZ sufficiently to reduce the joint strength compared to FSW. It is often the case in thin section aluminum alloys that the joint strength in arc welding and FSW are comparable. However, in thick materials, up to 75 mm thick, the fact that FSW can be accomplished in a single pass can result in significantly improved joint strength and ductility. In some applications, this may be sufficient to justify the use of FSW over arc welding and mechanical fastening.

Mechanized process: technical justification

FSW is typically operated as a completely mechanized process, as described further below. While this can lead to increased capital cost compared to arc welding and mechanical fastening techniques, the mechanized nature of the process leads to improved joint path control and more consistent quality than manually operated processes. The improvement in joint quality alone may be sufficient to justify the use of FSW, especially in applications that demand very high joint quality, such as in the construction of launch vehicles and other aerospace structures.[7]

While FSW offers many technical bases for justification of its use, there are also unique technical requirements that may offset its technical benefits to some degree. Some of the main technical requirements that must be considered are described below.

High robustness, few process variables

Although the relative newness of FSW can make it seem complex, the fact remains that FSW has relatively few process variables compared to conventional arc welding processes, making it fundamentally a simpler process to describe and operate. This relative simplicity can contribute to the overall technical justification of the process. The process variables of FSW are all easily controllable, leading to a relatively stable process. Also, since heat input in FSW is fundamentally driven by the response of the workpiece to these relatively simple, controlable process parameters, the process stability is far superior to arc welding processes, where heat input is the result of numerous independent variables. This, in turn, leads to the characteristically low defect rates of FSW, which can be a central feature of the technical justification of the process.

Mechanized process: technical requirement

The fact that FSW is a mechanized process was described above as a positive factor in justifying the process for production use. At the same time, the process forces generated during FSW are typically too high to permit

hand operation. In the case of very thin materials, the forces may be sufficiently low to permit manual operation, but typically the welding tool is so small in these cases that mechanical means are needed to maintain accurate tool path control to consume the joint. Certainly, in thick materials FSW can only be operated as a mechanized process. For example, for 25-mm thick 5083 aluminum plate, it may be necessary to apply a force of 44 kN along the tool's rotation axis to keep the tool embedded in the workpiece, while simultaneously pushing the tool laterally with a 15 kN force and applying a torque of about 360 N-m.[8] The forces for thinner sections are understandably lower, for example, for 8-mm thick 2195-T8 aluminum, a force of about 40 kN along the tool axis and 4 kN in the travel direction would be typical.[9] As a result, relatively expensive, custom made equipment is often necessary for production use of FSW. Although new, lower cost equipment is currently being developed for some applications, the high capital cost is often a significant barrier to developing the business case for the use of FSW. As a result, it is often necessary to develop the application as a nearly continuous production operation, maximizing the economic value of goods produced by the process.

Special fixture requirements

As mentioned earlier, FSW requires that the workpiece be rigidly held in position during welding, to ensure that the joint does not separate under the force of the welding tool and to ensure that the workpiece stays in intimate contact with the anvil during welding, thus achieving a smooth weld. Although the special fixture requirements of FSW do impose an economic burden on the justification of the use of the process, which will be discussed below, fixture requirements also place a practical restriction on the size of workpiece that can be produced. For example, the requirement to restrain the workpiece against the anvil may make it difficult to secure very large and thin workpieces, or the requirement to restrain lateral separation of the joint can be difficult for very thick workpieces. These are surmountable requirements, but ones which must be considered.

Joint design limitations

Since FSW is an autogenous process, it is impossible to make what is generally considered a fillet weld, where a significant amount of material is added to fill a transition between two workpieces. Although it is possible to form a small fillet during FSW of plates at some angle, this is usually achieved at the expense of material from the joint. Typically, FSW is used to produce butt welds, corner welds and lap welds, as shown in Fig. 6.4.
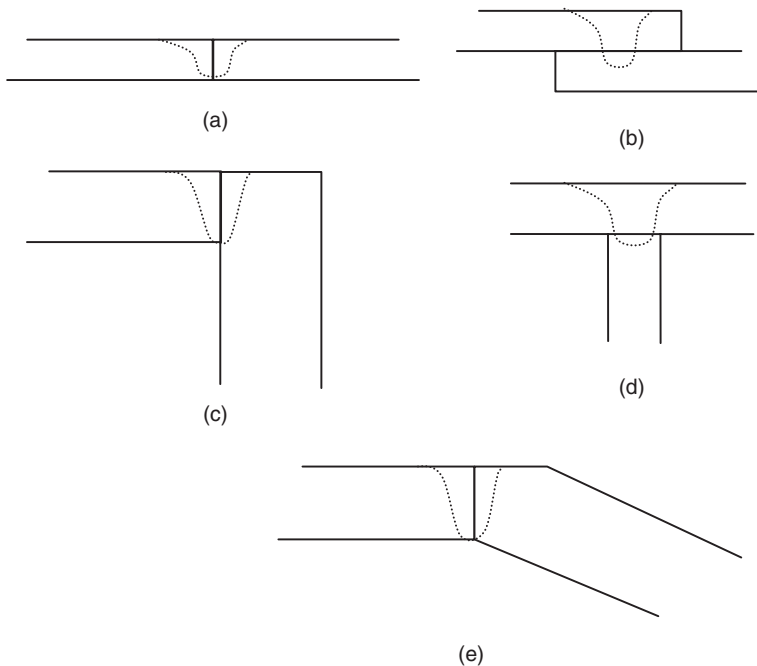
6.4 Common FSW joint configurations: (a) straight butt joint, (b) lap joint, (c) 90° corner joint, (d) T-joint, (e) oblique angle joint.

Weld keyhole

FSW is a keyhole welding process, as described previously. As a result, in some applications it is necessary to consider how the welded joint will be started and terminated to result in a serviceable assembly, such as in the construction of cryogenic fuel tanks and in welding marine structures. Typically, the start and stop ends are cut away from the main portion of the assembly and discarded. Alternatively, run-on/run-off tabs may be used to reduce the loss of base metal. For structures such as sealed tanks, it may be possible to use friction tapered plug welding, arc welding, or even a sealed fastener to eliminate the keyhole.

6.2.2 Economic justification

The positive and negative aspects of economic justification of the use of FSW over more traditional methods are briefly discussed in this section. Very few published studies have been produced that give details of the economic justification of FSW, presumably because every application has a unique justification and it is difficult to develop a general cost model. In

spite of this, some publications have addressed the economic justification of FSW by presenting case studies.[10–12] The main factors in economic justification for FSW are:

- processing time/labor,
- licensing,
- capital investment,
- production volume,
- robustness – low defect rate.

Other factors play a lesser role in the economic impact of FSW. These secondary factors include the elimination or reduction of conventional welding consumables, such as shielding gas and filler metal, the increased cost of friction stir welding tool, itself a consumable item, the reduced production of fumes and the reduced energy consumption. In this section the main economic factors in the justification of FSW are described.

Processing time/labor

There are a number of factors that contribute to the reduced processing time and direct labor that can be expected from the use of FSW. FSW can often be accomplished in a single pass compared to the multiple passes often required for arc welding processes, especially as the workpiece thickness increases. Each pass in arc welding can require interpass cooling time, cleaning, inspection and repair, and may require rotation of the workpiece to allow welding from the opposite side. Further, the superior cosmetic appearance of friction stir welds can lead to reduced manufacturing costs associated with post-weld processing.

Licensing

At the time of this writing, FSW is a patented process in many countries,[13] and a license fee must generally be paid for its use. The specific terms are restricted from publication by agreement with TWI, the owner of the intellectual property rights to the process. That said, the license fee for the use of the basic process is a significant factor in the economic justification of the use of the process and should be considered until the time of expiration of the patents.

Capital investment

FSW is a fully mechanized process, so naturally the process is limited by the capabilities of the equipment used. This includes the welding system that rotates the welding tool and traverses it along the joint and the welding

fixture used to restrain the workpiece during welding. Owing to the high forces generated by the process, the equipment and fixture can represent a significant cost, especially for large or thick section workpieces. Some welding system providers have recognized that the capital investment required for FSW is prohibitive for many applications and are developing low cost approaches for FSW equipment. As an alternative, there are several FSW service providers that can produce welded products without imposing the burden of capital investment on a single production application.

Production volume

Production volume is a factor in the economic justification of FSW in the way that it amplifies savings from labor and processing time and distributes fixed costs from licensing and capital investment. In some applications, the production volume may make traditional arc welding processes impractical simply because of limitations in the available skilled workforce.

The combined effect of technical and economic justification for the process is essential for the successful implementation of FSW in the production environment. This justification has been successfully demonstrated in several industries, as evidenced by the list of early production applications presented above in Table 6.1. The expiration of the FSW patents and the development of lower cost FSW equipment and fixtures will, over time, ease the fixed costs associated with implementation of the process and will improve the business case even further.

6.3   Welding tools

Since its original development, friction stir welding advances have often been driven by the development of new welding tools and new welding equipment. The development of welding tools has two aspects: the development of welding tool designs and the development of welding tool materials, which will be introduced in this section.

Welding tool designs can be divided into two main classes, conventional and bobbin. Conventional FSW tools approach the workpiece from one side, typically while the workpiece is restrained on an anvil. This type of tool only partially penetrates the workpiece, leaving a very thin gap between the end of the pin and the anvil. Material which passes through this gap is plasticized to a sufficient degree to ensure complete consumption of the original joint, when the pin ligament is maintained.

In contrast to the conventional FSW tool, bobbin FSW tools consist of two shoulders which are connected by the pin, all of which typically rotate in unison. The two shoulders act to contain the softened weld metal from either side, as shown in Fig. 6.5, while generating heat from friction and

Pin connects shoulders
(obscured from view by
workpiece)

Spindle-side shoulder

Workpiece

Back-side shoulder
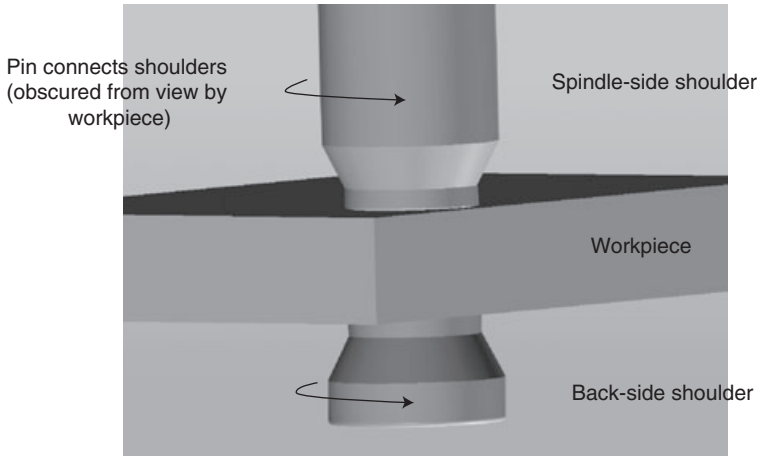
6.5 Bobbin FSW tool.

plastic work. The action of the pin is primarily to distort the faying surfaces and generate additional heat to sustain the process while providing the mechanical connection between the shoulders. Bobbin FSW tools can allow the production of welds without imparting force normal to the workpiece plane and they eliminate the possibility of incomplete penetration of the weld to the anvil side of the workpiece.

There are two further subdivisions of bobbin tool designs, as shown in Fig. 6.6. Although the notion of a bobbin tool was first described in the original patent filing for FSW,[13] it was never practically demonstrated in its original form. The original bobbin tool consisted of a pair of smooth, bare shoulders that tapered outward, presumably to ensure contact with the workpiece surfaces in the event of random or planned variation in the workpiece thickness. A workable bobbin FSW tool was later developed in which flat shoulders were supplemented with spiral grooves or scrolls which acted to pull workpiece material toward the pin.[14–20] The shoulders were forcibly actuated relative to each other in order to provide a variable gap between the shoulders, which facilitated the development of controllable compressive force between the shoulders, even in the case where workpiece thickness varies along the length of the weld. This type of tool requires a mechanism to actuate the welding tool's pin in order to achieve the variable shoulder gap. This variable shoulder gap bobbin tool, known as a self-reacting tool, has been demonstrated to produce sound welds in a wide variety of material thicknesses and alloy selections. Later, a practical fixed gap bobbin tool was demonstrated, eliminating the need for a mechanism to actuate the welding tool pin. This tool, known as a tapered shoulder tool,
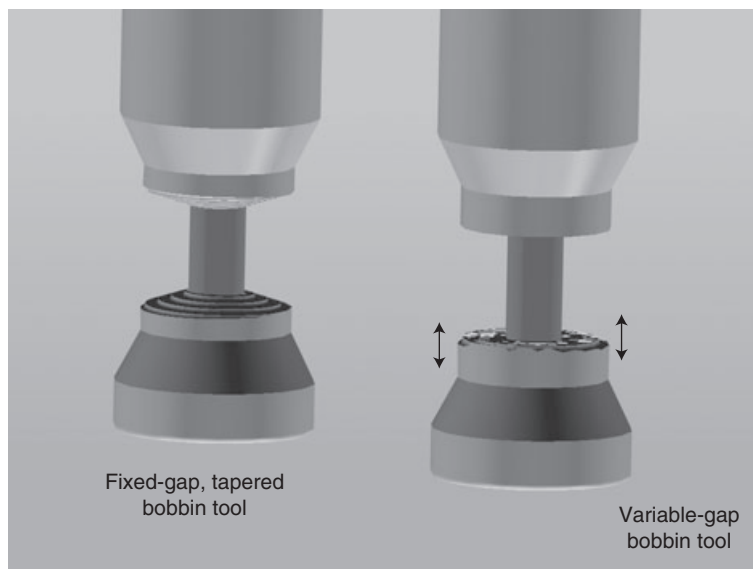
6.6 Variable and fixed gap bobbin FSW tools.

has also been demonstrated to produce welds in a variety of materials.[21,22] The tapered shoulder tool takes advantage of a protruding shoulder profile combined with spiral shoulder scrolls to produce in a tool that has variable shoulder penetration and variable effective shoulder width. Variations of this tool employ non-linear shoulder profiles.

Welding tool features have been introduced over time to produce a number of desirable effects and new tool design features are continually being introduced. Table 6.2 shows a summary of some of the key FSW tool design features that have been developed to date, along with appropriate references. Various combinations of these design features make possible a wide variety of conventional and bobbin FSW tools.

In addition to welding tool design features, welding tool 'motions' have been developed as a means of achieving desirable effects in weld formation. These have primarily been introduced by TWI and include variations such as 'Skew Stir' (tool axis inclined relative to axis of rotation), dual-rotation FSW (pin and shoulder rotate at different speeds or in different direction), 'Re-Stir' (tool rotation direction periodically reverses), 'Com-Stir' (compound motion of tool rotation and tool axis orbit) and tandem FSW (two tool operating in tandem).[23] These tool motions have been shown to give different material flow patterns during welding, yielding improved weld formation, for example, to improve lap weld performance.

Table 6.2 Summary of key welding tool design features

Feature	Intended effect	Examples
Threads on pin	Compression of weld zone against anvil	
Flats or other re-entrant features	New mode of plastic work, thicker section welding, higher heat input	
Flat pin tip	Improved TMAZ penetration, higher penetration ligaments, better robustness	
Frustum pin profile	Reduced lateral forces, thicker section welding	
Flare pin profile	Wider root profile	
Shoulder scrolls	Elimination of tool tilt requirement, containment of softened workpiece material	
Tapered shoulder	Variable shoulder contact width, variable shoulder penetration	
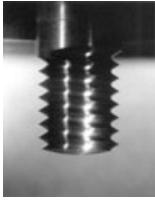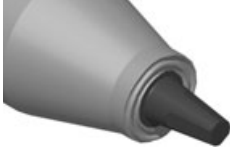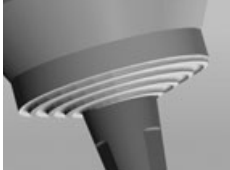
New welding tool materials have been introduced in order to increase the strength of the welding tool's pin, to manage thermal conduction,[24] and to permit welding of high melting point materials. Although aluminum alloys can be friction stir welded using inexpensive tool steel, such as H13, in order to maximize production rate and tool life, it is necessary to use materials that have high strength at the temperature of welding, such as

MP159. Copper is commonly welded using Nimonic 105 and Densimet for the pin and shoulder materials, respectively.[25–27] Titanium is generally welded using refractory metals, such as lanthanated tungsten or tungsten rhenium tools.[28] Steel is also welded with tungsten-based tools, or with tools made from polycrystalline cubic boron nitride (PCBN).[29,30] In addition, tool coatings are occasionally used to improve the wear or chemical resistance of tools.[31]

Certainly, welding tool design and material selection are important considerations in developing a successful friction stir welding process. Careful consideration must be given to tool cost, useful life and the limitations that the tool strength might place on the welding speed. The development of new welding tool designs and materials has been an active area of research in the past, leading to expansion of the utility of the process and this trend likely to continue in the future. As a result, attention to the latest advancements in welding tool construction is important for optimizing performance in any FSW application.

6.4   Parameter effects

While the general principles of the effect of process variables on the friction stir welding process have much in common with other welding processes, the details are completely different, as one might expect. The main process variables in friction stir welding are listed in Table 6.3.

These variables all act to determine the outcome of the welding process. The main interest in studying the effect of the process variables lies in understanding the effect of the process on joint properties, including static mechanical properties, fatigue strength, corrosion properties, stress corrosion cracking resistance and toughness, with the goal of maximizing productivity, performance and reproducibility. The welding process affects these joint properties primarily through heat generation and dissipation, so primary attention should be given to the effect of the welding process

Table 6.3 Main FSW process variables

Tool design variables	Machine variables	Other variables
Shoulder and pin materials	Welding speed	Anvil material
Shoulder diameter	Spindle speed	Anvil size
Pin diameter	Plunge force or depth	Workpiece size
Pin length	Tool tilt angle	Workpiece properties
Thread pitch		
Feature geometry		

variables on heat generation and related outcomes. Other areas of study include the effect of process parameters on material flow, defect formation, process forces, grain size, and so on.

Numerous experimental and computed model studies into the effect of process parameters on heat generation have been published since the process was first introduced.[8,9,32–46] This work has demonstrated that, while FSW may seem at first to be a simple process, the fact that the process is a fully coupled thermomechanical process can lead to counterintuitive relationships between variables and in the resulting material flow. In arc welding the heat input is determined entirely by controllable machine parameters (voltage and current), while in FSW the temperature-dependent workpiece properties are important in determining the heat input, which in turn affects the workpiece conditions. As a result, seemingly unrelated variables can participate in the heat generation process. For example, the anvil size and material can have a dramatic effect on process forces and heat generation in FSW, based on their role in thermally preconditioning the workpiece material in advance of the welding tool. This self-referential relationship contributes to the stability of the welding process, but at the same time it complicates the determination of the effect of process variables on heat generation. Further, the fact that FSW is a fully coupled thermomechanical process means that one must carefully consider the unintended effect on interconnected variables when making a change to the process, such as when moving a process developed on one piece of equipment to a new welding system.

6.5   Materials

Friction stir welding has been shown to be effective in joining a number of different materials. Although aluminum was the first material to be friction stir welded, over time it has been shown that many of the benefits demonstrated for aluminum can also be seen in welding other materials, such as steel, titanium, copper, magnesium and lead. However, welding of high melting point materials is made more difficult by the harsh operating conditions placed on the welding tool material. As a result, while many materials can be friction stir welded, performance and economic justification must be developed in order to make practical use of the process.

No studies have been performed to define the specific characteristics that a material must have in order to be weldable by FSW, but examination of the characteristics of FSW in aluminum suggests some very general requirements for welding of other materials. For example, it is clear from FSW of aluminum that thermal softening of the workpiece material is necessary for the welding process to commence, so it is reasonable to expect that in other materials the welding process will take place at a temperature that is near

the material's melting point. This also implies that it is necessary that heat be generated with sufficient intensity to overcome the loss of heat from the welding zone through conduction into the workpiece. Another consideration is the need to achieve heat generation, either by friction, plastic work, or by auxiliary heating, at the full spectrum of temperatures from the initial material temperature up to the welding temperature. Although it is not normally needed for FSW of aluminum, a shielding gas may be needed for some materials to prevent reactions with atmospheric gasses.

In high melting point materials it appears that the main limitation to weldability is the availability of suitable welding tool materials. The development of new welding tool materials and geometries has made it possible to join materials such as steel and titanium in the laboratory environment and in a limited number of production applications.[47] In FSW of steel it has been shown that the lower welding temperature can lead to very low distortion and unique joint properties.[29,30,48,53] FSW of steel is an area of active research, so it is reasonable to expect other production applications to emerge over time. A very attractive application is FSW of steel plate for shipbuilding applications, based primarily on the reduction in welding distortion, but the development of low cost welding equipment and more robust welding tool materials is required before this application can be exploited.

Titanium alloys are generally considered to be weldable by fusion welding processes, but FSW is of interest as a joining method for some specific titanium-based alloys, for some product forms, such as castings, and for some alloy combinations which are more difficult to fusion weld.[28,54,55] Friction stir welding of titanium has been demonstrated in the laboratory environment and it has been used in the construction of relatively large prototype structures. Although titanium is considered a high melting point material, its low thermal conductivity makes it necessary to reduce the heat input of the tool design, either by minimizing the shoulder diameter or by eliminating shoulder rotation altogether.[56,57] Friction stir welding of titanium is presently an area of active research, which may ultimately lead to production applications.

Friction stir welding of copper has been developed for several years in the construction of canisters for storing nuclear waste.[25–27] In this application, which requires very low defect rates, FSW was selected over electron beam welding for welding 50-mm thick circumferential joints for attaching canister lids. Although it was initially thought that FSW of thick copper would be adversely affected by the high thermal conductivity, it has been found that, by using a relatively high spindle speed, sufficient heat intensity can be developed to accomplish sound, high quality welds.

Several other materials have been joined using FSW in the laboratory environment and the evaluation of weldability in new materials is an area

of ongoing research.[58,59] Also, some work has been done recently to demonstrate the use of FSW to join dissimilar materials, such as aluminum to steel.[60,61] Certainly, it is conceivable that titanium could be welded to aluminum using a similar approach. The development of technical or economic justification is required to move the FSW of these materials to the production floor.

6.6   Joint geometries

A variety of joint geometries are possible with FSW; however, there are certain limitations and requirements that are unique to the process. Since FSW is an autogenous welding process, some types of joint, such as fillet welds, are fundamentally impossible with FSW, although fillet welds can be simulated by special material or fixture designs, as will be discussed below.

A summary of common joint geometries is presented in Fig. 6.7. The figure also shows typical anvil sections for each joint type, since anvil and fixture requirements are closely related to joint design. It is assumed in these diagrams that the anvil sections are rigidly mounted relative to the workpieces. Certainly, other joint geometries are possible. In each of these joint designs and fixture arrangements, it is necessary to:

- provide sufficient area for the welding tool's shoulder path
- provide sufficient containment of softened weld metal
- provide sufficient force to prevent motion of the workpieces and
- provide an adequate heat sink to dissipate the heat of welding.

The area required for the welding tool's shoulder is a function of material thickness and alloy. Typically, for aluminum alloys, the area required for the shoulder is about three to five times the material thickness. Steel and titanium typically would require less shoulder area, since these materials have lower thermal conductivity and therefore require a smaller shoulder diameter.

Containment of softened weld metal is necessary along the full length of FSW joints. Machined details, such as drilled holes or pockets, that are very close to a weld joint should be avoided or temporarily plugged during welding to provide additional heat sink and to prevent softened material from pushing out. One exception to this rule is the case where an anvil is specifically designed with rounded corners to produce a small fillet, as shown in Fig. 6.8. Here, the fillet is kept small so that the workpiece material that pushes into the void does not result in internal voids in the weld. This corner radius acts to reduce the stress concentration in the corner.[62]

As indicated in Fig. 6.7, it is necessary forcibly to constrain the workpiece components from motion under the process forces. Test data that indicate the magnitude of the force required are almost non-existent, so experience
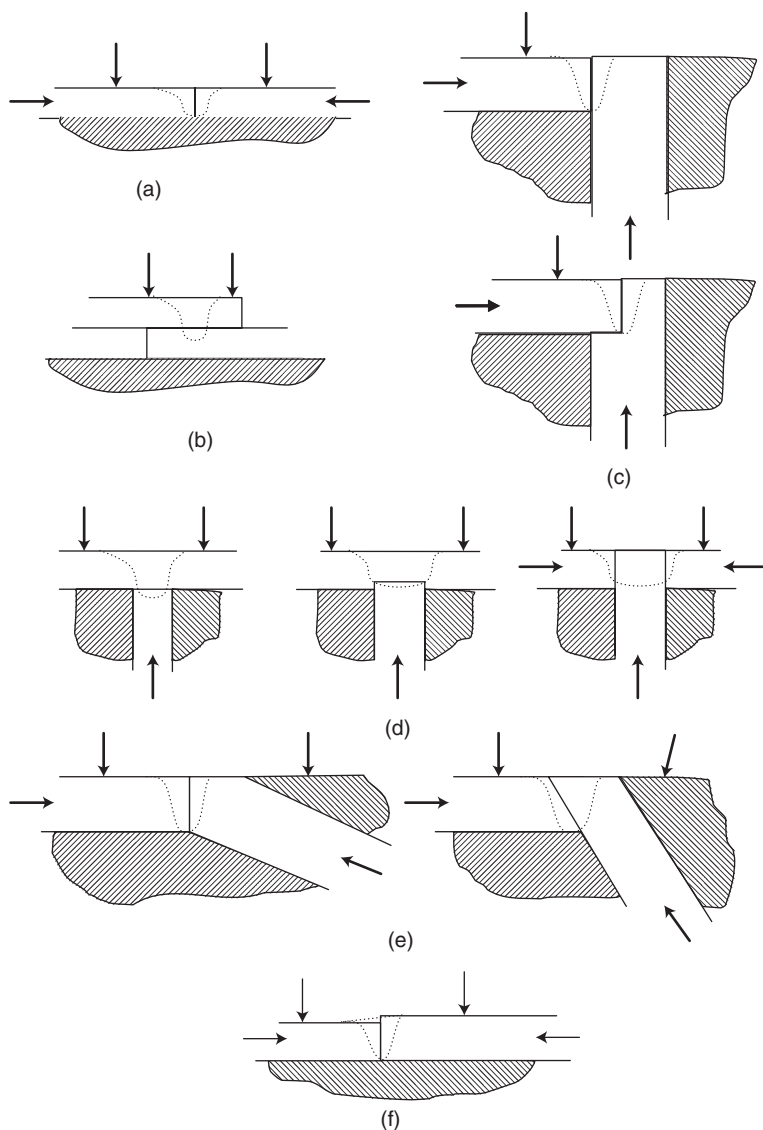
6.7 Summary of common joint designs with anvil sections and fixture force requirements. (a) Straight butt joint, (b) lap joint, (c) 90° corner joints, (d) T-joints, (e) oblique angle, (f) butt joint with mismatch.

and trial-and-error approaches are necessary for this aspect of fixture design. An example of the negative effect of inadequate fixture force is 'drop-out' which is the result of inadequate vertical force in a butt weld, preventing the workpiece from lifting from the anvil, as shown in Fig. 6.9.
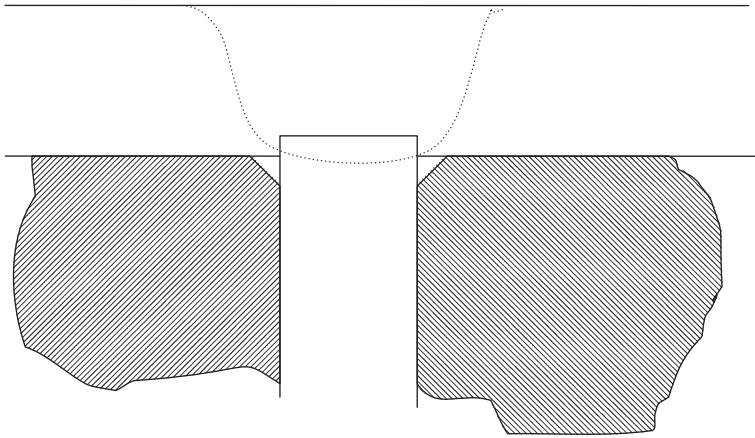
6.8 Anvil corner for producing small fillets.

Example of drop-out on right side of weld, 6 mm 2094 aluminum FSW, transverse view
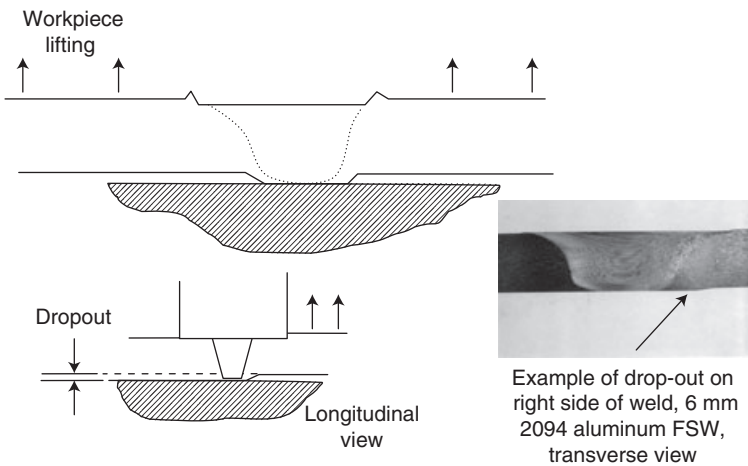
6.9 Drop-out in a butt weld produced by inadequate vertical holding force on the workpiece.

This commonly occurs at the start of welds, where the process of plunging the welding tool pin into the workpiece tends to bulge the back of the workpiece and lift the surrounding material off the anvil. Once this has occurred, it is very difficult to get the workpiece back into contact with the anvil, since forward motion of the tool tends to push the drop-out in advance of the pin. As a result, drop-out is much better prevented in advance by good fixture design, rather than trying to resolve it during a weld.
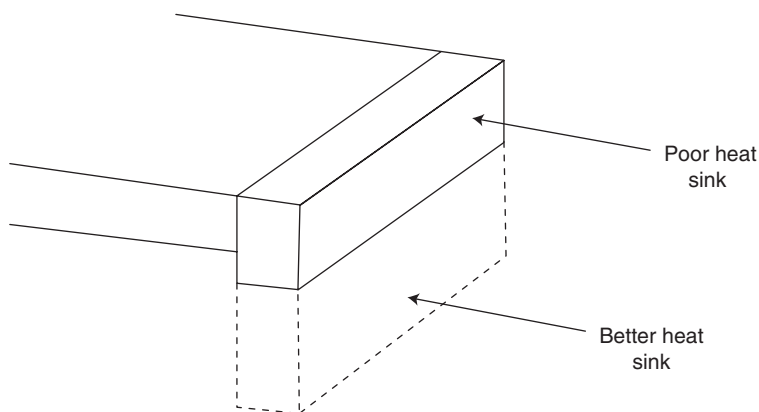
6.10 90° corner joint with inadequate heat sink.

Joint design also plays a role in establishing an adequate heat sink for a stable welding process. An example of a poor joint design from the standpoint of heat dissipation is shown in Fig. 6.10. In this case, one side of the corner joint is very small, which would result in excessive heat build-up during welding, possibly making it impossible to weld. A better joint design would have left more material on the right side of the joint, to be machined away after welding.

A few additional guidelines relative to joint design are necessary. First, it is most generally desirable to consume the original faying surfaces to the greatest extent possible, since remnant oxide bands can provide crack initiation sites. This may require multiple weld passes, such as in the case of a severe oblique angle joint, or it may require special welding tool designs to generate adequate coverage to consume the joint. Second, lap joints can be problematic, since they inherently involve leaving a remnant oxide band that enters the weld. Careful consideration must be given to the welding procedure and applied load path in this type of joint in order to have reliable results. Finally, it is important to consider the effect of the joint's properties across the weld zone and how it relates to the applied load in service when formulating a joint design. For example, in some applications it may be desirable to replace the oblique angle joint shown in Fig. 6.7 with a machined angle piece and two butt joints, in order to move the welded joints away from the corner region, which may be the area with the highest loading.

Friction stir welding is a relatively new welding process, but it has rapidly developed into a viable production process in a number of industries. This has been accomplished through intense research in universities and research institutions around the world, contributing to our understanding of the

process and expanding its capabilities through technical innovation. The chapters that follow provide a more detailed description of the important aspects of the process, which is required in developing a complete understanding of its unique characteristics.

6.7   References

1. PACCHIONE, M. and LOHWASSER, D., *Friction Stir Welding Application to Aircraft Primary Structures*, Aircraft Design Principles PR0407463, Airbus, 2004.

2. KUMAGAI, M. and TANAKA, S., 'Properties of aluminum wide panels by friction stir welding', *1st International Symposium on Friction Stir Welding*, Thousand Oaks, CA, USA, June 14–16, 1999.

3. TALWAR, R., BOLSER, D., LEDERICH, R.J., and BAUMANN, J., 'Friction stir welding of airframe structures', *2nd International FSW Symposium*, Gothenburg, Sweden, June 26–28, 2000.

4. CHRISTNER, B., MCCOURY, J., and HIGGINS, S., 'Development and testing of friction stir welding as a joining method for primary aircraft structure', *4th International FSW Symposium*, Park City, UT, USA, May 14–16, 2003.

5. LOHWASSER, D., 'Application of friction stir welding for aircraft industry', *2nd International FSW Symposium*, Gothenburg, Sweden, June 26–28, 2000.

6. SHEPHERD, G.E., 'The potential for using solid phase welding to repair cracks that may occur on thin aluminum aircraft wing structures', *2nd International FSW Symposium*, Gothenburg, Sweden, June 26–28, 2000.

7. JONES, C. and ADAMS, G., 'Assembly of a full scale external tank barrel section using friction stir welding', *1st International Symposium on Friction Stir Welding*, Thousand Oaks, CA, USA, June 14–16, 1999.

8. COLLIGAN, K.J., XU, J. and PICKENS, J.R., 'Welding tool and process parameter effects in friction stir welding of aluminum alloys', *Friction Stir Welding and Processing II*, Jata, K.V., Mahoney, M.W., Lienert, T.J. and Mishra, R.S., (eds), TMS, The Minerals, Metals and Materials Society, 181–90, 2003.

9. REYNOLDS, A.P. and TANG, W., 'Alloy, tool geometry, and process parameter effects on friction stir welding energies and resultant FSW joint properties', *Friction Stir Welding and Processing*, Jata, K.V., Mahoney, M.W., Mishra, R.S., Semiatin, S.L. and Field, D.P. (eds), TMS, The Minerals, Metals and Materials Society, 15–23, 2001.

10. MONONEN, J.T., 'Cost comparison of FSW and MIG welded aluminum panels', *3rd International FSW Symposium*, Kobe, Japan, September 27–28, 2001.

11. KALLEE, S.W. and MISTRY, A., 'Friction stir welding in the automotive body in white production', *1st International Symposium on Friction Stir Welding*, Thousand Oaks, CA, USA, June 14–16, 1999.

12. MIDLING, O.T., KVALE, J.S. and DAHL, O., 'Industrialization of the friction stir welding technology in panels production for the maritime sector', *1st International Symposium on Friction Stir Welding*, Thousand Oaks, CA, USA, June 14–16, 1999.

13. THOMAS, W.M., NICHOLAS, E.D., NEEDHAM, J.C., MURCH, M.G., TEMPLE-SMITH, P. and DAWES, C.J., *Improvements Related to Friction Welding*, PCT Patent Application No. PCT/GB92/02230, June 10, 1993.

14. CAMPBELL, C.L., FULLEN, M.S. and SKINNER, M.J., *Welding Head*, US Patent 6,199,745, March 12, 2001.

15. LI, T., HARTLEY, P., HALPIN, J., SKINNER, M. and EDWARDS, B., 'Characterization of 2195 and 2219 self-reacting friction stir welds', *Aeromat 2002*, Orlando, Florida, USA, unpublished reference, June 10–13, 2002.

16. SKINNER, M. and EDWARDS, R.L., 'Improvements to the FSW process using the self-reacting technology', *Thermec 2003*, Leganes, Madrid, Spain, July 7–11, 2003.

17. MARIE, F., 'Development of the bobbin tool technique on various aluminum alloys', *5th International FSW Symposium*, Metz, France, September 14–16, 2004.

18. THOMAS, W.M., VERHAEGHE, MARTIN, J., STAINES, D.G. and STANHOPE, C., 'Friction stir welding – process variants – an update', *Inalco 2007*, Tokyo, Japan, October 24–26, 2007.

19. NEUMANN, T., ZETTLER, R., VILACA, P., DOS SANTOS, J. and QUINTINO, L., 'Analysis of self-reacting friction stir welds in a 2024-T351 alloy', *Friction Stir Welding and Processing IV*, Mishra, R.S., Mahoney, M.W., Lienert, T.J. and Jata, K.V. (eds), *TMS*, 39–54, 2007.

20. SYLVA, G., 'Simultaneous opposed FSW of large hollow Al-7249-T6511 extrusions using the self-reacting pin tool process', *7th International FSW Symposium*, Awaji Island, Japan, May 20–22, 2008.

21. COLLIGAN, K.J., *Tapered Friction Stir Welding Tool*, US Patent 6,669,075, December 30, 2003.

22. COLLIGAN, K.J. and PICKENS, J.R., 'Friction stir welding of aluminum using a tapered shoulder tool', *Friction Stir Welding and Processing III*, Jata, K.V., Mahoney, M.W., Mishra, R.S. and Lienert, T.J. (eds), *TMS*, 161–170, 2005.

23. THOMAS, W., NORRIS, I.M., STAINES, D.G. and WATTS, E.R., 'Friction stir welding – process developments and variant techniques', *The SME Summit 2005*, Oconomowoc, Milwaukee, Wisconsin, USA, August 3–4, 2005.

24. MIDLING, O.T. and RORVIK, G., 'Effect of tool shoulder material on heat input during friction stir welding', *1st International Symposium on Friction Stir Welding*, Thousand Oaks, CA, USA, June 14–16, 1999.

25. ANDERSSON, C-G. and ANDREWS, R.E., 'Fabrication of containment canisters for nuclear waste by friction stir welding', *1st International Symposium on Friction Stir Welding*, Thousand Oaks, CA, USA, June 14–16, 1999.

26. HAUTALA, T. and TIAINEN, T., 'Friction stir welding of copper', *6th International Trends in Welding Research Conference Proceedings*, Pine Mountain, GA, USA, April 15–19, 2002, *ASM International*, 324–8, 2003.

27. CEDERQVIST, L. and ANDREWS, R.E., 'A weld that lasts for 100,000 years: FSW of copper canisters', *4th International FSW Symposium*, Park City, UT, USA, May 14–16, 2003.

28. JONES, R.E. and LOFTUS, Z., 'FSW of 5 mm Ti 6Al 4V', *6th International FSW Symposium*, Saint Sauveur, Canada, October 10–13, 2006.

29. SORENSEN, C.D. and NELSON, T.W., 'Progress in polycrystalline cubic boron nitride FSW tooling', *4th International FSW Symposium*, Park City, UT, USA, May 14–16, 2003.

30. NELSON, T.W. and SORSENSEN, C.D., 'Advances in PBN tooling for friction stirring of high temperature alloys', *6th International FSW Symposium*, Saint Sauveur, Canada, October 10–13, 2006.

31. SUBRAMANIAN, P.R., BEWLAY, B.P., HELDER, E.C. and TRAPP, T.J., *Apparatus and Method for Friction Stir Welding of High Strength Materials and Articles Made Therefrom*, US Patent Application 2004/0238599, December 2, 2004.

32. RECORD, J.H., COVINGTON, J.L., NELSON, T.W., SORENSEN, C.D. and WEBB, B.W., 'Fundamental characterization of friction stir welding', *5th International FSW Symposium*, Metz, France, September 14–16, 2004.

33. COLLIGAN, K.J., 'Relationships between process variables related to heat generation in friction stir welding of aluminum', *Friction Stir Welding and Processing IV*, Mishra, R.S., Mahoney, M.W., Lienert, T.J. and Jata, K.V. (eds), *TMS*, 39–54, 2007.

34. COLLIGAN, K.J. and MISHRA, R.S., 'A conceptual model for the process variables related to heat generation in friction stir welding of aluminum', *Scripta Materialia*, **58**, 327–31, 2008.

35. COLLIGAN, K.J., 'A proposed conceptual model of the process variables related to heat generation in FSW of aluminum', *7th International FSW Symposium*, Awaji Island, Japan, May 20–22, 2008.

36. ZETTLER, R., LOMOLINO, S., DOS SANTOS, J., DONATH, T., BECKMANN, F., LIPPMAN, T. and LOHWASSER, D., 'Effect of tool geometry and process parameters on material flow in FSW of an AA 2024-T351 alloy', *5th International FSW Symposium*, Metz, France, September 14–16, 2004.

37. CHEN, Z.W., PASANG, T. and QI, Y., 'Shear flow and formation of nugget zone during friction stir welding of aluminum alloy 5083-O', *Materials Science and Engineering A*, **474**, 312–16, 2008.

38. COLLIGAN, K.J., 'Material flow behavior during friction stir welding of aluminum', *Welding Journal*, July 229–37, 1999.

39. COLLIGAN, K.J., 'Material flow behavior during friction stir welding of aluminum', *1st International Symposium on Friction Stir Welding*, Thousand Oaks, CA, USA, June 14–16, 1999.

40. COLLIGAN, K.J. and CHOPRA, S.K., 'Examination of material flow in thick section friction stir welding of aluminum by a stop-action technique', *5th International FSW Symposium*, Metz, France, September 14–16, 2004.

41. BENDZSAK, G.J., NORTH, T.H. and SMITH, C.B., 'An experimentally validated 3D model for friction stir welding', *2nd International FSW Symposium*, Gothenburg, Sweden, June 26–28, 2000.

42. COLEGROVE, P., PAINTER, M., GRAHAM, D. and MILLER, T., '3-dimensional flow and thermal modeling of the friction stir welding process', *2nd International FSW Symposium*, Gothenburg, Sweden, June 26–28, 2000.

43. XU, S., DENG, X., REYNOLDS, A.P. and SEIDEL, T.U., 'Finite element simulation of material flow in friction stir welding', *Science and Technology of Welding and Joining*, **6** (3), 191–3, 2001.

44. WILLIAMS, S.W., COLEGROVE, P.A., SHERCLIFF, H., PRANGNELL, P., ROBSON, J., WITHERS, P., RICHARDS, D., SULLIVAN, A., KAMP, N., LOHWASSER, D. and POAD, M., 'Integrated modeling of the FSW process', *6th International FSW Symposium*, Saint Sauveur, Canada, October 10–13, 2006.

45. ASKARI, A., SILLING, S., LONDON, B. and MAHONEY, M., 'Modeling and analysis of friction stir welding processes', *Friction Stir Welding and Processing*, Jata, K.V., Mahoney, M.W., Mishra, R.S., Semiatin, S.L. and Field, D.P. (eds), *TMS*, 43–54, 2001.

46. FRIGAARD, O., GRONG, O., BJORNEKLETT, B. and MIDLING, O.T., 'Modeling of the thermal and microstructural fields during friction stir welding of aluminum alloys', *1st International Symposium on Friction Stir Welding*, Thousand Oaks, CA, USA, June 14–16, 1999.

47. NELSON, T., SORENSEN, C., PACKER, S. and ALLEN, C., 'Qualification of friction stir processing for production applications', *7th International FSW Symposium*, Awaji Island, Japan, May 20–22, 2008.

48. THOMAS, W.M., THREADGILL, P.L. and NICHOLAS, E.D., 'Feasibility of friction stir welding steel', *Science and Technology of Welding and Joining*, **4** (6), 365–72, 1999.

49. LIENERT, T.J. and GOULD, J.E., 'Friction stir welding of mild steel', *1st International Symposium on Friction Stir Welding*, Thousand Oaks, CA, USA, June 14–16, 1999.

50. POSADA, M., DELOACH, J., REYNOLDS, A.P., SKINNER, M, and HALPIN, J.P., 'Friction stir weld evaluation of DH-36 and stainless steel weldments', *Friction Stir Welding and Processing*, Jata, K.V., Mahoney, M.W., Mishra, R.S., Semiatin, S.L. and Field, D.P. (eds), *TMS*, 43–54, 2001.

51. KONKOL, P., MATHERS, J.A., JOHNSON, R. and PICKENS, J.R., 'Friction stir welding of HSLA-65 steel for shipbuilding', *3rd International FSW Symposium*, Kobe, Japan, September 27–28, 2001.

52. SORENSEN, C.D., NELSON, T.W., PACKER, S.M. and STEEL, R.J., 'Innovative technology applications in FSW of high softening temperature materials', *5th International FSW Symposium*, Metz, France, September 14–16, 2004.

53. MAHONEY, M., STEEL, R., NELSON, T., PACKER, S. and SORENSEN, C., 'FSW of HSLA-65 steel with low/no distortion', *7th International FSW Symposium*, Awaji Island, Japan, May 20–22, 2008.

54. JUHAS, M.C., VISWANATHAN, G.B. and FRASER, H.L., 'Microstructural evolution in Ti alloy friction stir welds', *2nd International FSW Symposium*, Gothenburg, Sweden, June 26–28, 2000.

55. TRAPP, T., HELDER, E. and SUBRAMANIAN, P.R., 'FSW of titanium alloys for aircraft engine components', *Friction Stir Welding and Processing II*, Jata, K.V., Mahoney, M.W., Lienert, T.J. and Mishra, R.S. (eds), *TMS*, 173–8, 2003.

56. RUSSELL, M.J. and BLIGNAULT, C., 'Recent developments in FSW of Ti alloys', *6th International FSW Symposium*, Saint Sauveur, Canada, October 10–13, 2006.

57. RUSSELL, M.J., THREADGILL, P.L. and HORREX, N.L., 'Recent developments in the stationary shoulder FSW of Ti alloys', *7th International FSW Symposium*, Awaji Island, Japan, May 20–22, 2008.

58. JOHNSON, R., 'FSW of magnesium alloys', *4th International FSW Symposium*, Park City, UT, USA, May 14–16, 2003.

59. ESPARZA, J.A., DAVIS, W.C., TRILLO, E.A. and MURR, L.E., 'Friction-stir welding of magnesium alloy AZ31B', *Journal of Materials Science Letters*, **21**, 917–20, 2002.

60. KIMAPONG, K. and WATANABE, T., 'Friction stir welding of aluminum alloy to steel', *Welding Journal*, **83** (10), 277–82, 2004.

61. FUKUMOTO, M., TSUBAKI, M., YASUI, T. and SHIMODA, Y., 'Joining of ADC12 and SS400 by means of friction stir welding', *Quarterly Journal of the Japan Welding Society*, **22** (2), 309–14, 2004.

62. SMITH, C.B., HINRICHS, J.F., CERVENY, L.M., ANDERSON, R. and WALKER, B., 'Fabricated shapes using FSW/forging process', *7th International FSW Symposium*, Awaji Island, Japan, May 20–22, 2008.

7
Failure mechanisms in friction stir welds

M. N. J A M E S, University of Plymouth, UK, D. G. H A T T I N G H,
H. L O M B A R D, I. W E D D E R B U R N, D. L. H. B U L B R I N G, and
A. E L S - B O T E S, Nelson Mandela Metropolitan University, South
Africa, and A. S T E U W E R, ESS Scandinavia, Sweden

Abstract: This chapter provides an overview of the types of defect that
can occur in friction stir (FS) welds and identifies their influence on
failure mechanisms under static and cyclic loading. Consideration will
primarily be given to FS welding for linear joints, although some results
of a new repair welding technique for pipework, friction taper stud
welding (FTSW), will also be presented. FS spot welds will also be
briefly considered. Whilst certain defect types are generic across a broad
range of alloys, there appear to be several defect categories specific to
particular strain hardening FS welded aluminium alloys, which have
been termed 'onion skin' and planar defects by the present authors,[1,2]
these will also be discussed in this chapter. Finally, brief attention will
be paid to the residual stress distributions arising from FS welding as
relationships exist between process parameters, heat input, peak values
of longitudinal residual stresses and weld performance.[3]

Key words: failure mechanisms, fractography, friction stir welding,
friction taper stud welding, process parameters, residual stress.

7.1   Introduction

Friction stir welding (FSW) is a solid state hot-shear joining process that
generally requires a low level of weld preparation, little post-weld dressing
and gives joints with high tensile and fatigue strength. Other benefits include
generally low defect populations (compared with fusion welding) and the
ability to join dissimilar metals. The technique has hence attracted signifi-
cant interest in a number of major industrial sectors, including aerospace,
thermal power generation, land transportation (automotive and rail) and
ship building. An extensive literature now exists that deals with FSW (see,
for instance, the comprehensive reviews given by Mishra and Ma[4] and
Nandan *et al.*[5]). FS welding of linear joints is well established as a routine
choice in the welding of aluminium alloys, and has also been extensively
applied to magnesium alloys,[6] thin titanium alloys[7] and even to steels, par-
ticularly in the power generation industry.[8] Difficulties with FS welding of
high melting point alloys are the high power input required to plasticise the

164

metal and hence make the bond and the requirement for expensive refractory tools with a limited life.

The FS process is nonetheless relatively new and still evolving rapidly; it has been extended from linear butt welds in flat plates to include compound curves via special tool design and to welds in cylinders, although most of the work is proprietary and has not been reported in the open literature. Novel variants of the process have been proposed, including friction stir spot welding,[9,10] friction stir knead welding which has been applied to lap joints between thin steel and aluminium,[11] and friction taper stud welding.[12] In friction knead welding the edge of the bottom steel plate has a scalloped keyhole shape and the tool does not have a pin. The softer aluminium alloy is 'kneaded' into the cut-outs to form an interlocking joint.[11] Friction taper stud welding was developed to deal with the problem of *in situ* creep crack repair in thermal power station pipelines and involves machining a tapered hole in the pipe wall to remove the damaged material and then plugging it with a rotating tapered stud of the same alloy.[12]

The number of papers that have focussed on defects and failure mechanisms in FS welds is, however, relatively limited, although weld performance is governed by defects and their influence on fracture and fatigue. Equally, the type of defect that occurs and the residual stresses in a weld are a function of the weld process parameters, the alloy and its condition (temper or strain hardening). The aim of this chapter is to provide a brief overview of these aspects for linear and spot FS welds, and for friction taper stud welds.

7.2   Defects in linear friction stir welds

The typical surface appearance of an FS weld is shown in Fig. 7.1 and with the linear and rotational movements of the tool in the directions shown, the left-hand side of the weld is termed the 'advancing' side (linear and rotational movements in the same direction) and the 'retreating' side is on the right. This distinction reflects the difference in the plastic flow processes on the two sides of the weld, where observations have indicated[13] that material is entrained on the advancing side, rotated around the pin and deposited at the rear of the retreating side. Material picked up on the front part of the retreating side of the weld is entrained (but does not rotate around the pin) and deposited to 'fill in' material in the wake of the pin.[13] Thus the FS weld nugget consists of an amalgam of two streams of material with different histories and mechanical properties which often leads to a so-called 'onion skin' macrostructure (Fig. 7.2).[14] The onion skin macrostructure is also influenced by tool geometry, rotational speed and feed rate (which can be characterised by tool pitch = tool feed per revolution). A heavily thermomechanically affected zone (TMAZ) lies outside the recrystallised[15] nugget region and this is also seen in Fig. 7.2.
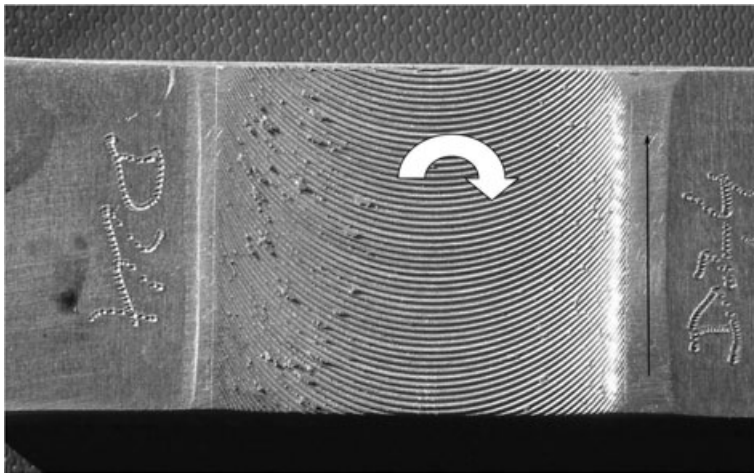
7.1 Surface marks on an FS weld in aluminium alloy arising from forwards tool tilt and the linear movement of the tool in each cycle of rotation. The black arrow indicates the direction of tool travel and the white arrow indicates the clockwise tool rotation. Flash at the edge of the shoulder has been ground off.

Semi-analytical thermomechanical modelling by Heurtier *et al.*[16] has linked material flow and mixing to strain and temperature histories in the various weld zones. The model allows estimation of the resulting microhardness profile across the weld and its evolution is stated to point to the welding parameters which reduce the inhomogeneties in weld zone properties.[16] Thus increasing the tool translational velocity (feed rate) for a constant rotational speed reduces the softening in the weld nugget. This improvement in hardness is assigned to a decrease in the average temperature of the weld zone.

For threaded pin geometries, the onion skin macrostructure can be observed in L–T weld sections as well as in T–ST sections such as that shown in Fig. 7.2(a). Figure 7.2(b) identifies the L, T and ST directions using standard rolled or extruded plate terminology. This has been found to reflect a vertical vortex motion imparted by the threads to material within the rotational nugget zone, which thus follows an unwound helical trajectory formed by the rotational motion, the vortex flow and the translational motion of the pin.[13] The apparent layering in the macrostructure is therefore related to the tool pitch along the weld joint.

It would be expected that the complex plastic deformation processes involved in entrainment and mixing of dual streams of deformed material

(a)

(b)
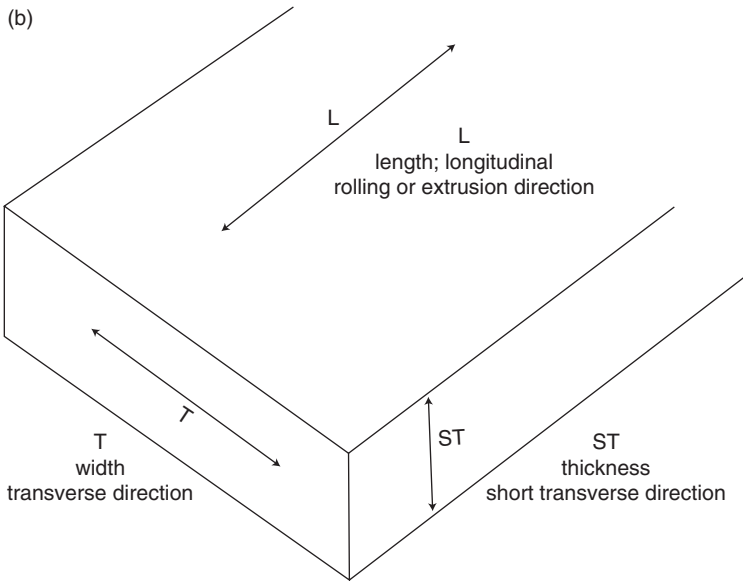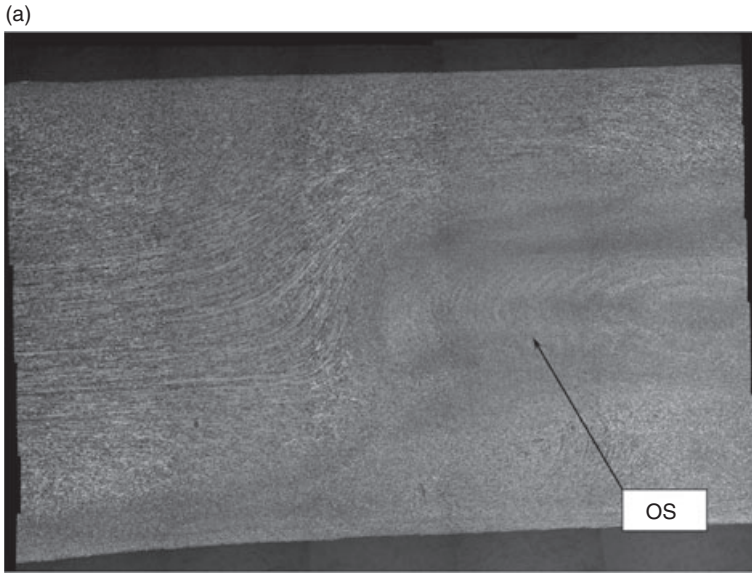
7.2 (a) The so-called 'onion skin' structure in the weld nugget (indicated by the letters OS); the TMAZ region can be clearly seen in this image of a double pass FS weld in 5383-H321 aluminium alloy. (b) Definition of standard directions in a rolled or extruded plate. These allow identification of fracture planes and metallurgical directions in an unambiguous fashion.

influence the defect population and residual stresses in the weld zone and this has been observed to be the case by a number of authors.[17] The peak magnitudes of residual stresses are lower on the retreating side by up to 20%, although the difference between advancing and retreating data is affected by weld process parameters (tool rotational speed and feed rate) which determine heat input during welding.[17]

A number of papers have considered the FSW defects that arise as a consequence of plastic flow mechanisms around the tool or of process parameters such as tool tilt or penetration into the joint (which has, of necessity, to be less than the full-plate depth). Commonly occurring defects include lack of penetration (tool length too small for the plate thickness), voids and root defects, which are also known as 'kissing bonds', 'lazy-S' or zigzag defects. However, other plasticity-related defects can occur in strain hardening alloys which appear to be contingent upon alloy and strain condition. These fall into the category of partial bonds but occur in the interior of the weld nugget, often as regular sequences related to the tool pitch and have been described as 'onion skin' or planar defects.[1–3]

7.2.1   Lack of penetration

Tool penetration is generally around 90–95% of the plate thickness, and lack of penetration defects can occur if, for example, plate thickness is variable along the weld line or the plate is bowed. Dickerson and Przydatek[18] have noted that Lloyd's Register suggests a tolerance on nominal plate thickness in FSW of +0.2 mm to avoid defects. Welding of bowed plates can be resolved by appropriate plate restraint or seam tracking strategies.

Tool penetration problems lead to extruded flash at the root of the weld near the pin if the tool depth is too high[19] and to long root grooves on the advancing side of the weld if the pin is too short.[19,20] Additional problems can arise if the gap between the abutting plates to be welded is not tightly controlled. Unpublished work by the present authors has indicated that a gap of around 5% of the plate thickness leads to a reduction in fatigue strength of some 10% at a fatigue life of 10^6 cycles. The induced defects are large voids and partial bonding which significantly reduce the fatigue crack initiation period. Chen et al.[19] also note that the generation of root defects is assisted by very small tool tilt angle (≤1.5°) and by higher angles ≥4.5°. They attribute this to influences of tool tilt angle on heat input and forging force and hence on the position of defects in the weld. At low tilt angles they postulate that there is insufficient downwards forging of the plasticised metal leading to a root groove from lack of penetration. At larger tool tilt angles, weld flash can be generated on the retreating side with insufficient plasticised metal remaining to fill up the cavity left in the nugget zone.
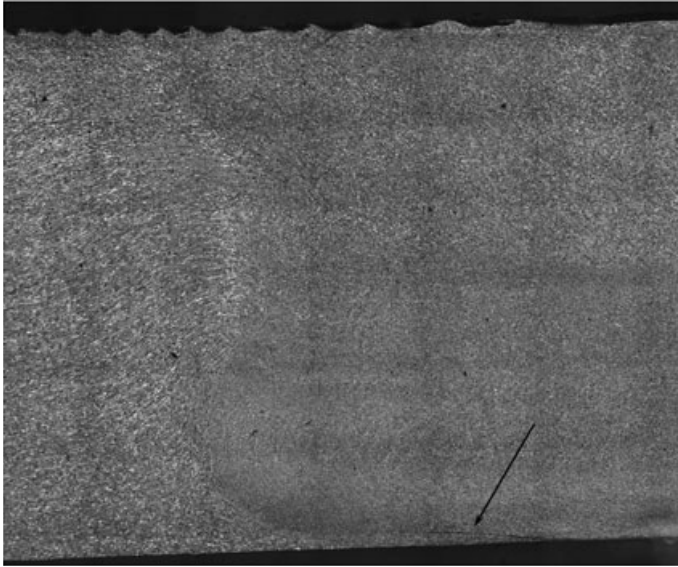
7.3 Root defect in an FS weld made in 6 mm 5083-H321 aluminium alloy plate. Tool rotational speed 617 rpm, feed-rate 185 mm min⁻¹, giving a tool pitch of 0.32 mm/rev.

7.2.2   Root defects

Root defects are strongly affected by process parameters and occur as a result of partial bonding which reflects insufficient heat input and/or incomplete break-up of surface oxide layers.[18,19,21] A typical root defect is shown in Fig. 7.3. The plastic flow mechanisms in the TMAZ region also make it likely that the occurrence of partial bonding defects will be alloy dependent and that strain hardening alloys in certain conditions will be more susceptible to root defects. Work by Dickerson and Przydatek[18] has indicated, for example, that 5083-H321 is more susceptible to root defects than either 5083-O or 6082-T6 alloys. In their work on 6–7 mm thick plates, defects detrimentally influenced tension–tension fatigue performance ($R = 0.1$) if the root flaw was >0.35 mm in depth.[18] There is an obvious link between plate thickness and the size of flaw that will reduce fatigue performance; work by Zhou *et al.*[22] on 4-mm thick plates of 2024-T3 aluminium alloy has demonstrated a reduction in fatigue strength of some 50% at 2×10^6 cycles in the presence of root flaws 0.31–0.33 mm long.

   Strain hardened aluminium alloys are also susceptible to other forms of partial bonding defect associated with the onion skin structure and hence with the tool feed rate. These have been termed onion skin and planar
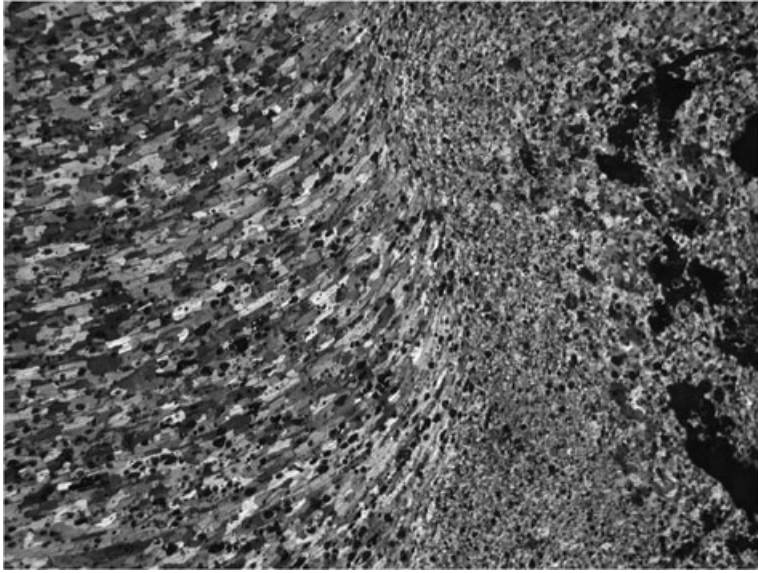
7.4 Extensive voiding in the nugget of an FS weld made with sub-optimum process parameters.

defects by the present authors[1–3] in extensive work on 5083-H321 aluminium alloy, and similar defects have been described as 'kissing bonds' in other work on 5456 aluminium alloy.[19] These defects will be further discussed below.

Partial bonds are difficult to detect using dye penetrant techniques and, because they can occur in any orientation and at any angle, may also be difficult to detect with directionally specific techniques such as radiography and ultrasonics.[2,18] Phased array inspection techniques have therefore been proposed as a route to overcome this problem.[23]

7.2.3   Voids

Voids are a common defect in FS welds; in such an autogenous process large voids can occur when the choice of tool and weld parameters is sub-optimum (e.g. Colligan *et al.*[24]; Leonard and Lockyer[25]). An example of serious process parameter-related voiding is shown in Fig. 7.4, while small voids have been proposed to occur as a consequence of the fluid dynamics associated with plastic flow in the weld nugget. In numerical three-dimensional modelling of the flow dynamics in the weld region, Bendzsak *et al.*[26] found that there is a zone on the advancing side of the weld where chaotic flow occurs. They proposed that there is a location within this zone above
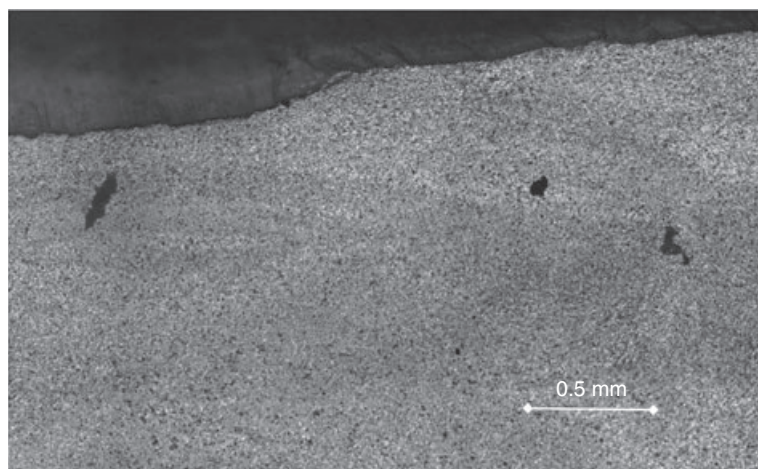
7.5 Voids up to 0.25 mm in dimension near the root of an FS weld in 5083-H321 aluminium alloy.

and below which the flow is in opposite directions, creating a vortex. Such vortices could lead to the generation of a series of voids in the weld nugget, potentially with significant sizes. Metallurgical sections of FS welds routinely indicate voids with sizes up to perhaps 0.2–0.5 mm and the incidence of voids appears to be higher near the surfaces of the plate, although they occur throughout the weld nugget. Figure 7.5 shows such voids observed on a metallographic section of an FS weld in 5083-H321 aluminium alloy.

These observations indicate that the vortex generation proposed by Leonard and Lockyer[25] may provide one mechanism underlying voiding in the interior of the weld nugget, while a second mechanism arises from the complex plastic deformation processes involved in entrainment and mixing of dual streams of deformed material[13] and the overall behaviour of the plasticised zone in the metal. A very interesting recent paper by Arbegast[27] considers the relationships between the complexities of flow zone formation and a number of characteristic volumetric defects in FS welding. An illustration of such relationships is given in Fig. 7.6[2] which shows the fatigue crack initiation region in a reversed bend fatigue specimen cut from an FS welded 5083-H321 alloy. A void is associated with two small planar facets, which show clear evidence of dynamic recrystallisation[28] in the fine (~5 μm average diameter) polygonal grains (marked with arrows A and B). The planar facets must arise from partially bonded regions formed between different layers of plasticised metal, entrained either on the advancing and retreating sides of the tool, or during sequential revolutions of the tool. The polygonal shape of the void, together with its association with partial
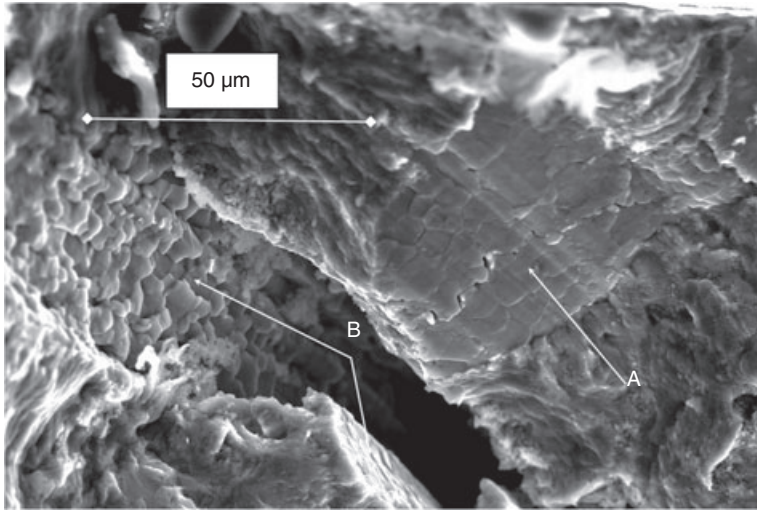
7.6 Polygonal void and associated planar regions showing evidence of dynamic recrystallisation during FS welding. Such defects arise from the complexity of plastic flow in the weld nugget.

bonding and dynamic recrystallisation, indicates the complexity of the plastic flow processes and their role in defect formation, particularly in strain hardening alloys.

Voids are often associated with the initiation of fatigue cracks and Fig. 7.7 indicates this association for another 4-mm diameter specimen of 5083-H321 aluminium alloy tested in reversed bend at a peak stress of 136 MPa. The influence of the void cluster on the fatigue strength of that particular welded specimen is evident in Fig. 7.8; fatigue life has been reduced to that found for defect-free specimens at an applied stress 30% higher (180 MPa).

7.2.4   Onion skin and planar defects

The discussion of root defects and voids indicates that FS welds are susceptible to regions of partial bonding, which is unsurprising since FSW is a complex hot shear and forging process that takes place in an air environment. As noted earlier, work on a strain hardening 5083-H321 aluminium alloy has demonstrated the existence of very significant partial bond defects in the form of extensive planar facets or a series of planar defects that can be related to the onion skin macrostructure and hence to tool feed rate along the weld.[1–3] Figure 7.9 indicates that voids and onion skin partial bonding defects can occur together, that they affect crack initiation significantly and that they are related to the tool pitch. It also provides a good
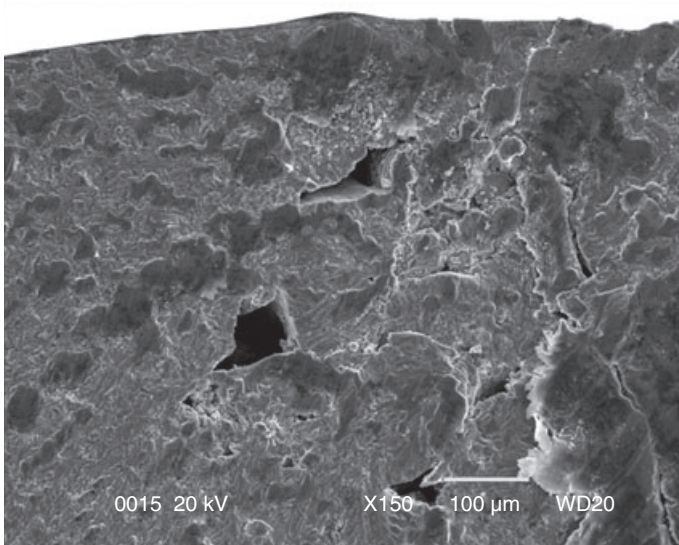
7.7 Association of voids with fatigue crack initiation site in reversed bend loading of 5083-H321 aluminium alloy at 136 MPa peak stress.
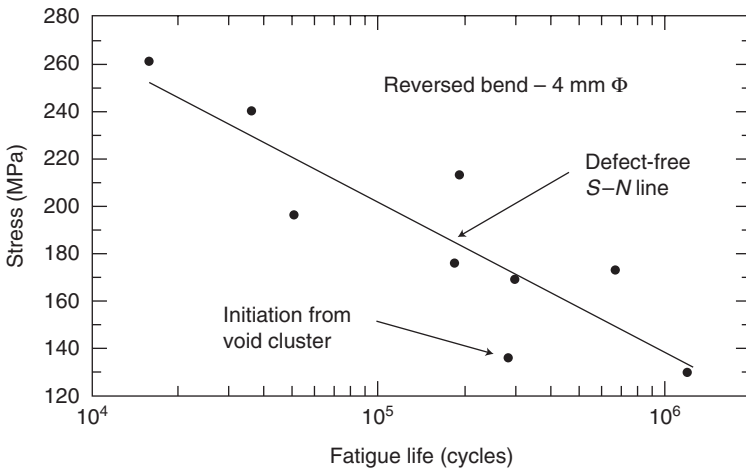
7.8 Influence of void cluster on fatigue strength of 4-mm diameter FS welded specimen of 5083-H321 aluminium alloy; fatigue life for the specimen tested at 136 MPa has been reduced to that found for defect-free specimens at an applied stress 30% higher (180 MPa).

(a)   (b)
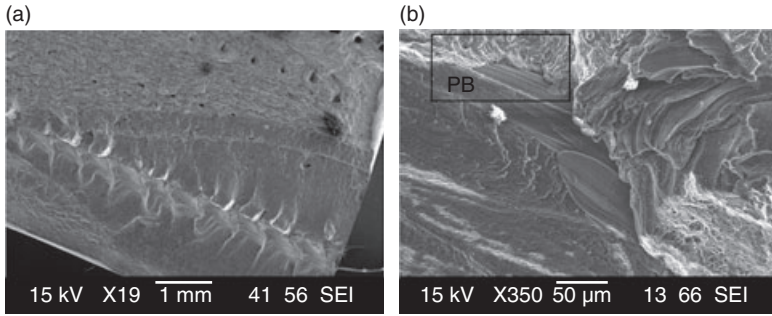
7.9 (a) FS weld in 5083-H321 made with a tool feed rate of
135 mm min^{-1} and a pitch of 0.51 mm/rev. Voids and onion skin
defects are present on the fracture surface and are associated with
crack initiation and the tool pitch. (b) Magnified image of part of the
fatigue region; details of the plastic flow and partial bonding (PB) are
clearly apparent.
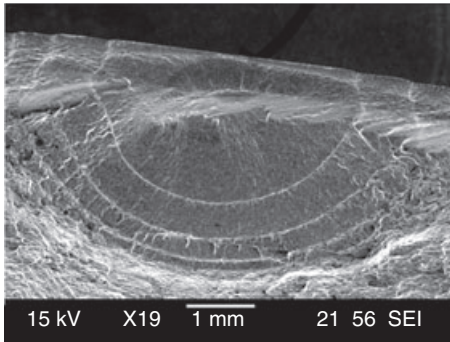
7.10 Large planar defect on the fracture surface of a weld made in
5083-H321 alloy with a tool feed rate of 85 mm min^{-1} and a pitch of
0.32 mm/rev.

illustration of the concept of 'partial bonding' (Fig. 7.9b). A large planar
defect associated with fatigue crack initiation is shown in Fig. 7.10.

Both types of defect appear to be activated preferentially by high levels
of plasticity, for example during fast fracture or at high fatigue crack growth
rates.[1] One explanation for this observation lies in the different deformation
histories of the two streams of metal entrained from the advancing and
retreating sides of the tool. The different thermomechanical histories lead
to different dislocation densities and distributions and hence to the observed
macrostructure during etching. It would also be expected that adjacent

layers would show different strain hardening exponents and microhardness values. This causes scatter in microhardness values in the weld nugget and, more importantly, could also lead to strain partitioning in the layers during subsequent deformation processes. Limited work by the present authors has indicated that the Vickers microhardness does indeed vary between different layers in the onion skin macrostructure.

Figure 7.11(a) demonstrates this for measurements made with a 25 gf load. For comparison, measurements made under a 200 gf load average out the hardness values in the onion skin macrostructure and give a much smoother transition from the parent plate hardness of around HV98 to perhaps HV77 in the weld nugget (Fig. 7.11b). Coupling this weld artifact with subsequent plastic deformation during loading offers the possibility of strain partitioning occurring with strain localisation at interfaces between adjacent 'hard' and 'soft' layers. Fracture would then preferentially occur along these partially bonded interfaces, leading to defects of the type seen in Figs. 7.9 and 7.10.[2]

7.3   Crack paths in tensile and fatigue fracture

A strain-hardening alloy like 5083-H321 therefore provides an interesting case study in terms of failure mechanisms, defects and their effect on tensile strength and fatigue performance. Welds made under different process conditions often show a crossover in dynamic performance in going from the high-stress short-life regime (~5×10^4 cycles) to the low-stress long-life regime (>10^6 cycles). This reflects their ability to reduce local strain concentrations through plastic flow and, for an alloy like 5083-H321, the presence and triggering of partial bond defects. Previous work[3] has shown that relationships exist between defect type, average fatigue life, average tensile strength and frictional power in 5083-H321 alloy.

Frictional power can be calculated using the equation given below, which is from Frigaard and Midling[29] and uses an effective coefficient of friction defined by Santella *et al.*[30]

$$P_{in1} = \frac{4}{3}\pi\mu F_z\omega r$$

where μ is an effective coefficient of friction under the tool shoulder, F_z is the downwards force on the tool, ω is the tool rotational speed in radians per second and r is the radius of the tool shoulder.

Frictional power correlates well with tensile strength and with fatigue life (here measured at a single value of peak applied stress of 242 MPa, which is equivalent to a life of 2×10^5 cycles in unwelded parent plate) as demonstrated in Fig. 7.12. Lower values of frictional power input provide higher tensile strengths and this can be related to the necessity to establish high

(a)

(b)
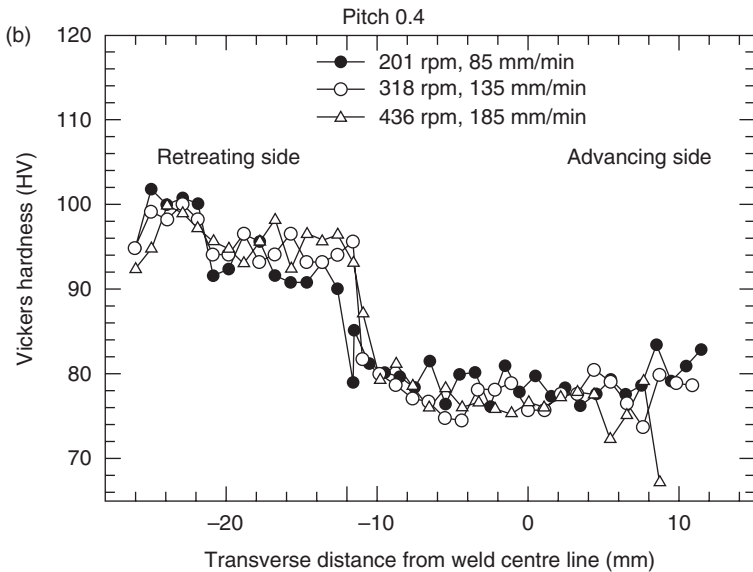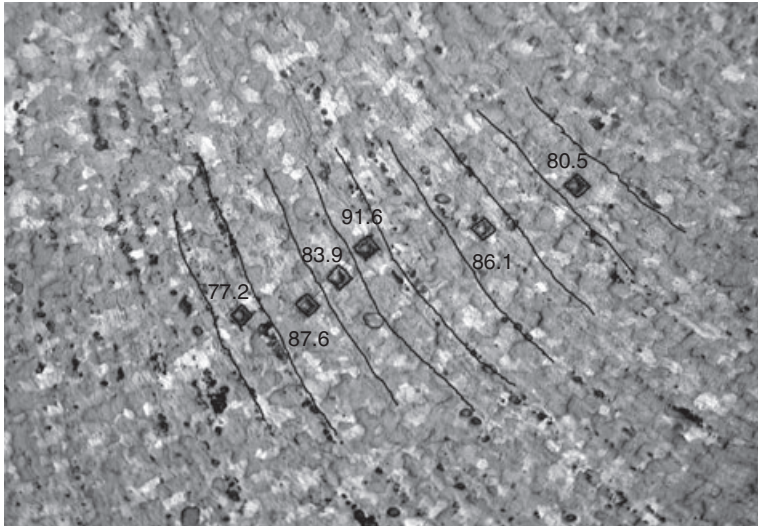
7.11 (a) Vickers microhardness (HV_{25}) measurements in the onion skin structure vary between approximately 77 and 92. (b) HV_{200} values range from around 98 in the parent plate to 77 in the weld metal.

enough temperatures to ensure adequate plasticisation of the alloy during the welding process (coefficient of friction has an inverse linear relationship to tool temperature); this in turn leads to a lower power requirement during welding. Lower frictional power (which, as noted above, occurs when
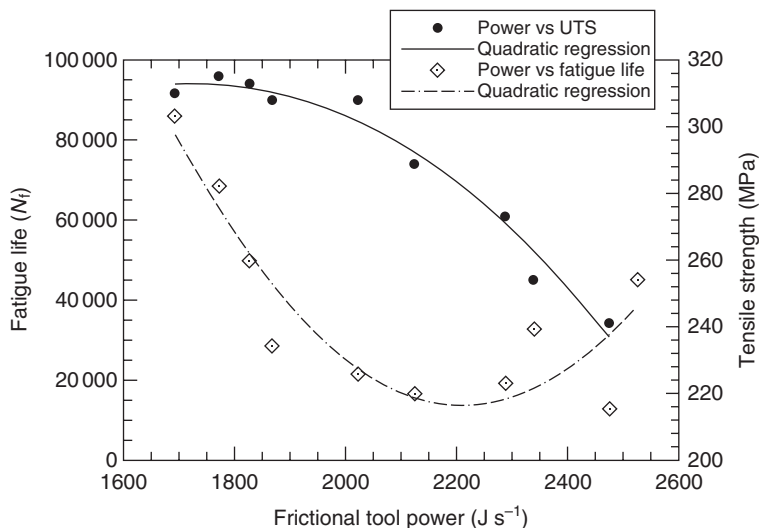
7.12 Frictional power input correlates well with tensile strength and with fatigue life (measured at a single value of peak applied stress of 242 MPa, which is equivalent to a life of 2×10^5 cycles in unwelded parent plate).

temperatures during welding are high enough to give 'adequate' plasticisation for a good weld bond to be made) also gives the highest observed fatigue lives at this value of applied stress. The message is clear; a low frictional power requirement during welding occurs at higher temperatures, which ensure adequate plasticisation and the creation of a sound metallurgical bond during welding.

It is, however, interesting to note that, although both fatigue life (at one specific value of applied stress) and tensile strength have a good correlation with frictional power, there is no strong correlation between the two performance parameters. This is believed to reflect the greater influence that the partial bond defects have on fatigue crack paths, in particular the very detrimental effects of large planar facets on crack initiation. No correlation was found between the 0.2% proof strength and the fatigue life. Since fatigue crack initiation is a yield-related phenomenon, this observation supports a conclusion that crack path effects are the primary cause of the relatively low ratios of tensile strength (expressed as welded/parent plate values) observed in this alloy and that they also dominate fatigue crack initiation and growth. Thus high performance welds would be expected to show less evidence of defects on the fracture surface and this is supported by fractographic observations (Fig. 7.13).
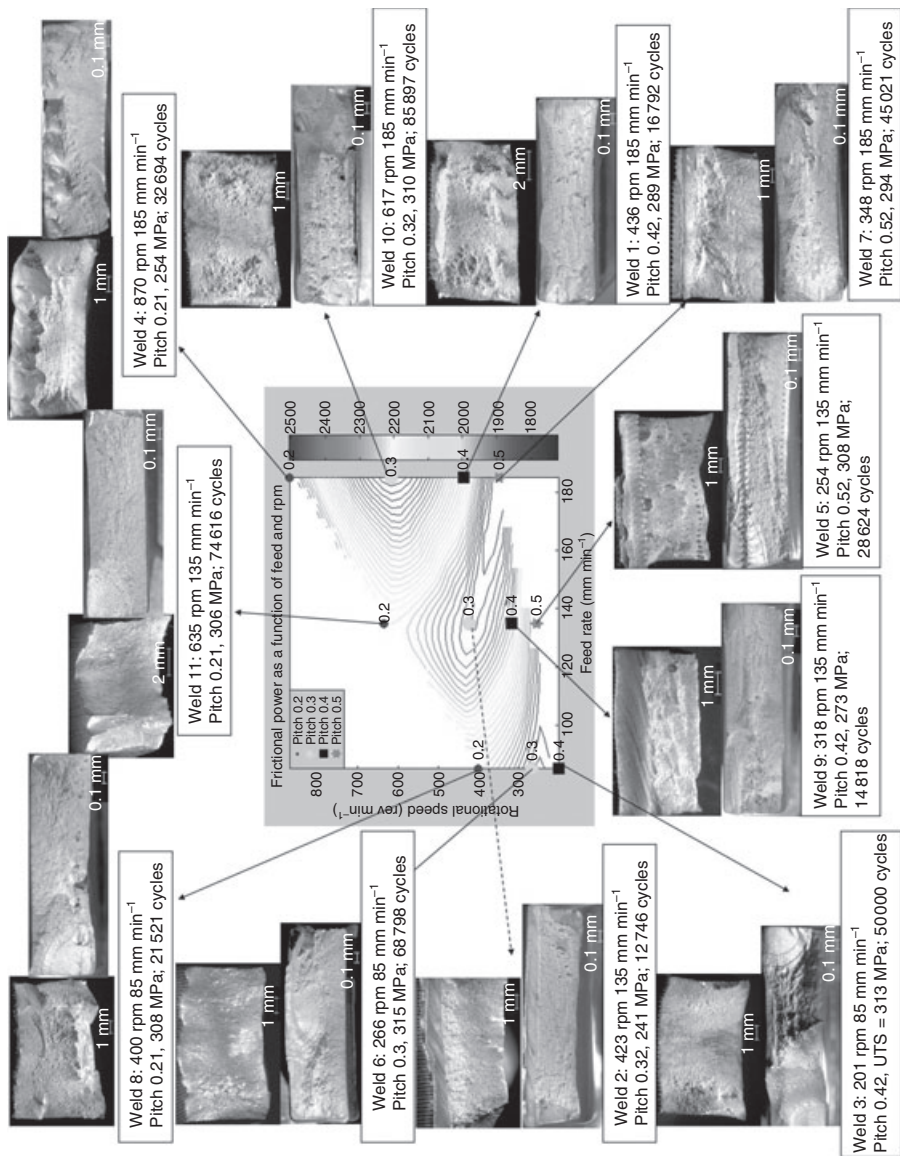
7.13 Correlation observed fractographically between the presence of planar and onion skin defects, tensile strength and fatigue performance.

Weld 4: 870 rpm 185 mm min⁻¹
Pitch 0.21, 254 MPa; 32 694 cycles

Weld 10: 617 rpm 185 mm min⁻¹
Pitch 0.32, 310 MPa; 85 897 cycles

Weld 1: 436 rpm 185 mm min⁻¹
Pitch 0.42, 289 MPa; 16 792 cycles

Weld 7: 348 rpm 185 mm min⁻¹
Pitch 0.52, 294 MPa; 45 021 cycles

Weld 11: 635 rpm 135 mm min⁻¹
Pitch 0.21, 306 MPa; 74 616 cycles

Weld 5: 254 rpm 135 mm min⁻¹
Pitch 0.52, 308 MPa; 28 624 cycles

Weld 9: 318 rpm 135 mm min⁻¹
Pitch 0.42, 273 MPa; 14 818 cycles

Weld 8: 400 rpm 85 mm min⁻¹
Pitch 0.21, 308 MPa; 21 521 cycles

Weld 6: 266 rpm 85 mm min⁻¹
Pitch 0.3, 315 MPa; 68 798 cycles

Weld 2: 423 rpm 135 mm min⁻¹
Pitch 0.32, 241 MPa; 12 746 cycles

Weld 3: 201 rpm 85 mm min⁻¹
Pitch 0.42, UTS = 313 MPa; 50 000 cycles

Frictional power as a function of feed and rpm

Fatigue life appears to be increasing again at the higher values of frictional power albeit with greater scatter than is observed at lower values of frictional power. It is not easy to identify any underlying rationale for an increase in fatigue strength occurring concomitantly with a continuing decrease in tensile strength and further work is required to explore this possibility.

Many other authors have also considered performance issues as a function of choice of FS welding parameters, defect type and alloy.[6,7,9,18,21,24,31]

7.4   Friction taper stud welding

As noted above, friction taper stud welding was developed to deal with the problem of *in situ* creep crack repair in thermal power station pipelines. The friction stir processing research group at the Nelson Mandela Metropolitan University has taken the concept to the stage of industrial trials using a portable welding machine. Details of the process have been reported in the literature[32] and Fig. 7.14 shows a metallurgical cross-section of a typical weld in 9CrMo910 creep-resistant steel, 40 mm thick. Welding involves machining a tapered hole in the pipe wall to remove the damaged material and then plugging it with a rotating tapered stud of the same

7.14 Friction taper stud weld made in 40 mm plate of 10CrMo910 creep-resistant steel. The tool is a consumable in this process and has been cut off after completing the weld. In practice the protruding part of the stud tool would be ground back to the surface with care taken to eliminate the 'flash crack' (arrow).

(a)

(b)
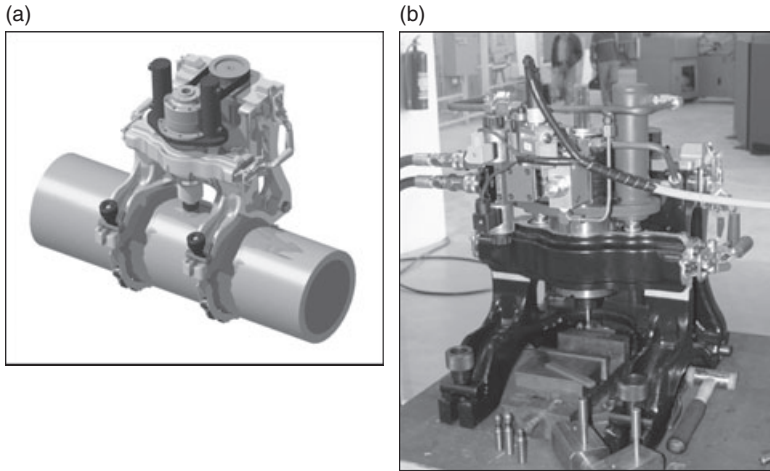
7.15 (a) Schematic of the FTSW machine mounted *in situ* on thick-walled pipe. (b) Prototype FSTW machine in the NMMU laboratories.

alloy.[12] Critical parameters include the taper angles of the hole and stud, the downwards force and the time taken to make the weld.[12]

The prototype portable welding machine is illustrated in Fig. 7.15 and utilises a fully automated welding cycle with pre-programmed rotational speed, welding force, tool travel, forging force and forging time. This results in very consistent process control, the details of which are monitored and recorded for verification purposes. Maximum operating parameters are a spindle speed of 6000 rpm, vertical welding force of 40 kN and a vertical head travel of 100 mm. The equipment consistently produces a fully bonded interface on a 25 mm deep friction taper plug weld in 40 mm thick steel, with a typical weld time of 20–60 s.

Observed defects in the FTSW process include voids and incomplete bonding, particularly towards the bottom of the hole to be plugged. Typical examples of such defects are shown in Fig. 7.16 and their avoidance is primarily a function of achieving the correct relative taper for the hole and the rotating stud, and correct choice of process conditions (particularly welding duration). These need to be determined empirically, but once they have been identified, repeatable sound welds are easily achieved (Fig. 7.15a). A new type of defect observed with this process has been termed 'flash cracking' by the present authors, as it occurs at the interface between two streams of extruded metal. The location of such defects is indicated in Fig. 7.14, while Fig. 7.17 shows a typical defect observed in 709M40 steel. The other potentially significant class of defect in FTS welds are what

7.16 Voids and incomplete bonding at the bottom of a friction taper stud weld.
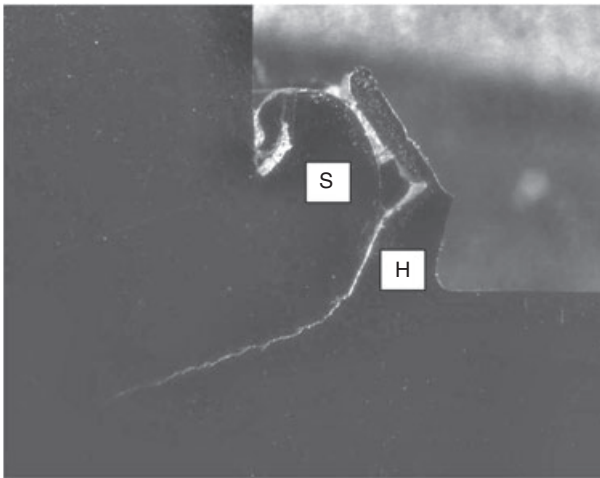
7.17 Typical flash defect observed at the interface between metal extruded from the rotating stud (S) and that extruded from the side of the hole (H).

appear to be intergranular solidification cracks in the zone at the bottom of the weld (Fig. 7.18). This region will be the last to cool after welding and the mechanism of cracking is thought to be similar to centre-line cracking observed in fusion welding as a result of constitutional supercooling.
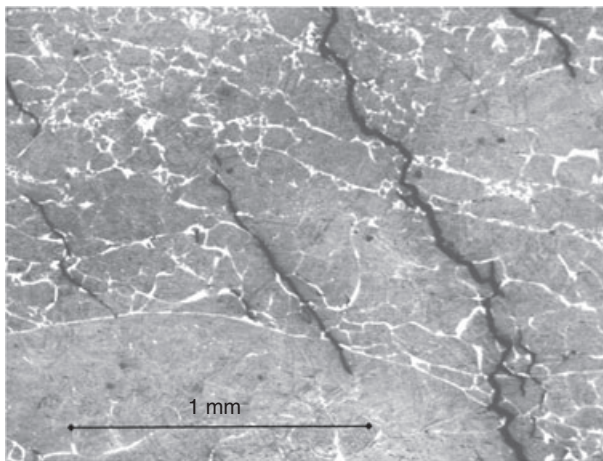
7.18 Apparent intergranular solidification cracks in the zone near the bottom of the weld.

7.5   Friction stir spot welds

Spot friction stir welding (SFW) or friction stir spot welding (FSSW) was developed and patented by Mazda Corporation and Kawasaki Heavy Industries in 2003 as a solid state joining technique for aluminium alloys. As reported by Thoppul and Gibson,[33] work by Briskham *et al.*[34] which compared joints made by resistance spot welding (RSW) and SFW, on the basis of strength, process time and cost (equipment and running cost), concluded that the lap shear strength of joints produced by the SFW process were comparable to those produced by RSW. SFW process advantages are lower power consumption and hence lower running costs than RSW, long tool life, high productivity and high reliability. The SFW process is essentially similar to the first part of the FSW process where the tool is plunged into the workpiece and a dwell time is allowed to heat the alloy to an appropriate temperature for plasticisation to occur. Withdrawal of the tool leaves a characteristic pin-diameter hole in the centre of the weld.

Parameters that influence the properties of SF welds are similar to those that are influential in FSW; tool rotational speed, temperature, depth and rate of tool penetration, vertical force and dwell time. Thoppul and Gibson[10,33] have reviewed a number of these aspects and refer to other recent review papers. Their own work concluded that short processing times (less than 1.6 s) cause formation of cracks and holes above the joint interface in the direction of flow and below the shoulder.

Tool geometry effects are known to be highly influential in FSW[35] and this would be expected to carry over into SFW. Thus recent work has con-

sidered tool shoulder influences (flat and concave) on SFW joints[36,37] and pin depth effects.[38] Lin *et al.*[36,37] concluded from their work on failure modes and fatigue life of SFW joints in aluminium alloys that the failure mechanisms are different when the joint is subjected to quasi-static and cyclic loading conditions and that the failure mechanisms at low fatigue lives (10^3 to 10^4 cycles) are different to those observed at longer lives (10^4 to 10^5 cycles). Under quasi-static loading conditions, failure occurs predominantly by necking around the circumference of the weld nugget. Under low cycle fatigue loading, failure occurs as a result of interfacial cracks developing though the stir zone, whereas in high cycle loading failure occurs as a result of the propagation of cracks in the through-thickness direction. In their work on pin length Tozaki *et al.*[38] observed two fracture modes: shear fracture of the nugget and mixed mode fracture under shear loading of the lap joint, and nugget debonding and pull-out under loading perpendicular to the lap joint. The wide observed range of failure mechanisms reflects the complexity of loading attendant on a spot welded lap joint.

7.6   Residual stresses in friction stir welds

Plastic flow is the key feature underlying failure mechanisms and weld performance in friction stir welds. It is controlled by tool geometry and process parameters and influences microstructure, hardness, residual stresses and defect population. In this brief overview of failure mechanisms in friction stir welds, it is relevant to consider typical residual stress distributions and their relationship to weld process parameters. Modern synchrotron and neutron radiation sources are well suited to non-destructive strain scanning experiments aimed at measuring residual stress/strain and the influences of post-weld loading. A number of such studies have been carried out and typical results are reported by James and co-workers.[17,32,39]

Stresses in a solid-state process like friction stir welding will be lower than those associated with fusion welding and peak tensile values of stresses in the longitudinal direction (parallel to the weld) are typically around 40% of the 0.2% proof strength (254 MPa in 5083-H321 alloy). Peak tensile values of stress in the direction transverse to the weld are some 15–20% of the 0.2% proof strength. Tensile stress values tend to be slightly higher on the advancing side than on the retreating side and details of the residual stress distributions reflect the tool pin and shoulder diameters. Peak tensile values occur at the TMAZ–parent plate interface, corresponding to the tool shoulder diameter.

The data presented by Lombard *et al.*[17] indicate that, in 5083-H321 alloy at a given feed rate, changes in tool rotational speed (reflecting changes in heat input) have a significant effect on residual stresses in the weld nugget

and TMAZ regions, with a decrease in peak tensile longitudinal stresses of around 50% occurring at a feed rate of 135 mm/rev, as the tool rotational speed increases from 254 rpm to 635 rpm. Peak tensile values of the transverse residual stress are less affected, with perhaps a 10–20% change observed. Figure 7.19 presents the residual stress data measured using synchrotron X-ray diffraction for a feed rate of 135 mm/rev. Peak tensile values of longitudinal residual stress have a linear correlation with heat input, calculated from the welding parameters, and heat input appears to be dominated by the feed rate rather than pitch or tool rotational speed.

Many authors have considered residual stresses in FS welds and their influence on fatigue crack growth. Even though their peak magnitudes are lower than observed in fusion welding, residual stress has still been found to dominate fatigue crack growth behaviour.[40] A much smaller number of studies have explicitly considered the influence of fatigue loading on residual stress in FS welded specimens.[39] In the work by James *et al.*[39] a progressive sequence of loads was applied to different FS welded plates in which the as-welded residual stresses had been measured using synchrotron X-ray diffraction. The load sequence went from a single load cycle at $R = 0$, through a single cycle at $R = -1$, to 100 cycles at $R = -1$ and several values of peak load were used. Residual stresses were then remeasured.

Results indicated that fatigue loading accentuates the compressive and tensile peak stresses in these plates of a cyclically hardening alloy, whilst retaining the overall form of the residual stress distribution. There is an associated translation of the stress distribution to be more tensile. Increasing the number of applied fatigue cycles from 1 to 100 tends to increase this translation effect. Thus fatigue cycling did not relax the residual stresses in these strain hardening plates of FSW 5383-H321 aluminium alloy, but rather led to a two-fold increase in peak tensile residual stresses after an applied bending stress of 150 MPa and a four-fold increase after an applied bending stress of 250 MPa. These bending stresses corresponded to fatigue lives of around 10^7 cycles and 10^5 cycles, respectively, in 40 mm wide specimens.

The overall conclusions to be drawn from the various studies of residual stresses in FS welds are that their magnitudes may increase (at least initially) under cyclic loading, depending on whether the alloy is hardened by heat treatment or applied strain, and that, even though the peak values are a relatively low, the percentage of the proof strength fatigue life is still dominated by residual stress effects and the presence of defects.

7.7   Conclusions

This chapter has outlined a body of work on FS welds that demonstrates that their properties, performance and failure mechanisms are dependent on plasticisation phenomena and hence on heat input and frictional power

(a)

(b)
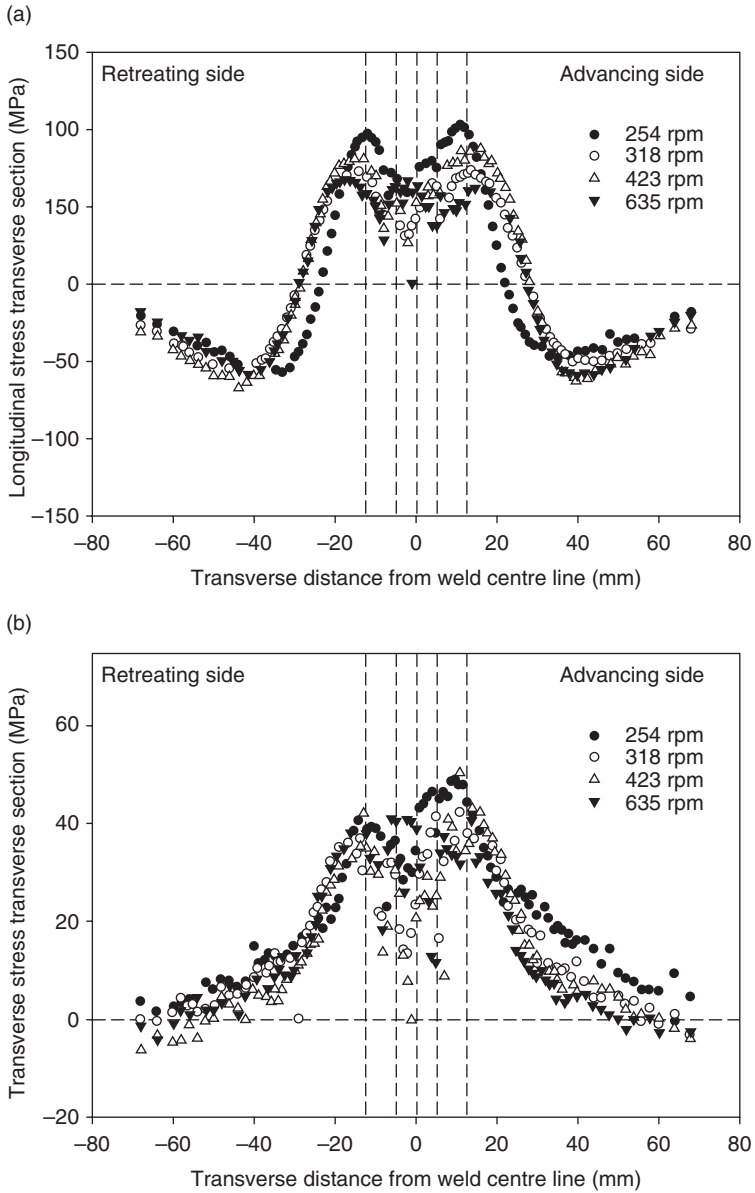
7.19 (a) Longitudinal residual stress for FS butt welds in 5083-H321 aluminium alloy as a function of tool rotational speed at a fixed feed rate of 135 mm min⁻¹. (b) Transverse residual stress for FS butt welds in 5083-H321 aluminium alloy as a function of tool rotational speed at a fixed feed rate of 135 mm min⁻¹.

input. Because of this dependence on complex plastic flow processes, strain hardening alloys may show additional plastic-deformation triggered failure mechanisms to those observed with heat treatable alloys. Tool geometry and weld process parameters have a controlling influence on performance and failure mechanisms, with an additional influence for the case of friction spot welds arising from the direction of loading relative to the spot joint.

Low levels of frictional power at appropriate levels of heat input, and hence temperature, lead to high levels of tensile and fatigue performance. It is clear that on-line monitoring of tool forces and torque might give insight into the choice of process parameters to produce good welds. Graphical depiction of these parameters via a lobed 'force footprint' has been proposed[41] to provide a useful way of choosing optimum tool parameters in FSW. The magnitude of the lobed diagram, its area and its rotation during welding are believed to reflect fundamental information about plastic deformation processes.

Although a significant body of work exists that deals with failure mechanisms, static and dynamic performance of FS welds, far less information exists on the role of residual stresses and their modification by service loads. Advanced strain scanning techniques, coupled with numerical modelling will lead to progress in this area.

7.8   Acknowledgements

7.9   References

1. M N JAMES, D G HATTINGH and G R BRADLEY (2003), 'Weld tool travel speed effects on fatigue life of friction stir welds in 5083 aluminium', *International Journal of Fatigue*, **25**, 1389–98.

2. M N JAMES, G R BRADLEY, H LOMBARD and D G HATTINGH (2005), 'The relationship between process mechanisms and crack paths in friction stir welded 5083-H321 and 5383-H321 aluminium alloys', *Fatigue and Fracture of Engineering Materials and Structures*, **28**, 245–56.

3. H LOMBARD, D G HATTINGH, A STEUWER and M N JAMES (2008), 'Optimising FSW process parameters to minimise defects and maximise fatigue life in 5083-H321 aluminium alloy', *Engineering Fracture Mechanics*, **75**, 341–54.

4. R S MISHRA and Z Y MA (2005), 'Friction stir processing and welding', *Materials Science and Engineering: R: Reports*, **50**(1–2), 1–78.

5. R NANDAN, T DEBROY and H K D H BHADESHIA (2008), Recent advances in friction-stir welding – Process, weldment structure and properties, *Progress in Materials Science*, **53**(6), 980–1023.

6. W XUNHONG and W KUAISHE (2006), Microstructure and properties of friction stir butt-welded AZ31 magnesium alloy, *Materials Science and Engineering*, **431A**(1–2), 114–17.

7. Y ZHANG, Y S SATO, H KOKAWA, S H C PARK and S HIRANO (2008), Microstructural characteristics and mechanical properties of Ti–6Al–4V friction stir welds, *Materials Science and Engineering*, **485A**(1–2), 448–55.

8. F LEGENDRE, S POISSONNET, P BONNAILLIE, L BOULANGER and L FOREST (2009), Some microstructural characterisations in a friction stir welded oxide dispersion strengthened ferritic steel alloy, *Journal of Nuclear Materials*, **386–8**, 537–9.

9. D-A WANG and S-C LEE (2007), Microstructures and failure mechanisms of friction stir spot welds of aluminum 6061-T6 sheets, *Journal of Materials Processing Technology*, **186**(1–3), 291–7.

10. S D THOPPUL and R F GIBSON (2009), Mechanical characterization of spot friction stir welded joints in aluminum alloys by combined experimental/numerical approaches – Part II: Macromechanical studies, *Materials Characterization*, **60**(11), 1352–60.

11. M GEIGER, F MICARI, M MERKLEIN, L FRATINI, D CONTORNO, A GIERA and D STAUD (2008), 'Friction stir knead welding of steel aluminium butt joints', *International Journal of Machine Tools and Manufacture*, **48**(5), 515–21.

12. D L H BULBRING (2009), *Characterization of Friction Taper Stud Weld Properties as Applied to AISI 4140 High Tensile Steel*, Magister Technologiae Dissertation, Nelson Mandela Metropolitan University, South Africa.

13. M GUERRA, C SCHMIDT, J C MCCLURE, L E MURR and A C NUNES (2003), Flow patterns during friction stir welding, *Materials Characterisation*, **49**, 95–101.

14. K N KRISHNAN (2002), On the formation of onion rings in friction stir welds, *Materials Science and Engineering*, **A327**, 246–51.

15. K V JATA and S L SEMIATIN (2000), Continuous dynamic recrystallization during friction stir welding of high strength aluminum alloys, *Scripta Materialia*, **43**, 743–9.

16. P HEURTIER, M J JONES, C DESRAYAUD, J H DRIVER, F MONTHEILLET and D ALLEHAUX (2006), mechanical and thermal modelling of friction stir welding, *Journal of Materials Processing Technology*, **171**(3), 348–57.

17. H LOMBARD, D G HATTINGH, A STEUWER, M N JAMES (2009), Effect of process parameters on the residual stresses in AA5083-H321 friction stir welds, *Materials Science and Engineering*, **A501**(1–2), 119–24.

18. T L DICKERSON and J PRZYDATEK (2003), Fatigue of friction stir welds in aluminium alloys that contain root flaws, *International Journal of Fatigue*, **25**, 1399–409.

19. H-B CHEN, K YAN, T LIN, S-B CHEN, C-Y JIANG and Y ZHAO (2006), The investigation of typical welding defects for 5456 aluminum alloy friction stir welds, *Materials Science and Engineering*, **A433**, 64–9.

20. H-J LIU and H-J ZHANG (2009), Repair welding process of friction stir welding groove defect, *Transactions of the Nonferrous Metals Society China*, **19**, 563–7.

21. S DI, X YANG, D FANG and G LUAN (2007), 'The influence of zigzag-curve defect on the fatigue properties of friction stir welds in 7075-T6 Al alloy', *Materials Chemistry and Physics*, **104**, 244–8.

22. C ZHOU, X YANG and G LUAN (2006), Effect of root flaws on the fatigue property of friction stir welds in 2024-T3 aluminum alloys, *Materials Science and Engineering*, **A418**, 155–60.

23. A LAMARRE and M MOLES (2000), 'Ultrasound phased array inspection technology for the evaluation of friction stir welds', in *Proceedings of the 15th World Conference on Nondestructive Testing*, Rome, Italy, October 2000. http://www.ndt.net/article/wcndt00/index.htm

24. K J COLLIGAN, J XU and J R PICKENS (2003), 'Welding tool and process parameter effects in friction stir welding of aluminium alloys', *Friction Stir Welding and Processing II*, K V Jata, M W Mahoney, T J Lienert and R S Mishra (eds), Minerals, Metals and Materials Society (TMS), 181–90.

25. A J LEONARD and S A LOCKYER (2003), 'Flaws in friction stir welds', *Proceedings of the 4th International Friction Stir Welding Symposium*, Salt Lake City, Utah, May 2003, TWI Cambridge.

26. G J BENDZSAK, T H NORTH and C B SMITH (2000), 'An experimentally validated 3D model for friction stir welding', *Proceedings of the 2nd International Friction Stir Welding Symposium*, Gothenburg, Sweden, June 2000, TWI Cambridge.

27. W J ARBEGAST (2008), A flow-partitioned deformation zone model for defect formation during friction stir welding, *Scripta Materialia*, **58**(5), 372–6.

28. T J LIENERT, W L STELLWAG, B B GRIMMETT and R W WARKE (2003), Friction stir welding studies on mild steel, *Welding Journal*, January, 1S–9S, 2003.

29. ø G FRIGAARD and O T MIDLING (2001), 'A process model for friction stir welding of age hardening aluminum alloys', *Metals and Materials Transactions*, **32A**(5), 1189–200.

30. M SANTELLA, G GRANT and W ARBEGAST (2003), Plunge testing to evaluate tool material for friction stir welding of 6061 + 20 wt% Al_2O_3 composites, *Proceedings of the 4th International Friction Stir Welding Symposium*, Salt Lake City, Utah, May 2003, TWI Cambridge.

31. H J LIU, H FUJII, M MAEDA and K NOGI (2003), Tensile properties and fracture locations of friction-stir-welded joints of 2017-T351 aluminum alloy, *Journal of Materials Processing Technology*, **142**, 692–6.

32. D G HATTINGH, M NEWBY, A STEUWER, I N WEDDERBURN, P DOUBELL and M N JAMES (2009), 'Friction taper stud welding of creep resistant 10CrMo910', *Proceedings of Friction Stir Welding and Processing – V*, R S Mishra, M W Mahoney and T J Lienert (eds), Minerals, Metals and Materials Society (TMS), 75–84.

33. S D THOPPUL and R F GIBSON (2009), Mechanical characterization of spot friction stir welded joints in aluminum alloys by combined experimental/numerical approaches – Part I: Micromechanical studies, *Materials Characterization*, **60**(11), 1342–51.

34. P BRISKHAM, N BLUNDELL, L HAN, R HEWITT, K YOUNG and D BOOMER (2006), *Comparison of Self-pierce Riveting, Resistance Spot Welding and Spot Friction Joining for Aluminum Automotive Sheets*, SAE Technical Paper 2006-01-0774, SAE World Congress, Detroit, MI, USA, 2006.

35. D G HATTINGH, C BLIGNAULT, T I VAN NIEKERK and M N JAMES (2008), Characterization of the influences of FSW tool geometry on welding forces and weld tensile strength using an instrumented tool, *Journal of Materials Processing Technology*, **203**(1–3), 46–57.

36. P C LIN, J PAN and T PAN (2008), 'Failure modes and fatigue life estimations of spot friction welds in lap-shear specimens of aluminum 6111-T4 sheets Part I: Welds made by a concave tool', *International Journal of Fatigue*, **30**, 74–89.

37. P C LIN, J PAN and T PAN (2008), Failure modes and fatigue life estimations of spot friction welds in lap-shear specimens of aluminum 6111-T4 sheets Part II: Welds made by a flat tool, *International Journal of Fatigue*, **30**, 90–105.

38. Y TOZAKI, Y UEMATSU and K TOKAJI (2007), Effect of tool geometry on microstructure and static strength in friction stir spot welded aluminium alloys, *International Journal of Machine Tools and Manufacture*, **47**(15), 2230–6.

39. M N JAMES, D J HUGHES, D G HATTINGH, G R BRADLEY, G MILLS and P J WEBSTER (2004), Synchrotron diffraction measurement of residual stresses in friction stir welded 5383-H321 aluminium butt joints and their modification by fatigue cycling, *Fatigue and Fracture of Engineering Materials and Structures*, **27**, 187–202.

40. L FRATINI, S PASTA and A P REYNOLDS (2009), Fatigue crack growth in 2024-T351 friction stir welded joints: Longitudinal residual stress and microstructural effects, *International Journal of Fatigue*, **31**(3), 495–500.

41. D G HATTINGH, T I VAN NIEKERK, C BLIGNAULT, G KRUGER and M N JAMES (2004), Analysis of the FSW force footprint and its relationship with process parameters to optimise weld performance and tool design, Invited Paper (INVITED-2004-01), IIW *Journal Welding in the World*, **48**(1–2), 50–8.

8

Microstructure characteristics and mechanical properties of the magnesium and aluminium alloy laser weld bonded joint

L. L I U, Dalian University of Technology, China

Abstract: Laser weld bonding (LWB) is a new welding technique which combines laser welding and adhesive bonding and is used here for the formation of a magnesium and aluminium alloy. The LWB joint exhibits better mechanical properties than either the adhesive bonded or the laser welded joint alone. Distributions of magnesium–aluminium compounds in an LWB joint differ from those in a laser welded joint. The addition of adhesive changes the surface tension of the aluminium alloy and subsequently influences the microstructures in the fusion zone of the joint. There are fewer micro-cracks in the fusion zone of an LWB joint than in that of a laser welded joint. The properties of the LWB magnesium to aluminium joint are improved by a combination of adhesive bonding and laser welding.

Key words: adhesive, Al alloy, laser weld bonding, mechanical properties, Mg alloy, microstructure.

8.1 Introduction of laser weld bonding technique

With the rapid development of magnesium alloys, the joining of these alloys to aluminium alloys is attracting increased attention. Joining processes such as tungsten inert gas welding (TIG) (Liu L *et al.*, 2006), laser welding (Borrisutthekul *et al.*, 2005), laser–TIG hybrid welding (Liu X *et al.*, 2005), friction stir welding (FSW) (McLean *et al.*, 2003; Somasekharan and Murr 2004; Gerlich *et al.*, 2005; Yan and Xu, 2005; Sato *et al.*, 2004; Chen and Nakata, 2008) and diffusion bonding are typically employed to join magnesium and aluminium alloys (Liu L *et al.*, 2007, Zhao and Zhang 2008; Wang *et al.*, 2008; Mahendran *et al.*, 2009). Mg–Al intermetallic compounds are found in most Mg–Al joints and are known as a brittle phase in the fusion zone which adversely influences the joint strength. Thus it is difficult to join these alloys with fusion welding alone and new welding techniques need to be developed in order to improve the strength of the joint.

190

Adhesive is known to contribute to structural integrity, ease of manufacturing, enhanced performance, improved safety and savings in cost and time. When loaded, there is a uniform distribution of stress over the bonded area (Darwish and Ghanya, 2000) and there are other advantages, such as excellent fatigue resistance and good energy absorption (Pocius, 1996). There are also some shortcomings, such as limited tolerance of a low, or even moderately high and short working life (Landrock, 1985). Weld bonding may improve these to a certain extent, especially in the automobile industry. However, the weld bonding process makes heavy demands on space and technological procedures and therefore is not widely applied in the manufacturing industry. Consequently, laser (spot) weld bonding technology, a combination of adhesive bonding and laser spot welding, is studied and used to join the AA5754n aluminium alloy in automobile structures (Messler *et al.*, 2003). The manufacture of aircraft skin structures by this method is still under development in the Edison Welding Institute (Grant Wilson, 2005).

Laser weld bonding technique is a new kind of welding technology. It has been developed as an alternative to adhesive bonding and laser welding. Laser welding has a small heat effect zone, which has little effect on the adhesive bonding area. The adhesive in the fusion zone decomposes during the laser welding process, which produces little effect on the properties of the joint. Thus, it can be assumed that laser welding and adhesive bonding hardly affect each other. The advantages of laser welding and adhesive bonding are both included in the laser weld bonding technique. Adhesive provides excellent stress distribution over large bonding areas and laser welding improves the peel resistance of adhesives. Thus a laser weld bonded joint has better mechanical properties than either a laser welded or adhesive bonded joint alone. Laser weld bonding is a new hybrid technique that combines metallurgical joining, mechanical joining and chemical bonding.

Laser weld bonding technology was first reported for joining magnesium and aluminium alloys in 2006 (Liu L *et al.*, 2007b). Element distribution in laser weld bonded joints was analysed for the first time in 2007 (Liu L *et al.*, 2007a). Aspects of laser weld bonded joints were differentiated and explained in 2007 (Wang *et al.*, 2007). The addition of adhesive changed the distribution of the magnesium–aluminium intermetallics, which helps to improve the bond quality. The strength of the laser weld bonded joint is approximately 80% that of magnesium base metal.

The sample configuration of the laser weld bonded joint of magnesium and aluminium alloys is shown in Fig. 8.1. In the laser weld bonding process, the sheet of magnesium is placed on top of the aluminium sheet and adhesive is applied between the layers. Laser power is applied to the surface of the magnesium sheet. The welding parameters are the main factors influencing the joint properties.
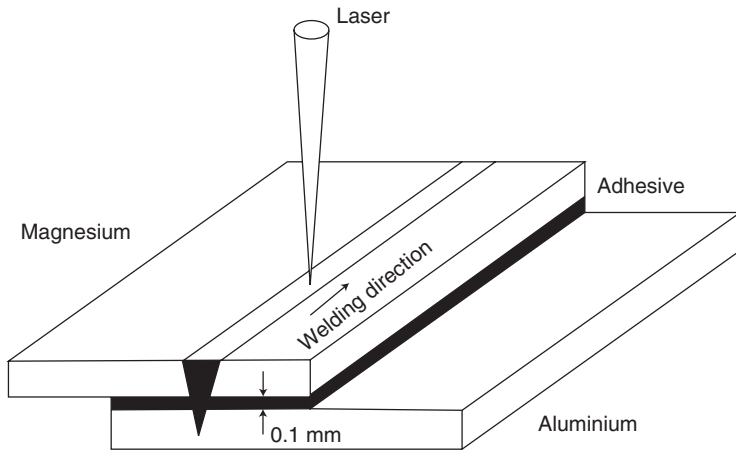
8.1 Configuration of the LWB Mg to Al joint.
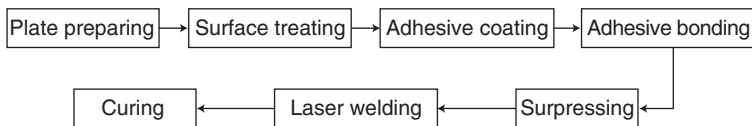
8.2 Process of laser weld bonding Mg alloy to Al alloy.

8.2   Laser weld bonding process

In the process of regular adhesive bonding, the surface condition of the alloys must be controlled carefully. But laser weld bonding is even more complex. Figure 8.2 shows the process of laser weld bonding. The materials are first abraded by 800 grit emery paper and then degreased with acetone. Afterwards, the magnesium and aluminium alloys are etched clean with sodium dichromate and sodium hydroxide solutions, respectively. Both the magnesium and aluminium sheets are coated with adhesive with a thickness of about 0.1 mm. Laser power is applied to join the alloys. Finally, the joints are cured at 175°C for 30 min.

The adhesive decomposes under the effect of the laser. In order to decrease the effect of this decomposition on the joint, the laser power, defocusing amount and welding speed must be accurately controlled, which determines the power density of the laser welding. There is an interrelation-ship between laser power, defocusing amount and welding speed. Once the thickness of adhesive is determined, a change in any one parameter will
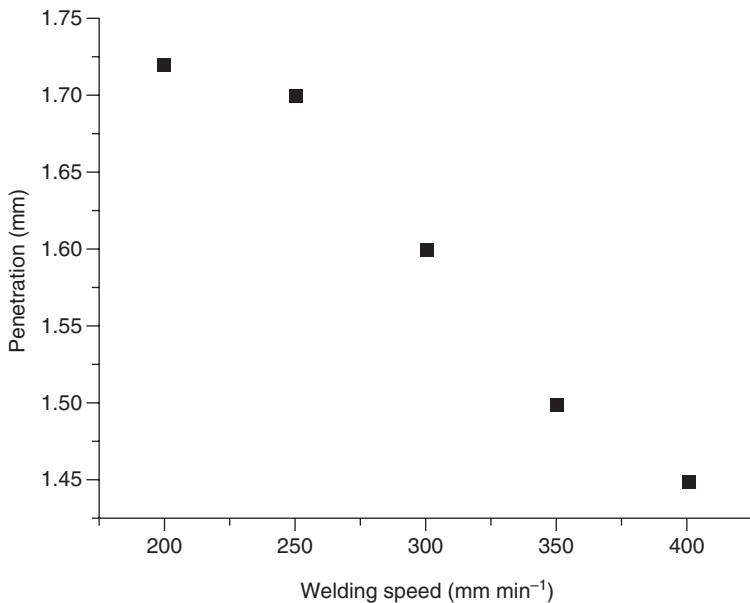
8.3 Penetration varies with welding speed.

influence the others. The influences of the welding parameters are discussed separately below.

8.2.1   Influence of welding speed on penetration

The main welding parameters discussed in this chapter are laser power, defocusing amount and welding speed. Each parameter is discussed with the other two fixed. In these experiments, the thickness of the adhesive is about 0.1 mm, as often used in weld bonding and adhesive bonding processes (Al-Samhann and Darwish 2003; Vable and Maddi, 2006).

Welding speed is an important parameter in the laser weld bonding technique. Figure 8.3 shows the different penetrations when welding speed is increased. The welding depth is initially almost constant and then decreases quickly. When the welding speed is low, more adhesive decomposes. But when the welding speed increases to an upper limit, the adhesive cannot decompose completely. Here, only a small part of the laser beam power can be absorbed by the aluminium alloy, reducing welding depth in that alloy. If the welding speed is very high, the decomposed products cannot escape from the fusion zone. Subsequently, some porosity will appear in the joint, influencing its mechanical properties.

Table 8.1 Tensile shear forces on LWB samples at different welding speed

Welding speed V (mm min^{-1})	Tensile shear force F (kN, average)
200	2.56
250	3.45
300	6.07
350	5.84
400	3.21

Laser power: 350 W; Defocusing amount: –3 mm
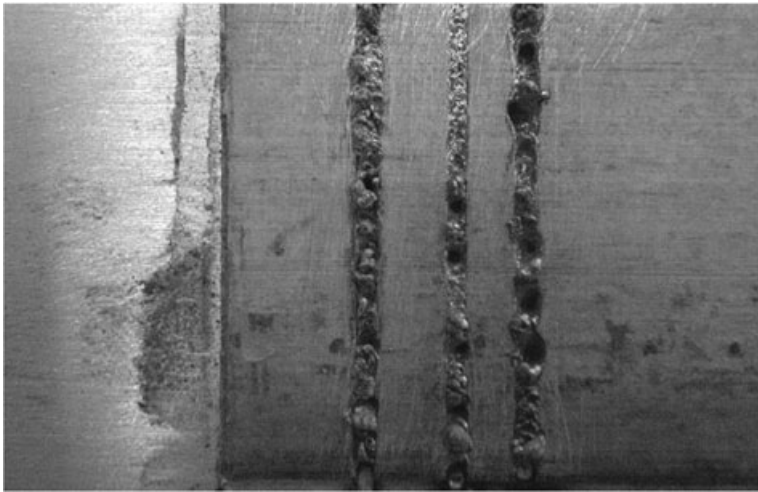
8.4 Surface of weld in LWB joint with low welding speed.

The results of tensile shear testing of the joints at different welding speeds are shown in Table 8.1. It is obvious that the sample with the highest welding speed and deepest penetration does not show the highest shear strength, but the sample with the speed of 300 mm min^{-1} does. If the welding speed is low, the part of the laser power absorbed by the alloys is large, and the magnesium alloy evaporates easily. With the thermal effect of laser beam power, some of the evaporated magnesium alloy makes a depression on the surface of the LWB joint, as shown in Fig.12.4. Consequently, the welding speed must neither be too high nor too slow.
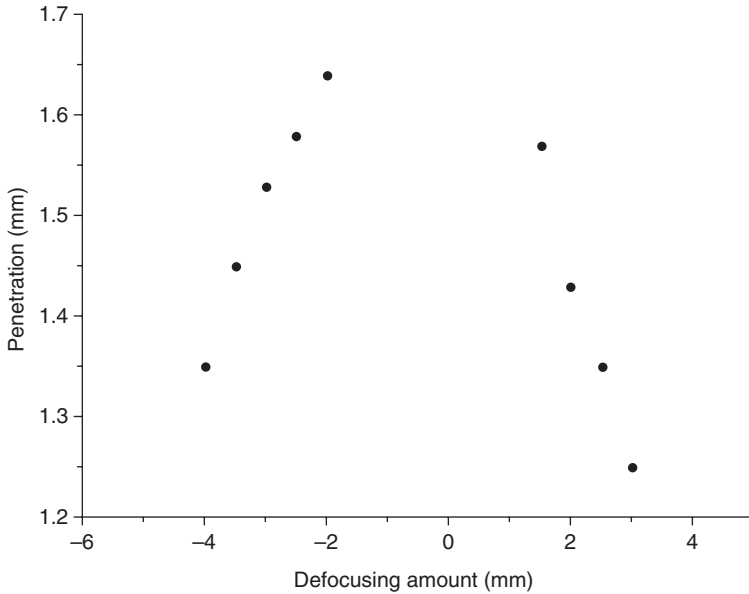
8.5 Penetration varies with defocusing.

8.2.2 Influence of defocusing amount

Defocusing amount is another important factor in the laser weld bonding technique, which can determine the energy density of laser beam power to a certain extent. There are two kinds of defocusing amount, positive and negative. Figure 8.5 shows the varied penetration that occurs with different defocusing amounts. When the absolute value of the defocusing amount is too small, it is impossible to obtain a good joint. Thus in the middle of the image, there are no value points. The energy density of laser beam power increases with decreasing absolute values of the defocusing amount. Figure 8.5 shows that, with the increase in the absolute value of the defocusing amount, the welding depth of the joint decreases gradually. Table 8.2 shows the results of a tensile shear test on the joints under different defocusing amounts. As the absolute value of the defocusing amount decreases, the tensile shear strength of the joint first increases and then decreases. Decreasing the absolute value of the defocusing amount increases the welding depth, but doubles and redoubles the plasma force of the laser beam. The plasma force will act on a small area, which is determined by the walk-off angle and the defocusing amount. If the plasma force is too large, the surface of the welding joint will be destroyed by the force, resulting in a similar performance, shown in Fig. 8.4.

Table 8.2 Tensile shear forces on LWB samples with different defocusing amount

Defocusing amount D (mm)	Tensile shear force F (kN, average)
−4	4.27
−3	6.12
−2	4.76
2	4.85
3	3.02

Laser power: 350 W; Welding speed: 300 mm min^{-1}

It can also be observed that, with the same penetration, the absolute value of the positive defocusing amount is smaller than that of the negative one. In a positive defocusing amount welding process, the distribution of the laser beam power is in a triangular form, thus more adhesive decomposes during the process, which will have a deleterious effect on the mechanical properties of the welded joint. It is easier to obtain a deeper penetration in the negative defocusing amount welding process, during which the distribution of laser beam power is in an inverted triangular form, resulting in a lesser degree of adhesive decomposition. Thus the negative defocusing amount laser weld bonding process has a lesser effect on the mechanical properties of the welded joint.

8.2.3   Influence of laser power

Laser beam power is the decisive factor in the penetration in an LWB joint. Figure 8.6 shows different penetrations with increasing laser beam power. The welding depth increases as the laser beam power increases. As the laser beam power exceeds 400 W, the penetration increases more quickly. Here, the laser welding mode in both aluminium and magnesium alloys is a keyhole model. The results of a tensile shear test on the joints are displayed in Table 8.3. A laser beam power of 350 W produces a joint with the highest tensile shear strength.

Figure 8.7(a)–(c) shows the characteristics of the microstructure models with different laser beam powers in the LWB fusion zone. When the laser beam power reaches 260 W, a small part of the aluminium alloy is melted in the welding process and a magnesium–aluminium intermetallic layer appears at the bottom of the fusion zone.

An X-ray diffraction (XRD) pattern of the fracture, shown in Fig. 8.8, confirms the composition of Mg–Al intermetallics. Thus the joint, having poor mechanical properties, will fail at the intermetallics layer. When the
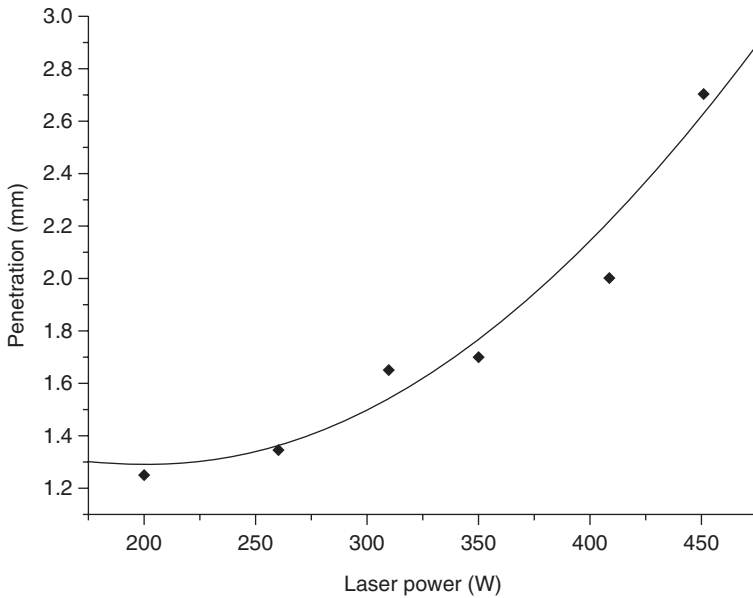
8.6 Penetration varies with laser beam power.

Table 8.3 Tensile shear forces on LWB samples at different laser power

Laser power P (W)	Tensile shear force F (kN, average)
200	2.95
260	4.12
310	5.02
350	5.98
409	3.02
451	2.44

Welding speed: 300 mm min^{-1}; defocusing amount: –3 mm

laser beam power is increased to 350 W, a larger quantity of the aluminium alloy melts and more of the adhesive decomposes. Diffusion between magnesium and aluminium alloys is prevented by the decomposition of the adhesive and the thickness of the intermetallic layer decreases. This kind of joint will fail at the edge of the magnesium fusion zone.

X-ray diffraction analysis of the fracture shown in Fig. 8.9 confirms not many combinations of magnesium–aluminium intermetallics. This improves the mechanical properties of the joint. When the laser beam power is increased to 400 W, more aluminium alloys melt and the adhesive
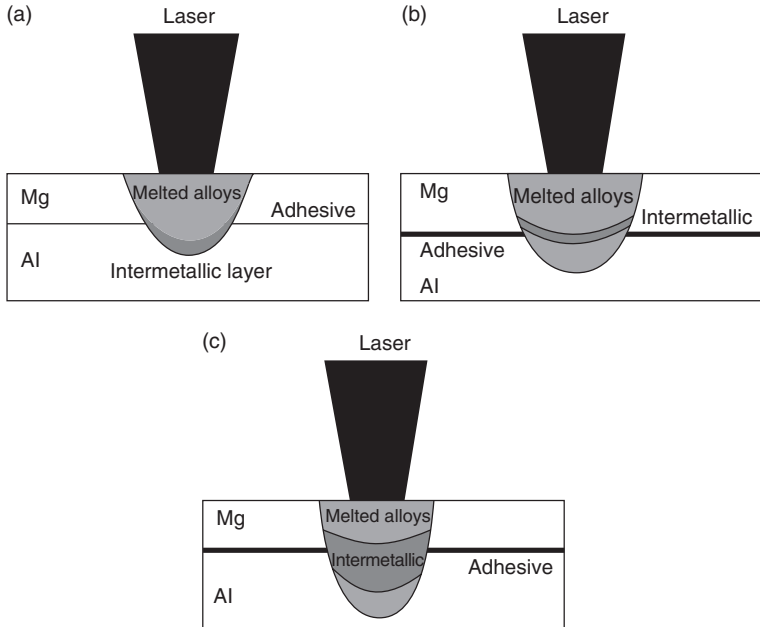
8.7a Microstructure mode in the LWB joint laser power: (a) 260 W, (b) 350 W, (c) 400 W.
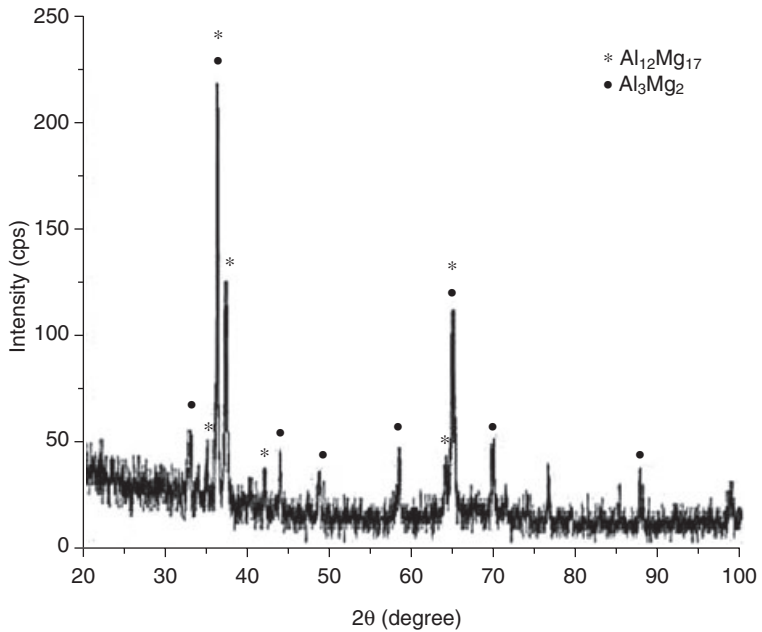
8.8 XRD pattern of the LWB joint fracture (laser power: 260 W).
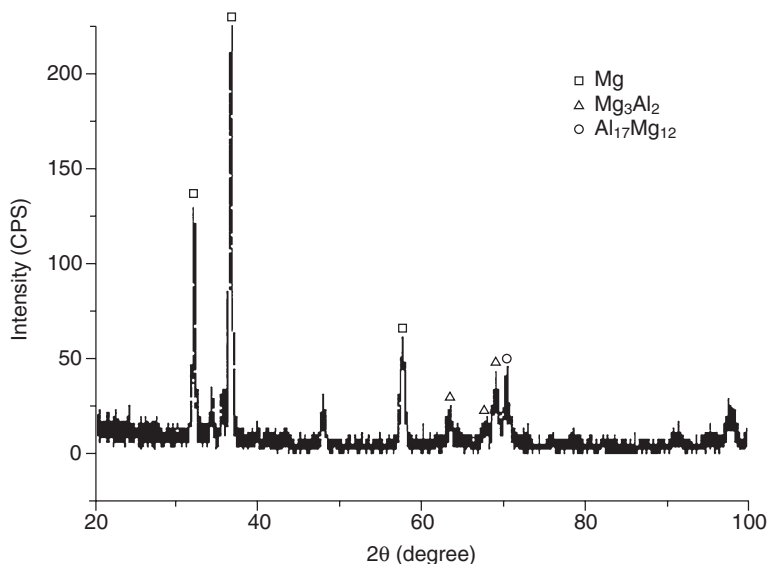
8.9 XRD pattern of the LWB joint fracture (laser power: 350 W).

decomposes rapidly, with a complex effect on the fusion zone. The interme-tallic compounds are observed across almost the entire fusion zone. Many continuous cracks are observed in the high power LWB magnesium to aluminium joint. This results in inferior mechanical properties in this kind of joint.

As laser beam power is increased, the amount of melted aluminium increases. With low laser beam power, all the melted aluminium reacts with the melted magnesium forming Mg–Al intermetallic compounds at the bottom of the fusion zone. With higher laser beam power, more aluminium is melted and more adhesive decomposition occurs, preventing the diffusion between the melted magnesium and aluminium alloys. Thus the thickness of the intermetallic layer is reduced. As the laser beam power is increased further, the welding mode in aluminium alloy turns into a keyhole mode, where more alloy is melted, with a greater reaction between the melted magnesium and aluminium alloys. Here, the decomposition of the adhesive has a complex effect on the entire fusion zone, resulting in more Mg–Al intermetallics in the fusion zone. In the LWB process, the Mg–Al interme-tallics and the microstructure in the fusion zone change as the laser beam power is varied, thus determining the properties of the joint. After numer-ous experiments, the welding parameters are optimized, as shown in Table 8.4, and the corresponding joint performance is exhibited in Fig. 8.10.

Table 8.4 Welding parameters in laser weld bonding Mg alloy to Al alloy

Welding parameters	Quantity
Laser power	300~400 W
Welding speed	300~500 mm min^{-1}
Defocusing amount	–3 mm
Adhesive thickness	0.1~0.2 mm
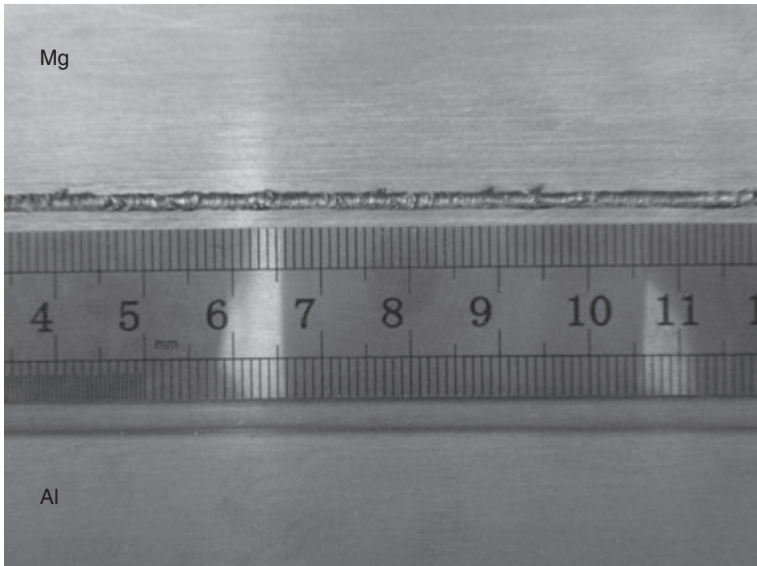
8.10 LWB Mg to Al joint with good performance.

8.3   Microstructure analyses of the laser weld bonded Mg to Al joint

8.3.1   Microstructure in the fusion zone

In a LWB joint, the magnesium alloy is melted completely, while the aluminium alloy is welded in a conductive mode or a keyhole mode. The joint with the keyhole welding mode in the aluminium alloy does not result in good properties, as discussed in the previous section. Thus, the microstructure of this kind of joint has not been analysed in detail. The microstructure analysed below focuses mainly on joints with a conductive welding mode in aluminium alloy.
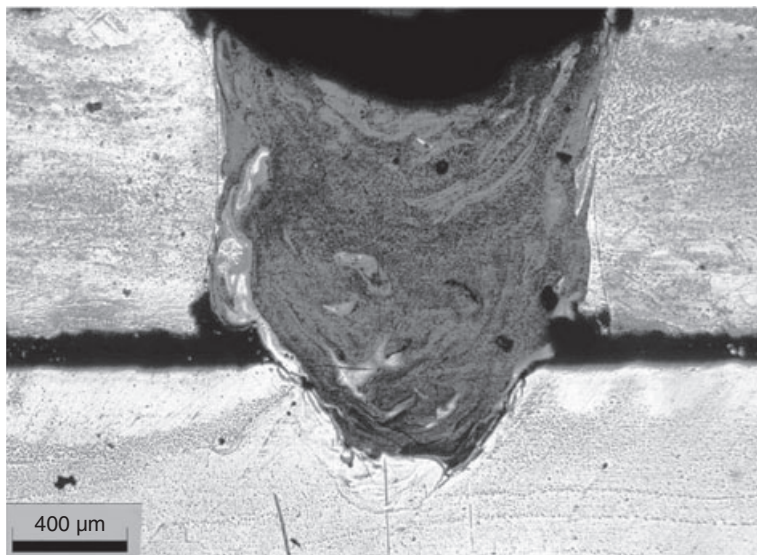
8.11 Microstructure of a laser weld bonding Mg to Al joint.

The transverse section of the laser welded joint and the LWB joint are observed using a scanning electron microscope (SEM), as shown in Fig. 8.11. In the fusion zone, there are no obvious welding defects. As the characteristics of the magnesium and aluminium alloys differ, the microstructures of the magnesium and aluminium fusion zones are analysed separately.

Figure 8.12 shows the SEM image of the fusion zone of the magnesium alloy. The grains in the fusion zone are refined in the laser welding process. There are not many combinations of Mg–Al intermetallics in the magnesium fusion zone and no residual adhesive remains.

The Microstructures of the interface between magnesium and aluminium alloys are shown in Fig. 8.13. Fine gains are mostly observed in the interface of the joint with some microcracks. These microcracks are located in the Mg–Al intermetallics or in the interface between the Mg–Al eutectic phase and the Mg–Al intermetallics, as shown in Figs 8.14 and 8.15. These small and scattered microcracks have little effect on the properties of the joint. However, large and continuous microcracks can also be observed in the laser welded magnesium to aluminium joint and these do have an adverse effect on the properties of the joint. Variation in microcracks in the laser weld bonding process is apparently caused by the addition of adhesives.

With the same welding parameters in the LWB joint and laser welded joint, different microcracks in the fusion zone are observed. Accordingly, the addition of the adhesive affects the formation of microcracks. Their
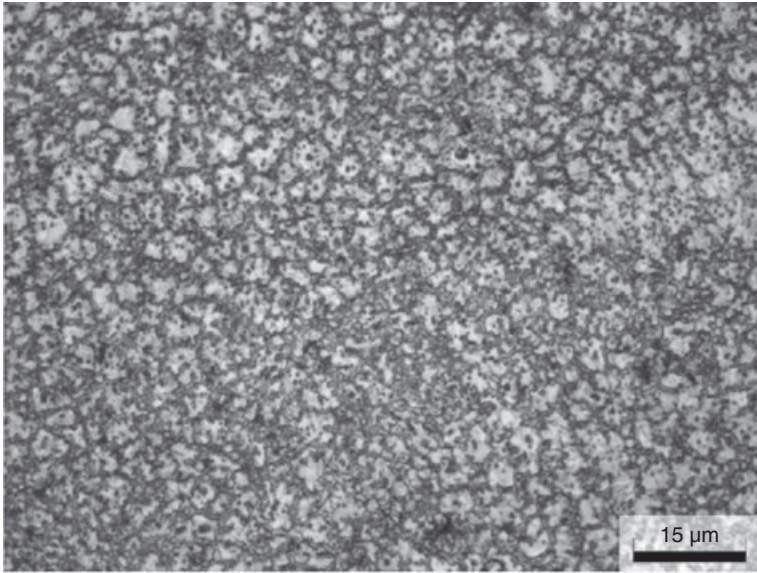
8.12 Optical microstructure in Mg fusion of a LWB Mg to Al joint.
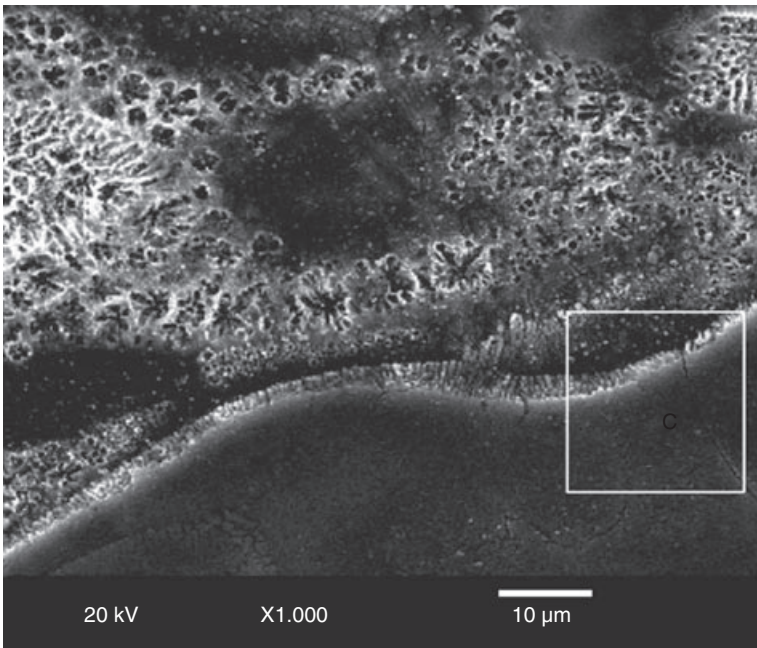
8.13 Microstructure of the interface between the Mg alloy and the Al alloy in the joint.
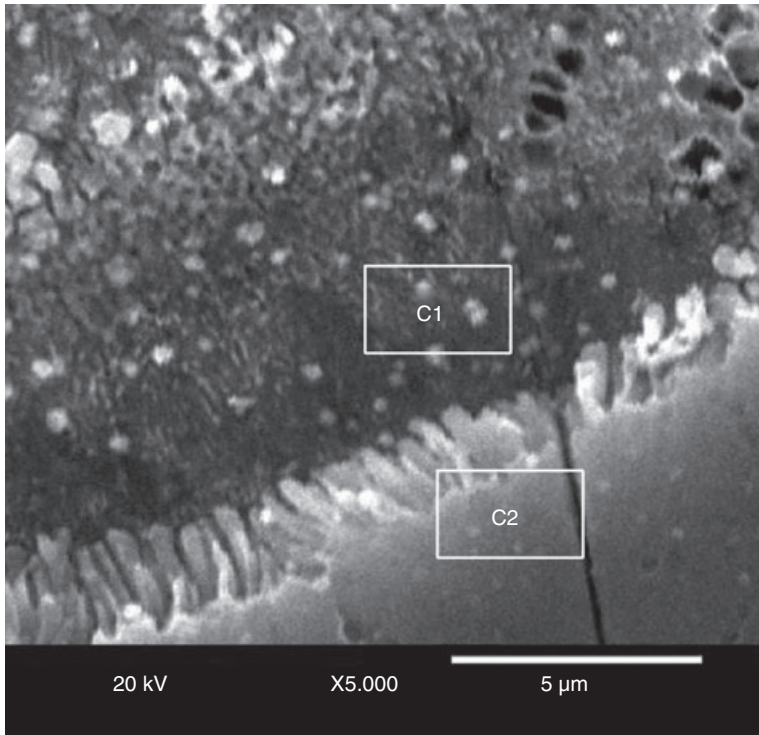
8.14 Microcracks in laser weld bonding Mg to Al joint.
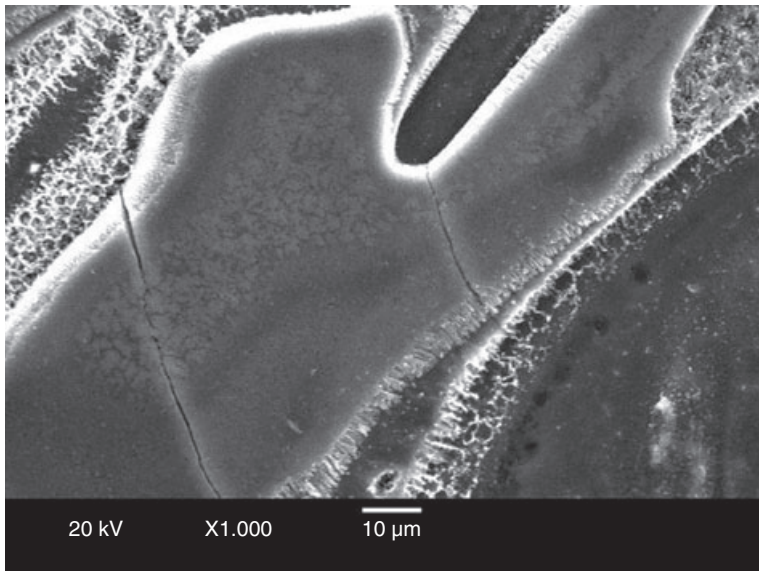
8.15 Microstructure of laser weld bonding Mg to Al joint.
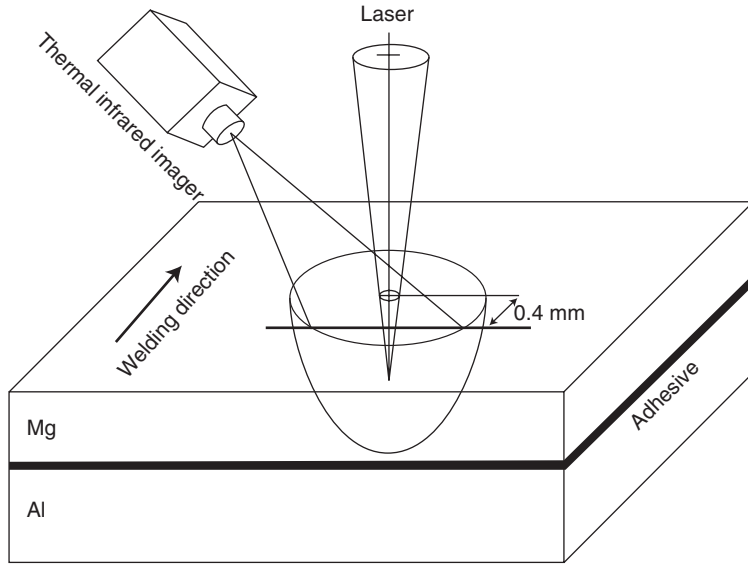
8.16 Diagram of thermal infrared imager analysis system.

formation is originally influenced by the temperature distribution and phase composition in the fusion zone. The addition of adhesive is the reason why the temperature distribution in the LWB joint differs from that in the laser welded joint. In order to prove the temperature changes in the LWB joint, thermal infra-red imager analyses of the surface of the magnesium alloy are performed and thermal couples are used to analyse the surface temperature of the aluminium alloy.

Figure 8.16 is a diagram of the thermal infrared imager analysis system. As the laser induced plasma influences the thermal infrared image measurement, the temperature at the centre of the fusion zone is not investigated. Instead, a temperature line scan is performed in the fusion zone, 0.4 mm away from the centre of the laser beam. In this experiment, the radiance of the magnesium is 0.9. For comparison, the temperature of the magnesium alloy in the laser welding process without adhesive is measured in a similar manner. Figure 8.17 shows the results of the temperature line scan on magnesium alloy. It is clear that the temperature in the laser welding process is higher than in the LWB process. And the high temperature range (>300°C) in laser welding is higher than that in the LWB process. Conclusively, the energies absorbed by the magnesium alloy in the laser welding process are greater than those absorbed in the LWB process and subsequently the temperature of the magnesium alloy in the laser welding process is higher than in the LWB process.
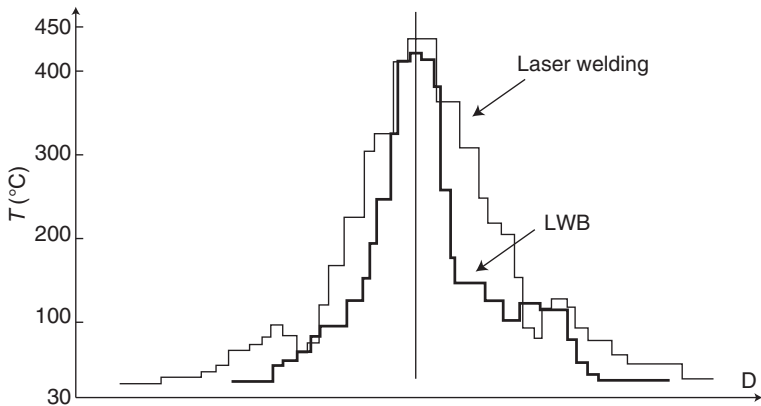
8.17 Results of the line scan of temperature on the surface of Mg alloy.
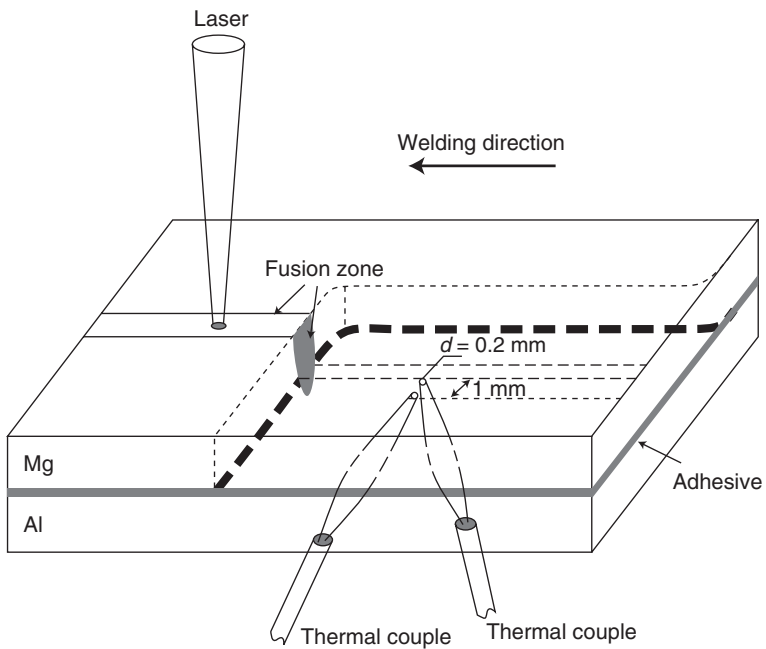
8.18 Set-up of the temperature analysis system with the thermal couple.

Figure 8.18 shows the set-up of the temperature analysis system with a thermal couple. The diameter of the thermal couple is 0.2 mm and the temperature measured is the average value in this area. In order to obtain the accurate temperature of the aluminium alloy, thermal couples are not
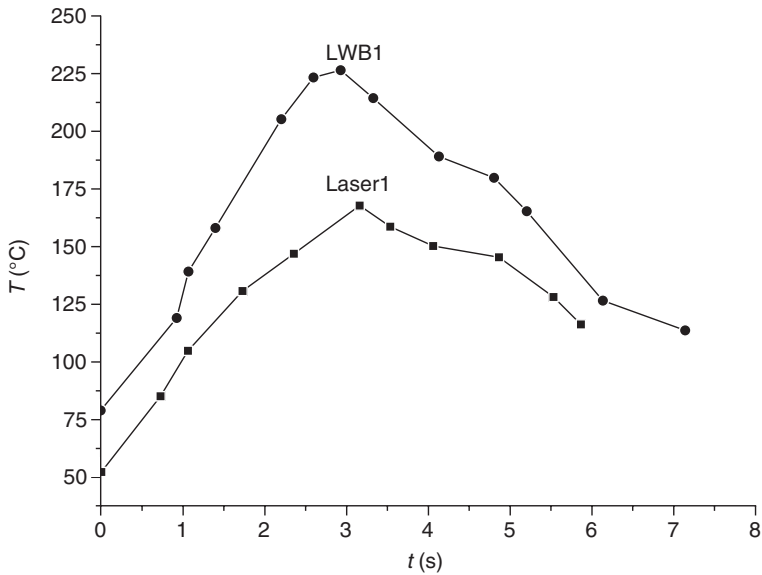
8.19 Results of temperature measurement of point 1 on the surface of the Al alloy.

put in the fusion zone. Instead, the first measured point is located at the edge of the fusion zone as shown in Fig. 8.18, and the second point is placed 1 mm away from the first point. For comparison, the temperature of the aluminium alloy is measured similarly in the laser welding process.

Figures 8.19 or 8.20 show the thermal couple measured temperatures of aluminium alloys. It is evident that the temperature of the aluminium alloy in the laser welding process is lower than that in the LWB process and that the cooling rate in laser welding is slower than in the LWB process. In addition, the temperature difference at the first point between the LWB and the laser welding in the fusion zone is larger than that at the second point. The energy absorbed by the aluminium alloy in the LWB process is larger than that in the laser welding process. Accordingly, the temperature on the surface of the aluminium alloy in the LWB fusion zone is higher than that in the laser welding fusion zone as a result of the addition of adhesive.

According to the temperature measurements on the surface of the magnesium and aluminium alloys, the temperature distribution in the LWB fusion zone is also observed to differ from that in the laser welding fusion zone. In the LWB process, the adhesive changes the surface state of the aluminium alloy, increasing its capacity to absorb laser power and subsequently raising its temperature in the melted state. However, the temperature of the magnesium alloy in the LWB process is lower than in the laser
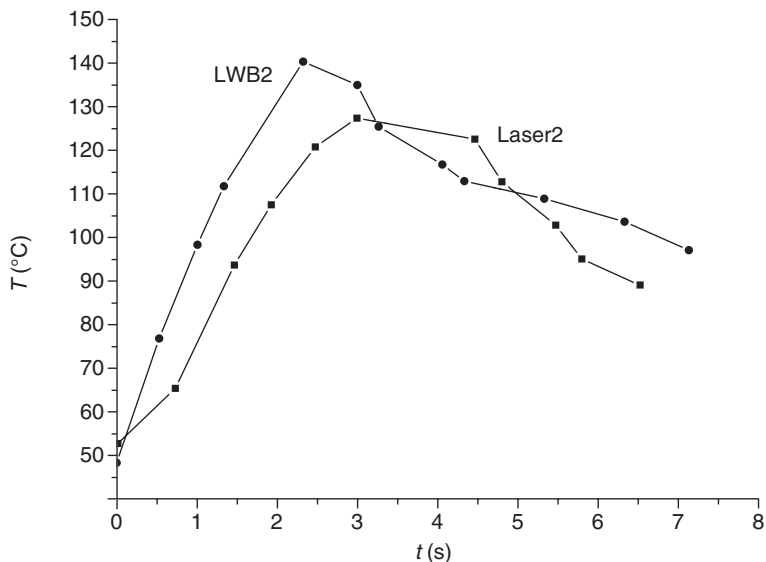
8.20 Results of temperature measurement of point 2 on the surface of the Al alloy.

welding process. The distribution of temperature in the LWB fusion zone is more consistent than in the laser welding fusion zone. Thus, the temperature difference between the melted magnesium alloy and the melted aluminium alloy in a LWB joint is lower than in the laser welded joint. In laser welding and in the LWB process, the Mg–Al intermetallic phase and the Mg–$Mg_{17}Al_{12}$ hyper-eutectic phase are observed at the interface between the alloys. In addition, a temperature gradient exists in the interface between the alloys. Thus it may be deduced that the temperature gradient exists at the interface between the Mg–Al intermetallic phase and the Mg–$Mg_{17}Al_{12}$ eutectic phase. In the cooling process, the higher the temperature gradient, the larger the thermal stress, with a greater tendency to form microcracks. In addition to the temperature gradient, the difference between the Mg–Al intermetallic phase and the Mg–$Mg_{17}Al_{12}$ eutectic phase also promotes the formation of microcracks.

Figure 8.21 shows the longitudinal cross-sectional hardness values in the LWB fusion zone. From the top to the bottom of the fusion zone, the hardness values first increase slowly, then sharply, reaching approximately 150 Hv and finally decrease at the bottom of the fusion zone. The hardness of the $Mg_{17}Al_{12}$ eutectic phase is obviously lower than that of the Mg–Al intermetallic compounds. As a result of the compressive residual stress, the interface between the Mg–Al intermetallic phase and the Mg–$Mg_{17}Al_{12}$
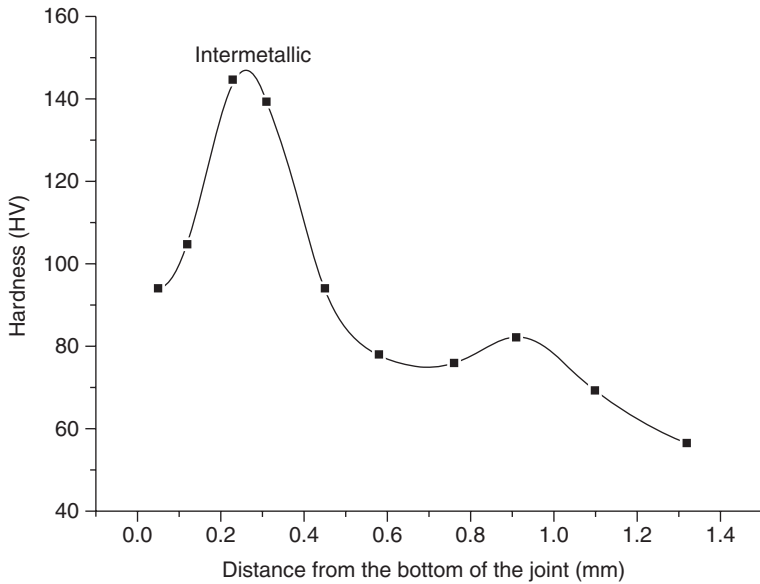
8.21 Longitudinal cross-sectional hardness profile in LWB fusion zone.

eutectic phase is the weakest spot in the fusion zone. The temperature difference between the intermetallic and Mg–Al eutectic phases in the laser welding process is obviously higher than that of the LWB process. Thus in the laser welding process, the thermal stress will significantly increase the formation of microcracks when compared with the LWB process. In conclusion, the formation of microcracks in the fusion zone is mainly determined by the characteristic difference and the temperature difference between the Mg–Al intermetallic phase and the Mg–$Mg_{17}Al_{12}$ eutectic phase.

8.3.2   Element distributions in the fusion zone

The transverse sections of the laser welded joint and the LWB joint are examined by Electron probe micro analyser (EPMA), as characterised in Fig. 8.22. In the laser welded joint, a layer of intermetallic compounds is observed at the bottom of the fusion zone, indicated by the arrows in Fig. 8.22(a) and (b). The Mg–Al intermetallic is about 100 μm thick. In the laser welding process, only a few aluminium alloys are melted and the weakness of the joint lies in the interface between the Mg–Al eutectic phase and the intermetallics. Figure 8.22(c) and (d) illustrate the distributions of magnesium and aluminium elements at the LWB joint. It is observed that the content of the magnesium element at the bottom of the LWB fusion zone
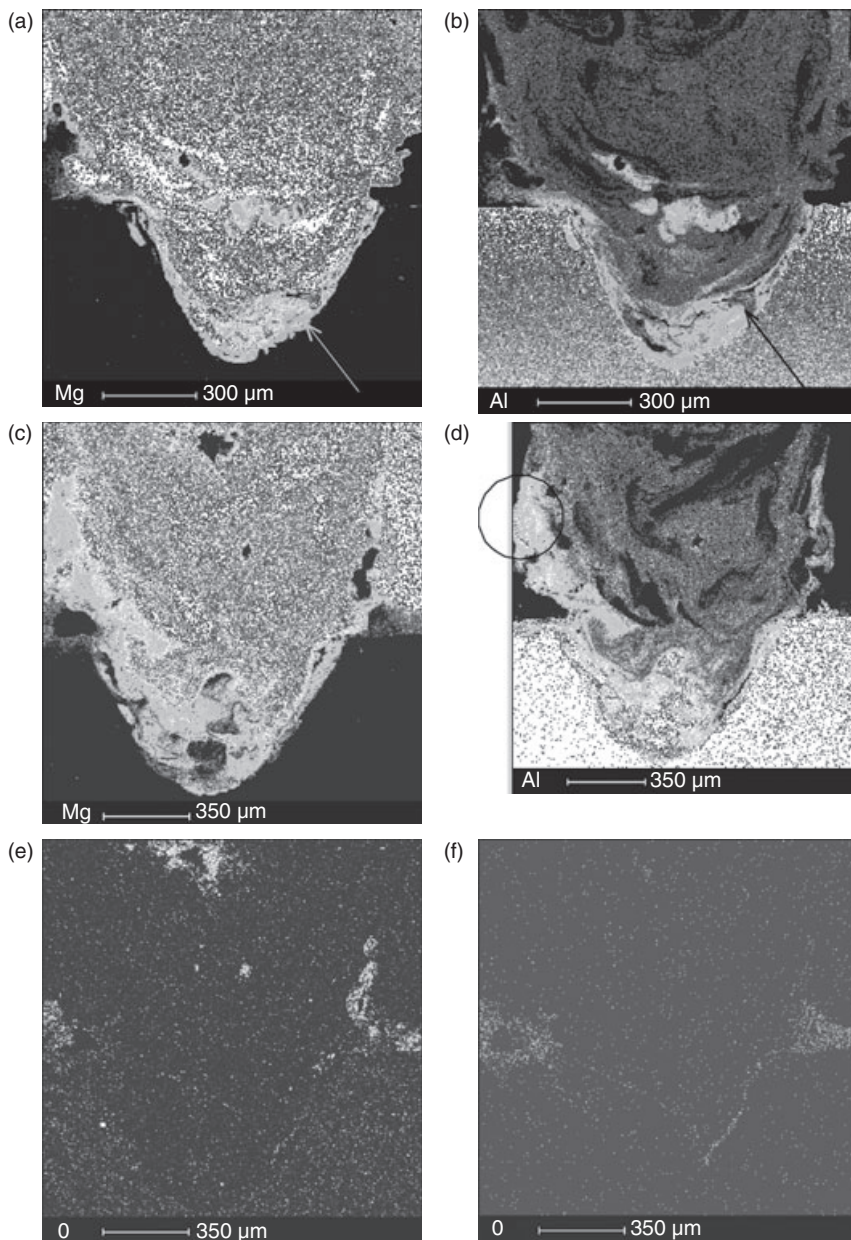
8.22 Transverse section EPMA analyses of the joint of laser welding and LWB. (a) Face scan of element Mg in laser welding joint, (b) face scan of element Al in laser welding joint, (c) face scan of element Mg in LWB joint, (d) face scan of element Al in LWB joint, (e) face scan of element C in LWB joint, (f) face scan of element O in LWB joint.
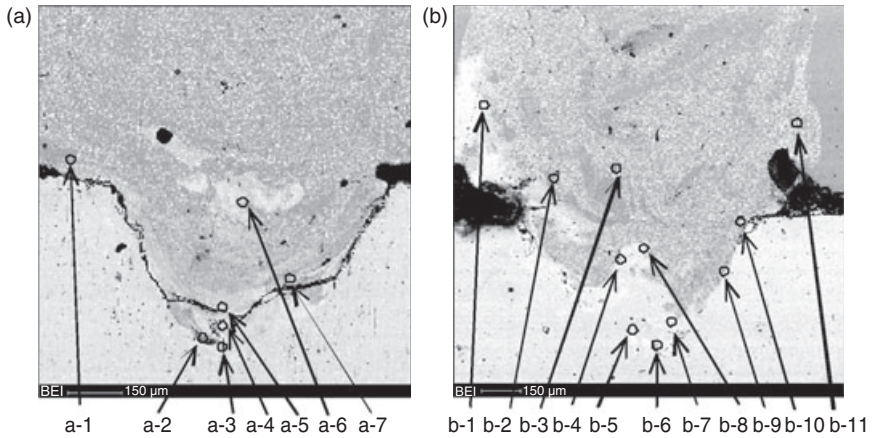
8.23 Secondary electron images and quantitative analysis of laser welding and LWB joint. (a) Secondary electron images of laser welding joint, (b) secondary electron images of LWB joint.

is lower than that in the laser welded joint. At the edge of the fusion zone, the concentration of the aluminium element in the LWB joint is higher than in the laser welded joint. In contrast to the laser welded joint, the aluminium element can enter the centre of the fusion zone in the LWB joint. The different distributions of magnesium and aluminium elements are apparently induced by the adhesive decomposition and the flow of melted metal. The Mg–Al intermetallic layer in the LWB joint is about 50 μm thick, but is not continuous. On the left of the fusion zone, there are hardly any Mg–Al intermetallics. Thus the influence of the intermetallic layer on the properties of the LWB joint is limited. It is known that epoxy resin adhesive is composed of carbon, oxygen and hydrogen elements. The property of the joint is directly influenced by the distribution of these elements. Figure 8.22(e) and (f) show the distributions of carbon and oxygen elements in the LWB joint. It can be seen that there is only a small amount of carbon and oxygen elements in the centre of the LWB fusion zone. It is therefore concluded that the adhesive in the fusion zone has little effect on the properties of the LWB joint.

Figure 8.23 shows the secondary electron images of laser welded and LWB joints. Quantitative analyses of magnesium and aluminium elements are conducted in different continual spots labelled as a1–a7 in the laser welded joint and b1–b11 in the LWB joint, as shown in Table 8.5. The spots analysed are circles 20 μm in diameter. It may be observed that the area a2–a5 of the laser welded joint is composed of the intermetallic compounds Mg_2Al_3 and $Mg_{17}Al_{12}$. These two kinds of intermetallic compounds can be found in the Mg–Al binary equilibrium phase diagram shown in Fig. 8.24.

Table 8.5 Quantitative analysis of Mg and Al elements about laser welding and LWB joints

Serial number	Element	Percentage composition (%)	Whole number proportion (Mg/Al)	Inference composition	Serial number	Element	Percentage composition (%)	Whole number proportion (Mg/Al)	Inference composition
a-1	Mg Al	84.206 15.794	10:53	Mixture	b-1	Mg Al	56.779 43.221	17:12.9	$Al_{12}Mg_{17}$
a-2	Mg Al	63.813 36.187	17:11	$Al_{12}Mg_{17}$	b-2	Mg Al	31.174 68.826	5:11	Mixture
a-3	Mg Al	39.398 60.602	2:3	Al_3Mg_2	b-3	Mg Al	98.586 1.414	70:1	Mg alloy
a-4	Mg Al	52.843 47.157	14:17	$Al_{12}Mg_{17}$	b-4	Mg Al	33.244 66.756	1:2	Mixture
a-5	Mg Al	54.401 45.599	14:17	$Al_{12}Mg_{17}$	b-5	Mg Al	14.637 85.363	5:29	Mixture
a-6	Mg Al	55.308 44.692	17:12	Al_3Mg_2	b-6	Mg Al	31.174 68.826	5:11	Mixture
a-7	Mg Al	68.869 31.131	10:22	Mixture	b-7	Mg Al	24.638 75.326	1:3	Mixture
					b-8	Mg Al	21.739 78.261	5:18	Mixture
					b-9	Mg Al	22.372 77.628	5:18	Mixture
					b-10	Mg Al	73.803 26.197	14:5	Mixture
					b-11	Mg Al	26.784 73.252	1:3	Mixture

Instruction: Mixture is the intermetallic compounds and the solid solution.
The intermetallic compounds, such as $Al_{12}Mg_{17}$ and Al_3Mg_2, are the primary composition of the area.

8.24 Mg–Al binary phase diagram.

However, the situations are not the same in areas b2–b11 of the LWB joint. It is obvious that the content of the aluminium element in this region is too low to form intermetallic compounds, so this must be a mixture of interme-tallic compounds and the eutectic phase. For area b1, the $Mg_{17}Al_{12}$ interme-tallic compounds, which adversely influence the strength of LWB joints, are found at the edge of the fusion zone. So the cause of the reduction in inter-metallic compounds in the LWB joints is the fluid from the decomposition of the adhesive. The vapour from this decomposition may slow down the flow of liquid magnesium metal, resulting in a decreased level of magnesium at the bottom of the LWB fusion zone and a reduction in intermetallic compounds in the LWB joint. Figure 8.23 also shows that many continuous microcracks exist at the bottom of the fusion zone, decreasing the strength of the laser welded joint, while no obvious cracks are observed in the LWB joint in Fig. 8.23b.

8.4   Mechanical properties of laser weld bonded Mg to Al joint

The LWB joint is divided into two parts: the zone of adhesive bonding and the zone bonded by the combination of laser welding and adhesive bonding. These are analysed separately in the next section.
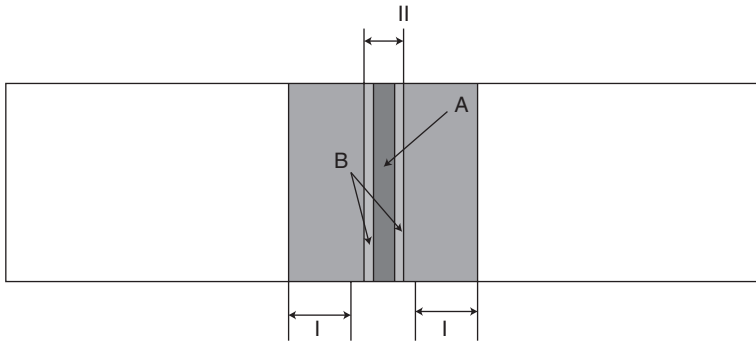
8.25 Different zones in the LWB joint.

8.4.1 Zone of adhesive bonding

Figure 8.25 shows that laser welding melts the magnesium alloy completely, while the laser operates in a conductive mode within the aluminium alloy. The zone of adhesive bonding is much wider than the zone affected by the combination of laser welding and adhesive bonding. If the mechanical properties of both laser welding and adhesive bonding are low, the mechanical properties of the total LWB joint will also be low.

During the LWB process, the zone of adhesive bonding is not affected by the laser process, indicating the same joining performance as the adhesive bonding. The adhesive layer and the metal are joined together by diffuse force or mechanical force. In addition, both the aluminium and magnesium alloys are abraded before being coated with the adhesive to improve the bonding performances by increasing their wetting abilities.

8.4.2 Zone bonded by the combination of laser welding and adhesive bonding

In this zone the adhesive is completely decomposed, making a favourable fusion between the aluminium and magnesium alloys. It is well known that epoxy resin adhesive is composed of carbon, oxygen and some other organic elements such as hydrogen. In the weld, no carbon is observed, indicating that the microstructures of the LWB weld are minimally influenced by the adhesive and that a favourable metal fusion can be achieved with proper welding parameters. Apparently, the fusion welding of magnesium and aluminium alloys will result in intermetallic compounds. Based on X-ray diffraction analyses of the joint (Fig. 8.11), Mg_2Al_3 and $Mg_{17}Al_{12}$ are obtained in the LWB weld, as is observed in laser welds between these two alloys.

(a)
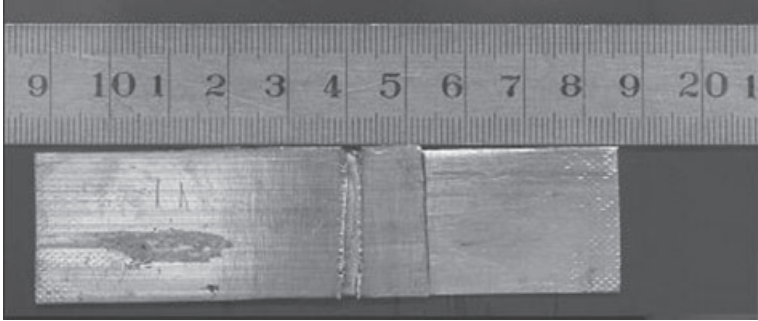
(b)
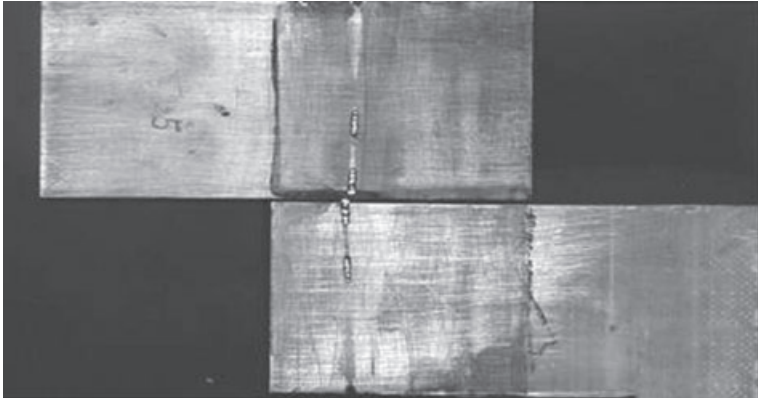
8.26 (a) Fracture of sample with favourable fusion, (b) fracture of sample with imperfect fusion.

It is very important to obtain consistent penetration between the two alloys. During the LWB process, the laser beam impacts first on the magnesium sheet and then on the adhesive layer. On reaching the aluminium sheet, the power of the laser beam is weakened significantly. Various laser powers will have different levels of penetration. In tensile shear test of LWB joints, two kinds of fracture patterns are observed. Figure 8.26(a) shows the fracture of the sample with favourable fusion, which fails at the edge of the welding joint. Favourable fusion is characterised by a joint containing no weld flaws, little residual adhesive and a continuous penetration between the two bonded sheets. Figure 8.26(b) shows the fracture of the sample with unfavourable fusion. In this joint, inconsistent penetration between the aluminium and magnesium sheets is evident. The sample with unfavourable fusion fails at a lower tensile shear force than either of the samples that have favourable fusion or adhesive bonding. Consequently, only the LWB

Table 8.6 Tensile shear force of the laser welded samples and LWB samples

Form of welding	Serial number	Shear force (KN)	Average (KN)
Laser welding	1	0.17	0.18
	2	0.18	
	3	0.18	
LWB	1	5.88	5.79
	2	6.15	
	3	5.33	

joint with the favourable fusion zone where the adhesive decomposes completely can result in satisfactory mechanical properties.

Unfortunately, the laser beam does not distribute its energy evenly, making the joint at the edge of the beam, with incomplete adhesive decomposition, the most complex zone in the LWB joint.

Tensile shear test results for the two types of joints, laser welded and LWB, are given in Table 8.6. The tensile shear load on the adhesive joint is determined by the adhesive used in the experiment and differs with the adhesive and its thickness, therefore the tensile shear load of the adhesive joint is not shown.

In the tensile shear test of the LWB joint, the adhesive layer and laser welded joint will share the shear force. The adhesive layer distributes the shear load to the whole joint. As the loading increases, it cannot be borne by the adhesive layer alone. Subsequently, the metal fusion zone formed by the laser participates in the load bearing. As the loading increases, the sample finally fractures at the edge of the joint. In this process, without a favourable metal fusion zone, the adhesive will quickly fail at a lower shear force. But without an adhesive layer, the strength of the favourable metal fusion alone is limited, causing the joint to fracture at a lower load. Thus, only the LWB joint with the combination of an adhesive layer and a favourable metal fusion zone is capable of enduring a high shear force.

8.5   Future trends

Laser weld bonding is a new welding technique, which successfully joins magnesium and aluminium alloys and in which metallurgic and chemical joining are accomplished simultaneously. With the addition of adhesive, the microstructures of the magnesium to aluminium fusion zone in the LWB joint differ from those in laser welded joints. The properties of the joint improve as a result of Mg–Al intermetallic compound reduction. Welding

parameters in LWB processing are not easy to control and some welding defects still occur in the fusion zone. To apply the LWB method in industry, the welding processing must become more simple and consistent. In addition, welding parameters need to be controlled more accurately to minimise welding defects in the fusion zone. With a varying series of welding parameters, the LWB technique may be applied to other metals such as magnesium to steel, aluminium to steel, and so on. In summary, the LWB method is still in its early stages and a broader application of the technology will depend on the robustness of the process which will be the topic of current and future studies.

8.6   References

AL-SAMHANN A and DARWISH S M H (2003), 'Strength prediction of weld-bonded joints', *International Journal of Adhesion and Adhesives*, **23**, 23–8.

BORRISUTTHEKUL R, MIYASHITA Y and MUTOH Y (2005), 'Dissimilar material laser welding between magnesium alloy AZ31B and aluminum alloy A5052-O', *Science Technology of Advanced Materials*, **6**, 199–204.

CHEN Y C and NAKATA K (2008), 'Friction stir lap joining aluminum and magnesium alloys', *Scripta Materialia*, **58**, 433–6.

DARWISH S M H and GHANYA A (2000), 'Critical assessment of weld-bonded technologies', *Journal of Materials Processing Technology*, **105**, 221–9.

GERLICH A, SU P and NORTH T H (2005), 'Peak temperatures and microstructures in aluminium and magnesium alloy friction stir spot welds', *Science and Technology of Welding and Joining*, **10**, 647–52.

GRANT W (2005), 'Laser weld-bonding method developed for aluminium', *Advanced Materials and Processes*, **163**, 31.

LANDROCK A H (1985), *Adhesives Technology Handbook*, Novyes Publications, Park Ridge, N J.

LIU X, LIU L, WANG H and SONG G (2005), 'Microstructure of laser-TIG hybrid welding joint of dissimilar metals of Al and Mg', *Transactions of The China Welding Institution*, **8**, 32–6.

LIU L, LIU X and LIU S (2006), 'Microstructure of laser-arc hybrid welds of dissimilar magnesium alloy and aluminium alloy with Ce as interlayer', *Scripta Materialia*, **55**, 383–6.

LIU L M, TAN J H, LIU X J (2007a), 'Reactive brazing of Al alloy to Mg alloy using zinc-based brazing alloy', *Materials Letters*, **61**, 2373–7.

LIU L, WANG H and SONG G (2007b), 'Microstructure characteristics and mechanical properties of laser weld bonding of magnesium alloy to aluminium alloy', *Journal of Materials Science*, **42**, 565–72.

LIU L-M, WANG H-Y and ZHANG Z-D (2007), 'The analysis of laser weld bonding of Al alloy to Mg alloy', *Scripta Materialia*, **56**, 473–6.

MAHENDRAN G, BALASUBRAMANIAN V and SENTHILVELAN T (2009), 'Developing diffusion bonding windows for joining AZ31Bmagnesium–AA2024', *Journal of Material and Design*, **30**, 1240–4.

MCLEAN A A, POWELL G L F, BROWN I H and LINTON V M (2003), 'Friction stir welding of magnesium alloy AZ31B to aluminium alloy 5083', *Science and Technology of Welding and Joining*, **8**, 462–4.

MESSLER JR R W, BELL J and CRAIGE O (2003), 'Laser beam weld bonding of AA5754 for automobile structure', *Welding Research*, **6**, 151–9.

POCIUS V (2002), *Adhesion and Adhesives Technology: An Introduction*, 2nd edition, Hanser Gardner Publications, USA.

SATO Y S, PARK S H C, MICHIUCHI M and KOKAWA H (2004), 'Constitutional liquation during dissimilar friction stir welding of Al and Mg alloys', *Scripta Materialia*, **50**, 1233–6.

SOMASEKHARAN A C and MURR L E (2004), 'Microstructures in friction-stir welded dissimilar magnesium alloys and magnesium alloys to 6061-T6 aluminum alloy', *Materials Characterization*, **52**, 49–64.

VABLE M and MADDI J R (2006), 'Boundary element analysis of adhesively bonded joints', *International Journal of Adhesion and Adhesives*, **26**, 133–44.

WANG H, LIU L, ZHU M and WANG H (2007), 'Laser weld bonding of A6061Al alloy to AZ31B Mg alloy', *Science and Technology of Welding and Joining*, **12**, 261–5.

WANG J, LI Y, LIU P and GENG H (2008), 'Microstructure and XRD analysis in the interface zone of Mg/Al diffusion bonding', *Journal of Materials Processing Technology*, **205**, 146–50.

YAN J, XU Z (2005), 'Microstructure characteristics and performance of dissimilar welds between magnesium alloy and aluminum formed by friction stirring', *Scripta Materialia*, **53**, 585–9.

ZHAO L M and ZHANG Z D (2008), 'Effect of Zn alloy interlayer on interface microstructure and strength of diffusion-bonded Mg–Al joints' *Scripta Materialia*, **58**, 283–6.

9
Fatigue in laser welds

V. C A C C E S E, University of Maine, USA

Abstract: A description of fatigue in laser welds is presented in this chapter. The processes of laser welding and hybrid laser arc welding are discussed briefly. Properties of laser welds are summarized related to their influence on fatigue resistance including comparisons to conventional welding techniques. The advantages of laser and hybrid laser welding are presented including a description of applications where laser welding can be used advantageously. The results of fatigue studies of several common connection details are presented including: butt-welds, T and double T joints, lap welds and stake welds used in sandwich panels. The large variation in fatigue test results which are dependent on material and process parameters are demonstrated. Fatigue testing of connections fabricated with new materials and processes is essential. Research on fatigue response of laser welded connections is active.

Key words: butt-welds, CO_2 laser, fatigue testing, hybrid welding, lap-joints, laser stake welds, laser welding, Nd:YAG laser, T-joints.

9.1   Introduction

Laser beam welding (LBW) has the potential to achieve excellent fatigue resistance, especially when used in combination with other more traditional methods such as gas-shielded metal arc welding (GMAW) in a hybrid laser arc welding (HLAW) process. LBW and HLAW will continue to have an increasing impact on engineering design, manufacturing and production. Laser welding is a high energy density process that can be used on a wide variety of metals and alloys. The automotive industry has used laser welding in production since the 1980s. More recently, the ship building and construction industries are looking toward laser welding to provide cost effective and robust structural solutions. Much hope is being placed in laser techniques to weld structural components economically such as fabricated shapes made from plates, stiffeners and piping. Components such as sandwich panels, which have been troublesome to fabricate economically with conventional techniques, can be readily fabricated using laser welding techniques. Originally, laser welding for heavy structures such as ships utilized CO_2 lasers with up to 45 kW power. Current manufacturing systems are looking toward using more efficient, more versatile and modular state-of-the-art fiber lasers with power ratings of 10 kW or more.

218

Fatigue in welded structures is a major cause of failure and must be considered early in the design stage. The properties of laser welded joints can be significantly different from those of conventional welds. Experimental programs are required to assess the material properties and fatigue resistance of LBW and HLAW welded joints, especially when new processes and manufacturing systems are used in the fabrication. Efforts to improve the fatigue life of a welded connection will result in more economical and reliable structures.

Some of the advantages that can be achieved through laser welding are ease of process automation, high welding speed, high productivity, increased process reliability, low distortion of the finished part and no requirement for filler metal. With laser welding techniques it is possible, as described by Duhamel (1996), to achieve full penetration welds in one pass on materials of 25-mm thick, depending on laser power and weld speed, with no filler and preparation as simple as precision cutting of the edges. In addition, distortion of a laser fabricated shape is significantly less than the distortion measured in conventionally welded or hot-rolled shapes. Even though filler material is not required in all cases to achieve a full-penetration laser weldment, lack of filler may cause undue stress concentrations owing to the geometry of the joint, especially if a re-entrant corner exists. Stress concentrations can substantially reduce fatigue life of a high quality full-penetration weld, solely due to the geometry of the weld profile. The combination of laser welding with other processes such as GMAW, which is used to add filler material, can dramatically improve the weld geometric profile and quality. HLAW joints become much more tolerant of accidental gaps, which can result in severe geometric defects such as undercut. An improved weld geometry results in lower stress concentrations and hence improved fatigue life.

One of the primary advantages of laser welded assemblies is control of distortion, which is proportional to heat input. Heat input causes residual stresses and can cause buckling, which is more prevalent when welding thinner material compared to thicker. Studies have shown (Masubuchi, 1984) that an increase in heat input as little as 1% can cause a 25% increase in out-of-plane distortion. Conventional submerged arc welding (SAW) imparts approximately three to four times more heat than HLAW. Reutzel *et al.* (2008) welded 6.25-mm thick steel panels with 6.2 kJ cm^{-1} heat input and the distortion consisted of minor angular distortion and no buckling. The estimated heat input with laser welding was approximately 71% less than a conventional welding process.

9.2   Methods of laser welding

The process of using lasers for welding results in differences in properties of a welded connection in comparison to arc welding, especially with regard

to heat affected zone (HAZ) geometry, hardness, local material strength and residual stresses. Laser energy is one of the highest energy density sources known. The high energy density of the laser welding process results in deep penetration, narrow beam width and a narrow HAZ. A focused laser beam results in heat input that is much more localized when compared to conventional arc welding and is comparable in energy density to an electron beam. In laser welding, melting occurs owing to the collision of photons with the metal compared to electron beam where the kinetic energy of accelerated electrons is converted to heat as they collide with the metal. The material is heated at rates much higher than the conduction rate, making it possible to join thick to thin materials. In a laser welding operation, shielding gases are used to prevent oxidation and to eliminate the formation of plumes and it is typically accomplished under atmospheric conditions.

Table 9.1 gives a comparison of the power density of several welding processes. At energy levels associated with typical laser beam welding, metals will evaporate if this energy is absorbed by the material. A high energy focused beam will result in an evaporated region called a 'keyhole'. Steen (2003) describes the keyhole formation in a laser weld as depicted in Fig. 9.1. The high power density of the focused laser energy causes the metal to boil. The weld pool has strong stirring forces driven by variation in temperature and surface tension. The keyhole is made stable by the pressure from the generated vapor. The keyhole behaves like a black body and nearly all of the energy of the beam is absorbed once the keyhole is formed. A minimum laser power density of 1.0×10^6 W cm^{-1} is required to boil the metal and form a keyhole (Ion, 2005). A compromise needs to be reached between maintaining the keyhole, minimizing burn through and having an economical welding rate. The high power density occurs because lasers can focus the photons on a spot typically smaller than 1 mm in diameter. The molten metal seals up the keyhole as the laser energy traverses through the material. This keyhole type process results in a smaller, narrower HAZ, potentially deeper penetration and hardness variation with a high gradient.

Table 9.1 Comparative power density of welding processes (after Steen, 2003)

Type of process	Power density (kW m^{-2})
Gas or flux shielded arc welding	5×10^3–5×10^5
Plasma	5×10^3–5×10^7
Laser or electron beam	10^7–10^9
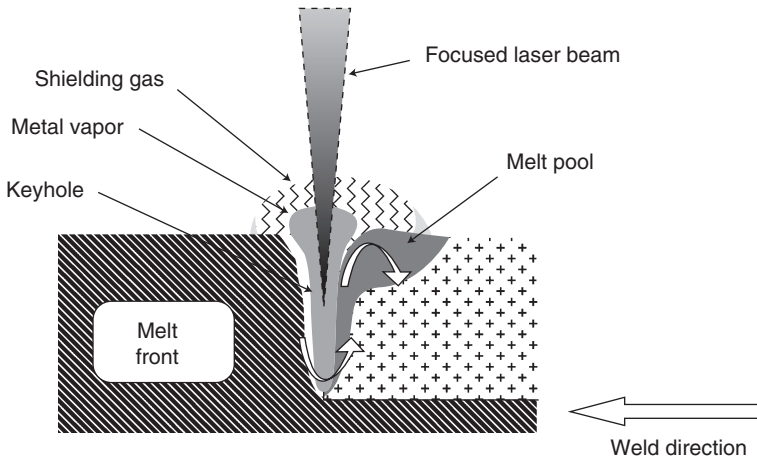
9.1 Schematic of the laser welding process.

A less energetic and/or less focused laser weld results in a conduction limited weld with no keyhole formation.

CO_2 lasers for welding were introduced in the mid-1980s and solid state Nd:YAG lasers in the mid-1990s. CO_2 lasers have a 10.6 μm wavelength with a rating of up to 45 kW maximum, in operation. Roland and Metschkow (1997) describe welding of thick plates for the shipbuilding industry with CO_2 lasers with up to 45 kW power. In CO_2 laser welding, rigid tubes and rotating mirrors are used to transfer the beam energy.

ND:YAG (neodymium-doped yttrium aluminium garnet; $Nd:Y_3Al_5O_{12}$) lasers are nearly twice as efficient as CO_2 lasers (Rooks, 2000). ND:YAG has a 1.06 μm wavelength which is 1/10 that of a CO_2 laser. The laser power can be transmitted in a pulsed manner through flexible fiber optic cable, which results in more advantage for robot and machine design. Recently, high power (>10 kW) continuous fiber lasers have become available. In ND:YAG the plasma does not absorb as much of the laser energy compared to CO_2 laser welding where the laser energy is strongly absorbed by the arc plasma; enough distance must separate the arc from the laser radiation point.

Laser welding with no filler metal, autogenous welding, relies on low tolerance fit-up of the materials usually achieved through processes such as laser cutting, precision machining and sophisticated fixturing. Weld geometries with high stress concentrations may also be the result of lack of filler. Some typical imperfections in laser welded joints formed in this manner can include porosity (Remes, 2008), solidification cracking and heat distortion (Roland *et al.*, 2004). Also, the focused laser energy results in a
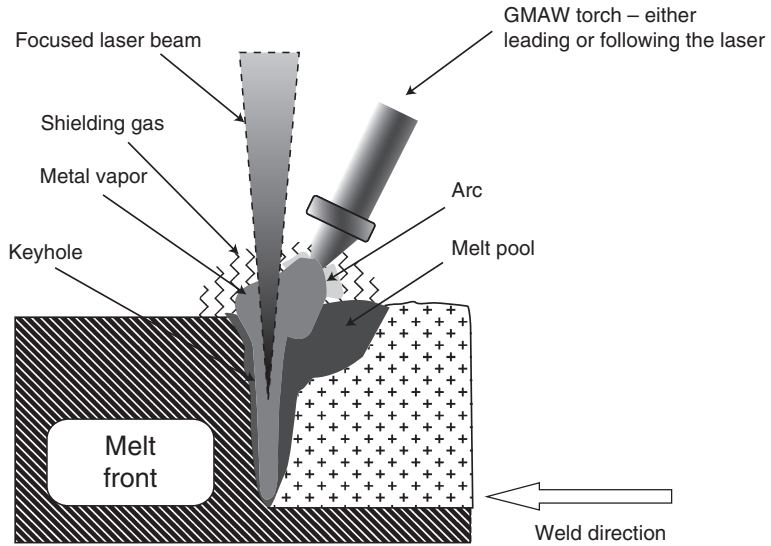
9.2 Schematic of the HLAW process.

narrow HAZ that can lead to brittle microstructure (Reutzel *et al.*, 2008). The simple laser weld, in conjunction with high speeds, results in welds with little or no tolerance for fit-up gaps, making this type of weld inadequate in certain situations. In autogeneous laser welding, the gap between parts is limited to small tolerances, otherwise burn through will occur (Ono *et al.*, 2002a). Deleterious geometric considerations include potential undercutting especially when gaps exist in the fit-up of the materials to be welded. Low tolerance fit-up can also substantially increase costs.

Hybrid laser arc welding (HLAW) was developed, where laser is combined with gas metal arc welding (GMAW) to mitigate some of the issues related to low tolerance fit-up. Figure 9.2 shows a HLAW system with the GMAW torch following the laser. The basic premise of this process is that the laser is used for deep penetration while the metal active gas (MAG) torch is used to melt the filler metal. GMAW has very good gap bridging capabilities and when used in combination with laser welding results in welds with deep penetration, low heat input, small HAZ and improved reinforcement geometry. HLAW can be done at even higher speeds compared to laser or GMAW alone (Roland *et al.*, 2004). The HLAW process increases the tolerance on the joint root openings and improves the control of the weld metallurgy (Defalco, 2007). HLAW results in several advantages and improvements to laser welding including improved fatigue performance and weld toughness, higher weld speeds, deeper weld penetration, wider weld root, lower heat input, better mechanical properties, ceramic

backing not required for butt-welding, smooth transition between weld and base metal on the root side and greater stability of process.

9.3   Applications of laser welding

Laser welding shows much promise to achieve improved quality and economics. Some promising critical applications where laser welding shows potential include fabricated beam shapes, panels including sandwich panels, assemblies, piping and pipelines, bridges, durable goods, rail cars and airframe structures. Fabricated beam shapes made from plate have been in use for decades. They are typically employed in weight critical situations or for larger members where rolled sections of the proper size are not available. Automated laser welding of fabricated shapes offers an alternative to conventional welding, which results in increased quality, high weld speeds, low shape distortion and reduced production costs. Laser fabricated shapes can be especially advantageous in the production of T-shapes, which were typically made either by cutting an I-shape in half or stripping away the bottom flanges (Blomquist and Forrest, 1999) . With fabricated shapes, a manufacturer needs to stock plates of various thicknesses and then can tailor the dimensions to the design. The net result of an HLAW welding process of a fabricated shape is either a double- or sometimes a single-sided weld with a fillet connecting the plates in a T-type joint. The deep penetration accomplished by a laser weld can result in full penetration without edge beveling.

Laser welding also holds much promise in the production of steel panels, including sandwich panels. Bird and Furio (1997) discuss application of laser welding to frame stiffened panels and corrugated core structures in ship construction. Corrugated or orthotropically stiffened panels can be HLAW fabricated using a two-dimensional (2D) gantry system. In this case, both sides of the plate to be welded are visible. When thicker plating is used, a groove weld at the stiffeners edge is typically employed. For thinner sections, a stake weld through the thinner material is typically used. Continuous laser stake welds have demonstrated substantially more fatigue resistance than the alternative of spot or plug welding. Several efforts are under way to develop laser welded sandwich panels in the USA (Defalco, 2007) and Europe (Roland and Metschkow 1997; Roland *et al.*, 2002; Kujala *et al.*, 1999a). The sandwich panel is a system which typically has an inaccessible space, making inspection difficult in many cases. Reliable processes with high quality control are essential and conventional welding processes are not practical for fabrication of sandwich panels.

Laser welding shows promise in the manufacture of durable goods such as washing machines, dishwashers, ovens, and so on, which are fabricated from thin sheets. It has potential advantage over resistance seam welding

that is used typically (Koçak, *et al.*, 2001). The steel industry has recently considered use of laser welding in building and bridge construction. There is still much work and much potential here. Eibl *et al.* (2003) studied the fatigue resistance of laser welded thin sheet aluminum. The use of laser welding of aluminum alloy for the aircraft industry is being considered including airframe fabrication and sandwich panels. This solution can be used to reduce weight and to replace the conventional riveted construction. Cost reduction potential is observed.

9.4   **Future trends in laser welding**

Much of the future of laser welding lies in process automation using high speed, energy efficient systems developed to improve productivity and reduce cost. Great promise lies in the HLAW technique which can be implemented at increased speeds, is more tolerant of lack of fit-up and reduces demand on clamping systems. Applications such as HLAW structural shape fabrication from plate material including Ts, wide flange and channels will allow more flexibility in choosing sizes, potentially less weight, the use of specialty plate material and less distortion in the end product (Blomquist and Forrest, 1999). Specialty shapes made from plate also result in fewer material inefficiencies. In ship fabrication, for example, deflanginig an I-beam into a T-shape results in the scrapping of one-quarter of the purchased material (Blomquist *et al.*, 2004). In fabricated shapes, the deep penetration of the laser reduces the requirement for filler material and the reduced distortion lessens or eliminates the need for straightening and rework. Cost-effective, and weight efficient designs are the result. As with any new process, qualification studies are required to demonstrate that the strength and fatigue life are not compromised by the process. Also, HLAW makes the efficient fabrication of metallic sandwich panels possible using a stake weld which can be used through the outer plating (face sheet) material to connect the core. Roland *et al.* (2004) discuss the numerous advantages of steel sandwich panels in shipbuilding including high strength, high stiffness, high accuracy, modular design and ease of assembly. They reported that, in some cases, structural weight can be reduced by up to 40% using sandwich panels in lieu of other structural systems. Myer Werft operates a plant that includes a fixed gantry with a 12 kW CO_2 laser and sliding table that moves the workpiece and a welding head that is equipped with a pressure roller used to minimize the gap between the face sheet and the core elements.

The development of automated gantry type and robot laser welding machines is facilitated by fiber lasers (Rooks, 2000). Cost-effective systems for accurate edge preparation will enhance laser welding and further machine development and integration (Roland *et al.*, 2002). In the USA, a

closed loop process control system was developed to monitor actively the laser welding process by Applied Thermal Sciences (ATS) of Sandford, Maine, in conjunction with ESAB (Defalco, 2007). This system uses a 10 kW fiber laser mounted on a movable gantry. The system can be configured with laser only, laser with cold wire feed or HLAW. It includes active weld joint tracking, weld monitoring and control of critical welding parameters, automated weld surface inspection, automatic flaw detection and process documentation and reporting. This system is being used in the fabrication of laser fabricated shapes from plate material and steel sandwich panels. It was developed to work with material that is laser and/or plasma cut and then welded with no subsequent operations other than cleaning. This is ideal for situations where machining the edges is cost prohibitive. This system is operated as a 2D gantry or a three-dimensional (3D) robotic (Orozco *et al.*, 2004). When defects occur, they are marked and the system automatically modifies the welding process parameters (Blomquist *et al.*, 2004).

Figure 9.3 shows the weld profile monitoring and marking of a defect in the profile at position B. This type of geometric defect would cause high stress concentration in the joint. Figure 9.4 demonstrates the improvements made by the inclusion of closed loop control and the addition of filler metal
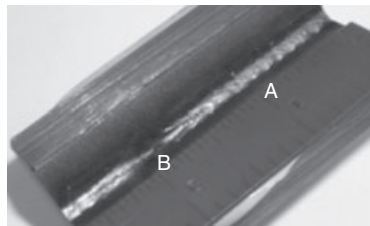
(a)
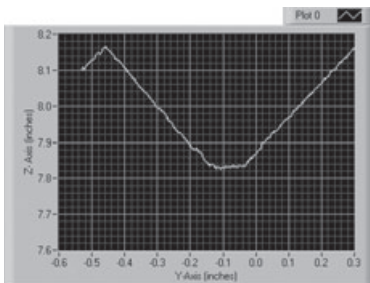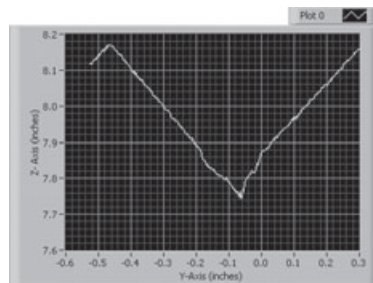
(b)   (c)

9.3 Real-time control system demonstrating weld profile monitoring and flaw marking. (a) laser welded joint, (b) profile at A, (c) profile at B showing flaw (after Orozco *et al.*, 2004).

0.000 gap   0.030 gap
(a)

0.030 gap
(b)
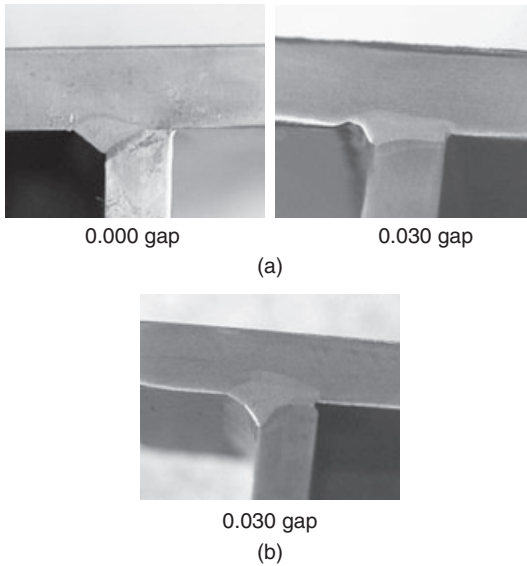
9.4 HLAW (a) without and (b) with closed loop control (after Orozco *et al.*, 2004).

in the process in the fabrication of a T-joint with a 25 kW CO_2 laser in combination with a cold wire feed. Near zero tolerance is required to minimize the undercut of a laser welded connection. As the tolerance is increased, undercut occurs if an inadequate amount of filler metal is added. This results in poor weld geometry that can substantially reduce the fatigue life. The control system tracks the weld geometry and other parameters and supplies the appropriate amount of filler, resulting in a smooth geometric profile as shown in Fig. 9.4(b).

9.5   Properties of laser welded metals

There are significant differences in properties between joints made by laser welding and by conventional welding processes. In conventional processes, distortions usually increase owing to welding and cutting operations, especially for thin materials. Complications caused by distortion can result in lower productivity and throughput and hence are costly. At a microscopic level, laser welded joints differ from conventional joints because of the very narrow fusion zone, strength mismatch and high gradient of hardness. The possible formation of martensite in the weld zone of C–Mn steels is also of concern and there is a significant strength mismatch in different regions. For a steel with approximately 550 MPa ultimate strength in the base metal, the ultimate strength in the HAZ was reported by Koçak *et al.* (2001) to be

approximately between 750 and 850 MPa and the ultimate strength in the weld metal to be between 1150 and 1250 MPa. The fracture strains were reduced from 28% in the base metal to approximately 11% in the HAZ and 9% in the weld material.

Weld properties depend upon speed, power and focus as well as on the properties of the material constituents. Olabi *et al.* (2006) described the use of Taguchi methods and neural networks to optimize the laser parameters in CO_2 laser welds. Defects in laser welded joints are similar in scope to those in other welded joints and include formation of cracks in the narrow weld zone, voids, porosity and undercut, among others. Crack formation caused by inhomogenities can also occur under service loads. Kendrick (2005) outlined the flaws observed in welded joints and placed them in three categories as follows:

- Planar: cracks, lack of fusion, lack of penetration, undercut, root undercut, concavity and overlap
- Non-planar: cavities, solid inclusions slag, porosity
- Geometrical/shape imperfections: axial misalignment, angular misalignment, imperfect weld profile, undercut and root undercut.

The mechanical properties mismatch between the weld and base material can significantly affect the fatigue performance. The tensile strength and toughness of the material can be evaluated in the weld zone by microtensile specimen tests. This technique was developed for the nuclear industry to assess properties in the HAZ of conventional multi-pass welds. Çam *et al.* (1998) performed microtensile testing of ferritic and austenitic steels laser welded by CO_2 lasers using 6-mm thick plates. The welds were full penetration and produced without filler wire using combinations of two ferritic steels, st37(F1) and st52(F2), and an austentitic stainless steel, 1.4404(A) with properties given in Table 9.2.

Microhardness testing was performed across the weld root, midsection and top part of the joint. Metallurgical analyses of the ferritic materials show a structure consisting of martensite and bainite caused by rapid cooling while the austentic material showed a dendritic structure with no

Table 9.2 Material properties of steel used in the hardness study (after Cam, 1998)

Material	Yield (MPa)	UTS (MPa)	Elongation (%)
St 37 (F1)	233	368	36
St 52 (F2)	382	528	30
Austenitic 1.4404 (A)	308	626	66
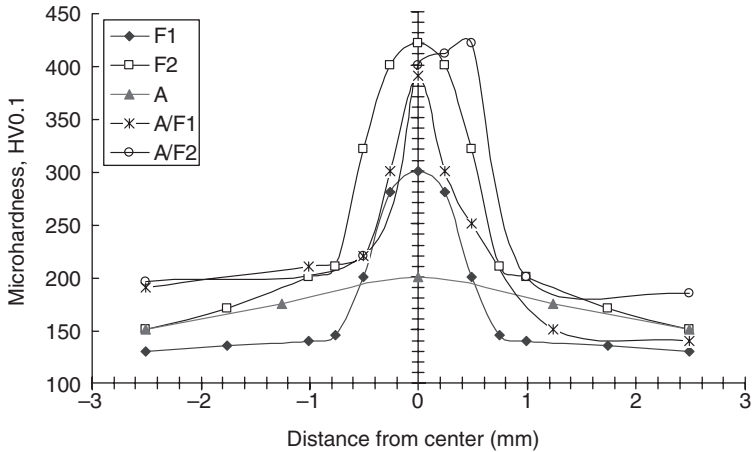
9.5 Hardness profile for laser welded ferritic and austentic steels (after Çam *et al.*, 1998).

evidence of martensite. In general, hardness at the root, middle and top of the weldment were essentially the same for any given weld. The primary difference was attributed to distance from the weld center and the weld material.

Figure 9.5 provides a rough estimate of the average hardness profile adapted from the data presented by Çam *et al.* (1998) with hardness versus distance from weld center plotted for the various material configurations. The ferritic steel (F2) and weldements of the austentic to ferritic (A–F1 or A–F2) showed the higher hardness gradients, while the austentitic steel (A) showed a relatively lower gradient. This study also addressed the strength of weld metal compared to the base metal and strength in the HAZ, using microtensile specimens. The weld metal strength of the ferritic material was generally much greater than the base metal with much lower ultimate strain values (<10%). The ratio of the weld metal to base metal yield strength ranged from 3.09 for F1–F1 to 2.53 for F2–F2. Welded specimens failed at the lower strength base metal side owing to strength mismatch of the weldment. The strength of the material and failure strain of the material in the HAZ lies between the weld metal and base metal. In the austenitic joints the weld and base metal strength were nearly the same with a yield strength ratio of 1.13 and the failure strains were slightly reduced (approx. 50% in weld metal, 55% in HAZ). In the dissimilar joints there was a relatively large difference in the weld to base metal strength with a yield strength ratio of 2.28 (F1–A) and 2.21 (F2–A). The strength in the HAZ zone on the ferritic side generally displayed higher strength and lower failure strain than

the base metal, whereas the samples taken on the austenitic side displayed properties similar to the base metal.

Kitagawa *et al.* (2002) tested laser welded lap joints of SMA 400 steel with a yield strength of 305 MPa, ultimate tensile strength of 454 MPa and 31% elongation. Weld metal yield and ultimate tensile strength were found using a 2-mm diameter mircotensile test and were 481 MPa and 659 MPa, respectively with an elongation of 25% at failure. Weld metal hardness ranged from 224 to 293 HV1 with an average value of 243 HV1. Remes and Kujala (2004) measured the hardness in laser welded, hybrid laser welded and SAW joints made from 12-mm thick RAEX S275 steel with mean base metal hardness of 131 HV5. The hybrid laser welded joints showed a maximum hardness of 248 HV5 in the weld zone and HAZ. The laser weld specimen showed a maximum hardness of 251 HV5 and 245 HV5 in the weld zone and HAZ, respectively. The SAW weld gave values of 188 HV5 and 173 HV5 in the weld zone and HAZ, respectively. Boronski (2006) indicated that the heterogeneity in material caused by laser welding results in a strong mismatch in static and fatigue properties. Butt welded specimens using 5 mm plate were made with a 3.8 kW laser operating at 1.2 m min^{-1}. The base metal ultimate strength of 495 MPa can be compared to a weld metal strength of 1115 MPa. A ferritic-pearlite structure was found in the base metal with a hardness of approximately 140 HV, baininte in the HAZ with a hardness of about 190–200 HV and bainite with small quantity of martensite in the weld metal with hardness between 325 and 390 HV.

Cho *et al.* (2004) discussed the influence of residual stresses on fatigue. Residual stresses are a consequence of the heating and cooling cycles that occur during the welding process. Tensile residual stresses at the weld on the order of the yield strength of the material may exist. The distribution is complex and depends on the process details, geometry and material properties. They tested lap joints from 1-mm thick ASTM A366 plate welded with a 4 kW CO_2 laser and argon shielding. They used finite element analysis (FEA) to estimate the thermal effects of the welding process. Moraitis and Labeas (2009) also used FEA analysis to evaluate residual stresses in laser welded butt-joints. They proposed a model that could reliably predict keyhole shape for welds in aluminum and steel. In their simulation of residual stress, they demonstrated that peak residual stress upwards of 300 MPa in the longitudinal direction can exist near the weld line and drops to near zero at a distance of about 40 mm from the weldline to the weldment of a 4-mm thick plate. Similar results were found for steel and aluminum.

Aluminum butt-joints welded with a CO_2 laser operating at 2.5 kW with helium shielding gas were investigated by Ancona *et al.* (2007). Good quality welds were made when laser power was adequate to form the keyhole. At weld speed of 100 mm s^{-1}, tensile strength was found to be 90% of the base

metal strength. Porosity was less than 3% and a small hardening across the weld zone with peak hardens values of 105 HV was measured in the fusion zone compared to a base metal hardenss of 85 HV. The keyhole became unstable at 2 kW power and resulted in a large dispersion in test results.

According to Cao *et al.* (2006) with proper welding parameters, crack free laser welds with low porosity can be obtained in some magnesium alloys, especially in wrought material. Some magnesium materials exhibit problems such as unstable weld pool, sag, undercut, porosity, liquidation and solidification cracking and more research into the process is warranted.

The static and fatigue strength of laser welded titanium butt-welds made from grade-2 and grade-5 titanium was studied by Casavola *et al.* (2009). Titanium has an affinity toward atmospheric gases such as oxygen, nitrogen and hydrogen; therefore it must be especially protected by shielding during welding. They closely measured the weld profile and misalignment of the welds ranging from 0.1° to 0.3°, which is much less than in arc welded joints. Based on the actual weld profile, they estimated a stress concentration factor of 1.4 from the theory of elasticity.

9.6   Fatigue life prediction in welded joints

There are several popular approaches to fatigue life prediction in welded joints including the following:

*   nominal stress approach
*   structural or hot spot stress approach
*   notch stress or notch strain approaches
*   fracture mechanics crack propagation approach.

Ideally, fatigue analysis results should be independent of the method chosen to perform the analysis; however, that may not always be the case, as demonstrated by Fricke *et al.* (2002). A summary of the various approaches is presented by Fricke (2003) who lists a host of references on the subject. Hobbacher (2009) describes new International Institute of Welding (IIW) recommendations, which attempt to harmonize these methods. For example, clear recommendations have been given for finite element meshing when hot spot stress is to be determined. A direct assessment of weld imperfections, recommendations for multiaxial fatigue, direct fatigue assessment without the need for component testing and fatigue classification for aluminum is also provided in the new recommendations.

The characteristic *S–N* curve approach uses fatigue test data and assumes that fatigue damage accumulation is a linear phenomenon. Using an *S–N* approach, the expression for fatigue life of a welded joint can be cast into a general form as follows:

$$N = \frac{A}{S^m} \tag{9.1}$$

where N is the number of cycles to failure, S is the appropriate stress level for the analysis approach being used and A and m are material parameters which will also depend on connection details. Equation [9.1] can be linearized by taking the logarithm of each side resulting in the expression:

$$\log(N) = \log(A) - m \cdot \log(S) \tag{9.2}$$

One of the key objectives of an experimental program is to determine appropriate values for m and A. An alternative objective may be to assess conformance of a process and welded connection to existing standards.

9.6.1   Nominal stress approach

Use of the nominal stress approach requires a series of standard S–N curves used to classify a particular joint detail and uses fatigue data derived from experimental testing of the structural detail. Guidelines have been based upon these data along with statistical approaches which are used to generate an S–N curve unique to a particular detail. Fatigue curves are typically designated by arbitrary letters or by a stress level at 2×10^6 cycles (Maddox, 2000). A nominal stress analysis does not include the stress concentration due to the weld geometric profile and/or notch effects in the analysis, since it is assumed that the connection specific S–N curve already characterizes these influences. The stress, S, in Equations [9.1] and [9.2] is then equal to the nominal stress, S_{nom}, which is the far field stress caused by the forces and moments at the potential site of cracking. In this regard, neither the local geometry of the weld toe nor the local material properties are taken into account in the analysis. Most design codes use different classifications when implementing the nominal stress approach for different structural details. A different S–N curve, characterized by m and A, is provided for each classification.

Munse et al. (1983) categorized numerous weld and attachment details that are typical in steel ship construction. They provided fatigue parameters including uncertainties for over 50 welded connection details. British Standards, AASHTO, AWS and Det Norske Veritas (DNV), for example, use classification giving a letter designation and fit specific joint details into a category. In the European code, a typical category uses a value of $m = 3$ before the knee of the S–N curve at 5×10^6 cycles and a value of $m = 5$ thereafter. Design is based upon a 95% probability level with 95% confidence. The DNV procedure uses a similar alphanumeric description with the knee of the S–N curve occurring at 10^7 cycles and design curves are based upon environmental conditions such as in air, seawater with cathodic
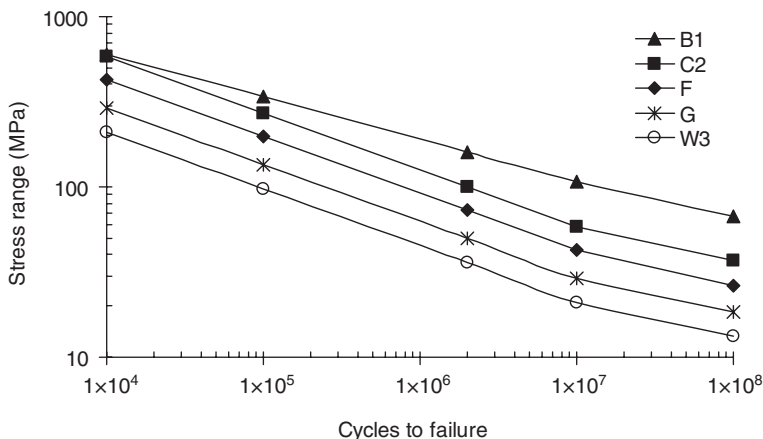
9.6 Abbreviated set letter based *S–N* curves for fatigue in air from DNV.

protection and free corrosion. Figure 9.6 provides an abbreviated sample of several category designations for fatigue in air with the knee of the *S–N* curve at 10^7 cycles.

The IIW designates a fatigue class, FAT, which is the allowable nominal stress in MPa at 2×10^6 cycles with a survival probability of 97.7% (Radaj *et al.*, 2009). In so doing, this provides some numerical meaning to the fatigue classification. For example, curves C2, F, G and W3 in Fig. 9.6 are classified FAT-100, FAT-73, FAT-50, FAT-36, respectively. The curve knee is also at 10^7 cycles with $m = 3$ before the knee and $m = 5$ after. Use of the Palmgren–Miner damage accumulation procedure is recommended. The higher FAT number is an indicator of improved fatigue resistance.

9.6.2   Hot spot stress approach

In a hot spot or otherwise called geometric stress approach, the hot spot stress, S_{hs}, is determined at the location where the fatigue stress is the highest. This approach typically estimates stresses at the hot spot (i.e. weld toe) where fatigue cracking is likely to initiate using stresses at specified distances away from this point. Computational difficulty may arise because the stress at the transition point of the joint is usually a singularity. This results in a mesh-dependent solution when the finite element method is used for the analysis. To overcome this effect, the hot spot stress is estimated using results at predetermined distances from the weld and not at the point of singularity where the stresses are mesh dependent. Various extrapolation standards are used and some of the uncertainties of the effect of weld geometry are removed.

The hot spot stress is derived from a detailed analysis of the connection and will include global effects and to some extent the influences of the local geometry. With this approach, each material requires a single S–N curve for fatigue life assessment. However, a detailed finite element analysis is necessary. The hot spot stress, S_{hs} can be related to S_{nom} using a stress concentration factor for the gross geometry, K_g as:

$$S_{hs} = K_g S_{nom} \qquad [9.3]$$

S_{hs} is then used in Equation [9.1], along with a baseline S–N curve to predict the fatigue life. The resulting hot spot stress may differ depending upon the finite element program, element type, element mesh and method used for dealing with the singularity.

Several methods have been prescribed for determination of the hot spot stress. Doerk *et al.* (2003) and Fricke and Kahl (2005) compared different methods for several weld configurations. Fricke (2002) and Niemi and Marquis (2002) recommend using results at $0.4t$ and $1.4t$ from the weld toe to extrapolate the stress at the hot spot for certain types of weldments. Extrapolation at $0.5t$ and $1.5t$ has also been recommended as described by Kendrick (2005). Other recommendations include using a fine mesh to predict the stress distribution. Error can also be introduced in the hot spot stress calculation if the weld profiles have a high degree of variability or if the finite element (FE) model does not accurately represent the as-welded joint geometry. Also, the extrapolation technique used to compute the hot spot stress will significantly influence the results. A standard method that is consistently applied is required for analysis. In a test program, the weld profile needs to be accurately recorded so that a proper assessment can be made.

Procedures for experimental determination of stress concentration factors, similar to the approach used in hot spot analyses, have been demonstrated by Niemi and Marquis (2002) and Dong (2005), among others. These techniques extrapolate the response recorded by two or more strain gages to the hot spot. Strains are converted to stress and extrapolation techniques similar to those used in hot spot analyses are employed. Also, Dong (2003) suggested a method for determination of the hot spot stress that is insensitive to the FE mesh. A FEA is performed and the resulting nodal forces across the thickness of the plate in the area in question are used to compute a mesh-insensitive structural stress, S_{mi}, which can be used in a fatigue analysis.

9.6.3   Notch stress approach

The notch stress approach assumes a state of very high or infinite stress at the weld toe or root which contains sharp notches. These notch stresses

reduce the stress necessary to cause crack initiation or propagation. The notch stress approach uses *S–N* curves based upon smooth material specimens without notches. A stress concentration factor is then determined to account for various imperfections. Approaches have been developed that assume a fictitious but finite notch radius. For example, Radaj (1990) found that a notch radius of 1 mm worked well for ductile steel. This approach allows the joint and weld geometry to be considered in detail. Finite or boundary element methods can then be used to evaluate the stress concentration factor which can also include details regarding the actual weld geometric profile. According to Kendrick (2005), this method can be used to predict the effect of an imperfect weld profile on fatigue life. It will include an additional stress concentration factor for the actual weld geometry, K_w as well as factors for increased stress caused by misalignment and angular mismatch. Applied fatigue stress, S_n, can then be written in terms of an aggregate stress concentration factor, K, and the nominal stress as:

$$S_n = K \cdot S_{nom} \qquad\qquad [9.4]$$

where K is the product of the individual stress concentration factors given as:

$$K = K_g \cdot K_w \cdot K_{te} \cdot K_{t\alpha} \cdot K_n \qquad\qquad [9.5]$$

where K_g is the stress concentration factor due to the gross geometry, K_w is the stress concentration factor due to the weld geometry, K_{te} is the additional stress concentration factor due to eccentricity tolerance (used for plate connections only), $K_{t\alpha}$ is the additional stress concentration factor due to angular mismatch (used for plate connections only) and K_n is the additional stress concentration factor for unsymmetrical stiffeners on laterally loaded panels applied when nominal stress is derived from simple beam analysis.

For an ideal case with no eccentricity or angular mismatch, the notch stress, S_n, is related to the nominal and hotspot stresses as follows:

$$S_n = K_w \cdot K_g \cdot S_{nom} = K_w \cdot S_{hs} \qquad\qquad [9.6]$$

9.6.4   Crack propagation approach

The crack propagation approach is established for details where the crack propogation phase is longer that the crack initiation phase. It allows an approach to evaluate cases with flaws and cracks that have been generated by loads or that pre-exist in a member. The approach can be used to investigate the effects of such geometrical details as misalignment, residual stresses, undercut and attachments. Also, the method can be used to analyze complex structures and various load combinations.

9.6.5   Analysis for complex details

When complex details are analyzed, it may be difficult to fit the connection into a fatigue design classification for nominal stress type analysis. In these cases, a local approach is necessitated and the structural stress approach or the notch stress approach can be used. These methods model the overall geometry of a complex detail. Hobbacher (2009) and Radaj *et al.* (2009) discuss these approaches relative to fatigue analysis where complex details can be accounted for, including such effects as misalignment.

9.7   Fatigue tests of laser welded specimens

This section discusses fatigue test results of several laser welded specimens and joint configurations including single-T and double-T joints, butt welded specimens, lap welds and stake welds. There are significant differences in the fatigue response of LBW, HLAW and conventionally welded joints including variation in the slope of the *S–N* curve (Remes *et al.*, 2003, Remes and Kujala, 2004). Miyamoto *et al.* (2001) noted that fatigue strength of laser welded joints does not exhibit an endurance limit and continues to decrease even in the range to 10^8 cycles. Other researchers such as Taban *et al.* (2009), Anand *et al.* (2006) and Onoro and Ranninger (1997) noted a fatigue limit in their work.

Evaluation of the cause of the variation in fatigue test results is made difficult, owing to the many different materials studied, laser types employed, equipment used and other process variables including the use of cold wire feed and GMAW. Therefore, testing and evaluation specific to the materials and process are required to ensure high quality and durability whenever new welding approaches or joint configurations are developed. Fatigue resistance of welded joints is typically quantified by empirical means. At present, in design the fatigue strength of a particular connection detail or welding method is not theoretically formulated from fundamental engineering principles, owing to the extreme variation in the process. As new materials, processes and new analytical approaches emerge, fatigue testing and analysis is still a very active area of research.

In fatigue testing, a minimum number of specimens and percent replication is suggested by ASTM E739 (2004). Exploratory or preliminary research is suggested to use 6 to 12 specimens with 17–33 and 33–55 minimum percent replications, respectively. A test program with 12 samples and 3 stress levels would have a percent replication of $(1–3/12) \times 100 = 75\%$, for example. Programs to determine design allowables or reliability use 12 to 24 samples with 50–75 and 75–88 minimum percent replication, respectively. It is recommended that no more than three variables are studied when designing an experimental program. A plan can be developed using high
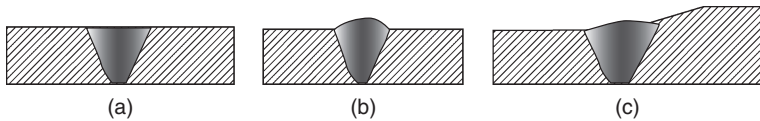
9.7 Butt weld geometry types: (a) straight, (b) concave, (c) stepped.
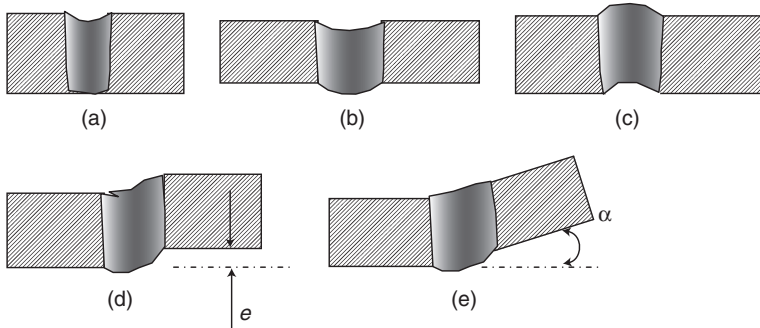
9.8 Geometry defects encountered in butt welds: (a) incompletely filled groove, (b) sagging, (c) root concavity, shrinkage groove, (d) offset, (e) angular misalignment.

and low values of each variable that envelope the range of possible configurations.

9.7.1 Butt joints

Butt-joint tests with dogbone shaped test articles are a common configuration for fatigue studies of welded joints. Butt joints are used frequently for piping and to connect plate materials oriented in the same plane. A laser butt-weld can be done autogeneously or filler metal can be added using cold wire feed or an HLAW processes. When loaded axially, butt joints offer an improved stress condition compared to a lap point in that the bending moment induced by the offset in the plates is minimized. Full penetration butt welds in thick plates can be created by beveling of the edges before welding. The hope is that HLAW will allow for full penetration butt welding of plates of 2″ (~5 mm) or more without the need for specialized edge preparation.

Butt welds can be produced with or without steps, as shown in Fig. 9.7 and the weld geometry used will have a significant impact on fatigue life. Some of the potential geometric defects in butt welds are shown in Fig. 9.8
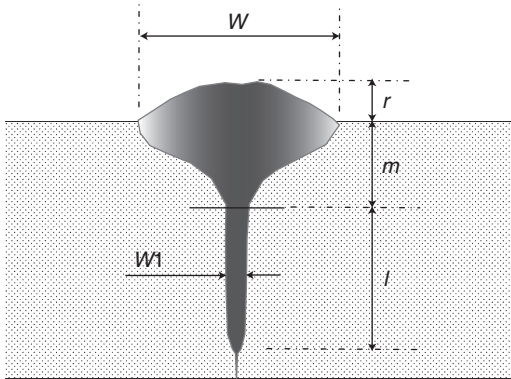
9.9 Geometric parameters of a butt weld.

and include root gap, sagging, out of alignment, angular misalignment, incompletely filled groove and root concavity. Reutzel *et al.* (2006) performed a study of laser butt-welded connections for use in piping. Gong and Olsen (1999) discuss geometric defects and the influence of fixture design on flaws observed in laser butt welding. Longitudinal, transverse and bending shrinkage occurs which requires adequate clamping devices. Thermal stresses can cause gap edge movement during the welding process. The defects lead toward stress concentrations that may affect fatigue life. In welds without filler metal, gaps in the material are of a significant consequence, as weld speed must be reduced and power increased. A cold wire feed or HLAW can be used to apply filler metal to gaps and allows for increased gap tolerance.

The influence of welding parameters including laser power, arc power and weld speed on the weld bead geometry of hybrid GMAW-CO_2 laser welds was quantified by El Rayes *et al.* (2004). Figure 9.9 show a schematic of a typical laser butt weld showing the key geometric parameters. They found a relationship between arc power and bead radius and width and they found that the penetration and bead height are significantly influenced by the mode of metal transfer in the arc. Reutzel *et al.* (2008) used HLAW to study the effect of weld speed and distance to the welding torch in HLAW butt welds. In their welding of AB/DH36 plate they found average hardness values of 157 HV in the base metal, 222 HV in the HAZ and 244 HV in the weld metal. Welds done at 50.8, 76.2 and 101.6 cm min^{-1} with 2–16-mm torch separation lead to various weld qualities and other phenomena. Slow speeds and a closely spaced torch resulted in good mixing

of the laser melt pool and filler metal; however, backside blow through was prone to occur. At the slower speeds, more distance spacing reduced the blow through, although full penetration was not achieved. Increasing the travel speed reduced the amount of blow through and, as the torch distance increased, full penetration was achieved and the laser and filler metal interaction was minimal.

Fatigue testing of laser butt-welded joints was reported by Hobbacher (2001) where the results of 391 small specimens with thickness between 8 mm and 12 mm were quantified. Slope of the S–N diagram was approximated at $m = 3.75$ and the results were evaluated at this value and also at $m = 3.0$. In the analysis, the reduced amount of edge misalignment was accounted for along with thickness effects. A FAT for the laser butt-welded joints of 114 MPa was determined, which was subsequently reduced to a recommended value of 69 MPa when assembly stresses, misalignment and thickness effects are taken into account. This can be compared to an IIW recommended value of 71 MPa for a butt-weld joint with a root crack checked by non-destructive tests (NDT).

Remes and Kujala (2004) reported on the fatigue resistance of laser and HLAW butt joints. They used a CO_2 laser and conventional MAG welding torch to study autogenous laser, hybrid laser and SAW joints in fatigue. I-type groves were used for the laser and hybrid laser welds and a Y-type groove was used in a hybrid weld. Tests were force controlled axial tension with a load ratio $R = 0$. Fatigue results showed a survival probability of FAT 172 for the SAW joints, FAT 154 for laser welds with $m = 5.8$ and FAT 200–220 for the hybrid laser welds. The testing also resulted in a S–N curve slope ranging from 3.7 to 9.6 to be greater than the IIW baseline of 3.0 for FAT 100 class for transversely loaded butt welds. Specimens with an out-of-alignment defect where bending stresses are induced showed an 85% reduction in fatigue strength compared to relatively straight samples.

Fatigue of laser welded tailor made blanks (TMBs) is of interest in the automotive industry. TMBs are metal sheets joined together before forming and can be made from plate with different thicknesses, surface coatings and material types. Anand et al. (2006) fatigue tested butt-welded specimens of steel typically used in the automotive industry for laser welded TMBs. Galvanized and ungalvanized thin sheets of different thickness from 0.75 to 1.5 mm were tested. The yield strength of the material ranged from 297–324 MPa. The fatigue endurance limit of galvanized coated laser welded sheets (85 MPa) was found to be 77% of the endurance limit of the base metal (110 MPa). The endurance limit of uncoated specimens (120 MPa) was equivalent to the base metal. Vickers hardness testing shows a zone of increasing hardness of about 2.5–3 times that of the base metal. The narrow hardness zone extended wider in the thinner material and was approxi-

mately 1.5 times the plate thickness in the thinner material and was about one-third to one-half of the plate thickness in the thicker material. Fatigue fracture was found to occur in the thinner material. Ono *et al.* (2002b) demonstrated that the fatigue life of a laser welded TMB is less than the parent material and fracture occurs in the base metal for failures 95×10^5 cycles and that fracture occurs near the weldline for longer fatigue life components. They also observed that fatigue strength diminishes with thickness. In testing of the same gage HSLA steel, Onoro and Ranninger (1997) found that fatigue cracks in LWBs begin in the fusion zone near the HAZ border.

Taban *et al.* (2009) discuss laser butt welding of X2CrNi12 stainless steel with a 12% Cr content and 363 MPa yield strength, 500 MPa ultimate strength and 30% strain at fracture. They use a CO_2 laser at power of 13 kW and 20 kW to weld 12-mm thick plates with no observed defects. Fatigue endurance limit was estimated to be 250 MPa, which is 68.9% of the yield strength.

In a limited study, Caccese (2004) compared the results of HLAW 12.5-mm thick butt-welded HSLA-65 steel fabricated at ATS to the results of fatigue tests performed on various materials typical of ship structures reported by Kihl (1990). Figure 9.10 gives a summary of the fatigue test results compared to the FAT 100 design curve. A typical failure is shown in Fig. 9.11 with cracking at the weld toe. The laser welded specimens show good fatigue performance at the stress levels tested.

In their fatigue tests on laser weld titanium, Casavola *et al.* (2009) studied 3-mm thick grade 5 and 1.5-mm thick grade 2 dogbone coupons. They found
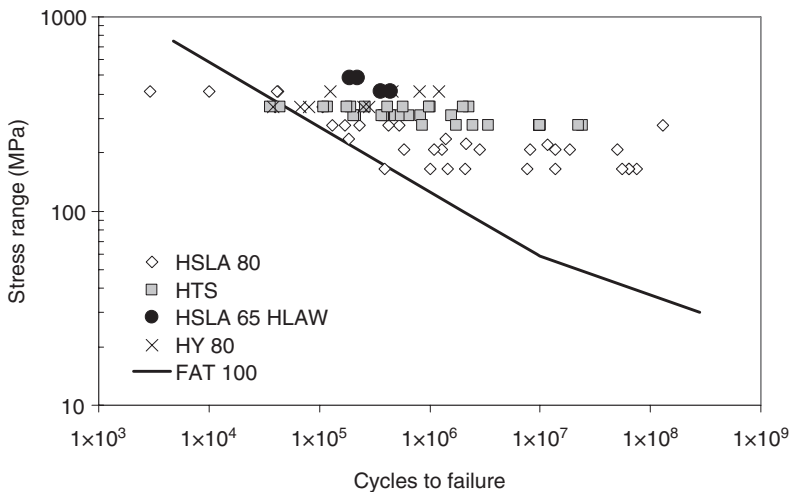
9.10 Fatigue tests of various materials.

(a)

(b)
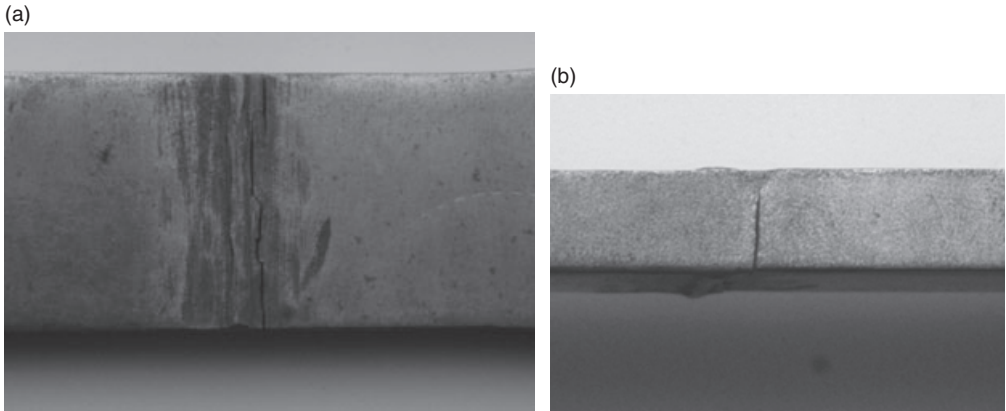
9.11 Failure in butt-welded specimen: (a) top view, (b) side view.

that 11 of the 12 fatigue specimens tested failed in the base metal not at the weld toe. This was attributed to the limited HAZ size, virtually no misalignment and low stress concentration due to the regular profile. Tests resulted in a fatigue strength at 2 M cycles of 85 MPa and 127 MPa for grades 2 and 5, respectively, compared to ultimate tensile strength of 423 MPa and 969 MPa recorded for these materials.

Eibl *et al.* (2003) used different alloys to study the fatigue of laser butt welds in aluminum. Alloys included GD-AlSi/10Mg T6, AlMgSiO T6 and AlMg4.5Mn. Samples were welded with root gaps between 0 and 0.5 mm. A substantial reduction in fatigue endurance limit compared to the base metal was observed, ranging between approximately 50–60%. High porosity was also observed in the welds.

9.7.2 Fatigue of single-T and double-T joints

Fabricated sections made from plate material are often formed using T-joints, with full penetration, or fillet welds. Full penetration laser T-joint welds are currently achievable on sections up to 25 mm thick without the need for beveling. While full-penetration autogeneous laser T-joint welds are possible, they typically result in high stress concentrations at the weld root and it may be advantageous to use filler material in an HLAW process to reduce these effects by creating a fillet at the T interface. Typical geometric imperfections in fabrication include offset of the elements and angular misalignment.

Fatigue resistance of laser and HLAW T-welds can be evaluated using double-T (cruciform) sections where there is a substantial database of tests on different materials and welding processes. In the cruciform test, the
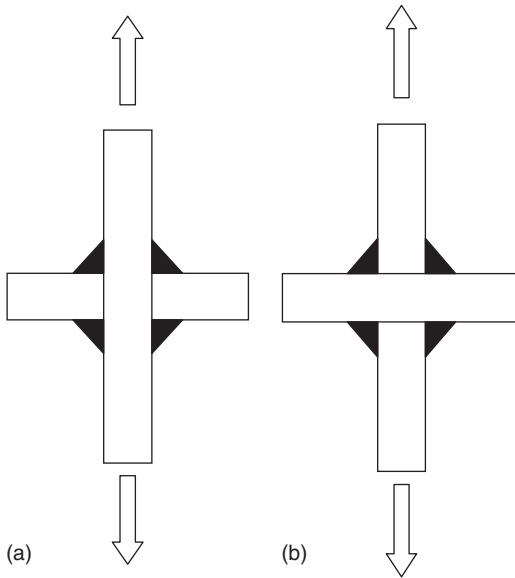
9.12 Types of cruciform specimens: (a) non-load carrying, (b) load carrying.

specimen is loaded axially with typical loads being either fully reversed ($R = -1$) or tension only ($R = 0$), where R is the ratio of minimum load to maximum load. Specimens are of two types, load carrying or non-load carrying, as shown in Fig. 9.12 and represent the case of a mode-1 type failure. Weld geometry has been shown to have a significant influence on fatigue life and an improved weld profile can reduce stress concentrations and subsequently increase the cycles to failure. Techniques for post-weld geometry improvement such as grinding or peening have been successfully implemented (Kirkhope *et al.*, 1999a,b). The cruciform connection is listed in the Munse *et al.* (1983) report as structural detail 14 and the fatigue parameters compiled for these connections encompass data that span years of testing conventionally welded systems with reported fatigue parameters of $m = 7.35$ and $\log(A) = 23.2$ for stress, S_{nom}, in MPa. Mansour *et al.* (1996) report an abbreviated joint classification for BS 5400 and DNV, where a load-carrying full-penetration fillet weld without undercutting at the corners dressed out by local grinding is placed in category F. Design parameters associated with category F are $m = 3$ and $\log(A) = 11.855$ with stress, S_{nom}, in MPa and its associated FAT class is 73.

Load-bearing type cruciform sections made from AISI 304 and AISI 316 stainless steel were tested by Dattoma (1994). Plates of 5 mm thick and beveled edges were used in fabrication with a 2 kW maximum power CO_2

laser with helium and nitrogen as shielding gases. In the fatigue tests, the average slope was reported to be $m = 5.65$, which is more like the base metal than typical welded cruciform joints where the recommended m is 3.

Onoro & Ranninger (1997) reported on the fatigue testing of CO_2 laser welded double-T joints made with 6-mm thick HSLA steel with a yield and ultimate strength of 435 MPa and 560 MPa, respectively. They used a laser power of 6 kW with helium as the shield gas. Fatigue test were done in flexure with load ratio $R = 0.1$ under sinusoidal load with a frequency of 10 Hz. They observed a fatigue limit of 260 MPa. Cracking began in the fusion zone near the HAZ borderline. The surface profile was observed to have an important effect in the generation of fatigue cracks.

Hobbaker (2001) evaluated fatigue test results for 194 laser welded load-bearing double T-joints where one side of the joint was welded with no edge preparation. The joints exhibited complete weld penetration and cracks typically started at the weld root. The behavior was between a T-joint with a fillet weld and one with a double bevel butt weld. When complete penetration does not occur at the root, the fatigue life of a joint response is reduced and is similar to the life of a partial penetration fillet weld. The FAT class for the load-bearing laser double-T of 61 MPa was estimated and was subsequently reduced to a recommended value of 37 MPa when assembly stresses, misalignment and thickness effects are taken into account. This can be compared to an IIW recommendation of FAT = 36 for a T or double-T joint fillet weld with a root crack in the weld.

Caccese *et al.* (2004, 2006) discuss tests used to quantify the fatigue life of cruciform welds that were laser fabricated with various weld geometric profiles, using differing process parameters. The studies focused upon estimating the influence of the weld geometric profile on the fatigue life based upon the stress concentration factor due to the weld geometry. This was part of a larger effort to qualify uses of laser welding in fabrication of structural T-shapes made from HSLA steel for US Navy ships (Kihl, 2002).

In developing an economical and practical weld profile for a line of product such as fabricated shapes with T-type welds, tradeoffs must be made regarding desired weld geometry, operation speed and amount of filler metal. In this study, the weld geometry of cruciform specimens was varied, measured and categorized. There were four series of 12.5-mm thick test articles detailed for this investigation and Fig. 9.13 shows a typical cruciform specimen. Weld process parameters for the fabricated specimens are summarized in Table 9.3.

The test articles were fabricated using either a laser 'cold-wire' (LBW-CW) or a laser-hybrid (HLAW) welding process. In the LBW-CW process, filler material is added by using a small percentage of the laser energy to melt wire fed to the weld pool. The first series (Series-A) was fabricated at
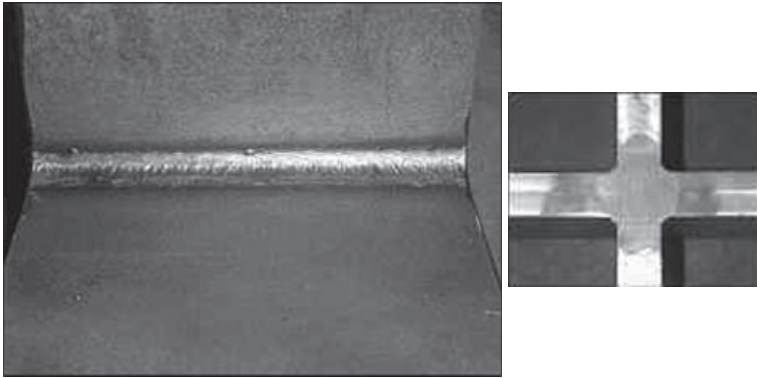
9.13 Cruciform specimen.
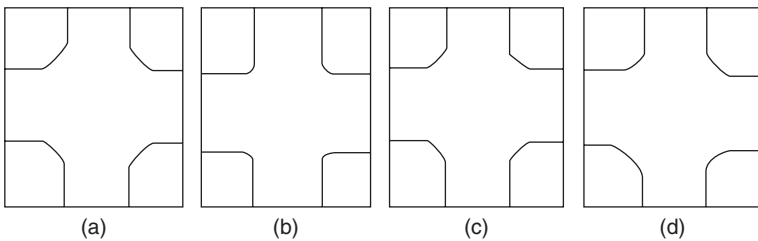
9.14 Traced laser weld profiles of a cruciform specimen: (a) Series A, (b) Series B, (c) Series C, (d) Series D.

Table 9.3 Weld process parameters for the 12.5-mm thick cruciform specimens

Weld series	Weld process	Laser delivered power (kW)	Laser weld rate cm min^{-1}(in min^{-1})	Wire type[a]	GMAW power (kW)
A	LBW-CW	10.0	25.4 (10.0)	ER70S-2	N/A
B	LBW-CW	14.3	190.5 (75.0)	ER70S-2	N/A
C	LBW-CW	16.4	114.3 (45.0)	ER70S-2	N/A
D	12.5-mm HLAW	15.5	133.4 (52.5)	ER70S-6	10.5

[a] Wire size used for all series is 0.889 mm (0.035 in) diameter.

the Applied Research Laboratory (ARL) of Penn State University, using the LBW-CW process with a 14 kW CO_2 laser operating at 10 kW delivered power and a weld speed of 25.4 cm min^{-1} (10 in min^{-1}). This resulted in a weld with profile shown in Fig. 9.14(a). The weld is characterized by a very
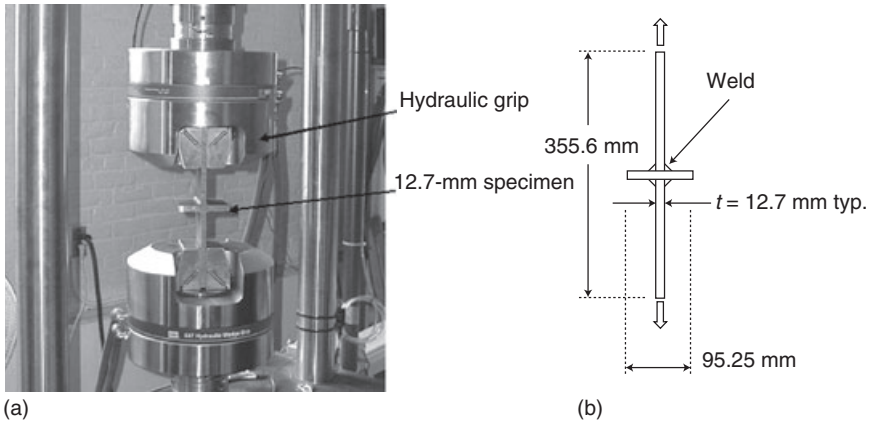
9.15 Fatigue test specimen and test setup: (a) specimen in test machine, (b) test article.

good geometry, which has a small region that is somewhat flat in the center and a smooth radius towards the ends. The next three series of specimens were fabricated at Applied Thermal Sciences (ATS) in Sanford, ME using a system equipped with a real-time adaptive feedback control of the weld process. The first series fabricated by ATS, Series-B, used the laser cold-wire process with a 25 kW CO_2 laser operating at 14.3 kW delivered power and weld speed of 190.5 cm min^{-1} (75 in min^{-1}). The weld profile resulted in a fair geometry, small flat-shaped fillet as shown in Fig. 9.14(b).

Series-C, Fig. 9.14(c), was fabricated at a reduced process rate with increased wire feed and resulted in a good geometry with a larger fillet of the same general profile as Series-B. Figure 9.14(d) shows the resulting welds for the last series (12.5-mm HLAW), which used a laser-hybrid process and resulted in a very good geometry with a geometric profile that was as near to circular as can be expected.

Fully reversed ($R = -1$) fatigue testing was performed at the University of Maine (Berube *et al.*, 2005) using a 50 metric ton (110 kips) MTS^{TM} 810 universal testing machine with a TestStar^{TM} digital controller, as shown in Fig. 9.15(a). The 355.6-mm long, 95.25-mm wide test specimens (Fig. 9.15b) were cruciform shaped and fabricated from 12.7-mm thick HSLA-65 steel plating. The gage length used for the testing was 177.8 mm with an 88.9 mm grip length. The testing was performed in load control, at a rate of 2.22 MN s^{-1}, and the specimens were loaded axially, under completely reversed sinusoidal loading, at stress levels of 103.4, 206.8, and 310.3 MPa. The controller automatically terminated the test when the extension of the specimen had doubled, which is indicative of a significant crack in the specimen.
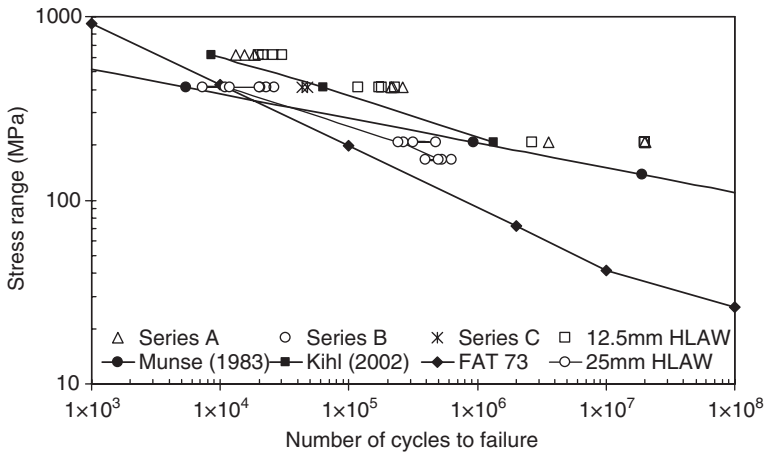
9.16 HSLA-65 steel cruciform fatigue test results.

Fatigue data are plotted in Fig. 9.16 along with the *S–N* curve using parameters reported by Munse *et al.* (1983) and the average of the experimental results performed by Kihl (2002) on conventionally welded HSLA-65 steel cruciforms. In addition, the FAT 73 design based curve is also provided along with results from 25-mm thick HSLA steel cruciforms fabricated by HLAW. An objective of this study was to assist in developing welding parameters that would yield results that improved welding speed and had fatigue life equal to or better than conventional welds. Series-B and Series-C welds were preliminary studies to determine the effect of fillet size and shape on fatigue life. These series were tested at the intermediate 206.8 MPa stress range only, so that timely results could be obtained. Series-D is the final production detail of the fillet to be used in beam fabrication and was fabricated at a weld rate of 133.4 cm min^{-1} (52.5 in min^{-1}), which is 5¼ times faster than the rate used for the Series-A welds, with virtually equivalent fatigue life. All 12.5-mm thick laser welded tests show longer fatigue life than predicted by the Munse curve. Series A and the 12.5-mm HLAW specimens show fatigue life better than that reported by Kihl (2002) for conventional welds of the same material. The thicker 25-mm HLAW test articles showed a substantially lower fatigue life where the average was below the curve by Kihl (2002) for conventionally welded HSLA-65 cruciforms.

9.7.3 Lap joints

Lap joints are used quite frequently especially when attaching thin sheets together. They allow welding with less restrictive joint fit-up tolerances.
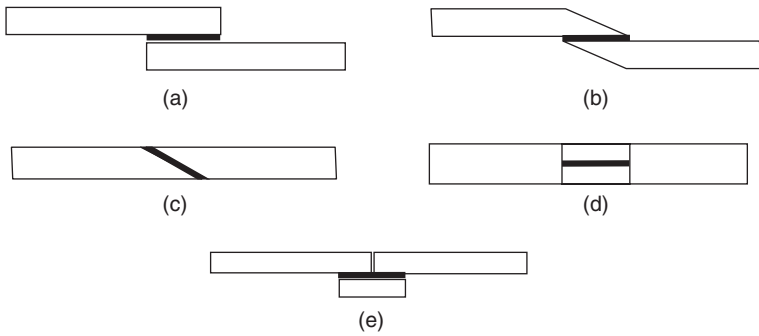
9.17 Various weld configurations for the lap joint: (a) simple single lap joint, (b) tapered lap, (c) scarf joint, (d) stepped lap, (e) strap joint.
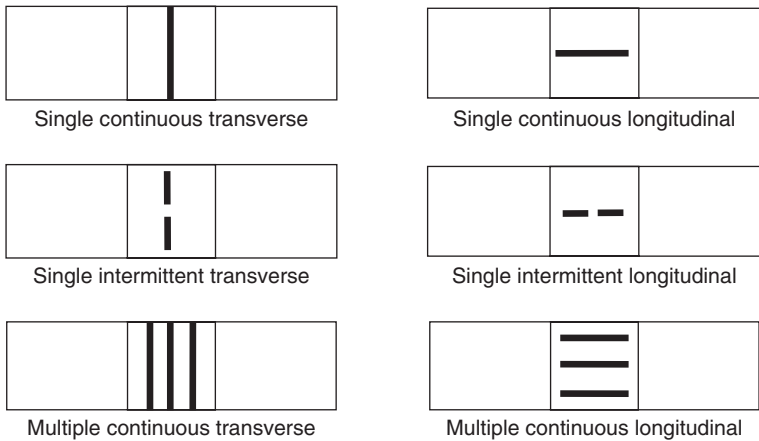
9.18 Various weld configurations for the lap joint.

Laser welding is a popular method of creating a lap connection in sheet metal owing to its simplicity, since a stake weld can be used where the laser energy penetrates the top sheet of a thin metal without the need for plug or spot welding. The net result is a weldment at the interface of the plates. The lap weld can be fabricated in various configurations as shown in Figs. 9.17 and 9.18. The fatigue performance is a function of weld configuration, among other effects. Since the actual weld dimensions are internal to the structure, the performance of lap-welds is often rated on a resistance per unit length basis in lieu of stress. In the case of a single lap, the connection is subjected, in general, to a combination of axial force, shear force and bending moments as shown in Fig. 9.19. The fatigue response of the lap connection has been analyzed, based upon the stress state at the weld root (Zhang, 2002a).
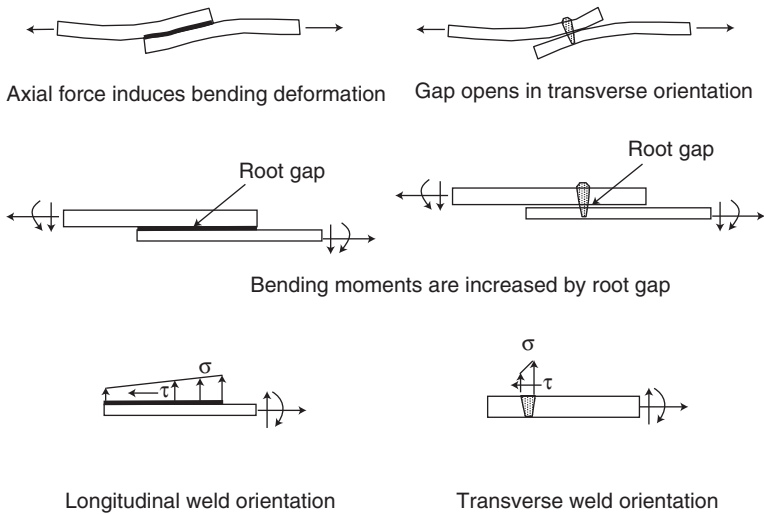
9.19 Stresses on an axially loaded single lap joint.

Determination of the stress at the weld root is done on an empirical basis or by using a structural stress approach. However, there are still difficulties in determining a proper value for structural stress in some cases. Fracture mechanics approaches using energy release rates, stress intensity factors and notch stress also have difficulty in predicting fatigue response. This difficulty can be attributed to variability in the weldment including post-weld material and geometric properties and to experimental uncertainties. During testing of a lap connection, the critical interface is not accessible until the material has broken apart. The critical stresses in this joint are the shear stress across the interface, τ, and the normal stress, σ, at the weld root. Zhang (2002b) presents a method using strain gages in combination with finite element analysis to estimate the stresses at the critical locations and shows that a more representative prediction of the structural stress results in an improved correlation of fatigue results.

Lap joints subjected to axial loads represent a critical condition in the structure where fatigue is possible or likely. An axially loaded single-lap joint will include bending stresses in addition to the axial and shear stresses, as demonstrated in Fig. 9.19. Any unintentional gap between the plates that exists owing to manufacturing will further exacerbate the bending stresses. Lap joints suffer from the notch effect, surface cracks and residual stresses (Cho *et al.*, 2004). The relative strength of the lap joint weld to base plate material is also highly dependent on the thickness of the plates being welded. Thin plates have a tendency to fail in the base material, whereas thick plates normally fail in the weld.

Lap joints made from AISI 304 and AISI 316 stainless steel were tested by Dattoma (1994). Single lap specimens were welded with plate thicknesses of 1 mm and 2 mm using a CO_2 laser. In the fatigue tests, the average slope was reported to be $m = 4.73$, which is more like the base metal than typical welded cruciform joints where the recommended value of m is 3.

Hsu and Albright (1989, 1991) demonstrated that multiple longitudinal welds parallel to the loading direction give a better performance than a transverse configuration. Increasing sheet thickness reduces the fatigue strength of the weld. The fatigue response of a laser welded lap joint was three-quarters that of an unwelded smooth material. The one-quarter reduction in strength was attributed to residual stresses, material changes and possible discontinuities caused by the welding.

Wang and Ewing (1991) reported the fatigue strength of laser welded sheets of SAE 1008 grade steel to be better than resistance spot welds. Lazzarin *et al.* (1995) found similar strengths in laser welded bars and hot dipped galvanized sheets. The fatigue strength of most lap connections is generally lower than the base metal owing to the moment created by the offset of the sheets and any stress concentrations. Tests by Flavenot *et al.* (1993) on 0.7-mm thick mild steel sheets also demonstrated that laser welded lap joints have better fatigue resistance than spot welds. Microhardness values reported peaked at approximately 260 HV0.1 to a basis of about 110 HV0.1 with a HAZ of about 3 mm. A gap between the sheets can have a significant influence on the fatigue response. Intermittent welds also show less fatigue life than continuous beads owing to stress concentrations at the point where the weld starts and stops. A single transverse lap weld results in the poorest response to fatigue. Again, increasing the sheet thickness also tends to reduce the fatigue life.

Nordberg (2005) compared laser welded lap joints to spot welded, clinched and adhesively bonded joints in stainless steel. Compared to spot welding, the continuous laser weld dramatically reduces stress concentration in the connections. A line load resistance at 2×10^6 cycles of 118 N mm^{-1} for a 0.8-mm wide weld (nominal 147.5 MPa) was reported in 3-mm thick laser welded AISI 304 stainless steel. Doubling the welds or a wider bead resulted in a higher fatigue strength. The fact that the line load strength is related to the sheet thickness was also reported. A study on AISI 304CS steel reported line load resistance at 2×10^6 cycles of 60 N mm^{-1} for a 0.6-mm wide weld (nominal 100 MPa) in a 1-mm thick plate and 75 N mm^{-1} for a 1-mm wide weld (nominal 75 MPa) in a 2-mm thick plate.

Larsson *et al.* (1999) investigated the effect of laser bead on the fatigue properties of lap joints. Cold rolled sheet steel 0.9 mm thick was used at a laser power of 6 kW with speeds between 5 and 10 m min^{-1}. The resulting bead widths ranged from 0.47 mm to 0.94 mm from higher to lower weld speeds. A single lap specimen with a single transverse weld bead was

Single weld in I-core stiffener   Double weld in I-core

Double weld in a truss-core panel
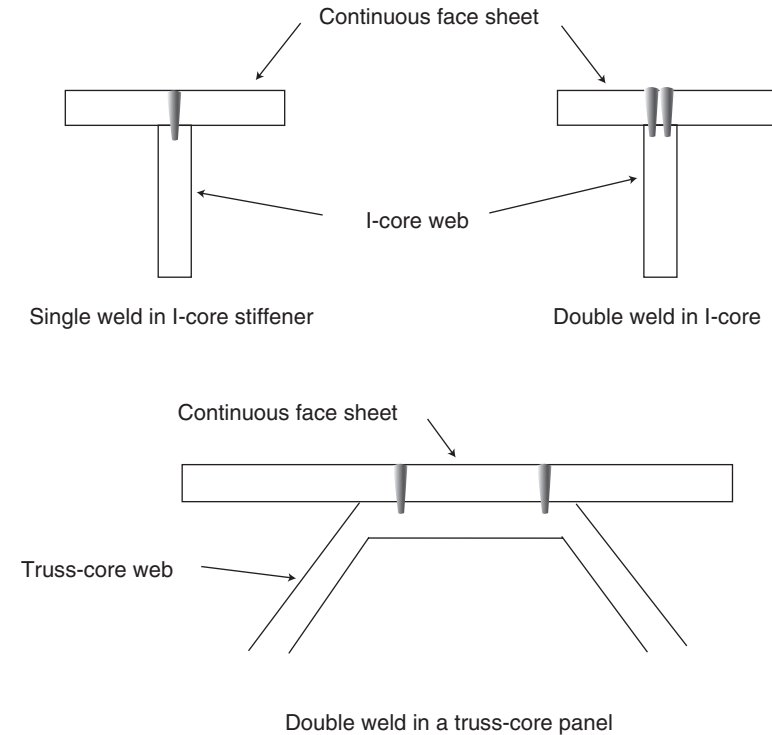
9.20 Laser stake weld in I-core and truss-core panels.

used. The test results show that fatigue life increased with weld bead, as expected.

Sonsino *et al.* (2006) tested tube connections fabricated by laser welding with an overlapped joint. The tube sections were subject to multi-axial loading. They modeled the weld root as a notch with fictitious radius of 0.05 mm. The effective equivalent stress hypothesis resulted in satisfactory prediction of fatigue life of these joints under complex multiaxial stress.

9.7.4   Stake welds in sandwich panels

Laser stake welding can be used to fabricate effectively a closed structure such as a sandwich panel. Welding of closed structures is normally difficult and weld types such as spot welds and plug welds have been used in the past. A laser stake weld provides the means to obtain a high quality continuous weld. This allows welding of thin closed sections where it is not possible for a human or robot to enter and eliminates the need for human intervention in larger structures. Figure 9.20 provides schematics of stake welds in

Zero root gap closely
centered weld

Offset weld

Varying root gap

Maximum root gap
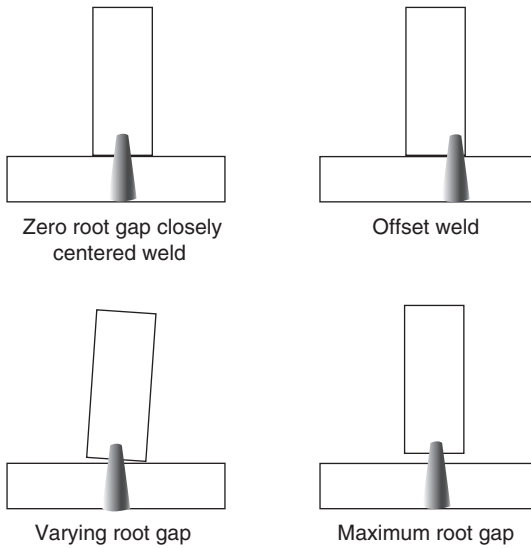
9.21 Geometric variations in an I-core stake weld.

T-shaped and corrugated plate type structures. In a stake weld, the weld energy must penetrate through the top plate material in order to fuse the top sheet to the enclosed underlying material. The weld interface then becomes internal to the closed structure. A stake welded section may consist of one or more welds parallel to each other and placed in close proximity so that they may interact. Stake welds have been performed on thick material from 8–20 mm using CO_2 lasers with up to 40 kW output (Socha and Kujala, 2002; Kujala *et al.*, 1999a,b). Some defects that can exist in stake welds are shown in Fig. 9.21.

Kujala *et al.* (1999b) performed a hardness investigation for T-shaped type stake welds in 12 different steel grades and plate thickness combinations. The resulting weld width varied typically from 2–3 mm. Hardness values were at their peak at the root of the weld and ranged from 260 HV to 380 HV where the base metal hardness was 140 HV and 150 HV, respectively. They compared the fatigue response of double run laser stake welds to arc fillet weld T-joints and found that the laser stake weld lies in a fatigue class of 78 MPa mean and 67 MPa design (mean – 2 standard deviations), whereas the arc weld was in a fatigue class of 96 MPa mean and 71 MPa design. Romanoff *et al.* (2007) studied the stiffness of laser stake welded T-joints. Specimens with 2.5-mm and 3-mm face plates were used. They identified several geometric inconsistencies in this type of weld including misaligned welds, varying and maximum root gap. The contact mechanism causes a significant difference in joint stiffness.

The fatigue performance of steel sandwich panels fabricated with laser stake welds for use in bridge decks was studied by Bright and Smith (2004) in the UK. They used a 25 kW CO_2 laser source that operated at about 10% efficiency and a mirror beam delivery system that focused the laser light down to a 0.6-mm diameter spot. Helium was used as the shielding gas. For a stake weld, they noted that penetration is dependent on welding speed with slower welds penetrating deeper. However, a weld performed too slowly would cause burn through. They noted that there are no standards for the amount of penetration required and they suggested that the maximum penetration possible without burn through should be used. Their sandwich panel concept welded HPE 240 steel beams spaced at 300 mm between 8-mm and 12-mm face plates. Deck bending and joggle type fatigue tests were conducted on cut sections with two, four or sinusoidal shaped stake welds per flange. Deck bending tests with two welds per flange showed the most favorable fatigue response and fell under class C with the four welds per flange falling between class D and E and a sinusoidal weld detail near class F2. In the joggle tests, failure occurred in the I-beam web at the root fillet with no weld failures observed.

The residual stress in laser welded truss-core type sandwich panels laser welded using a CO_2 laser with no filler metal was investigated by Daurelio *et al.* (2001). They used AISI 304 stainless steel with a trapezoidal (V-core) geometry. They found peak residual stress values to be on the order of the yield strength of the material. Alenius *et al.* (1999) fatigue tested laser welded sandwich panels consisting of AISI 304 stainless steel. The panels have a hollow square section core made 40 mm × 40 mm × 1.5-mm thick with 1-mm thick face sheets. Three panels were tested, two with polyurethane foam fill and one without. A single weld without filler was used per square tube at 1.6 kW power at 3.5 m min^{-1}. A four-point bending fatigue test was performed on the panels with stress ratio $R = 0.1$. The maximum force of 33 kN was approximately 63% of the static strength of the panel. Fatigue response curves plotting displacement of the panel centerline versus cycles showed that severe distress from fatigue began between 0.5 M and 1 M cycles. They concluded that the foam had no bearing on the results and that quality of the welds is very important for fatigue life.

9.8 Conclusions

Process techniques, new materials, automated equipment and use of laser welding are continuing to grow at a rapid rate, which often necessitates experimental study of the influence of the structural and manufacturing details on the fatigue life. Laser welds are characterized by a narrow HAZ with a steep hardness gradient compared to conventional GMAW and SAW welds. The changing microstructure results in strength mismatch between

the weld material, HAZ and base material. The localized heat input also results in considerably less distortion of the finished product when compared to GMAW or SAW, which is a definite advantage. The high hardness gradient indicates that the process control details need to be carefully monitored to mitigate weld flaws that can reduce the fatigue life. Automated quality control systems have been developed to modify weld parameters in real time, resulting in much improved weld quality.

Autogenous laser welding relies on low tolerance fit-up of the materials, as the gap between materials needs to be minimized for good quality welds. This is usually achieved by precision manufacturing techniques such as laser cutting, machining and precise fixturing. This can dramatically increase the cost of the welding operation. Also, weld geometries with high stress concentrations may be the result of lack of filler. Compared to laser beam welding alone, the combination of laser welding and GMAW into the HLAW process helps to mitigate some of these effects. Synergistic effects are observed with HLAW, where the laser can be used to provide the deep penetration desired and the GMAW process can be used to add filler material and create more desirable weld contours. This results in a weld that still has a low heat input, hence low distortion of the component. Welds can be done at higher rates than laser alone, improving the economy even further.

Popular welding equipment in use includes CO_2 and ND:Yag lasers. The CO_2 laser can achieve very high laser power output, with systems of up to 45 kW in use today. They rely on a system of mirrors and optics to deliver the concentrated photon energy. In comparison, NG:Yag lasers are currently of less power output (in the 10 kW maximum power range), but are much more efficient in their power usage. One of their main advantages is that the laser energy can be delivered through optical fiber, making them more versatile and amenable to use in automated systems.

Fatigue test results on laser welds come from a variety of sources and from programs with varied objectives. Some results from experimental programs where processes have not been fully developed may result in misleading conclusions, since fatigue in the final end product may be different. Fatigue life is influenced by a multiplicity of factors, which are weld process, joint detail and material dependent. Fatigue testing and evaluation, especially when new processes are being developed and new materials implemented, is still a very active area of research.

Fatigue testing typically results in wide scatter, especially when results from different test programs are compared to each other. More uniform fatigue results will be obtained as weld quality improves through real-time quality control and automated manufacturing results in a more consistent end product. Defects such as porosity, burn-through and lack of fusion can be minimized by proper selection of parameters. The surface geometric profile of the weldment is very important in the level of stress concentration

and generation of fatigue cracks. Processes that improve surface profile without the need for post-weld operations will be more cost effective and will substantially improve the fatigue life. As quality increases and automation improves the consistency of the laser welding process, it is envisioned that fatigue life predictions may be feasible on an analytical basis with knowledge of the process, materials and actual weld geometry.

Laser welding is a cost-effective high quality joining process. Guidelines accepting laser welding and conformance standards can foster the implementation of laser welding in some areas. The acceptance typically hinges upon substantial research demonstrating that laser welding results in an end product with cost-effectiveness, strength and durability comparable or superior to existing processes.

9.9   References

ALENIUS, M, VILPAS, M and HÄNNINEN, H (1999), 'Laser beam welded stainless steel sandwich panels', *7th NOLAMP (Nordic Laser Materials Processing) Conference*, Lappeenranta, Volume 1, 83–101.

ANAND, D, CHEN, DL, BHOLE, SD, ANDREYCHUCK, P and BOUDREAU, G (2006), 'Fatigue behavior of tailor (laser)-welded blanks for the automotive industry', *Materials Science and Engineering A*, **420**, 199–207.

ANCONA, A, LUGARA, PM, SORGENTE, D and TRICARICO, L (2007), 'Mechanical characterization of CO_2 laser beam butt welds of AA5083', *Journal of Materials Processing Technology*, **191**, 381–4.

ASTM E739 – (2004), *Standard Practice for Statistical Analysis of Linear or Linearized Stress–Life (S–N) strain life (e-N) Fatigue Data*, Vol 03.01 Mechanical Testing, American Society of Testing Materials, West Conshohocken, PA.

BERUBE, KA, CACCESE V and KIHL DP (2005), '*Fatigue Strength of Laser Welded HSLA-65 Steel Cruciforms*', University of Maine Department of Mechanical Engineering Report No. C2000-001-RPT-003, March, 40 pp.

BIRD, J and FURIO, A (1997), *Laser Welding in Ship Construction*, Ministry of Defence, Bristol, UK, Report No. DREA-SR-97-002-PAP-19, October, 20 pp.

BLOMQUIST, PA and FORREST, DL (1999), 'Laser-cutting and welding of DDG-51 structural shapes', *1999 Ship Production Symposium*, Arlington, VA, July.

BLOMQUIST, PA, OROZCO, N and PATCH, D (2004), 'Laser fabricated structural shapes for new construction, overhaul and repair', *Journal of Ship Production*, **20**(2), 114–21.

BORONSKI, D (2006), 'Cyclic material properties distribution in laser-welded joints', *International Journal of Fatigue*, **26**, 346–54.

BRIGHT SR and SMITH JW (2004), 'Fatigue performance of laser-welded steel bridge decks', *The Structural Engineer*, November, 31–9.

CACCESE, V (2004), '*Fatigue of Laser Hybrid HSLA-65 Steel Butt-welds in Tension*', University of Maine Departement of Mechanical Engineering Report No. C2004-001-R01, 5pp,

CACCESE, V, BLOMQUIST, PA, OROZCO, NJ and BERUBE, KA (2004), 'Fatigue life prediction of HSLA-65 welds made by laser/GMAW processes', *Proceedings of the 23rd*

International Congress on Applications of Lasers and Electro-Optics, San Francisco, October.

CACCESE, V, BERUBE, K, BLOMQUIST, PA, WEBBER, SR and OROZCO, NJ (2006), 'Effect of weld geometric profile on fatigue life of cruciform welds made by laser/GMAW processes', *Marine Structures Journal*, **19**(1), 1–22.

ÇAM, G, YENI, C, ERIM, S, VENTKZE, V and KOÇAK, M (1998), 'Investigation into properties of laser welded similar and dissimilar steel joints', *Science and Technology of Welding and Joining*, **3**(4), 177–89.

CAO, X, JAHAZI, M, IMMARIGEON, JP and WALLACE, W (2006), 'A review of laser welding techniques for magnesium alloys', *Journal of Materials Processing Technology*, **171**, 188–204.

CASAVOLA, C, PAPPALETTERE, C and TATTOLI, F (2009), 'Experimental and numerical study of static and fatigue properties of titanium alloy welded joints', *Mechanics of Materials*, **41**, 231–43.

CHO, SK, YANG, YS, SON, KJ and KIM, YK (2004), 'Fatigue strength in laser welding of the lap joint', *Finite Elements in Analysis and Design*, **40**, 1059—70.

DATTOMA, V (1994), 'Prediction of the fatigue life of laser welded stainless steel joints', *Fatigue and Fracture of Engineering Materials and Structures*, **17**(11), 1335–42.

DAURELIO, G, LA TEGOLA, V, PAPPALETTRE C and VALENTINI, E (2001), 'Thin stainless steel sandwich structural panels all welded by laser technology: residual stress measurements by the hole-drilling strain-gage method', *XIII International Symposium on Gas Flow Chemical Lasers and High-Power Laser Conference*, Florence, Italy, Volume 4184, 579–85.

DEFALCO, J (2007), 'Practical applications for hybrid laser welding', *Welding Journal*, October, pp. 47–51.

DOERK, O, FRICKE, W and WEISSENBORN, C (2003), 'Comparison of different calculation methods for structural stress at welded joints', *International Journal of Fatigue*, **25**, 359–69.

DONG, P (2003), 'A robust structural stress method for fatigue analysis of ship structures'. *Proceedings 22nd International Conference on Offshore Mechanics and Arctic Engineering*, Cancun, Mexico, June.

DONG, P (2005), '*Mesh-insensitive Structural Stress Method for Fatigue Evaluation of Welded Structures*', Battelle Memorial Institute, JIP training course, Houston, TX, May.

DUHAMEL, RF (1996), 'Laser welding of thick plates', *Structural and Heavy Plate Fabrication Conference*, New Orleans, LA, November.

EIBL, M, SONSINO, CM, KAUFMANN, H and ZHANG, G (2003), 'Fatigue assessment of laser welded thin sheet aluminum', *International Journal of Fatigue*, **25**, 719–31.

EL RAYES, M, WALZ, C and SEPOLD, G (2004), 'The influence of various hybrid welding parameters on bead geometry', Supplement to the *Welding Journal*, May, 147s–153s.

FLAVENOT, JF, DEVILLE, JP, DIBOINE, A, CANTELLO, M and GOBBI, SL (1993), 'Fatigue resistance of laser welded lap joints of steel sheets', *Welding in the World*, **31**(5), 12–15.

FRICKE, W (2002), 'Evaluation of hot spot stresses in complex welded structures' *Proceedings of The IIW Fatigue Seminar*, Commission XIII, International Institute of Welding, Tokyo.

FRICKE, W (2003), 'Fatigue analysis of welded joints: state of development', *Marine Structures*, **16**, 185–200.

FRICKE, W and KAHL, A (2005), 'Comparison of different structural stress approaches for fatigue assessement of welded ship structures', *Marine Structures*, **18**, 473–88.

FRICKE, W, CUI, W, KIERKERGAARD, H, KIHL, D, KOVAL, M, MIKKOLA, T, PRMENTIER, G, TOY-OSADA, M and YOON, J-H (2002b), 'Comparative fatigue strength assessment of a structural detail in a containership using various approaches of classification societies', *Marine Structures*, **15**, 1–13.

GONG, H and OLSEN, FO (1999), 'Gap width study and fixture design in laser butt-welding', *7th NOLAMP (Nordic Laser Materials Processing) Conference*, Lappeenranta, Finland, Volume 1, 231–8.

HOBBACHER, AF (2001), 'Fatigue strength of laser-beam-welded joints made of steel'. *Welding Research Abroad*, **47**(6), 32–7.

HOBBACHER, AF (2009), 'The new IIW recommendations for fatigue assessment of welded joints and components – A comprehensive code recently updated', *International Journal of Fatigue*, **31**, 50–8.

HSU, C and ALBRIGHT, CE (1989), 'The fatigue strength of laser-welded lap joints', *J. Laser Applications*, **2**, 26–32.

HSU, C and ALBRIGHT, CE (1991), 'Fatigue analysis of laser welded lap joints', *Engineering Fracture Mechanics*, **39**(3), 575–80.

ION, JC (2005), *Laser Processing of Engineering Materials*, Elsevier, Boston, MA, 556 pp.

KENDRICK, A (2005), *Effect of Fabrication Tolerance on Fatigue Life of Welded Joints*, Ship Structure Committee, Report No. SSC-436, NTIS, Springfield, VA 22161, 2005.

KIHL, DP (1990), *Fatigue Life Estimates for DDG-51 Base on Constant Amplitude and Variable Amplitude Component Fatigue Tests*, David Taylor Research Center, Report No. SSPD-90-173-31, April

KIHL, DP (2002), '*Fatigue Strength of HSLA-65 Weldments*', Naval Surface Warfare Center – Carderock Division; Survivability, Structures, and Materials Directorate Technical Report, July 2002

KIRKHOPE, KJ, BELL, R, CARON, L, BASU, RI and MA, KT (1999a), 'Weld detail fatigue life improvement techniques, Part 1: Application to ship structures'. *Marine Structures*, **12**, 447–74.

KIRKHOPE, KJ, BELL, R, CARON, L, BASU, RI and MA, KT (1999b), 'Weld detail fatigue life improvement techniques, Part 2: Application to ship structures'. *Marine Structures*, **12**, 477–96.

KITAGAWA, A, TAKEDA, S, FUKUDA, N and MATSUNAWA, A (2002), 'Strength of laser welded thick plate lap joint', *Science and Technology of Welding and Joining*, **7**(4), 197–203.

KOÇAK, M, DOS SANTOS, J and RIEKEHR, S (2001), 'Trends in laser beam welding technology and fracture assessment of weld joints', *Science and Technology of Welding and Joining*, **6**(6), 347–50.

KUJALA, P, ROMANOFF, J, SALMINEN, A and VATSIA, J (1999a), 'Design and production of all steel sandwich panels', *7th NOLAMP (Nordic Laser Materials Processing) Conference*, Lappeenranta, Finland, 1999, Volume 1, 81–92.

KUJALA, P, SOUCA, G, KOLI, K and TOUYONEN, T (1999b), 'Characteristics of stake laser welded joints', *7th NOLAMP (Nordic Laser Materials Processing Conference) Conference*, Lappeenranta, Finland, Volume 1, 120–33.

LARSSON, JK, ABDULWAHAB, F and MEURLING, F (1999), 'Fatigue properties and FE-simulation of laser welds', *7th NOLAMP (Nordic Laser Materials Processing Conference) Conference*, Lappeenranta, Finland, 1999, Volume 1, 55–1.

LAZZARIN, P, RABINO, E and ZONDONELLA NECCA D (1995), 'Fatigue behaviour of laser and resistance seam welds in the automotive industry (MITS WP 1697)', *Welding International*, **9**(1), 165–172.

MADDOX, SJ (2000), 'Fatigue design rules for welded structures', *Progress in Structural Engineering and Materials*, **2**, 102–9.

MANSOUR, A, WIRSCHING, P, WHITE, G and AYYUB, B (1996), *Probability Based Ship Design Implementation of Design Guidelines for Ships: a Demonstration*, Ship Structure Committee, Report No. SSC-392, NTIS, Springfiled, VA 22161.

MIYAMOTO, N, OHMI, Y and MIYAKAWA, S (2001), 'Study for fatigue strength of laser welded joints', *Japan Society of Automotive Engineers Review*, **22**, 221–36.

MORAITIS, GA and LABEAS, GN (2009), 'Prediction of residual stress and distortions due to laser beam welding of butt joints in pressure vessels', *International Journal of Pressure Vessels and Piping*, **86**, 133–42.

MASUBUCHI, K (1984), *Analysis of Welded Structures*, Pergamon Press, Oxford, 300 pp.

MUNSE, WH, WILBUR, TW, TELLALIAN, ML, NICOLL, K and WILSON, K (1983), *Fatigue Characterization of Fabricated Ship Details for Design*, Ship Structure Committee, 1983, Report No. SSC-318, NTIS, Springfiled, VA 22161.

NIEMI, E and MARQUIS, G (2002), 'Introduction to the structural stress approach to fatigue analysis of plate structures'. *Proceedings of the IIW Fatigue Seminar*, Tokyo, 18 pp.

NORDBERG, H (2005), *Fatigue Properties of Stainless Steel Lap Joints*, SAE document No. 2005-01-1324.

OLABI, AG, CASALINO, G, BENYOUNIS, KY and HASHMI, MSJ (2006), 'An ANN and Taguchi algorithms integrated approach to the optimization of CO_2 laser welding', *Advance in Engineering Software*, **37**, 643–8.

ONO, M, SHINBO, Y, YOSHITAKE, A and OHMURA, M (2002a), 'Development of laser-arc hybrid welding', *NKK Technical Review*, **86**, 8–12.

ONO, M, YOSHITAKE, A and OHMURA, M (2002b), 'Laser wledability of high strength steel sheets in fabrication of tailor welded blanks', *NKK Technical Review*, **86**, 13–18.

ONORO, J and RANNINGER, C (1997), 'Fatigue behavior of laser welds of high-strength low–alloy steels', *Journal of Material Processing Technology*, **68**, 68–70.

OROZCO, NJ, BLOMQUIST, PA, RUDY, RB and WEBBER, SR (2004), 'Real-time control of laser-hybrid welding using weld quality attributes', *Proceedings of the 23rd International Congress on Applications of Lasers & Electro-Optics (ICALEO 2004)*, October, San Francisco.

RADAJ, D (1990), *Design and Analysis of Fatigue-resistant Welded Structures*, Woodhead Publishing, Cambridge.

RADAJ, D, SONSINO, CM and FRICKE, W (2009), 'Recent developments in local concepts of fatigue assessment of welded joints', *International Journal of Fatigue*, **31**, 2–11.

REMES, H (2008), *Strain-based Approach to Fatigue Strength Assessment of Laser-Welded Joints*, Helsinki University of Technology Doctoral Dissertation, TKK 102.

REMES, H and KUJALA, P (2004), 'Experimental and theoretical investigation of fatigue characteristics of laser hybrid welded joints', *PRADS 2004*, Lubeck-Travemunde, 12–17 September, Volume 1, 457–64.

REMES, H, KUJALA, P and LAITINEN, R (2003), 'Fatigue characteristics of CO_2-laser MAG welded joints of LASER RAEX steel', *Proceedings of the 9th NOLAMP (Nordic Laser Materials Processing) Conference*, Trondheim, Norway, 37–48.

REUTZEL, E, SULLIVAN, MJ and MIKESIC, DE (2006), 'Joining pipe with the hybrid laser-GMAW process: weld test results and cost analysis', *Welding Journal*, June, 66–71.

REUTZEL, EW, KELLY, SM, SULLIVAN, MJ, HUANG, TD, KVIDAHL, L and MARTUKANITZ, RP (2008), 'Hybrid laser-GMA welding for improved affordability', *Journal of Ship Production*, **24**(2), 72–81.

ROLAND, F and METSCHKOW, B (1997), 'Laser welded sandwich panels for shipbuilding and structural steel engineering', *Marine Technology II*, **27**, 183–94.

ROLAND, F, REINERT, T and PETHAN, G (2002), 'Laser welding in shipbuilding – an overview of the activities at Meyer Werft', *Welding in the World*, **46**, 39–50.

ROLAND, F, MANZON, L, KUJALA, P, BREDE, M and WEITZENBOCK, J (2004), 'Advanced joining techniques in European shipbuilding', *Journal of Ship Production*, **20**(3), 200–10.

ROMANOFF, J, REMES, H, SOUCA, G, JUTILA, M and VARSTA, P (2007), 'The stiffness of laser stake welded T-joints in web-core sandwich structures', *Thin-walled Structures*, **45**, 453–62.

ROOKS, B (2000), 'Lasers become the acceptable face of precision welding and cutting', *Industrial Robot*, **27**(2), 103–7.

SOCHA, G and KUJALA, P (2002), 'Experimental investigation of laser stake welds in shipbuilding industry', *Fatigue 2002: Proceedings of the 8th International Fatigue Congress*, June, Stockholm, Sweden, Volume 1, 453–60.

SONSINO, CM, KUEPPERS, M, EIBL, M and ZHANG, G (2006), 'Fatigue strength of laser beam welded thin steel structures under multiaxial loading', *International Journal of Fatigue*, **28**, 657–62.

STEEN, WM (2003), *Laser Material Processing*, 3rd edition, Springer, Berlin, 408 pp.

TABAN, E, DELEU, E, DHOOGE, A and KALUC, E (2009), 'Laser welding of modified 12% Cr stainless steel: strength, fatigue, toughness, microstructure and corrosion properties', *Materials and Design*, **30**, 1193–200.

WANG, PC and EWING, KM (1991), 'Fracture mechanics analysis of fatigue resistance of spot coach peel joints', *Fatigue and Fracture of Engineering Materials and Structures*, **14**(9), 915–30.

ZHANG, G (2002a), 'Methods of predicting the fatigue life of laser-beam welded lap welds subjected to shear stress', *Welding Research Abroad*, **48**(10), 11–18.

ZHANG, S (2002b), 'Stresses in laser-beam-welded lap joints determined by outer surface strains', *Welding Journal*, 14s–17s.

<div align="right">

10

</div>

Weld metal ductility and its influence on formability of tailor welded blanks

A. A. Z A D P O O R[1,2], J. S I N K E[2]

[1]Materials Innovation Institute (M2i), The Netherlands, [2]Delft University
of Technology (TU Delft), The Netherlands

Abstract: Tailor welded blanks (TWB) are sheet metals varying in thickness, material, coating, and so on that are welded together prior to the forming process that gives them their final structural shape. The main issue in the application of TWB is reduced formability after welding. The main aim of this chapter is to present an overview of the different properties of TWB and to show links between the properties and formability of TWB. The three main topics of the chapter are mechanical properties of TWB, different aspects of the formability of TWB and methods for prediction of the formability of TWB.

Key words: ductility, formability, forming limit diagrams, mechanical properties, tailor welded blanks.

10.1 Introduction

10.1.1 Concept of tailor welded blanks

The concept of tailor welded blanks (TWB) originated in the 1960s, but the first applications were introduced later, in the 1980s (Rooks, 2001). The concept is simple: instead of forming different parts first and than welding them together into a substructure, the TWB concept reverses these activities, first welding, then forming. This reversal also makes it possible to create tailored blanks for a specific product or part. For example, the thickness can be adapted to the local requirements of the part or, as offered by friction stir welding (FSW), even greatly different alloys can be joined. In these cases a high degree of tailoring is achieved.

Among the applied welding methods, laser beam welding (LBW) and mash seam welding have received most attention. According to some reports, either CO_2 or Nd:YAG laser welding is used in approximately 99% of all TWB applications (Montgomery *et al.*, 2004). However, other types of welding such as FSW, electron-beam welding and induction welding can also be used for TWB (Zhao *et al.*, 2001). Laser beam welding is the dominant joining method for steel alloys and FSW is often used for aluminium alloys.

258

10.1.2 Advantages and disadvantages of tailor welded blanks

Changing the manufacturing order results in a number of advantages. First, welding flat sheets is much easier and cheaper than welding three-dimensional parts. Second, a weight reduction can be achieved when, for example in a car, the less efficient spot-welded overlap joints are replaced by continuous laser beam welded butt joints. Most welding processes offer the possibility of welding blanks with different thickness; some processes (like FSW) also allow the welding of greatly different alloys. The possibility of varying the thickness and material of each individual blank allows the designer to use the material optimally, resulting in a more efficient and, thus, lighter structure. For example, a high strength alloy in one location can be combined with the toughness of another alloy in another location, for example to resist fatigue. In this way both areas can be optimized for local requirements. Third, the weight and cost reduction have a positive effect on the sustainability of the parts by way of less fuel consumption, fewer resources, and so on.

The TWB concept also has several disadvantages. The most important disadvantage is the effect of the weld line on the formability of the TWB. The material in the weld line experiences high temperatures or becomes liquid (in case of fusion processes). As a result, locally the original microstructure changes and this has a significant impact on the yield strength, failure strain and strain hardening, three material properties that determine the formability of the blank. The reduced formability affects the application of the TWB.

10.1.3 Applications of TWB

The main area of applications for TWB is the automotive industry (Team, 2001). Today, many car and truck manufacturers apply the TWB concept in their products. Most favored are parts where a significant benefit is obtained in weight and/or structural efficiency. Examples are rails, pillars (Fig. 10.1), beams and boxes. For these parts, two or more sheets are (laser beam) welded to one blank. The introduction of aluminum parts in the car industry also gave a positive impulse to the application of TWB. Today, most required TWB are fabricated by specialized methods (Team, 2001).

An emerging and potential market is the aircraft industry. The highly loaded aircraft structures (wing, fuselage) are assembled from many different parts. Although welding is hardly used for aircraft parts, variations of the TWB concept could be used like blanks made by (chemically) machining or adhesive bonding, instead of welding. Combining these blanks with universal processes like press brake bending and rubber forming means
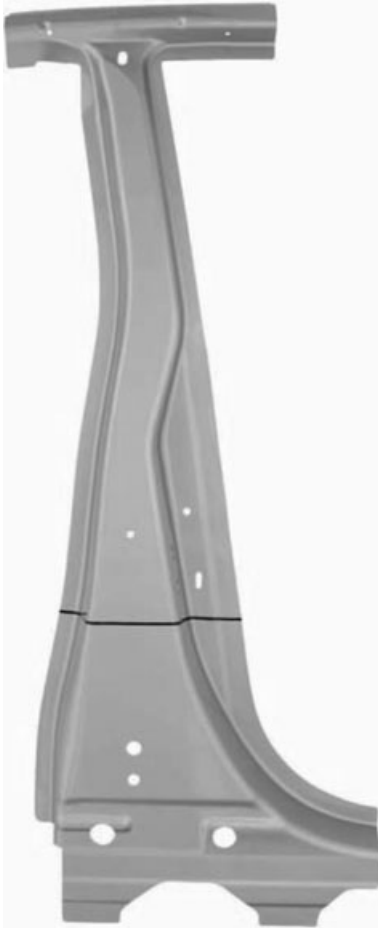
10.1 Press formed B-style, made of TWB (reproduced from Tomberg, 2007).

that significant decreases in weight and/or costs (order of 10–30%) can be achieved.

10.1.4 Scope and outline of this chapter

The main focus of this chapter is the relation between the properties of a TWB and the formability of TWB. As stated before, owing to the welding process, the formability of the material in the weld area is decreased. The chapter is composed of three main sections. First, the mechanical properties of TWB are discussed. The second section is devoted to the formability of

TWB. The last section focuses on the formability prediction methods that can be applied to TWB. Finally, the chapter makes some concluding remarks and some suggestions for further reading.

10.2   Mechanical properties of tailor welded blanks

10.2.1 Hardness

The hardness test is often used as an indirect mechanical testing technique. Generally speaking, harder materials are stronger, that is they have higher yield strengths, are more brittle and deform less until failure (Gedney, 2002). Several studies have shown that the hardness of the area near the weld seam of TWB is significantly changed by welding (Wild *et al.*, 2001; Seo *et al.*, 2000b; Min and Kang, 2000; Kang *et al.*, 2000; Chan *et al.*, 2005a; Cheng *et al.*, 2005b; Friedman and Kridli, 2000; Kampus and Balic, 2003). However, the changes in hardness and its distribution vary with different welding methods (Kampus and Balic, 2003), base metals (Min and Kang, 2000) and thickness ratios (Chan *et al.*, 2005a).

Similar to steels, studies show that the hardness increases in the weld seam in most cases (Wild *et al.*, 2001; Seo *et al.*, 2000b; Min and Kang, 2000; Kang *et al.*, 2000; Chan *et al.*, 2005a; Kampus and Balic, 2003). However, the level of the increase depends on the welding method and metal properties. In laser welding, hardness increases ranging from 50% (Chan *et al.*, 2005a) to 250% (Seo *et al.*, 2000b) are reported. The increase of hardness can also be dependent, for example, on the amount of carbon content (Min and Kang, 2000). Nevertheless, a level of 120% increase is typical for most applications (Kang *et al.*, 2000). Similar increases in hardness are reported for other welding methods. For example, it is shown that the hardness of the weld zone increases by about 50% for mesh and upset welding (Min and Kang, 2000; Kang *et al.*, 2000). The area of hardness increase can have a width from tenths of a millimeter to a few millimeters depending on the material and welding method (Min and Kang, 2000). Also the type of heat input is important in this regard, because a more concentrated heat input, like laser welding, results in narrower regions of increased hardness compared to other less concentrated methods, like metal inert gas (MIG) welding (Kampus and Balic, 2003).

Aluminum alloys can be categorized as being either heat treatable (precipitation-hardened) or non-heat treatable (solid solution hardened) (Mishra and Ma, 2005). Among the standard series of aluminum alloys, the 2000, 6000 and 7000 series are (generally) heat treatable, whereas the 1000, 3000, 4000 and 5000 series are (generally) non-heat treatable. The effects of welding on the hardness of heat treatable and non-heat treatable alloys tend to be different. Heat-treatable alloys normally undergo significant

precipitate dissolution and coarsening caused by high welding tempera-tures. This results in significant strength reductions after laser (Wu *et al.*, 2004; Friedman and Kridli, 2000) or gas tungsten arc welding (GTAW) (Miles *et al.*, 2004) and thus considerably lower hardness levels in the weld and heat-affected zones. Some non-heat treatable alloys such as 5182-O may develop a slightly higher hardness in the weld zone after FSW owing to grain refinement and residual work hardening (Miles *et al.*, 2004). It is also well established that, for (5000 series) aluminium alloys, a higher hard-ness and tensile strength are associated with higher magnesium content (Zhao *et al.*, 1999). Loss of ductility and tensile strength in laser-welded aluminums may originate from depletion of the magnesium content during welding (Shakeri *et al.*, 2002; Cheng *et al.*, 2005b; Venkat *et al.*, 1997; Pastor *et al.*, 1999). In general, vaporization of various volatile alloying elements such as zinc, lithium and magnesium takes place during the laser welding of aluminum alloys because these elements have much higher equilibrium pressure than aluminum (Zhao *et al.*, 1999). Since these volatile elements can form precipitates, their volatilization may contribute to the degradation of the mechanical properties and softening of the weld metal (Zhao *et al.*, 1999). In the case of FSW, the hardness profile may be asymmetric around the weld centerline, which is due to the different deformation and tempera-ture histories on the advancing and retreating sides (Zadpoor *et al.*, 2008) (Fig. 10.2).

10.2.2 Tensile testing methods

The fact that there might be different materials and thicknesses in one single sheet metal assembly results in potentially non-uniform distribution of strains and stresses in the tensile test specimens made of TWB. Therefore,
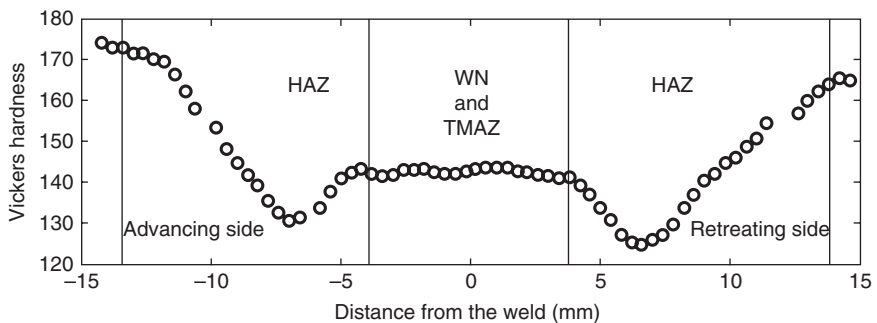
10.2 Hardness profile of a sample friction stir weld of aluminum alloy 7075-T6. Note that the different zones of the weld have different hardness levels and that the profile is asymmetric around the weld centerline (reprinted from Zadpoor *et al.*, 2009, with permission from Elsevier).

the uniform strain assumption that is the basis of many conventional strain measurement techniques, such as extensometers, is not valid any more and one may need to use tailor-made tensile tests specimens or resort to more elaborate measurement techniques.

One important factor in testing TWB is the size of the specimens. The size of the specimens depends on what needs to be tested: the joint or the weld. If the joint is tested, the specimen should include both the weld and the base metals. In this case, the size of the specimen can be as large as the size of the standard ASTM E8 specimens. If the weld is being tested, only the material of the weld should be present in the gauge length. Wild *et al.* (2001) showed that only sub-sized specimens (smaller than ASTM E8 specimens) can give reliable tensile properties. They argued that this is because the contribution of the weld to the tensile deformation diminishes as the size of the specimen increases. Indeed, the standard specimens overestimate the ductility of the weld metal (Davies *et al.*, 1999, 2000). When the relative size of the weld in the gauge length increases, the stress–strain curve of the specimen approaches the stress–strain curve of the weld metal (Wild *et al.*, 2001). Therefore, many researchers have chosen to use small (Wild *et al.*, 2001; Hetu and Siegert, 2005) or miniature test specimens (Davies *et al.*, 2001). The miniature test specimens are small enough to ensure that only the material of the weld is present in the gauge area. It is shown that reliable weld properties can be obtained by using this method (Davies *et al.*, 2001). Nevertheless, there are some difficulties associated with the miniature test specimens. For example, manufacturing of the miniature test specimens is not easy.

Owing to these problems, efforts are made to use other methods to measure the tensile properties of the material of the weld. The rule of mixtures (ROM) is one of the methods. This method can be applied only for longitudinal (standard) test specimens. The method assumes that the longitudinal strains are uniform across the welded specimen and that the tensile load, *P*, is divided between base metal 1, base metal 2 and the material of the weld as follows:

$$P = \sigma_1 A_1 + \sigma_2 A_2 + \bar{\sigma}_w A_w \qquad [10.1]$$

where *s* and *A* denote stress and cross-section area, respectively. Subscripts 1, 2 and w stand for base metal 1, base metal 2, and the material of the weld, respectively.

If the strength and strain-hardening coefficients of the base metals are known, the average stress in the material of the weld, $\bar{\sigma}_w$, can be calculated as:

$$\bar{\sigma}_w = \frac{P - K_1 \varepsilon^{n_1} A_1 - K_2 \varepsilon^{n_2} A_2}{A_w} \qquad [10.2]$$

where ε is the uniform longitudinal strain, K is the strength coefficient and n is the strain hardening component. The rule of mixtures was used by some researchers to determine the stress–strain curve of TWBs (Wild *et al.*, 2001; Ghoo *et al.*, 2001a; Hetu and Siegert, 2005). The most important difficulty associated with the ROM method is the determination of the cross-section of the weld. Micro-hardness measurements can be applied to determine this size. A more complete version of ROM, which works both for longitudinal and transverse specimens, is presented by Liu and Chao (2005).

A recent trend in the measurement of the local mechanical properties of TWB is to use non-contact optical methods such as the digital image correlation (DIC) technique. DIC uses digital imaging to trace back a pre-applied random ink pattern on the surface of the specimen. After the test, a computer program compares the successive digital images that are taken during the test and correlates the ink patterns of the images. Subsequently, the local strains can be determined using the calculated displacements of the ink pattern. DIC has been used by many researchers, see for example (Hatamleh, 2008; Genevois *et al.*, 2005, 2006; Lockwood and Reynolds, 2003; Sutton *et al.*, 2004). Figure 10.3(a) depicts the contour of the local yield strength of a sample friction stir weld as example (aluminum alloy 7075-T6). The speckle ink pattern and the calculated values of the local yield strength are superimposed in this figure. Figure 10.3(b) presents the local stress–strain curves for the same weld and identifies the 0.2% yield point for each single curve.

10.2.3 Global mechanical properties

The global mechanical properties of TWB are normally determined by using tensile test specimens that contain the different zones of the weld; the specimens may or may not contain base metal. This category of tests gives information concerning the TWB as a whole and is extensively used for study of the strength and ductility of tailor welded blanks. Whether the strength of the material is affected by welding is highly dependent on the materials and welding parameters. It is shown that post-weld strengths of some steels, for example SPCC, remain at the same level as the base metal regardless of the welding method (Chan *et al.*, 2003; Kang *et al.*, 2000; Chan *et al.*, 2005a). The same holds for O-tempered aluminum alloys (Cheng *et al.*, 2005a; Miles *et al.*, 2004; Davies *et al.*, 2000). However, precipitation-hardened aluminum alloys change in properties during welding and tend to have a lower strength compared to the base metals (Wu *et al.*, 2004; Miles *et al.*, 2004; Friedman and Kridli, 2000) because of the dissolution and coarsening of precipitates.

Wherever local remelting takes places, like in the case of laser welding, or if the material undergoes dynamic recrystallization, such as in the case of
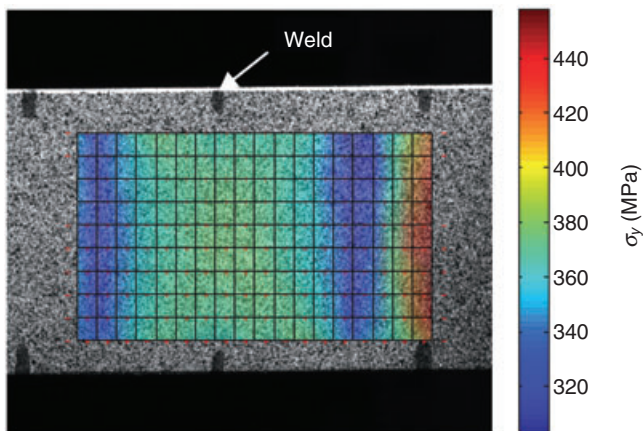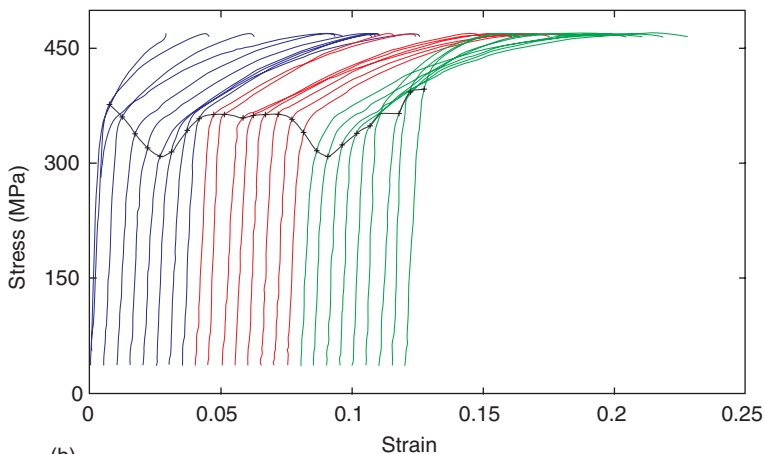
10.3 Local yield strength values around the weld centerline (a) and the local stress–strain curves and the local values of yield strength (b) from the advancing to the retreating sides of a sample weld (aluminum alloy 7075-T6).

FSW, the grain size in the weld zone may be different from that of the base metal. The disparity between grain sizes results in different yield stresses and, thus reduced strength (Hall–Petch relationship) (Friedman and Kridli, 2000). However, some experimental studies found that, despite the large disparity between grain sizes in the weld and the base metal zones, there is no considerable change in the tensile strength (Friedman and Kridli, 2000). Yield strength and tensile strength of TWB are shown also to be dependent

on orientation of the weld line. Seo *et al.* (2000b) reported that the yield and tensile strengths of longitudinally welded tensile specimens (laser welded SPC1 sheets) are 12% better than transversely welded specimens.

Experimental results show that ductility of tailor welded blanks decreases after welding. This decrease is highly dependent on, for example, the welding method (Miles *et al.*, 2004), weld line orientation (Cheng *et al.*, 2005a), size of the weld area in the cross-section of the specimens (Davies *et al.*, 2000) and the thickness ratio (Friedman and Kridli, 2000). Miles *et al.* (2004) showed that FSW TWB have better ductility compared with gas tungsten arc welded TWB (Cheng *et al.*, 2005a). Davies *et al.* (2000) argued that an increase in porosity of weld metal and in the size of the weld area in the cross-section of the specimen would decrease the ductility. Cheng *et al.* (2005a) showed that transversely welded 5754-O TWB are more ductile than longitudinally welded ones. Smaller thickness ratios will also result in improved ductility (Chan *et al.*, 2005a; Friedman and Kridli, 2000).

Zadpoor *et al.* (2008) studied the global mechanical properties of five different configurations of FSW TWB (AA2024-T3 and AA7075-T6) in two conditions: as-welded and machined. The machined specimens were shaved so that the thickness is the same throughout the specimen surface. They showed that the mechanical properties of the alloys are much influenced by FSW. The yield and tensile strengths as well as the elongation decrease after FSW. The percentage decreases in the yield and tensile strengths were lower than for the elongation. Furthermore, the level of the decrease in the mechanical properties was highly dependent on the welding configuration.

10.2.4 Local mechanical properties

TWB is a heterogeneous assembly which, in many cases, cannot be treated as a uniform material. In order to design and simulate TWB, one has to characterize the local mechanical properties of the different zones of TWB. The methods discussed in the previous sections such as DIC can be used for this purpose. The number and size of the zones depend on the welding technique. For example, in fusion welding there are two major zones: weld seam and heat affected zone (HAZ). The size of the zones is dependent on the welding parameters. However, the weld seam tends to be narrower than the weld nugget in FSW TWB. In the case of FSW TWB, there are at least three different zones: weld nugget (WN), thermomechanically affected zone (TMAZ) and HAZ. Moreover, owing to the different deformation and thermal patterns on the advancing and retreating sides, the mechanical properties of the different zones are asymmetric around the weld centerline even for same-thickness same-alloy welds (Zadpoor *et al.*, 2008). On top of all these difficulties, the mechanical properties may not be the same within

one single zone. Therefore, it may not be possible to use one single value to represent an entire weld zone of a given TWB.

The heterogeneity of the distribution of the mechanical properties has at least two implications for the fracture analysis and design of TWB. First, one needs to characterize a large number of mechanical properties. The tensile properties are relatively easy to characterize using automated optical methods such as DIC. However, the forming limits of the different zones are also different and the determination of the forming limits of different zones is not as straightforward. Therefore, a given TWB has to be characterized in just as much detail as needed. Secondly, design and analysis of a heterogeneous structure is much more difficult than a uniform structure, because the usage of the additional mechanical properties also comes at a cost. For example, implementation of the mechanical properties of the different zone of a TWB in FEM models is a delicate compromise between accuracy and computational cost. While implementation of too much detail can result in a model that is too complex and too computationally expensive, implementation of too little detail results in a model that is not accurate enough. Different authors have addressed the problem. Zadpoor *et al.* (2009a) studied the finite element (FEM) modeling of FSW TWB and whether or not the implementation of details affects simulated strain distribution and springback behavior of FSW TWB. They concluded that the implementation of weld details makes a significant contribution to the accuracy of the prediction of the failure, strain field and springback behavior.

10.3   Formability of tailor welded blanks

10.3.1 Forming limit diagram – (FLD)

For the evaluation of the formability of a metal alloy (Wagoner *et al.*, 1989) Keeler and Goodwin developed the so-called forming limit diagram, the FLD. This diagram (Fig. 10.4) consists of a (lower and upper) limit line (forming limit curve, FLC), separating the safe combinations of in-plane principle strains ε_1 and ε_2 below the line and combinations above that line, which result in failure. The lower and upper limits represent the scatter in the FLDs, which are retrieved by experimental testing. The material is regarded as isotropic with a congruent stress–strain curve; therefore, the plot is limited to a quarter of the ε_1–ε_2 field. The distinction between diffuse necking and local necking/fracture, which becomes apparent at $\varepsilon_2 < 0$, is illustrated by a set of (dashed) lines.

The FLD is primarily an experimental tool, determined by formability tests. Formability tests are divided into intrinsic tests and simulative tests. Intrinsic tests measure material properties; the results are not dependent on specimen dimensions, machine parameters, thickness, surface characteristics,
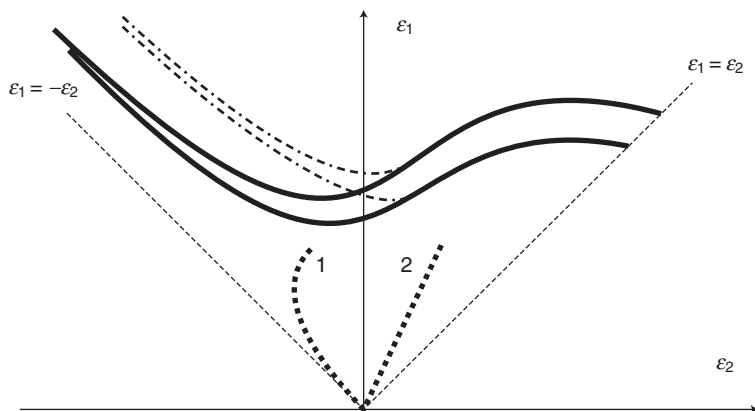
10.4 Schematic plot of a FLD.

or lubricants. Examples of intrinsic tests are the tensile test, bulge test, hardness test, plane strain tensile test and the Marciniak biaxial stretch test. Simulative tests are related to a particular forming process and/or geometry and account for effects of process variables like die and punch geometry, lubrication and punch speed. Examples of simulative tests are the Olsen test, limiting dome height (LDH) test, Ohio State University (OSU) method (Kim and Park, 1994), Yoshida test, bend test, Swift cup test and the plane-strain stretching test (Kim and Park, 1994).

The FLD is expressed in plastic strains, which are measured after the forming process, when the load is released. Therefore, no elastic strains are present in a FLD. Typical methods of measuring strains during testing are simple (etched) grids that can be evaluated by software.

The FLD can be divided in areas, each representing a specific deformation mode. At the left-hand side of the plot, the minor in-plane strain (ε_2) is negative. In this region the deformation is called 'drawing', a combination of tensile and compressive strains. At the right-hand side of the diagram, both in-plane strains are positive, which is referred to as 'stretching'. Between the two areas, at the vertical axis, the minor in-plane strain becomes zero, the 'plain strain' condition, which is representative for bending. The least formability usually occurs in the plane strain condition ($\varepsilon_2 = 0$). Therefore, it is a conservative approach to use this condition as a formability limit for the sheet metal.

In the diagram (Fig. 10.4) deformation paths are plotted, representing the increase or decrease in the strains. Two paths are plotted: a curved path (1) and a straight path (2). Based on the assumptions, the FLD is only valid for monotonous and proportional loading – the straight line (2). For curved lines like (1), the FLD becomes less reliable. Nevertheless, the FLD is often

used as a first-order analysis tool for the evaluation and prediction of the formability of a metal alloy.

The limit values in the FLD are dominated by material properties, although the FLD cannot be regarded as a material property since some non-material variables also have an impact on the limits. Three important material parameters are discussed here: the failure strain, the strain hardening and anisotropy.

The failure strain, measured during a tensile test, is one data point in the FLD and gives a first indication of the formability of a material. The higher the failure strain, the better the formability of the material. The failure or limit strain can be based on two criteria: end of homogeneous deformation (start of diffuse necking, solid lines) or the onset of local necking (dashed lines). Each metal alloy and temper has a specific FLD and a material with a better formability has higher limit values in its FLD. For some alloys the limits can be manipulated by strain or precipitation hardening processes.

The strain hardening does not influence the forming limits, but does influence the distribution of the strains over the part. A high strain hardening is beneficial for stretching operations when it distributes the strains more evenly over the sheet material. As result, the peak strains are reduced and the deformation becomes less critical. So, for processes involving a significant amount of stretching, a high strain hardening coefficient is favorable. However, for bending processes a small strain hardening coefficient is preferred.

The third parameter is anisotropy. Most metal blanks show some anisotropic behavior. A high normal anisotropy factor is favorable, but high in-plane anisotropy is not preferred. To quantify the anisotropy, the Lankford parameter is introduced: $R = \varepsilon_2/\varepsilon_1$. The R-value may vary with the orientation to the rolling direction (RD). The effect of the anisotropy on the FLD is in the changing of strain path orientations and in the limit values that may increase or decrease. A high normal anisotropy factor increases the in-plane formability of the material and moves the forming limit upwards (like for higher failure strains). Note that, in case of significant anisotropy, one should reconsider the original assumptions related to the FLD (ε_1–ε_2 area).

Non-material parameters also influence the FLD. The applied stress ratio influences the criticality of forming a specific process. If, for a specific product (represented by point A in Fig. 10.5), the applied loads in ε_2 direction are increased, then point A moves to the right, the distance to the FLC increases and the part manufacture becomes less critical.

Another parameter, lubrication, has an effect like strain hardening. The lower the friction between the tooling and the sheet, the more evenly the strains are distributed over the part. Again, the peak values are leveled and the deformation becomes less critical.
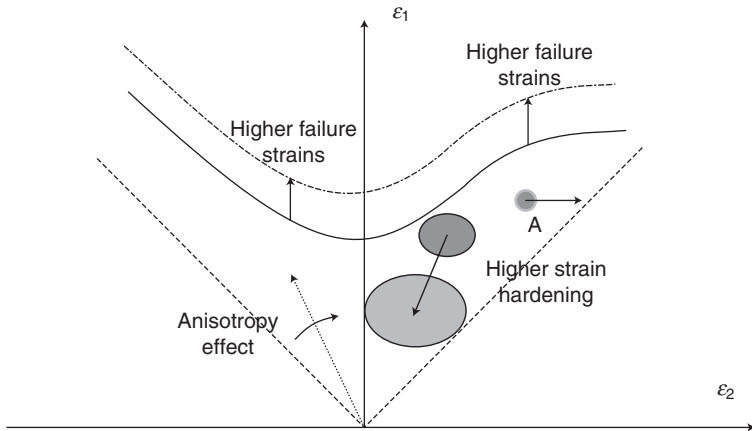
10.5 Effect of several material parameters on the FLD.

10.3.2 Effects of welding parameters

The forming limit diagrams in the previous sections are illustrated for monolithic sheets. Tailor welded blanks consist of at least two materials joined by a weld. First we focus on blanks made of sheets of the same alloy and thickness.

Concerning TWB, two approaches can be used to develop forming limit diagrams. The first approach combines the properties of the base metals and the weld material and creates one FLD representing the whole blank. The second approach provides different FLD for the base metals and the weld material. Most investigators have used the first approach. Ghoo *et al.* (2001b) proposed the second approach to improve the accuracy of FLD. In this approach, two different limit curves are plotted. One of the curves represents the forming limits of the base metal and another represents the forming limits of the weld metal. Since there can be a considerable difference between these two, the final FLD obtained by the second approach is generally more accurate. Note that, when different base metals are applied, more curves are presented in the FLD. The formability of TWB (and their limits in a FLD) is influenced by the resulting microstructure of the weld and the HAZ in particular.

Generally, before the welding process, the parent metal sheets have high mechanical properties owing to their composition and processing. The specific alloy, and its processing by heat treatments or cold work, have specific and dedicated microstructural features that will increase the (yield) strength, fatigue resistance or other properties. Once the sheets are welded together, along the weld line, these specific properties are (partly) disrupted. In a line

perpendicular to the weld line the hardness, yield strength and ultimate strength often decrease, which can be demonstrated by hardness measurements or DIC.

Whether the strength of the material is affected by welding is highly dependent on the materials and welding parameters. It is shown that postweld strengths of some steels, for example SPCC, remain at the same level as the base metal regardless of the welding method (Chan *et al.*, 2003; Kang *et al.*, 2000; Chan *et al.*, 2005a). The same holds for O-tempered aluminum alloys (Cheng *et al.*, 2005a; Miles *et al.*, 2004; Davies *et al.*, 2000). However, the properties of hardened aluminum alloys change during welding and tend to have a lower strength comparing to the base metals (Wu *et al.*, 2004; Miles *et al.*, 2004; Friedman and Kridli, 2000). Owing to local remelting, the grain size in the weld zone can be different from that in the base metal. The disparity between grain sizes results in different yield stresses and, thus, reduced strength (Hall–Petch relationship) (Friedman and Kridli, 2000).

Failure limits also change. The thermal and mechanical features of the welding process alter the microstructure and thereby also the failure strains. Often, the failure strain decreases and the material in the weld zone become more brittle. This results in a lowering of the forming limits in the FLD. Generally, aluminum alloys become more brittle when the grain size increases, because intergranular fracture occurs more easily. Sato *et al.* (2004) showed that there is an optimal grain size for which the formability reaches its maximum.

Experimental results show that ductility of TWB decreases after welding. This decrease is highly dependent on, for example, the welding method (Miles *et al.*, 2004), weld line orientation (Cheng *et al.*, 2005a), size of the weld area in the cross-section of the specimens (Davies *et al.*, 2000) and the thickness ratio (Friedman and Kridli, 2000). Miles *et al.* (2004) showed that FSW TWB have better ductility compared with gas tungsten arc welded TWB (Cheng *et al.*, 2005a). Smaller thickness ratios will also result in improved ductility (Chan *et al.*, 2005a; Friedman and Kridli, 2000).

The reduced formability of the material weld line influences the formability of the entire blank along the weld line as well as perpendicular to it. The reduced failure strain, smaller strain hardening and increased anisotropy have their impact on the forming limits and the strain paths or trajectories in the FLD.

10.3.3 Effects of design variables

One of the design variables is the thickness ratio. A thickness ratio results in a local stress concentration and a shift in the neutral axis. The stress concentration reduces the failure strain and the shift of the neutral axis causes local bending of the material.

Therefore, the thickness ratio affects the forming limits of the TWB. The formability of the TWB (presented by the FLD or minimum major strain) decreases generally with an increase in the thickness ratio (Chan *et al.*, 2003; Shakeri *et al.*, 2002; Chan *et al.*, 2005a,b). TWB with thickness ratios close to unity show a minimum major strain closer to those of the base metals (Seo *et al.*, 2000b; Chan *et al.*, 2005a).

The changes in material properties at the transition line may result in stress/strain localization. Therefore, it is generally better to design the weld line in low strain regions. The local effects may result in, for example, higher stress concentration factors. It is generally better to design the weld lines in the low strain regions. *A priori* knowledge of stress and strain distributions within the TWB is important for all of the above-mentioned purposes.

At the same time, the formability of the blank depends on the welding process too. For example, because of the narrow bead width and hard welding part in a laser welded joint and wide hardening part and the soft welding part in a mash seam welded joint (Kim *et al.*, 1996), it is believed that mash seam welded specimens have good formability in the ball-stretching test, whilst laser welded specimens have good formability in the ball hole-expansion test (Min and Kang, 2000).

The formability also depends on the loading conditions such as the orientation of loading with respect to the weld line. Cheng *et al.* (2005a) observed that the minimum major strain of TWB with longitudinal welds is almost the same as the base metal. However, the minimum major strain was reduced from 0.24 to 0.19 for TWB with transverse welds (Cheng *et al.*, 2005a). Miles *et al.* (2004) found that FSW aluminum TWB have lower forming limits in comparison with the base metals when biaxial strain conditions are reached. Although the formability of the TWB was similar to the base metals under plain-strain conditions, it rapidly decreased as biaxial strain conditions were approached and straining occurred across the weld line (Miles *et al.*, 2004). The above results are consistent with the results of Friedman and Kridli (2000). According to their findings, the formability decreases as the weld orientation becomes perpendicular to the stretching direction. However, they realized that 80% of the base metal formability could be retained with stretching direction oriented 45° to the weld line.

10.3.4 Weld line movement

The dissimilar properties of two pieces of sheet metal in a TWB also affect the metal flow. Different pieces of sheet metal, used in a typical TWB, have different strengths and deform differently. If the material is stretched perpendicular to the weld line, the deformation of the weaker parent material is larger, which results in movement of the weld line to the stronger material

and ultimately may cause tearing of the weaker material. Reversely, compressive stresses may lead to wrinkling in some forming applications. Here, the inability of the weaker material to withstand the high compressive stress and the reduced buckling strength in case of thinner sheet result in movement of the weld line towards the thinner material and eventually buckling of the thinner material (Kinsey *et al.*, 2004).

Three consequences of the metal flow are likely to occur in forming TWB that are associated with the above-mentioned failure modes (Kinsey and Cao, 2003). First, the weld line may move toward the stronger material. Second, the unsupported or unconstrained thin material may wrinkle or buckle. The unconstrained condition occurs (for rigid tools) as a result of the initial clearance between the step in the blank-holder plate and the weld line. The clearance is necessary to accommodate the thickness step between the thicker and the thinner material. Finally, an over-constrained condition of the material occurs in some (deep) drawing processes, resulting in a weld line movement toward the thinner material and may finally cause tearing failure (Kinsey and Cao, 2003).

The initial location of the weld line plays an important role in the weld line movement. Studies of deep drawing show that larger weld line movements are related to larger distances of the weld line to the centerline of the part (Seo *et al.*, 2000a; Heo *et al.*, 2001a). The maximum drawing depth and maximum drawing force increase when this distance decreases (Heo *et al.*, 2001a).

The blank shape influences the weld line movement as well (Seo *et al.*, 2000a). According to Meinders *et al.* (2000), the weld line movement is considerably dependent on the strain distribution, specifically when the blank is stretched perpendicular to the weld line. In addition, Shi *et al.* (1993) showed that the weld line movement toward the stronger parent material is a measure of strain localization in the weaker parent metal. Meinders *et al.* (2000) then argued that placing the weld in a region with low strains perpendicular to the weld line minimizes the weld line movement.

Although most studies use numerical simulation techniques to predict weld line movement, few analytical models are available. Kinsey and Cao developed a two-dimensional (2D) sectional model to calculate weld line movement and forming height when a uniform binder force is applied (Kinsey and Cao, 2003). The results of the model were in good agreement with numerical simulations.

10.3.5 Control of weld line movement

The material flow adversely affects the formability of the TWB. Some researchers have tried to find strategies to control the material flow during forming of TWB. Some of these are discussed in this section.

Placement of draw beads can help to control the material flow because they add local constraints to the TWB. Heo *et al.* (2001a,b) showed that the presence of the draw beads decreases weld line movement. They showed that the size and height of the draw beads are also important. Normally, the weld line movement decreases as the size and height of the draw beads increases.

Control of blank holding force (BHF) is another strategy for controlling the weld line movement and obtaining a uniform distribution of the deformation. The main idea is to control the weld line movement by adjusting the BHF. A number of researchers have tried to manipulate the BHF so that the weld line movement can be controlled. The manipulation can be done by segmented blank holders, tooling or other adapted devices. Siegert and Knabe designed a die with segmented blank holders in order to increase drawing in the forming area from the side of the tailor welded blank with the stronger material (Siegert and Knabe, 1995). Hetu and Siegert (2005) used a segmented blank holder and a 10-point cushion system to transfer the press force onto the blank. Other researchers have worked on modification of the forming die. Cao and Kinsey patented a method for reduction of the weld line movement (Kinsey and Cao, 1999). They used a segmented die with local adaptive controllers. A rubber edge, or pad, on the hydraulic cylinders prevents the clamping mechanism from deforming the sheet metal (Kinsey *et al.*, 1999a,b, 2001).

10.3.6 Post-weld heat treatment

Most metal alloys obtain their mechanical (and other) properties by selective and careful thermal and mechanical processing. To obtain the final properties, largely dominated by the microstructure, the material is heat treated or/and cold worked. The cold working (by rolling) reduces the failure strain and lowers the forming limits in a FLD, but it increases the strength. A similar effect is achieved by heat treatment in the micro-structural arrangement, characterized for example by small intermetallic particles, precipitates and grain boundaries. Again, when the strength values are increased, the failure strains decrease.

Heat treatment can also be used to increase the formability (to increase the failure limits in the FLD). For aluminum alloys, for example, solution treatment followed by quenching improves the formability of a wide range of different alloys. The particular treatment is unstable, but after forming its hardened microstructure is regained by natural ageing. Many other alloys can be processed in a similar way: first applying a heat treatment to improve its formability and, after forming, another heat treatment to restore the original strength values.

Post-welded heat treatments (PWHT) are applied to improve the properties of the welds after welding, often aiming for an increase in strength values. A number of papers (Feng *et al.*, 2006, Krishnan, 2002), discuss the PWHT for FSW of aluminum alloys. The most investigated heat treatment and properties are the solution heat treatment followed by quenching and ageing and the hardness of the material, respectively. Two things can be learned from these researches, first the hardness increased owing to the heat treatments and second the property becomes uniform over the weld zone. For a better formability, the ageing treatment is applied after the forming process to improve formability and retain good formability for the TWB. The uniformity of properties over the weld zone could improve its formability, because 'weak links' are eliminated.

10.4   Formability prediction for tailor welded blanks

Three major formability prediction techniques and their applications to TWB are discussed in this section. The techniques discussed are usually the same as the ones used for monolithic sheets. The major difference is that a prediction for TWB needs to be done for different materials representing different zones of the weld and the base material.

10.4.1 Marciniak–Kuczynski theory

In 1967, Marciniak and Kuczynski (M–K) proposed a new instability condition based on the initial imperfection approach (Marciniak and Kuczynski, 1967). In the M–K method, it is assumed that an initial imperfection is present in the sheet metal. The imperfection is modeled by a band of smaller thickness (Fig. 10.6). The initial imperfection can originate from a smaller thickness, a local variation of the strength, or a combination of both. The imperfection parameter, f_0, is defined as

$$f_0 = \frac{K_b t_{b,0}}{K_a t_{a,0}} = \frac{\hbar_{b,0}}{\hbar_{a,0}}$$

[10.3]

where K and t stand for strength and thickness, respectively. Subscript b denotes the imperfection zone and subscript a denotes the uniform zone. The parameters $\hbar_b$ and $\hbar_a$ represent the combined effect of the strength and thickness of both zones. The imperfection angle must be determined such that the limit strains are minimized.

During a biaxial straining process, the imperfection zone deforms more than the uniform zone. Therefore, the strain path of the imperfection zone is continuously ahead of the strain path of the uniform zone. At a certain point when strain localization occurs, the difference between the strain paths of the imperfection and uniform zones begins to increase drastically.
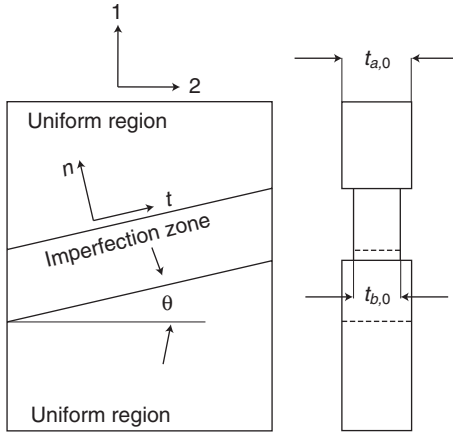
10.6 Schematic drawing of the Marciniak–Kuczynski model.

In the M–K analyses, the strain paths of the both zones are traced and a criterion is used to detect the high degree of discrepancy, which is presumed to be an indicator of strain localization. Once strain localization is detected, the sheet metal is assumed to have failed.

It is generally assumed that the velocity gradient and Cauchy stress tensors are known for the uniform zone and the task is to find the tensors in the imperfection zone. The velocity gradient, L, is defined as:

$$L = \frac{\partial v_i}{\partial x_j} \hat{e}_i \otimes \hat{e}_j \qquad [10.4]$$

and can be decomposed into a symmetric part, D, which represents rate of deformation of the material particle and an anti-symmetric part, W, which represents the continuum spin of the material particle, as:

$$L = D + W \qquad [10.5]$$

The compatibility condition at the interface of the imperfection zone requires that:

$$L_{b,ij} = L_{a,ij} + \dot{c}_i n_j, \quad i, j = 1, 2 \qquad [10.6]$$

where n_j are the components of the unit normal to the imperfection zone and $\dot{c}_i$ are parameters to be determined during the solution process. Equation [10.6] can be decomposed into a symmetric part, D_{ij}, and an anti-symmetric part, W_{ij}, as:

$$D_{b,ij} = D_{a,ij} + \frac{1}{2}(\dot{c}_i n_j + n_i \dot{c}_j), \quad i, j = 1, 2 \qquad [10.7]$$

$$W_{b,ij} = W_{a,ij} + \frac{1}{2}(\dot{c}_i n_j + n_i \dot{c}_j), \quad i,j = 1,2 \qquad [10.8]$$

Requiring equilibrium of the forces at the interface of the imperfection zone, one would obtain the following relationship:

$$n_i \sigma_{b,ij} \hbar_b = n_i \sigma_{a,ij} \hbar_a \qquad [10.9]$$

As the deformation takes place, the orientation of the imperfection zones changes according to the following relationship:

$$\tan(\theta + \delta\theta) = \tan(\theta) \frac{1 + \delta\varepsilon_{a,11}}{1 + \delta\varepsilon_{a,22}} \qquad [10.10]$$

where

$$\varepsilon_{ii} = \int_0^t D_{a,ii} \mathrm{d}t \qquad [10.11]$$

The evolution of imperfection parameter, f, can be described as:

$$f = f_0 \exp(\varepsilon_{b,33} - \varepsilon_{a,33}) \qquad [10.12]$$

and $D_{a,33}$ and $D_{b,33}$ are specified by the conditions $\dot{\sigma}_{a,33} = \dot{\sigma}_{b,33} = 0$.

A method for the determination of the material imperfection size is to fit the results of the failure/localization analysis to those of the uniaxial tensile tests (Chien *et al.*, 2003) or plane strain experiments. The material imperfection parameter can be then used to predict failure strains under biaxial straining conditions.

Davies *et al.* (2001) used the M–K technique to predict the FLD of gas tungsten arc welded (GTAW) blanks. The welded materials were of different thicknesses of aluminium alloys 5182 and 5754. Zadpoor *et al.* (2009a) studied the failure prediction and FEM modeling of the FSW blanks by using two different study cases, namely LDH test and the S-rail problem. The forming limit diagrams of the different zones within the FSW blanks were determined using the M–K theory. The imperfection parameter was determined such that the predicted failure strain matched the strain measured in tensile testing. The determined imperfection parameter was then used to predict the forming limits for the whole range of strain ratios. The FLDs obtained are presented in Fig. 10.7. One can see that the FLDs of HAZ and WN are much lower than that of the base metal (aluminium alloy 2024-T3). Lee *et al.* (2009) used the Marciniak–Kuczynski method to determine the right-hand side of the FLDs of FSW TWB made from aluminum (6111-T4, 5083-H18, 5083-O), dual phase steel (DP590) and AZ31 magnesium sheets. The imperfection parameter was determined using the failure limit at the plane strain condition.
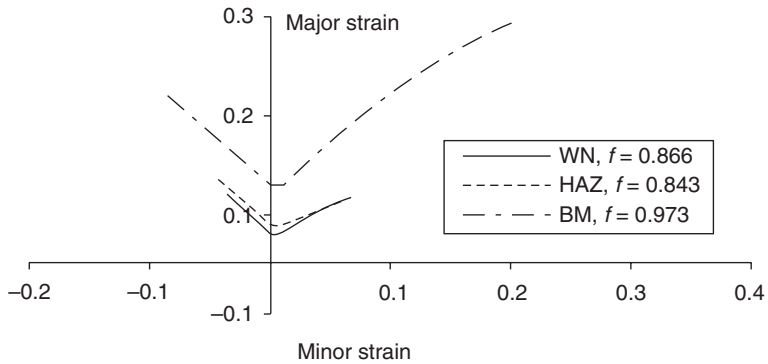
10.7 FLDs of different zones of a FSW TWB (base metal: aluminum alloy 2024-T3) determined by the M–K theory (reprinted from Zadpoor *et al.*, 2009, with permission from Elsevier).

10.4.2 Bifurcation methods

Stören and Rice (1975) used the J_2 deformation theory instead of conventional flow theory to determine the forming limits of sheet metals based on the vertex formation assumption. According to this assumption, localized necking takes place once a vertex is developed on the subsequent yield surface and the bifurcation emerges from the state of uniform deformation. The theory was later modified and extended by Zhu *et al.* (2001) and Chow *et al.* (2003). Chow *et al.* (2003) have given the failure strains for proportional loading and Hosford's yield criterion. The Hosford's yield criterion can be expressed as (Chow *et al.*, 2003):

$$\sigma_{eq} = \frac{1}{\left[R_{90}(1+R_0)\right]^{1/a}}\left(R_{90}|\sigma_1|^a + R_0|\sigma_2|^a + R_0R_{90}|\sigma_1 - \sigma_2|^a\right)^{1/a} \quad [10.13]$$

where σ_{eq} is the equivalent stress and superscript a is the characteristic exponent of the yield function. Chow *et al.* then give the failure strains at the left-hand side of the FLD as:

$$\varepsilon_{1,f} = \frac{(1+R_0)\left[\alpha^{a-2} + R_{90}(1+\beta)(1-\alpha)^{a-2}\right]f^a(\alpha)}{(a-1)(1+\beta)(1+\alpha\beta)\left[\alpha^{a-2} + (R_{90} + R_0\alpha^{a-2})(1-\alpha)^{a-2}\right]} + \frac{(a-1)n-1}{(a-1)(1+\beta)}$$

$$[10.14]$$

and for the failure strains at the right-hand side of the FLD as (Chow *et al.*, 2003):

$$\varepsilon_{1,f} = \frac{(1+R_0)\left[\alpha^{a-2} + R_{90}(1-\alpha)^{a-2}\right]f^a(\alpha)}{(a-1)(1+\alpha\beta)\left[\alpha^{a-2} + (R_{90} + R_0\alpha^{a-2})(1-\alpha)^{a-2}\right]} + \frac{(a-1)n-1}{(a-1)(1+\alpha\beta)} \quad [10.15]$$

where α and β are, respectively, the stress and strain ratios and $f^a(\alpha)$ is given as:

$$f(\alpha) = \frac{\mathrm{sgn}(\sigma_1)}{[R_{90}(1+R_0)]^{1/a}} \left[R_{90} + R_0 |\alpha|^a + R_0 R_{90} |1-\alpha|^a \right]^{1/a} \qquad [10.16]$$

Cheng *et al.* (2007) used the above formulae to determine the failure limits of laser-welded AISI 304 steel sheets with different thicknesses of 1.2 mm and 1.0 mm (Cheng *et al.*, 2007). The same approach was used by Jie *et al.* (2007) for failure analysis of laser-welded stainless steel (SUS 304a) with a thickness ratio of 1.2 mm (thicknesses 1.2 mm and 1.0 mm).

10.4.3 Ductile fracture models

The failure mechanism of some less ductile materials may be different from highly ductile sheet metal forming materials such as mild steels and 5000 and 6000 series automotive aluminum alloys. Examples of these less ductile materials are high strength steels, advanced high strength steels and high strength aluminum alloys such as precipitation-hardened 2000 and 7000 series alloys. Ductile fracture may be responsible for the final fracture of these materials. Therefore, one needs to use the theoretical approaches developed for modeling the ductile fracture mechanism. Ductile fracture models can be categorized into two major categories: phenomenological models and physical models. While phenomenological models try to predict the onset of fracture using a phenomenological function which may or may not have a physical interpretation, physical models try to model the actual mechanism of void growth and coalescence. Each of the following subsections deals with one of the modeling approaches.

Phenomenological models

The phenomenological models of ductile fracture predict the onset of fracture based on a macroscopically defined damage accumulation variable, D. Therefore, the scalar damage variable, D, can be defined as:

$$D = f(\boldsymbol{\sigma}, \boldsymbol{\varepsilon}^p) \qquad [10.17]$$

where $\boldsymbol{\sigma}$ and $\boldsymbol{\varepsilon}^p$ are the stress and plastic strain tensors, respectively. Different phenomenological models use different forms of the damage evolution function, f. The damage is assumed to take place once the damage variable reaches its critical value, D_c. Many different functions are suggested by various researchers for phenomenological prediction of the onset of ductile fracture. Some of the suggested phenomenological models are presented and compared with each other by Zadpoor *et al.* (2009b).

An example of the application of the phenomenological models to failure prediction of TWB is the work by Kim *et al.* (2004) where the Oyane's criterion was used to predict the bursting failure of a tailor welded tube made by high frequency electric resistance welding (HF-ERW) of rolled steel. The Oyane's criterion can be expressed as:

$$\int_0^{\varepsilon_{eq,f}} \left(\frac{\sigma_m}{\sigma_{eq}} + C_1 \right) d\varepsilon_{eq} = C_2 \qquad [10.18]$$

where σ_m and σ_{eq} are the mean and equivalent stresses, respectively, and C_1 and C_2 are material-dependent parameters. They realistically concluded that, for the tube studied, the fracture initiates in the HAZ.

A different approach to phenomenological modelling of ductile fracture is the use of continuum damage models that work with a damage tensor, **D**, to account for the progressive development of damage in TWB. For example, Chan *et al.* (2005c) used an anisotropic damage model and damage criterion for analysis of local necking in a laser-welded steel TWB. The elected materials were JIS G3141 steel sheet with thickness ratios of 1.25 (1 mm and 0.8 mm). The damage model was mainly based on the work of Chow and his co-workers (Chow and Wang, 1987; Chow and Wei, 1991a,b; Chow *et al.*, 1997, 2001a, 2001b). The method, which is mainly represented in Chow *et al.* (1997, 2001b), considers all three phases of non-uniform deformation in a unified approach. The method was originally developed for proportional loading (Chow *et al.*, 1997) and was improved to include the effects of non-proportional loading (Chow *et al.*, 2001b). The improved model can account for the strain-path dependency of the forming limit diagram.

Physical models of ductile fracture

Physical models of ductile fracture work directly with nucleation, growth and coalescence of voids. They are also known as Gurson type models (Gurson, 1977). The von Mises yield function is modified to account for the presence and evolution of voids. The modified yield function can be stated as follows (Tvergaard, 1987):

$$\Phi = \left(\frac{\sigma_{eq}}{\sigma_y} \right)^2 + 2\tilde{\alpha} f_{\text{void}} \cosh\left(-\tilde{\beta} \frac{3\sigma_H}{2\sigma_y} \right) - \left(1 + \tilde{\gamma} f_{\text{void}}^2 \right) = 0 \qquad [10.19]$$

where σ_{eq}, σ_H, and σ_y are, respectively, the effective Mises stress, hydrostatic pressure and yield stress of the fully dense matrix material. The parameter f_{void} is the ratio of the volume of voids to the total volume of the material and is called the void volume fraction. Three remaining parameters, namely $\tilde{\alpha}$, $\tilde{\beta}$ and $\tilde{\gamma}$, are experimentally determined material parameters. It is

assumed that there is an initial population of voids in the material that is represented by the initial void volume fraction, $f_{void,0}$. As the material deforms, voids nucleate, grow and coalesce, resulting in contraction of the yield locus. The evolution, of the void volume fraction is due to two contributing phenomena, namely void growth and void nucleation. Therefore, the time derivative of the void volume fraction can be calculated as:

$$\dot{f}_{void} = \dot{f}_{void,gr} + \dot{f}_{void,nucl} \qquad [10.20]$$

where subscripts 'gr' and 'nucl' stand for void growth and void nucleation, respectively. Based on the mass conservation law, the change in the void volume fraction due to void growth can be described as:

$$\dot{f}_{void,gr} = (1 - f_{void})\dot{\varepsilon}^p : \boldsymbol{I} \qquad [10.21]$$

where $\boldsymbol{I}$ is the identity matrix. The void nucleation dynamics is governed by the relationship:

$$\dot{f}_{void,nucl} = \tilde{A}\dot{\bar{\varepsilon}}_m^p \qquad [10.22]$$

where

$$\tilde{A} = \frac{f_{void,N}}{s_N \sqrt{2\pi}} \exp\left[-\frac{1}{2}\left(\frac{\varepsilon_{eq}^p - \varepsilon_N}{s_N} \right)^2 \right] \qquad [10.23]$$

In Equation [10.23], it is assumed that the nucleation strain is normally distributed within the material with a mean value of ε_N and a standard deviation of s_N. The volume fraction of nucleated voids is denoted by $f_{void,N}$. Voids are assumed to nucleate only in tension.

The constitutive equations discussed above are used for modeling TWB during the forming process. A failure criterion is also needed to detect the failure during the forming process. The yield function needs to be modified such that the effects of void evolution and the resulting loss of the stress carrying capacity are taken into account. The yield function can be then rewritten as:

$$\Phi = \left(\frac{\sigma_{eq}}{\sigma_y} \right)^2 + 2\tilde{\alpha} f_{void}^* \cosh\left(-\tilde{\beta} \frac{3\sigma_H}{2\sigma_y} \right) - \left(1 + \tilde{\gamma} f_{void}^{*2} \right) = 0 \qquad [10.24]$$

where the effective void volume fraction, f_{void}^*, is defined as a function of the void volume fraction, f_{void}, as follows:

$$f_{void}^* = \begin{cases} f_{void}, \ f_{void} \leq f_{void,c} \\ f_{void,c} + \dfrac{\overline{f}_{void,f} - f_{void,c}}{f_f - f_c}\left(f_{void,f} - f_{void} \right), \ f_{void,c} \leq f_{void} \leq f_{void,f} \\ \overline{f}_{void,f}, \ f_{void} \geq f_{void,f} \end{cases} \qquad [10.25]$$

where

$$\overline{f}_{\text{void,f}} = \frac{\tilde{\alpha} + \sqrt{\tilde{\alpha}^2 - \tilde{\gamma}}}{\tilde{\gamma}} \qquad [10.26]$$

The critical void volume fraction, $f_{\text{void,c}}$, is the void volume fraction at which the loss of stress carrying capacity starts. The material continues to lose its stress carrying capacity until the void volume fraction reaches the failure void volume fraction, $f_{\text{void,f}}$, at which point the material fails. The Gurson-type constitutive equations are often combined with Marciniak–Kuczynski or bifurcation models to predict the bifurcation localization which is often assumed to be responsible for failure. Bayley and Pilkey combined the Gurson-type constitutive equations with a bifurcation criterion to study the influence of welding effects on the localization behavior and predict weld line failures of an aluminum TWB made from AA5754-O sheets (2.1 and 1.6 mm) (Bayley and Pilkey, 2005, 2006). The sheets were butt welded together by non-vacuum electron beam welding. Chien *et al.* (2003) combined Gurson-type constitutive equations with Marciniak–Kuczynski theory to predict the failure of a laser-welded aluminum (AA5754) TWB.

10.5   Concluding remarks

The overall findings of this chapter can be summarized in a small number of statements:

- The potential benefits of TWB are widely accepted and the area of application will increase further in the next decades.
- The weld lines in TWB usually have a negative impact on the formability of these blanks.
- Good understanding, proper designs and appropriate manufacturing techniques may reduce the decrease in formability.
- The microstructure and mechanical properties of TWB are heterogeneously distributed, hence requiring more advanced methods of material characterization.
- In the design of TWB parts, the position and movement of the weld lines requires special attention.
- Post-weld heat treatment and other innovative post-weld processing techniques can help to improve the formability of TWB.
- The failure of TWB can be predicted using the same theories as for monolithic sheets. However, the calculations should be done for more than one single material as TWB are composed of different zones with different forming limits.

10.6   Future trends

Predicting future trends is subjective. The reader may have other thoughts or visions. Nevertheless, in this paragraph some ideas for the mid-term future are briefly discussed.

First, it is expected that the application of TWB will expand. When the experience increases and more problems are solved, the market for the concept will increase too. In addition, new tailored blank types, markets and applications will emerge.

In this chapter, no attention was paid to elastic phenomena like spring back and residual stresses. But, accurate prediction of the spring back behavior is an important and challenging problem, a problem that must be tackled to improve the quality of products. At the same time, more attention should be given to residual stresses after forming. For TWB these internal stresses are higher and located in areas of minimum formability.

The movement of the weld lines and the control of the weld line movement remains a topic for the future. When TWB become more complex, by adding more materials in one sheet, more thickness variations, and so on, the more complex will be the weld line orientations. This means that it becomes less easy to control the weld lines and to design good controllable weld line orientations.

This chapter is restricted to tailor welded blanks; however, the concept of tailor made blanks (TMB) is wider. As well as TWB, they include blanks with various thicknesses, made by (chemical) machining, or composed of different layers: metal laminates. These TMB are more suitable for small product series. The local thickness variations and bonding can be performed economically only on a small scale. The car industry with its large output may not benefit from these advances, unless the market becomes more and more customer driven.

Other production processes are involved for TMB, processes operating with rigid and soft tools (like rubber forming, hydro forming, etc.) that are very interesting for forming TMB with different thicknesses. The soft tool adapts easily and no additional effort is required to accommodate the thickness steps. These tailor made blanks, the markets and their series numbers, will increase the overall application of TMB and TWB and broaden the field of applications significantly.

10.7   Sources of further information and advice

The literature on TWB is vast and cannot be covered in its entirety. The interested reader is advised to browse through the issues of related journals such as *Journal of Materials Processing Technology*, *Materials Science and Engineering A*, *Metallurgical and Materials Transactions A* and *Journal of*

Engineering Materials and Technology (*Transactions of the ASME*). The Auto Steel Partnership has published a number of reports on the different aspects of design and analysis of TWB, which can be freely downloaded from their website (http://www.a-sp.org/publications.htm) (Team, 1995a,b, 1999, 2001) A review paper by the present authors explores the mechanics of TWB and can be consulted for some additional details that are not covered in this chapter (Zadpoor *et al.*, 2007). A volume edited by Kinsey and Wu tentatively entitled *Tailor welded blanks for advanced manufacturing* is expected to be published by Woodhead Publishing and should cover many more TWB topics.

10.8   Acknowledgements

10.9   References

BAYLEY, C. J. and PILKEY, A. K. (2005). 'Influence of welding defects on the localization behaviour of an aluminum alloy tailor-welded blank', *Materials Science and Engineering A*, **403**, 1–10.

BAYLEY, C. J. and PILKEY, A. K. (2006). 'A bifurcation criterion for predicting weld-line failures in AA5754 alloy tailor-welded blanks', *Materials Science and Engineering: A*, **435–6**, 62–70.

CHAN, L. C., CHAN, S. M., CHENG, C. H. and LEE, T. C. (2005a). 'Formability and weld zone analysis of tailor-welded blanks for various thickness ratios', *Journal of Engineering Materials and Technology-Transactions of the ASME*, **127**, 179–85.

CHAN, L. C., CHENG, C. H., CHAN, S. M., LEE, T. C. and CHOW, C. L. (2005b). 'Formability analysis of tailor-welded blanks of different thickness ratios', *Journal of Manufacturing Science and Engineering-Transactions of the ASME*, **127**, 743–51.

CHAN, L. C., CHENG, C. H., JIE, M. and CHOW, C. L. (2005c). 'Damage-based formability analysis for TWB', *International Journal of Damage Mechanics*, **14**, 83–96.

CHAN, S. M., CHAN, L. C. and LEE, T. C. (2003). 'Tailor-welded blanks of different thickness ratios effects on forming limit diagrams', *Journal of Materials Processing Technology*, **132**, 95–101.

CHENG, C. H., CHAN, L. C., CHOW, C. L. and LEE, T. C. (2005a). 'Experimental investigation on the weldability and forming behavior of aluminum alloy tailor-welded blanks', *Journal of Laser Applications*, **17**, 81–8.

CHENG, C. H., CHAN, L. C., TANG, C. Y. and CHOW, C. L. (2005b). 'Determination of true stress-strain curve for the weldment of aluminum laser-welded blanks', *Journal of Laser Applications*, **17**, 159–70.

CHENG, C. H., JIE, M., CHAN, L. C. and CHOW, C. L. (2007). 'True stress–strain analysis on weldment of heterogeneous tailor-welded blanks – a novel approach for forming simulation', *International Journal of Mechanical Sciences*, **49**, 217–29.

CHIEN, W. Y., PAN, J. and FRIEDMAN, P. A. (2003). 'Failure prediction of aluminum laser-welded blanks', *International Journal of Damage Mechanics*, **12**, 193–223.

CHOW, C. L. and WANG, J. (1987). 'An anisotropic theory of continuum damage mechanics for ductile fracture', *Engineering Fracture Mechanics*, **27**, 547–58.

CHOW, C. L. and WEI, Y. (1991a). 'A damage mechanics model of fatigue crack initiation in notched plates', *Theoretical and Applied Fracture Mechanics*, **16**, 123–33.

CHOW, C. L. and WEI, Y. (1991b). 'A model of continuum damage mechanics for fatigue failure', *International Journal of Fracture*, **50**, 301–16.

CHOW, C. L., YU, L. G. and DEMERI, M. Y. (1997). 'A unified damage approach for predicting forming limit diagrams', *Journal of Engineering Materials and Technology – Transactions of the ASME*, **119**, 346–53.

CHOW, C. L., YANG, X. J. and CHU, E. (2001a). 'Effect of principal damage plane rotation on anisotropic damage plastic model', *International Journal of Damage Mechanics*, **10**, 43–55.

CHOW, C. L., YU, L. G., TAI, W. H. and DEMERI, M. Y. (2001b). 'Prediction of forming limit diagrams for AL6111-T4 under non-proportional loading', *International Journal of Mechanical Sciences*, **43**, 471–86.

CHOW, C. L., JIE, M. and HU, S. J. (2003). 'Forming limit analysis of sheet metals based on a generalized deformation theory', *Journal of Engineering Materials and Technology – Transactions of the ASME*, **125**, 260–5.

DAVIES, R. W., OLIVER, H. E., SMITH, M. T. and GRANT, G. J. (1999). 'Characterizing Al tailor-welded blanks for automotive applications', *JOM*, **51**, 46–50.

DAVIES, R. W., SMITH, M. T., KHALEEL, M. A., PITMAN, S. G. and OLIVER, H. E. (2000). 'Weld metal ductility in aluminum tailor welded blanks', *Metallurgical and Materials Transactions A*, **31A**, 2755–63.

DAVIES, R. W., GRANT, G. J., KHALEEL, M. A., SMITH, M. T. and OLIVER, H. E. (2001). 'Forming-limit diagrams of aluminum tailor-welded blank weld material', *Metallurgical and Materials Transactions A*, **32A**, 275–83.

FENG, J. C., CHENAND, Y. C. and LIU, H. J. (2006). 'Effects of post-weld heat treatment on microstructure and mechanical properties of friction stir welded joints of 2219-O aluminium alloy', *Materials Science and Technology*, **22**, 86–90.

FRIEDMAN, P. A. and KRIDLI, G. T. (2000). 'Microstructural and mechanical investigation of aluminum tailor-welded blanks', *Journal of Materials Engineering and Performance*, 9, 541–51.

GEDNEY, R. (2002). 'Sheet metal formability', *Advanced Materials and Processes*, **160**, 33–6.

GENEVOIS, C., DESCHAMPS, A., DENQUIN, A. and DOISNEAU-COTTIGNIES, B. (2005). 'Quantitative investigation of precipitation and mechanical behaviour for AA2024 friction stir welds', *Acta Materialia*, **53**, 2447–58.

GENEVOIS, C., DESCHAMPS, A. and VACHER, P. (2006). 'Comparative study on local and global mechanical properties of 2024 T351, 2024 T6 and 5251 O friction stir welds', *Materials Science and Engineering A*, **415**, 162–70.

GHOO, B. Y., KEUM, Y. T. and KIM, Y. S. (2001a). 'Evaluation of the mechanical properties of welded metal in tailored steel sheet welded by CO_2 laser', *Journal of Materials Processing Technology*, **113**, 692–8.

GHOO, B. Y., PARK, S. W. and KEUM, Y. T. (2001b). 'New forming limit diagram of laser tailored blank', *Journal of Strain Analysis for Engineering Design*, **36**, 143–52.

GURSON, A. L. (1977). 'Continuum theory of ductile rupture by void nucleation and growth, 1. Yield criteria and flow rules for porous ductile media', *Journal of Engineering Materials and Technology – Transactions of the ASME*, **99**, 2–15.

HATAMLEH, O. (2008). 'Effects of peening on mechanical properties in friction stir welded 2195 aluminum alloy joints', *Materials Science and Engineering A*, **492**, 168–76.

HEO, Y., CHOI, Y., KIM, H. Y. and SEO, D. (2001a). 'Characteristics of weld line movements for the deep drawing with drawbeads of tailor-welded blanks', *Journal of Materials Processing Technology*, **111**, 164–9.

HEO, Y. M., WANG, S. H., KIM, H. Y. and SEO, D. G. (2001b). 'The effect of the drawbead dimensions on the weld-line movements in the deep drawing of tailor-welded blanks', *Journal of Materials Processing Technology*, **113**, 686–91.

HETU, L. and SIEGERT, K. (2005). 'Hydromechanical deep drawing of tailor welded blanks', *Steel Research International*, **76**, 857–65.

JIE, M., CHENG, C. H., CHOW, C. L. and CHAN, L. C. (2007). 'Limit dome height and failure location of stainless steel tailor-welded blanks', *Proceedings of the Institution of Mechanical Engineers Part C-Journal of Mechanical Engineering Science*, **221**, 1497–506.

KAMPUS, Z. and BALIC, J. (2003). 'Deep drawing of tailored blanks without a blank-holder', *Journal of Materials Processing Technology*, **133**, 128–33.

KANG, S. S., MIN, K. B. and KIM, K. S. (2000). 'A study on resistance welding in steel sheets using a tailor-welded blank. I. Evaluation of upset weldability and formability', *Journal of Materials Processing Technology*, **101**, 186–92.

KIM, Y. and PARK, K. (1994). 'A plane-strain punch stretching test for evaluating stamping formability of steel sheets', *Metallurgical and Materials Transactions A*, **25**, 2199–205.

KIM, J. O., SUH, J., HAN, Y. H. and KIM, H. Y. (1996). 'Laser beam welding and formability of steel plate for automobile', *Transactions of the Korea Society of Automotive Engineers*, **4**, 56–69.

KIM, J., KIM, Y.-W., KANG, B.-S. and HWANG, S.-M. (2004). 'Finite element analysis for bursting failure prediction in bulge forming of a seamed tube', *Finite Elements in Analysis and Design*, **40**, 953–66.

KINSEY, B. L. and CAO, J. (1999). 'Adaptive method and apparatus for forming tailor welded blanks', Northern University, USA. US Patent 5941110, 24 August 1999.

KINSEY, B. L. and CAO, J. (2003). 'An analytical model for tailor welded blank forming', *Journal of Manufacturing Science and Engineering – Transactions of the ASME*, **125**, 344–51.

KINSEY, B., LIU, Z. and CAO, J. (1999a). 'New apparatus and method for forming tailor welded blanks', *SAE Transactions: Journal of Materials and Manufacturing*, **108**, 653–60.

KINSEY, B., SONG, N. and CAO, J. (1999b). 'Analysis of clamping mechanism for tailor welded blank forming', *SAE Transactions: Journal of Materials and Manufacturing*, **108**, 1062–8.

KINSEY, B., VISWANATHAN, V. and CAO, J. (2001). 'Forming of aluminum tailor welded blanks', *Society of Automotive Engineers*, *SAE Transactions: Journal of Materials & Manufacturing*, **110**, 673–9.

KINSEY, B., KRISHNAN, N. and CAO, J. (2004). 'A methodology to reduce and quantify wrinkling in tailor welded blank forming', *International Journal of Materials and Product Technology*, **21**, 154–68.

KRISHNAN, K. N. (2002). 'The effect of post weld heat treatment on the properties of 6061 friction stir welded joints', *Journal of Materials Science*, **37**, 473–80.

LEE, W., CHUNG, K.-H., KIM, D., KIM, J., KIM, C., OKAMOTO, K., WAGONER, R. H. and CHUNG, K. (2009). 'Experimental and numerical study on formability of friction stir welded TWB sheets based on hemispherical dome stretch tests', *International Journal of Plasticity*, **25**, 1626–54.

LIU, S. and CHAO, Y. J. (2005). 'Determination of global mechanical response of friction stir welded plates using local constitutive properties', *Modelling and Simulation in Materials Science and Engineering*, **13**, 1–15.

LOCKWOOD, W. D. and REYNOLDS, A. P. (2003). 'Simulation of the global response of a friction stir weld using local constitutive behavior', *Materials Science and Engineering A*, **339**, 35–42.

MARCINIAK, Z. and KUCZYNSKI, K. (1967). 'Limit strains in the process of stretch-forming sheet metal', *International Journal of Mechanical Sciences*, **9**, 609–20.

MEINDERS, T., VAN DEN BERG, A. and HUETINK, J. (2000). 'Deep drawing simulations of tailored blanks and experimental verification', *Journal of Materials Processing Technology*, **103**, 65–73.

MILES, M. P., DECKER, B. J. and NELSON, T. W. (2004). 'Formability and strength of friction-stir-welded aluminum sheets', *Metallurgical and Materials Transactions A*, **35A**, 3461–8.

MIN, K. B. and KANG, S. S. (2000). 'A study on resistance welding in steel sheets for tailor welded blank. Evaluation of flash weldability and formability. II', *Journal of Materials Processing Technology*, **103**, 218–24.

MISHRA, R. S. and MA, Z. Y. (2005). 'Friction stir welding and processing', *Materials Science and Engineering R-Reports*, **50**, 1–78.

MONTGOMERY, A., WILD, P. and CLAPHAM, L. (2004). 'Defect characterisation using magnetic flux leakage inspection of tailor-welded blanks', *Insight*, **46**, 260–4.

PASTOR, M., ZHAO, H., MARTUKANITZ, R. P. and DEBROY, T. (1999). 'Porosity, underfill and magnesium loss during continuous wave Nd : YAG laser welding of thin plates of aluminum alloys 5182 and 5754', *Welding Journal*, **78**, 207s–16s.

ROOKS, B. (2001). 'Tailor-welded blanks bring multiple benefits to car design', *Assembly Automation*, **21**, 323–8.

SATO, Y. S., SUGIURA, Y., SHOJI, Y., PARK, S. H. C., KOKAWA, H. and IKEDA, K. (2004). 'Post-weld formability of friction stir welded Al alloy 5052', *Materials Science and Engineering A*, **369**, 138–43.

SEO, D., CHOI, Y., HEO, Y. and KIM, H. Y. (2000a). 'Investigations of weld-line movements for the deep drawing process of tailor welded blanks', *Journal of Materials Processing Technology*, **108**, 1–7.

SEO, D., KIM, H., HEO, Y., KIM, N. and KIM, H. Y. (2000b). 'Forming and drawing characteristics of tailor welded sheets in a circular drawbead', *Journal of Materials Processing Technology*, **105**, 294–301.

SHAKERI, H. R., BUSTE, A., WORSWICK, M. J., CLARKE, J. A., FENG, F., JAIN, M. and FINN, M. (2002). 'Study of damage initiation and fracture in aluminum tailor welded blanks made via different welding techniques', *Journal of Light Metals*, **2**, 95–110.

SHI, M. F., PICKETT, K. M. and BHATT, K. K. (1993). 'Formability issues in the application of tailor welded blank sheets', *Sheet Metal and Stamping Symposium*, Detroit, Michigan, Society of Automotive Engineers, 400 Commonwealth Dr, Warrendale, Pennsylvania 15096-0001, USA.

SIEGERT, K. and KNABE, E. (1995). 'Fundamental research and draw die concepts for deep drawing of tailored blanks', *SAE Transactions: Journal of Materials and Manufacturing*, **104**, 866–76.

STÖREN, S. and RICE, J. R. (1975). 'Localized necking in thin sheets', *Journal of the Mechanics and Physics of Solids*, **23**, 421–41.

SUTTON, M. A., YANG, B., REYNOLDS, A. P. and YAN, J. (2004). 'Banded microstructure in 2024-T351 and 2524-T351 aluminum friction stir welds: Part II. Mechanical characterization', *Materials Science and Engineering A*, **364**, 66–74.

TEAM, T. W. B. P. (1995a). *Tailor Welded Blank Acceptance Guidelines*. Auto-Steel Partnership, Southfield, MI, USA.

TEAM, T. W. B. P. (1995b). *Tailor Welded Blank Design and Manufacturing Manual*. Auto-Steel Partnership, Southfield, MI, USA.

TEAM, T. W. B. P. (1999). *The Identification and Analysis of Intangible Benefits of Tailor Welded Blank Applications*. Auto-Steel Partnership, Southfield, MI, USA.

TEAM, T. W. B. P. (2001). *Tailor Welded Blank Applications and Manufacturing – A State of the Art Survey*. Auto-Steel Partnership, Southfield, MI, USA.

TOMBERG R. (2007). 'Tailored plaatdelen-vervullen droomwensen automobielindustrie'. *Metaalmagazine*, **8**, 34–5.

TVERGAARD, V. (1987). 'Effect of yield surface curvature and void nucleation on plastic flow localization', *Journal of the Mechanics and Physics of Solids*, **35**, 43–60.

VENKAT, S., ALBRIGHT, C. E., RAMASAMY, S. and HURLEY, J. P. (1997). 'CO_2 laser beam welding of aluminum 5754-O and 6111-T4 alloys', *Welding Journal*, **76**, S275–82.

WAGONER, R. H., CHAN, K. S. and KEELER, S. P. (eds) (1989). *Forming Limit Diagrams: Concepts*, *Methods*, *and Applications*, TMS, Warrendale.

WILD, P. M., ABDULLAH, K., JESWIET, J. J. and GHASEMPOOR, A. (2001). 'Tensile testing for weld deformation properties in similar gage tailor welded blanks using the rule of mixtures', *Journal of Materials Processing Technology*, **112**, 91–7.

WU, N. Q., XIA, C., LI, M., PERRUSQUIA, N. and MAO, S. X. (2004). 'Interfacial structure and micro and nano-mechanical behavior of laser-welded 6061 aluminum alloy blank', *Journal of Engineering Materials and Technology – Transactions of the ASME*, **126**, 8–13.

ZADPOOR, A. A., SINKE, J. and BENEDICTUS, R. (2007). 'Mechanics of tailor-welded blanks: an overview', *Key Engineering Materials*, **344**, 373–82.

ZADPOOR, A. A., SINKE, J. and BENEDICTUS, R. (2008). 'The mechanical properties and microstructure of friction stir welded tailor-made blanks', *Materials Science and Engineering A*, **494**, 281–90.

ZADPOOR, A. A., SINKE, J. and BENEDICTUS, R. (2009a). 'Finite element modeling and failure prediction of friction stir welded blanks', *Materials and Design*, **30**, 1423–34.

ZADPOOR, A. A., SINKE, J. and BENEDICTUS, R. (2009b). 'Formability prediction of high strength aluminum sheets', *International Journal of Plasticity*.

ZHAO, H., WHITE, D. R. and DEBROY, T. (1999). 'Current issues and problems in laser welding of automotive aluminium alloys', *International Materials Reviews*, **44**, 238–66.

ZHAO, K. M., CHUN, B. K. and LEE, J. K. (2001). 'Finite element analysis of tailor-welded blanks', *Finite Elements in Analysis and Design*, **37**, 117–30.

ZHU, X. H., WEINMANN, K. and CHANDRA, A. (2001). 'A unified bifurcation analysis of sheet metal forming limits', *Journal of Engineering Materials and Technology – Transactions of the ASME*, **123**, 329–33.

11
Joining lightweight materials using reactive nanofoils

X. S U N, Pacific Northwest National Laboratory, USA

Abstract: In this chapter, we present the strength and failure modes of reactive NanoFoil® bonded joints for similar and dissimilar lightweight materials. First, solder and braze joints for similar and dissimilar material combinations of steel, aluminum and magnesium are fabricated. Static bond strength tests under tensile shear loading condition are then performed to quantify the bond strength for different material combinations. The through-thickness microstructure changes and modifications by the bonding process are quantified using SEM. Depending on the base material combinations, it is shown that the nanofoil bond strength is comparable to those of the conventional structural adhesive bonds.

Key words: adhesive failure, bonding, bond strength, cohesive failure, energy absorption, nanoscale layers, reactive NanoFoil.®

11.1   Introduction

Advanced joining technology remains the key enabler for original equipment manufacturers to implement new materials for lightweight designs. Currently, fusion welding, resistance spot welding and adhesive bonding are the main joining technologies being used in the automotive production environment. While proven to be reliable in joining conventional materials, these methods present different challenges in joining similar and dissimilar advanced lightweight materials such as advanced high strength steel (AHSS), aluminum and magnesium. For example, the high heat input of fusion welding tends to destroy the designed microstructures of AHSS, rendering less than desirable joint properties and performance.

In this chapter, we present the performance data of an alternative bonding technology, namely, reactive NanoFoil® bonding, for joining automotive related lightweight materials. NanoFoil® is a multi-layer foil typically fabricated through the growth of thousands of nano-scale layers of two or more materials by vapor deposition.[1–3] Initiated by an energy impulse, an exothermic reaction occurs in which the like-like bonds of the atoms of each layer in the foil are exchanged for the more stable unlike bonds between atoms from neighboring layers driven by a reduction in the atomic bond energy. As the atoms of each layer mix, heat is generated, creating a

289

Propagation direction

Reacted foil   Reaction zone   Unreacted foil

Ignition ✳

Thermal
diffusion

Atomic
diffusion
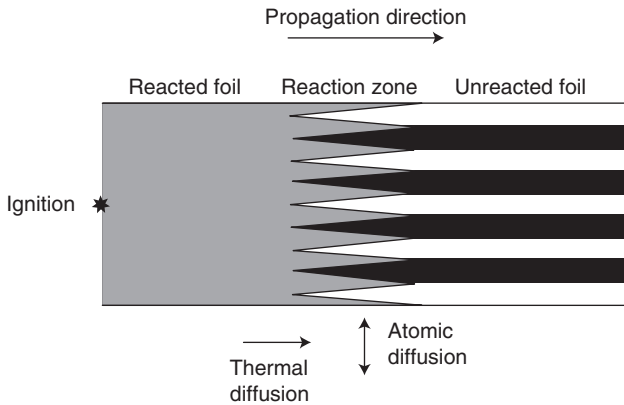
11.1 Schematic illustration of the NanoFoil reaction upon ignition.[1]

self-sustaining reaction traveling along the length of the foil, see Fig. 11.1. Joining applications using this technique can include and range to the following materials and their combinations: steel, aluminum, magnesium and titanium.[1–3] In this chapter, we focus on the bond strength and failure mode evaluations of nanofoil bonded steel, aluminum and magnesium. In addition, a bond strength comparison with conventional structural adhesive will also be presented.

This type of self-propagating high-temperature synthesis (SHS) process was first reported by Russian scientists in the 1960s in Ti and B powder compacts.[4] It was found that the formation of TiB_2 from Ti and B powders produced heat fast enough to propagate across the powder compact. The process was later explored in joining materials and in near-net shape production of hard materials. However, since the characteristic diffusion distance for achieving full particle mixing is controlled by particle size and voids between powder particles, fully self-driven synthesis of powders was often difficult to achieve.

In order to control the diffusion distance between different reactants, fully dense multilayer nanofoils can now be fabricated through modern thin film deposition techniques. The individual layers in a reactive foil are usually on the scale of tens of nanometers and the total number of layers for the nanofoil can be controlled during fabrication, allowing significant control over the heat generation properties of the foil.[1–3] As such, reactive multilayer nanofoils can be used as an accurate, localized and self-propagating heat source to melt solder or braze layers in bonding different materials without compromising the properties/integrities of the base metal.

Because reactive NanoFoil® joining is a new and emerging joining technology, bond strength and failure modes in comparison with the conven-

tional joining techniques need to be established. This information, together with the cost analyses and cycle time studies, will provide designers and manufacturing engineers with the necessary input to determine the feasibility of further applying this emerging technology in a production environment.[5]

11.2   Joint population definition and fabrication

In order to provide an objective evaluation of bond strength between similar and dissimilar lightweight metals bonds, the following material combinations, that is joint populations, are presented in this chapter:

- 1.4-mm SAE1008/1.4-mm SAE1008 solder joint
- 2-mm AA5182-O/2-mm AA5182-O solder joint
- 2-mm AA5182-O/2-mm AA5182-O braze joint
- 2-mm AA5182-O/2-mm AZ31 solder joint.

For each joint population, both non-destructive and destructive bond evaluations are performed to quantify the joint quality in terms of percentage of bonded area, bond strength and failure modes. The tensile shear sample size used in this study is $2'' \times 4''$ (5.1×10.2 cm) with a bonded area of $2'' \times 2''$ (5.1×5.1 cm). Comparisons with conventional adhesive bonded joints are also made.

11.3   Results

11.3.1 1.4-mm SAE1008/1.4-mm SAE1008 solder joint

First, a 96.5Sn–3.5Ag solder material is pre-applied to the bond surfaces on a hot plate using flux. Next, a thin layer of reactive NanoFoil®, slightly larger than the size of the bonded area, is sandwiched between the two bond surfaces. An energy impulse is then applied at one corner of the NanoFoil® by sparking it with a low voltage DC power supply. This method of ignition is used for all the joint populations presented in this chapter. The heat generated by the exothermic reaction of the NanoFoil® self-propagates over the entire bond area, melts the solder material on both sides and forms the bond. All the NanoFoil® used in this chapter is produced by Reactive Nano Technology (RNT) in Hunt Valley, Maryland, USA.

After the bonding process is completed, the bonded region is scanned to ensure bond quality. Figure 11.2 shows the typical scanned image of the bonded region for the 1.4-mm SAE1008/1.4-mm SAE1008 solder joint. The very dark areas correspond to cracks in the NanoFoil® that have been filled up with solder. Only the very bright white areas correspond to voids. The
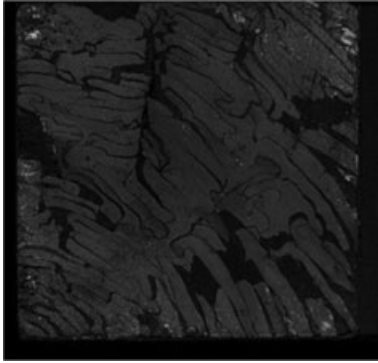
11.2 Scanned image of the bonded area of 1.4-mm SAE1008/1.4-mm SAE1008 solder joint.

bond scan here shows that bonded regions cover more than 99% of the entire surface. Therefore, good quality bonds have been achieved.

A quasi-static bond strength test is performed next by subjecting the bonded sample to tensile shear loading in a servo-hydraulic test frame. Ten samples are tested to examine the strength variation within this joint population. Figure 11.3(a) and (b) show the typical load versus displacement curve and failure mode for the 1.4-mm SAE1008 to 1.4-mm SAE1008 solder joint. Obviously, very high bond strength has been achieved since tensile shear failure for all the samples occurred in the base material. Table 11.1 tabulates the peak load, total displacement and energy absorption of each sample tested. Taking the averaged peak load from these tests and dividing it by the bonded area, it is determined that the nominal bond strength is in excess of 10.6 MPa.

Figure 11.3(c) shows the microstructure of the joint cross-section with different elements illustrated as lines in the scanning electron microscopy (SEM) image. Clearly, the solder (light grey) region is made of Sn and Ag and the central (dark grey) part represents the nanofoil layer with equal composition ratio of nickel and aluminum, indicating that the final reaction product is AlNi.

Since thicker foils can produce more heat upon reaction, Wang *et al.*[1] demonstrated that bond strength can be significantly improved by increasing the nanofoil thickness from 23 μm to 40 μm. They also showed that further increases in the foil thickness do not affect the shear strength of the stainless steel joints, which is approximately constant with an average value of 48 ± 3 MPa, for foil thicknesses ranging from 40 μm to 180 μm. It should be mentioned that the tensile shear strength of nanofoil bonds will also depend on many other factors such as the solder material used and sample

(a)

(b)

(c)
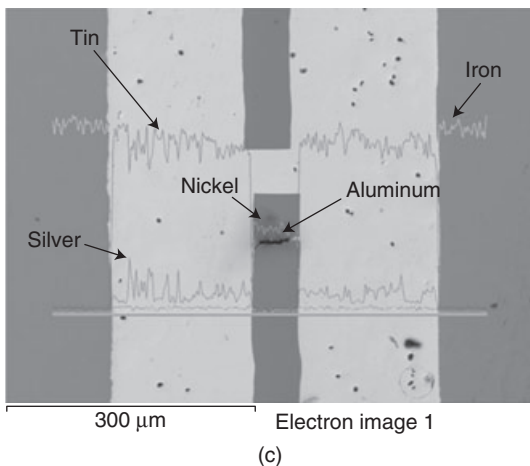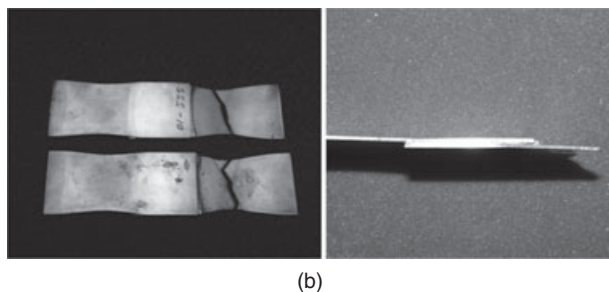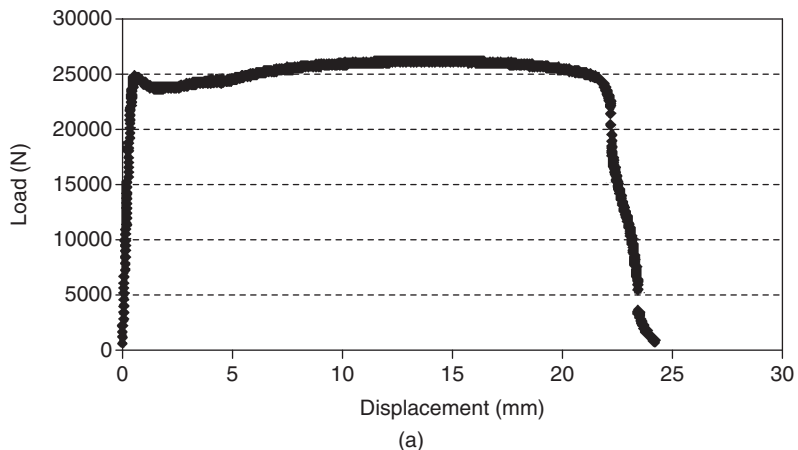
11.3 Typical bond strength test results for the solder joint of 1.4-mm SAE 1008/1.4-mm SAE 1008: (a) load versus displacement curve; (b) failure mode; (c) SEM cross-section of the joint area.

Table 11.1 Peak load, total displacement and energy absorption of the SAE1008 solder joints

Sample no.	Material description	Peak load (N)	Total displacement (mm)	Energy (J)
B-336-SSS-1	Steel to steel, solder	26 167.3	24.21	358.4
B-336-SSS-2	Steel to steel, solder	25 241.8	19.69	285.6
B-336-SSS-3	Steel to steel, solder	26 442.0	26.96	374.4
B-336-SSS-4	Steel to steel, solder	25 218.4	19.90	268.7
B-336-SSS-5	Steel to steel, solder	25 263.0	13.99	203.1
B-336-SSS-6	Steel to steel, solder	26 328.1	27.12	363.0
B-336-SSS-7	Steel to steel, solder	25 924.5	16.05	250.4
B-336-SSS-8	Steel to steel, solder	26 493.2	28.05	378.4
B-336-SSS-9	Steel to steel, solder	25 538.4	14.12	207.0
B-336-SSS-10	Steel to steel, solder	26 341.5	26.98	375.5

surface preparation. Here we note that the strength for the nanofoil bonded populations presented in this chapter for the various material combinations is not optimized.

11.3.2 2-mm AA5182-O/2-mm AA5182-O solder joint

Following similar bonding procedures described above, 2-mm AA5182-O is bonded with 2-mm AA5182-O with solder material 96.5Sn–3.5Ag. The solder material is pre-applied to sample surfaces on a hot plate using mechanical agitation. Again, NanoFoil® is used as the heat source for the actual bonding process. Figure 11.4 shows the typical scanned image of the solder joint with the percentage of the bonded region to be around 99.6%. Five tensile shear samples are made and good bond quality has been obtained with respect to the coverage area.

Figure 11.5(a) and (b) show the typical load versus displacement curve and failure mode for the 2-mm AA5182-O/2-mm AA5182-O solder joint. Cohesive failure at the bond surface and sample bending are consistently observed for all the samples tested, indicating that relatively good energy absorption is provided by the solder joint during tensile shear loading. Table 11.2 lists the peak load, total displacement to failure and energy absorption level for all the five samples tested in the population. Test results in Table 11.2 indicate that there are relatively large variations in peak load and total displacement, leading to large variations in total energy absorption by the solder joints. The nominal bond strength is calculated to be from 6.3 MPa to 9.5 MPa.

Figure 11.5(c) shows the SEM cross-section of the bonded region after the tensile shear test. A rugged fracture surface in the solder material is
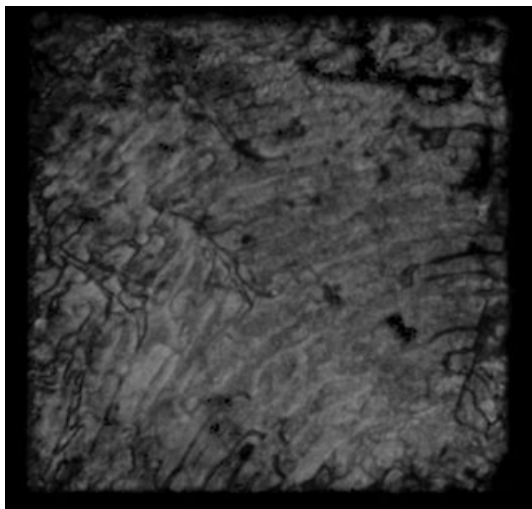
11.4 Scanned image of the bonded area of 2-mm AA5182-O/2-mm AA5182O solder joint.

observed in the SEM caused by the cohesive failure mode. It is interesting to note that most of the Ag element in the solder material is segregated to the edge of the solder interfacing with the AA5182-O substrate. In addition, some acicular Ag needles are also observed in the solder material in Fig. 11.5(c).

11.3.3 2-mm AA5182-O/2-mm AA5182-O braze joint

For this braze joint population, the AA5182-O samples are metalized with 95Ni–5Al via a thermal spray (wire arc spray). The NanoFoil® is coated with thin Ag alloy braze (61.5Ag–23.5Cu–15In) layers. During the bonding process, the braze material is melted by the heat generated by the Nano-Foil,® then sticks to the Ni coating, which does not melt during the bonding process. Figure 11.6 shows the typical scanned image of the braze joint in which about 98% of the area appears to be bonded. Good bond quality has been obtained with respect to the percentage of bonded area.

Again, five samples are bonded and tested in this population and Fig. 11.7(a) and (b) show the typical load versus displacement curve and failure mode for the 2-mm AA5182-O/2-mm AA5182-O braze joint. A cohesive failure at bond surface is consistently observed for all the samples tested, and all the failed samples show bending deformation, indicating ductile bond failure with good energy absorption capability. Table 11.3 lists the peak load, total displacement to failure and energy absorption level for all
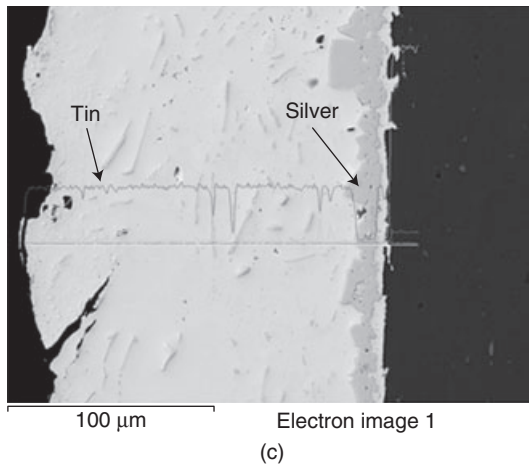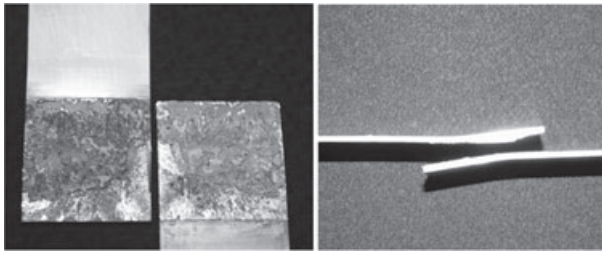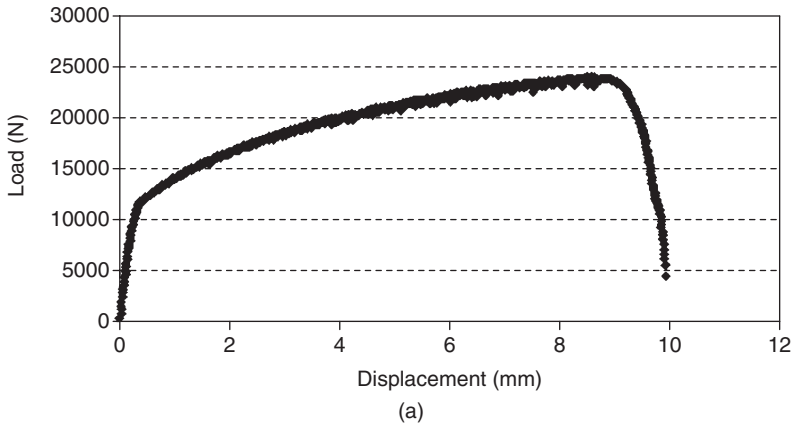
11.5 Typical bond strength test results for the solder joint of 2-mm AA5182-O/2-mm AA5182-O: (a) load versus displacement curve; (b) failure mode; (c) SEM of joint cross-section.

Table 11.2 Peak load, total displacement and energy absorption of the AA5182-O solder joints

Material description	Peak load (N)	Total displacement (mm)	Energy (J)
Al to Al, solder	23 895.5	9.93	164.6
Al to Al, solder	17 216.8	3.33	40.3
Al to Al, solder	18 645.5	4.05	50.9
Al to Al, solder	15 754.8	2.33	24.1
Al to Al, solder	19 234.7	4.73	60.1
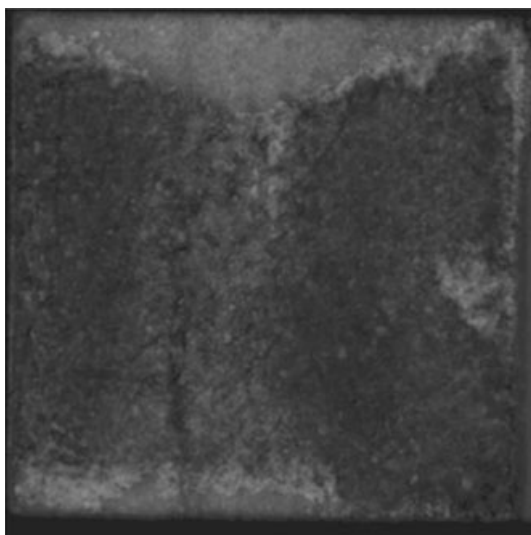
11.6 Scanned image of the bonded area of 2-mm AA5182-O/2-mm AA5182-O braze joint.

the five samples tested in the population. Compared with results in Table 11.2 for the solder joints, the results in Table 11.3 indicate that more consistent joint quality has been achieved in the braze joint with very low variations in peak load and total displacement, leading to less variation in total energy absorption. The nominal bond strength is from 7.5 MPa to 8.02 MPa.

Figure 11.7(c) shows the SEM cross-section of the bonded region after the tensile shear test. Rugged fracture surface in the braze material (nickel) is observed in the SEM caused by the cohesive failure mode. It is interesting to note that the interface between the AA5182-O substrate and the braze layer is also roughened, indicating that the AA5182-O substrate surface was
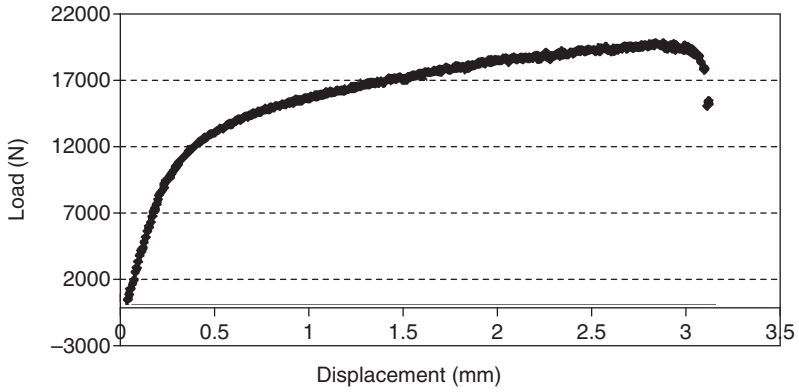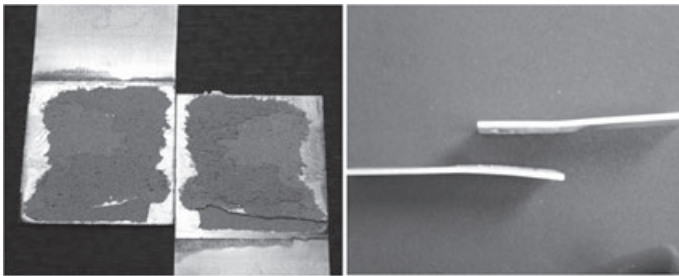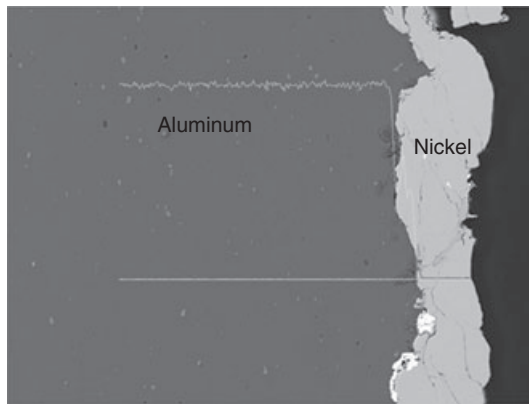
11.7 Typical bond strength test results for the braze joint of 2-mm AA5182-O/2-mm AA5182-O: (a) load versus displacement curve; (b) failure mode; (c) SEM cross-section of the joint area.

Table 11.3 Peak load, total displacement and energy absorption of the AA5182-O braze joints

Material description	Peak load (N)	Total displacement (mm)	Energy (J)
Al to Al, braze	18 770.4	2.41	34.4
Al to Al, braze	18 762.4	2.28	31.6
Al to Al, braze	20 067.6	3.15	45.7
Al to Al, braze	19 772.8	3.12	45.5
Al to Al, braze	19 398.6	2.95	38.0
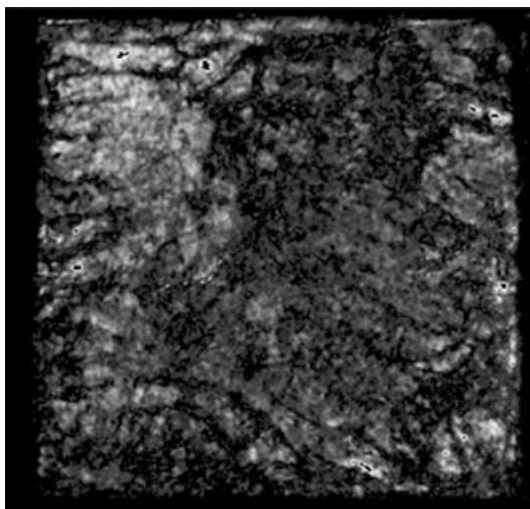
11.8 Scanned image of the bonded area of 2-mm AA5182-O/2-mm AZ-31 solder joint.

deformed by the relatively high temperature and kinetic energy of the thermal spray process.

11.3.4 2-mm AA5182-O/2-mm AZ-31 solder joint

For this dissimilar metals solder population, 96.5Sn–3.5Ag solder material is pre-applied to the aluminum samples on a hot plate using mechanical agitation. On the magnesium side, samples are vapor metallized with Ti/Ag alloy (61.5Ag–23.5Cu–15In) braze, with freestanding Sn–Ag–Cu (SAC) solder sandwiched between metallization and NanoFoil®. Figure 11.8 shows

the typical scanned image of the solder joint. For this joint population, many small bright white regions exist at the bond interface, indicating some degree of lack of bonding. The bonded region is about 96.86% of the total faying area in Fig. 11.8.

Five samples are bonded and examined in this population, and Fig. 11.9(a) and (b) show the typical load versus displacement curve and failure mode for the 2-mm AA5182-O/2-mm AZ31 solder joint. Adhesive failure at the bond surface is consistently observed for all the samples tested, with very little sample bending, indicating a brittle joint with a low level of energy absorption. Table 11.4 lists the peak load, total displacement to failure and energy absorption level for all five of the samples tested in the population. Very low displacements to failure are obtained in these solder joint samples, leading to extremely low levels of energy absorption of the joints in comparison to those of the solder and braze joints presented earlier. In addition, the bond strength variation is also very significant, with the nominal bond strength ranging from 2.86 MPa to 4.9 MPa.

Figure 11.9(c) shows the SEM cross-section of the bonded region after the tensile shear test. A flat fracture surface in the solder material is observed in the SEM owing to the adhesive failure mode. It is interesting to note that some degree of Ag element segregation also occurred near the Sn–Ag solder/AA5182-O interface. In addition, some large blocks of Ag occurred near the solder/Al interface, compared with the Ag needles observed in Fig. 11.5(c).

In order to improve the bond strength and its consistency, an improved surface preparation technique is next explored for both the aluminum and the magnesium surfaces. A Sn layer of 0.015 +/− 0.002″ (0.38 mm +/− 0.05 mm) thickness is deposited on the aluminum plate using thermal spray process. On the magnesium side, a Ni/Al (95/5 blend) layer of 0.01 +/− 0.002″ (0.254 mm +/− 0.05 mm) thickness is thermally sprayed on the Mg surface. The two surfaces are then bonded together using reactive Nano-Foil® as a heat source. Four samples are bonded in this improved Al/Mg population. Figure 11.10 shows the typical scanned image of the solder joint. Better bond quality has been obtained with respect to the percentage of bonded area in comparison with Fig. 11.8.

Quasi-static bond strength tests are then carried out with a servo-hydraulic load frame. Figure 11.11(a) and (b) show the typical load versus displacement curve and failure mode for the improved 2-mm AA5182-O/2-mm AZ31 solder joint. A cohesive failure at the bond surface is consistently observed for all the samples tested. Table 11.5 lists the peak load, total displacement to failure and energy absorption level for all the four samples tested in this improved bond population. Compared to results in Table 11.4, much more consistent joint strength and much higher displacements to failure have been achieved with the improved surface preparation. The
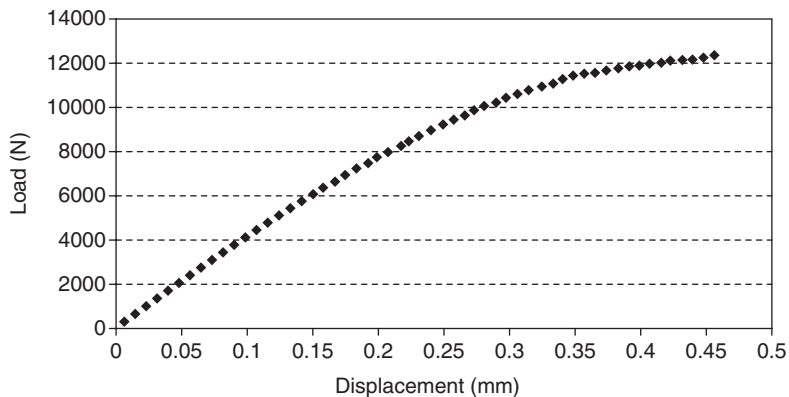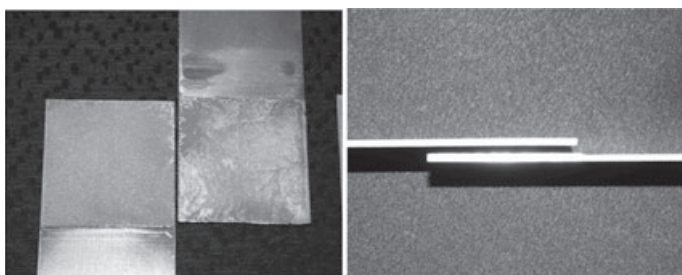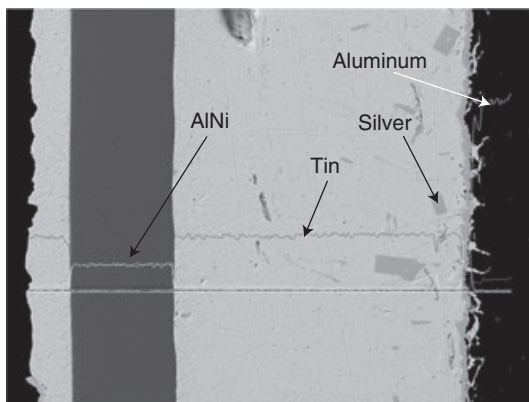
11.9 Typical bond strength test results for the solder joint of 2-mm AA5182-O/2-mm AZ31: (a) load versus displacement curve; (b) failure mode; (c) SEM cross-section of the joint area.

Table 11.4 Peak load, total displacement and energy absorption of the original 2-mm AA5182-O/2-mm AZ-31 solder joints

Material description	Peak load (N)	Total displacement (mm)	Energy (J)
Al to Mg, solder	7 425.2	0.22	0.8
Al to Mg, solder	10 871.1	0.34	2.1
Al to Mg, solder	12 311.4	0.46	3.5
Al to Mg, solder	7 161.0	0.22	0.9
Al to Mg, solder	9 917.2	0.27	1.4
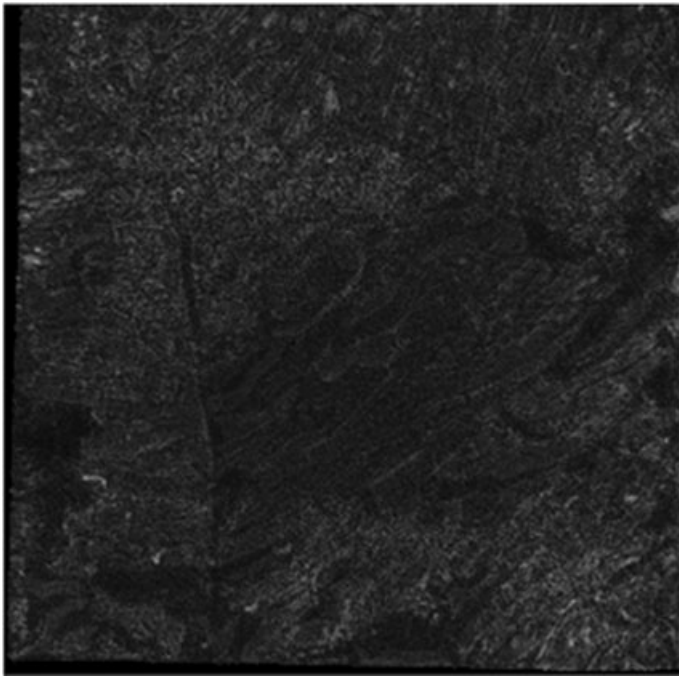
11.10 Scanned image of the bonded area for improved Al/Mg bond.

nominal bond strength measured is from 6.4 MPa to 7.0 MPa, which is comparable to those presented earlier for the Al5182-O/Al5182-O solder and braze joints, although the energy absorption level is still lower than those joints owing to the lower total displacements to failure.

(a)

(b)
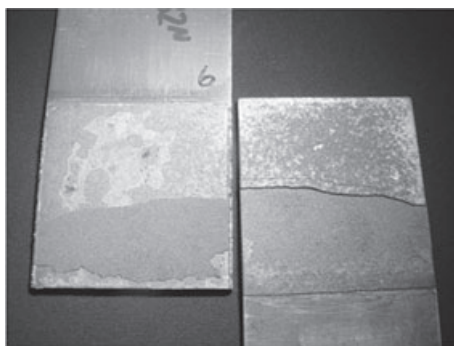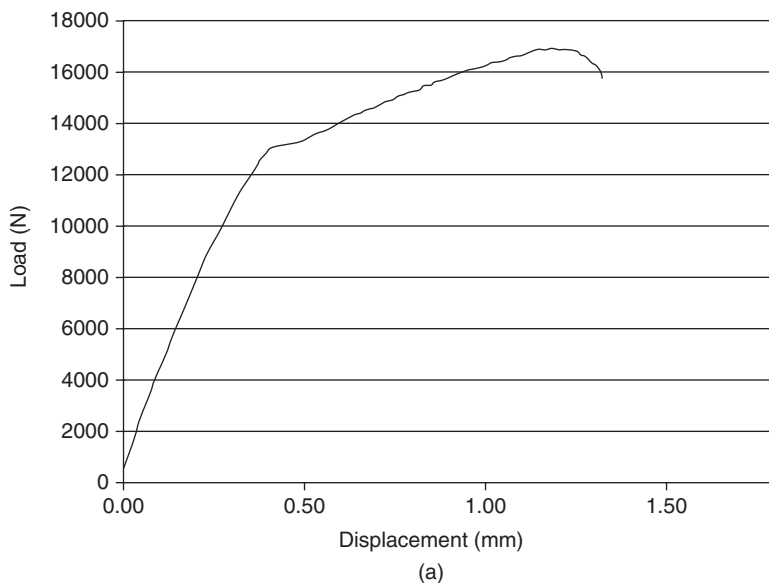
11.11 Typical bond strength test results for the improved solder joint of 2-mm AA5182-O/2-mm AZ31: (a) load versus displacement curve; (b) failure mode.

Table 11.5 Peak load, total displacement and energy absorption of the improved 2-mm AA5182-O/2-mm AZ-31 solder joints

Material description	Peak load (N)	Total displacement (mm)	Energy (J)
Al to Mg, solder	16582.8	1.37	17.3
Al to Mg, solder	16922.7	1.32	17.1
Al to Mg, solder	15888.7	1.10	13.1
Al to Mg, solder	17547.8	1.68	22.6

11.4   Comparison with automotive adhesive bonds

Figure 11.12(a) shows the typical joint strength test data for Dow Betamate 4601 and Betamate 1480 structure adhesives joining 2-mm AA5182-O to 1.6-mm DP600 steel.[6] Under tensile shear (lapshear) loading condition, the cohesive failure mode is consistently observed, see Fig. 11.12(b) and the nominal bond strength is around 7.2 MPa.

These results indicate that the bond strength achieved by the reactive NanoFoil® bonded solder and braze joints between similar and dissimilar metals are comparable to those of the structural adhesives typically used in the automotive industry. Note again that the bond strength is not opti-

(a)

(b)
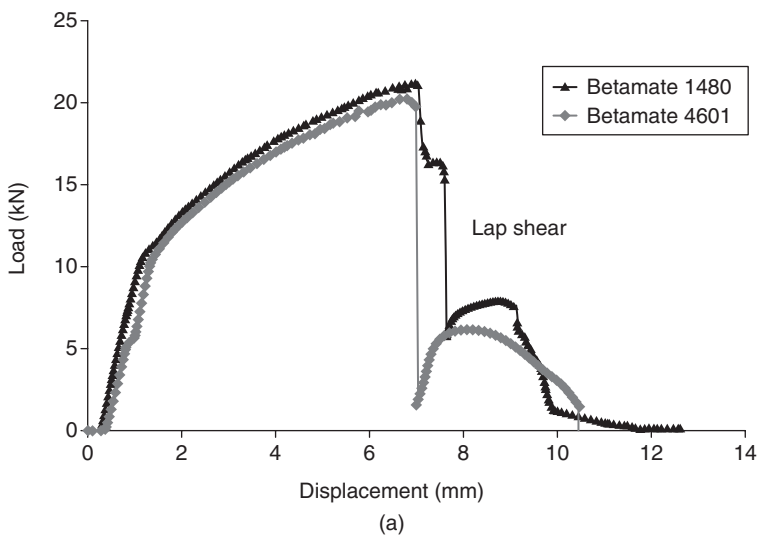
11.12 Bond strength test results for Dow Betamate 4601 and Betamate 1480 joining 2-mm AA5182-O to 1.6-mm DP600: (a) load versus displacement curve; (b) failure mode.

mized in this chapter. Since both bonding methods can produce hermetic joints, the specific advantage of using reactive nanofoil bonding therefore lies in the fact that it does not require the typical curing process that is required by the adhesive bonding process.

11.5 Conclusions and discussion

By comparing the bond strength of the four NanoFoil® bonded populations with those of the structural adhesives, the following observations and conclusions can be made:

- Similar bond strength can be obtained using reactive NanoFoil® bonding for the 2-mm AA5182-O/2-mm AA5182-O solder and braze joints and the 2-mm AA5182-O/2-mm AZ321 solder joints. The bond strength of the 1.4-mm SAE1008/1.4-mm SAE1008 solder joint is much higher than those for the aluminum and magnesium populations.
- The bond strength variation is higher for the solder joints than for the braze joints.
- The bond energy absorption level for the Al/Mg joints is consistently lower than that of similar material joints owing to low displacements to failure.
- NanoFoil® bonded joints can achieve a similar level of strength as those using the structure adhesive typically used in the automotive industry.

Note again that the bond strength is not optimized in this chapter and further strength improvements can potentially be achieved by enhanced surface treatment and optimized nanofoil thickness. In addition to the performance data presented in this chapter, wider and more rapid application of reactive nanofoil bonding technology will also depend on the cost and cycle time of this technology in mass production.

11.6 References

1. WANG, J., BESNOIN, E., DUCKHAM A., SPEY, S.J. REISS, M.E., KNIO, O.M. and WEIHS, T.P. *J. Appl. Phys*., **95**(1), 248–56, 2004.
2. DUCKHAM A., SPEY, S.J., WANG, J., REISS, M.E., WEIHS, T.P., BESNOIN, E. and KNIO, O.M. *J. Appl. Phys*., **96**(4), 2336–42, 2004.
3. QIU, X. *Reactive Multilayer Foils and Their Applications in Joining*, MSE Thesis, Louisiana State University, 2007.
4. MERXHANOV, A.G. *Combustion and Plasma Synthesis of High-Temperature Materials*, Z. A. Munir and J. B. Holt (eds), VCH, New York, 1–53, 1990.
5. SUN, X. and DUCKHAM, A. 'Strength evaluation of reactive nanoFoil bonded joints for automotive applications', *Proceedings of the XIII Sheet Metal Welding Conference*, Livonia, Michigan. May 14–16, 2008.
6. US DEPARTMENT OF ENERGY, *Joining of Dissimilar Metals for Automotive Applications: From Process to Performance*, US Department of Energy Automotive Lightweighting Materials Program, FY2004 Annual Progress Report, 2004.

Index

www.iran-mavad.com

مرجع دانشجویان و مهندسین مواد